COMPOSITE THERMAL STORAGE MATERIAL FABRICATION BY COLD SINTERING PROCESS

by

SULEIMAN BILYAMINU

A thesis submitted to The University of Birmingham

DEGREE OF DOCTOR OF PHILOSOPHY

School of Chemical Engineering
College of Engineering and Physical Sciences
The University of Birmingham,
Edgbaston, Birmingham UK
April 2022

ABSTRACT

In the 21st century, energy is critical to the world overall development agenda. Its daily requirement is always increasing to satisfy the global population growth and the rapid change in the standard way of living. The world major source of energy is fossil fuel which is gradually depleting and is largely associated with numerous environmental consequences responsible for global temperature rise. To achieve sustainable economic development of our society, there is an urgent need for efficient energy utilization, development of reliable technologies and use of sustainable renewable and clean energy sources. The supply of electrical energy from renewable sources is intermittent and its integration into the existing supply network requires energy storage technology which is reliable and environmentally friendly. The present thermal energy storage technologies storing heat in either solid materials or phase change materials (PCM) cannot meet the conflicting requirements of high energy storage density, fast charging/discharging rate, and low temperature drop. Sintering method to fabricate composite PCMs is limited by high temperature requirement and mismatch in melting temperature limiting proper material sintering and integration. Thus, there is the need to develop a new innovative method for the fabrication of an efficient composite thermal energy storage materials with the desired mechanical, structural, and thermal properties.

In this research work, the fundamental mechanism of a highly innovative and novel cold sintering approach was proposed and studied for the fabrication of composite PCMs suitable for energy charging and discharging in a direct-contact heat transfer multi-layered thermal stores system. The study comprises of the fabrication of form stable composite Al_2O_3-NaCl storage materials at low temperature sintering ≤300 ℃ to overcome the inherent high temperature requirement. The limit and influence of the major cold sintering process (CSP) parameters were investigated. Also, the Microstructure, and mechanical properties of cold

sintered porous alumina ceramics was studied as an alternative approach to develop a strong and porous structural scaffolding. The mechanism of the cold sintering process of Al_2O_3-NaCl composite is proposed from experimental understanding and theoretical defect chemistry analysis.

Results of this study showed that a very high dense Al_2O_3-NaCl composite thermal storage material with relative density of ~99% close to theoretical consistent with its microstructural observation. The composite mass ratio of 1:1 cold sintered with 30 wt% water had phase change enthalpy of 252 J/g consistent to the theoretical NaCl latent heat. The maximum limit of CSP parameters determined by single variable optimization to achieve desired composite density without failure during thermal cycle are the CSP temperature of 250℃, 400MPa pressure, 30 wt% water, and dwelling time of 90 minutes. The composite phase structure consists of Al_2O_3 and NaCl species only and the peak intensity of all species reduced and disappeared in the case of alumina at high 2θ positions. The FTIR spectrum shows a gradual decrease in peak intensity from dry pressed to the mix and to the cold sintered pellet. The dry pressed and cold sintered composite dissolved when placed in water. The CSP-post annealed composite at 850℃ remain undissolved in water signifying the beginning of alumina sintering. It sintered more with itself with increase in annealing temperature, but NaCl volatilized leaving a complete sintered porous alumina structure. Several repeated SEM-EDS analyses of CSP-POST annealed samples at 850℃ shows presence of only Al, O and Na at many grain boundaries. NaCl completely volatilized at 1200℃ to form a highly porous alumina with 48% maximum porosity, good mechanical, and structural properties. At 48% maximum porosity, the porous alumina had mechanical strength of 17.63 MPa. Further increase in annealing temperature to 1300℃, 1400℃ and 1500℃, its excellent mechanical strength increases to 36.57, 111.47 and 137.21MPa with corresponding porosity of 41%, 29% and 28% respectively. Experimental evidence from phase structure, microstructure, EDS and FTIR analysis combined with literature evidence of alumina insolubility in molten salt provide guides to the proposed CSP mechanism from the perspectives of defect chemistry, a lattice phenomenon. Conclusively, at CSP stage, full composite densification was achieved, and species interaction created modifications which at elevated temperature of 850 ℃ begin to cause sintering of alumina at temperature much lower than its conventional sintering temperature. The NaCl complete volatilization at 1200℃ provides a new innovative way to fabricate a strong porous ceramic structure that could be used as matrix support for PCMs for medium to high temperature application. Meanwhile, the proposed mechanism from the perspective of defect chemistry in addition to plastic deformation and dissolution precipitation process revealed the beginning of CSP complex mechanism understanding. It requires further attention to fundamentally explore different chemistries behaviour under CSP conditions. Finally, fabrication of composite thermal energy storage materials is compatible to CSP but requires further investigation to fully encapsulate PCMs.

ACKNOWLEDGEMENT

All praises and adorations are unconditionally due to Allah (SWT) for his guidance, protection, blessings and help to complete this thesis writing. We praise him and we always seek for his help and forgiveness. May the mercy and blessings of Allah be upon the noble prophet Mohammed (SAW), his households and companions.

My sincere and honest gratitude goes to my supervisor Professor Yongliang Li for his continuous guidance, support, patience, motivation, and invaluable contribution to knowledge. His experience, support and guidance helped me from the experimental stage to the writing stage and his motivation to write journal is well acknowledged.

My sincere and honest gratitude also goes to my second supervisor Professor Yulong Ding for his invaluable support and encouragement throughout the period of my PhD research and for his role as the director of Birmingham Centre for Energy Storage.

My sincere appreciations and prayer go to my dear parents; Alh Suleiman Ibrahim Mai-Rake (May Allah grant him Jannatil Firdausi ameen), to my mother for her love and continuous prayer, my wife and children for their patience, love, and to my friends for their moral support during my PhD study.

Finally, I would like to specially thanks the Nigerian Government through the Petroleum Technology Development Fund for the PhD scholarship award. Similarly, my appreciation also goes to the Usmanu Danfodiyo University Sokoto for the study fellowship award and to the staff and management for all their support.

PUBLICATIONS

Suleiman, B., Q. Yu, Y. Ding and Y. Li (2019). "Fabrication of form stable NaCl-Al2O3 composite for thermal energy storage by cold sintering process." Frontiers of Chemical Science and Engineering 13(4): 727-735.

Yu, Q., Z. Jiang, L. Cong, T. Lu, B. Suleiman, G. Leng, Z. Wu, Y. Ding and Y. Li (2019). "A novel low-temperature fabrication approach of composite phase change materials for high temperature thermal energy storage." Applied Energy 237: 367-377.

Suleiman B, H Zhang, Y.Ding, Y Li (2022) . Microstructure and mechanical properties of cold sintered porous alumina ceramics. Ceramics International 48(10): 13531-13540.

Table of Contents

LIST OF FIGURES

LIST OF TABLES

ABBREVIATIONS AND GREEK SYMBOLS

EA	Activation energy
k	Boltzmann constant
ρ_b	Bulk density
CPCM	Composite phase change material
CSP	Cold sintering process
CSPed	Cold sintered
ΔG	Change in free energy
ρ	Density
D	Diameter
ε_r	Dielectric constant
tan δ	Dielectric loss
EG	Expandable graphite
E_{es}	Energy storage efficiency
σ_0	Effective strength
λ	Electrical conductivity
σ_0	Exponential factor constant
P_x	Empty orbital
FAST	Field assisted sintering technology
FS	Flash sintering
R_g	Grain resistance
R_{gb}	Grain boundary resistance
c	Geometrical dimensionless constant
T_g	Glass transition temperature
$\boldsymbol{c'}$	Geometric constant

HDPE	High-density polyethylene
HIP	Hot isostatic pressing
HP	Hot pressing
HT	Heat treatment
KPFM	Kelvin Probe Force Microscope
LPS	Liquid phase sintering
L_v	Latent heat of vaporization
T_m	Melting temperature
$\bar{s}$	Molar surface
$\bar{s}_{nm}$	Molar surfaces of nanoparticles
$\bar{s}_{\mu m}$	Molar surfaces coarse particles
P_f	Maximum applied load at fracture
$\boldsymbol{a}$	Macroscopic (or critical) flaw size
y	Mechanical property at porosity P
y_0	Mechanical property at porosity P=0
P_S	Probability of survival
PCM	Phase change materials
K_{sp}	Product solubility constant
RT	Room temperature
R	Resistance
R_0	Pre-exponential resistance
SS	Structural support
SPS	Spark plasma sintering
T	Temperature
TCE	Thermal conductivity enhancer

TES	Thermal energy storage
t	Time
σ_t	Tensile strength
ρ_T	Theoretical density
VC	Volumetric capacity
V	Voltage
σ	Strength
Hv	Vickers Pyramid Number
m	Weibull modulus
δL	Widths of liquid bridges
δ_{gb}	Widths of solid bridges
XRT	X-ray tomography

CHAPTER ONE

INTRODUCTION

1.1 Background of Study

Energy is currently an essential resource for human life globally [1]. The quest to develop reliable, sustainable, and affordable energy storage system to satisfy the growing energy demand, recover industrial waste energy and utilize the abundant renewable energy resources is the most desirable. The energy waste is a great loss of valuable resources that can be captured, stored, and utilized. This has made energy storage devices such as electrochemical energy storage [2] and thermal energy storage devices [3, 4] relevant for efficient and flexible energy utilization. Storage of energy presently relies heavily on electrochemical energy with Li ion batteries as the leading brand characterized by high energy storage potentials in the current vast energy storage market. Batteries are known to have high energy density but are limited by cost and its environmental pollution associated with its disposal, especially the lead type [5]. Thermal energy storage (TES) systems are generally proven to be reliable and more environmentally friendly [6]. Globally, intermittent supply of renewable energy and mismatch between electricity supply and demand could be addressed using latent heat TES system made up of phase change materials (PCMs). PCMs can absorb and release large amount heat as it changes phase from solid to liquid or the reverse [3, 7, 8]. The thermophysical requirements of any PCM are its thermal conductivity, specific heat capacity, coefficient of thermal expansion, density, cycling stability, availability, costs, and production methods [9]. However, direct use of PCMs such as the molten salts are limited due to corrosion during storage and transport, chemical incompatibility, and poor thermal conductivity. The direct use of highly conductive materials proposed is quite ineffective to prevent against leakage of molten salts PCMs [1]. More so, the composite structure is mechanically weak due to physical incompatibility resulting from poor dispersion of conductivity enhancer like carbon materials leading to a porous structure without support. These are usually addressed using composites PCMs (CPCMs) made up of molten salts PCMs, high thermal conductivity enhancer (TCE) and structural support (SS) materials [1, 10, 11]. According to Li *et al.* [12], CPCMs are fabricated via three known methods: 1) mixing of milled PCM(s), TCE and SSM followed by shaping and sintering [1]; 2) mixing of milled SSM and TCE, shaping the mixture for sintering and subsequent vacuum infiltration of the molten salt into the porous structure [13, 14] ; 3) shaping the SSM, sintering to achieve porous structure and subsequent infiltration of the molten PCM-TCE mixture [12].

The composite PCMs are being studied for a wide range of application temperature. Low temperature composite PCMs are mostly investigated. High temperature latent heat storage systems are expected to be used in mass as future storage systems, hence requires extensive study to meet current and future requirements of thermal energy storage. The high temperature PCMs are characterized by high energy density, constant charging, and high discharge temperature. However, they are yet to be commercialized due to the high cost of the technology development and low thermal conductivity limiting their energy charging and discharging rate [15]. Furthermore, mismatch in the composite material melting temperature limits proper sintering of the matrix structural support material which is usually ceramic with high sintering temperature in excess of the PCM melting point [16]. Thus, limits the cyclability of the composites as it experiences structural deterioration due to defects emanating from improper sintering. The high temperature CPCMs experimentally studied and reported are the PCM-metal foam and PCM-graphite composites for thermal conductivity and structural support enhancement. Others are the PCM-metal oxide and PCM-nanocomposites for structural support and properties improvement respectively [17]. The PCM-metal oxide composite improves handleability and are fabricated either by sol-gel [18], melting infiltration [19, 20] and sintering method which is the most researched and sought for technique to fabricate PCM-metal oxide composites [17].

Sintering is a process of particulate matter consolidation into a solid compact form via diffusional processes to lower surface free energy through competitive processes of densification and coarsening with the aid of thermal energy [21]. The use of sintering process at high temperature to fabricate ceramics by mankind can be dated back to the upper Palaeolithic period as proven by the archaeological sites found containing assembled ceramic artefacts at Dolni Vêstonice, Czech Republic [22, 23]. Presently, attempts are being made to lower the energy budget of industrial processes such as in the sintering processes of ceramic particulate materials which according to [24] and [25] cited by [26] requires about 50-75% of its melting temperature to sinter within several hours or days. The mechanism of different sintering processes ranging from solid state to liquid phase and to pressure assisted sintering processes under hot pressing have been reported extensively from experimental and theoretical modelling perspectives [27, 28].

In conventional solid-state sintering, viscous flow is the major rate controlling mechanism in amorphous and glass materials. Meanwhile, crystalline materials are characterized by six mechanisms namely surface diffusion, vapour transport, lattice diffusion from particle surface, grain boundary diffusion, plastic flow, and lattice diffusion from the grain boundary [27, 28]. The later three mechanisms are the densifying mechanisms encouraging neck growth and shrinkage while the former leads to neck growth and particle coarsening only, a situation responsible for undesired porosity in most applications. In liquid phase sintering process, particle rearrangement, dissolution-precipitation and Ostwald ripening are the three overlapping stages and the latter two are the key densification mechanisms. The solution-precipitation and Ostwald ripening densification mechanisms could both be diffusion control mechanisms or phase boundary reaction rate control mechanism in the case of solution-precipitation [27, 29]. However, externally applied pressure in most hot-pressing enables new mechanisms or trigger the existing mechanisms such as the lattice diffusion, grain boundary diffusion, plastic deformation, viscous flow, grain boundary sliding and particle rearrangement mechanisms [27, 28]. The controlling mechanism of pressure assisted sintering could be diffusional or plastic deformation depending on the densification rate under the applied stress.

Sintering has received much attention and its recent development have led to several appealing techniques to lower sintering temperature and /or time scale. These include pressure enhanced sintering [30, 31], microwave sintering [32], flash sintering [31, 33], spark plasma sintering (SPS), SPS/Field assisted sintering technology [34], liquid phase sintering (LPS) [35] and recently cold sintering process (CSP). The term cold sintering process is an emerging technique recently developed by Randall et al. to sinter ceramics, ceramics-based composites, and other materials for various applications [36, 37]. Its discovery by Randall et al. at State University of Pennsylvania is recognized as the long-awaited low-temperature fabrication route, which is the most sought for and emerging technique presently receiving greater research attention. CSP could provide the much-needed opportunities for researchers in materials fabrication to address issues regarding high energy consumption, high temperature limiting material integration, high cost, use of sophisticated experimental setup, variation in stoichiometry, properties, and structure. It will further explore all possibilities of integration and synthesis of different chemistries that could together enables revolutionization of the material industry [38].

CSP has been described as the densification process of inorganic powder particles within short time in the presence of a small liquid phase, creating particle dissolution-precipitation under uniaxial pressure in MPa scale at temperature ≤300 °C [26, 38]. This method has been described as a pressure assisted liquid phase sintering at low temperature characterized by complex mechanisms [26, 38, 39]. The predominant is the dissolution-precipitation mechanism aided by transient liquid phase to achieve high densification [40], homogenous structure [41] and excellent mechanical properties comparable to those obtained from the conventional sintering method [42]. CSP has so far been applied in the fabrication of several materials such as the ferroelectrics [38], electrolyte materials [43], thermoelectric materials [40], microwave dielectric materials [44], refractory [45], and structural ceramics [46]. Recently, Al_2O_3-NaCl composite TES materials fabricated by CSP method were also reported [47-49].

A growing body of literature has shown that since the discovery of CSP, several research efforts have been made to advance the understanding of CSP with respect to material compatibility [26, 38, 50], influential variables, experimental routes and fundamental mechanisms [38, 50-53]. However, it is apparent that the understanding of cold sintering process since its discovery is still at its infant stage requiring greater research attention to unveil its underlying mechanisms yet not very clear.

Several approaches were reported to identify and establish the sintering mechanism, namely method of determining stress exponent [27, 28] grain growth exponent [54] and stress stepping method reported by Zhang *et al.* [55] during uniaxial compaction creep study of a wet granular calcite. However, CSP is a complex process influenced by both powder characteristics (composition, crystal structure, particle size and its distribution), transient liquid (type, amount, pH etc.) and processing parameters (temperature, pressure, heating/cooling rates and dwelling time). None of these methods reported alone could provide the desired explanation regarding CSP underlying and rate controlling mechanisms as several assumptions were made for simplification, given less information than expected with some compromises. Though, these methods put together within their limitations are adequate to identify the main underlying and rate controlling mechanisms. Thus, it forms the basis which most theoretical models were proposed and studied to model sintering process with varying assumptions at various stages.

The link between CSP and LPS is an instant relationship based on their process similarities. The mechanism of LPS is fully established and its process parameters are fully documented in literature [56, 57]. The successful densification of most of the cold sintered material chemistries to or near theoretical densities depends on the choice of the appropriate combination and proper understanding of the nature of interaction between the liquid transport phase (transient medium) and powder specie(s). The liquid transport phase is introduced into the powder by either adding required amount into the powder and mixing to achieve a homogenous mixture or to press powder compact and expose it to the liquid phase by vapour transport such as in the CSP of high water soluble NaCl [26]. In the former, enough liquid enables adequate capillary forces and transport routes responsible for particles redistribution influenced by applied uniaxial pressure. Meanwhile, in the latter process, a compact exposed to the liquid in the absence of external pressure influence are all sintered to or close to theoretical density. The presence of the liquid phase introduces complex mechanisms comprising of liquid-aided lubrication [35, 56], thick second phase formation on the powder surface [58], liquid-aided dislocation motion and recrystallisation [59, 60], lattice disorder formation by water-powder reaction [51, 54, 61] and liquid phase-aided pore shape adjustment [62]. The application of applied external pressure during CSP add to the several forces acting during hot pressing and drive the compaction of the powder towards minimization of its surface free energy.

Several efforts were made to explore CSP mechanism from its current understanding as well as experimental and theoretical perspectives of liquid and pressure enhanced sintering. Guo *et al.* [26] described dissolution-precipitation mechanism of CSP in three stages comprising of particle rearrangement-dissolution, dissolution-precipitation and Ostwald ripening that dominates the microstructure. The descriptions made are based on the early CSP studies and the current understanding of liquid phase sintering theory. These are further supported by the microstructural observations reported in CSP studies. Among all the materials cold sintered, CSP mechanism of ZnO is the must studied. Funahashi *et al.* [54] determined the grain growth exponent of cold sintered ZnO and was found to be consistent to the values reported for conventional solid-state sintering. However, limited understanding of the CSP and absence of literature reported grain growth exponent of similar system within the scope of CSP, limits the authors conclusion on the rate controlling mechanism. The growing research attention and availability of data on ZnO CSP has made Jesus and his co-workers to unveil the mechanism of cold sintered ZnO using water at 250 °C via Kelvin Probe Force Microscope (KPFM) boundary characterization and varied applied external stress [51]. Guillon and his co-workers concluded that solution-precipitation mechanism proposed by Randall and his co-workers is not adequate to fully activate densification of ZnO. According to Gonzalez-Julian *et al.* [39], densification results from high concentration of defect at the grain boundary. This provides diffusion path that aids transport and subsequent sintering at low temperature and addition of acetate further speed the process and enhances the densification due to large grain growth. Gonzalez-Julian *et al.* [39] determined strain rate at three different close pressure and temperature ranges to maintain a constant grain size. A point density was selected around which densification was determined and plotted as a function of effective stress. The stress exponent n, determined >1 as the slope of the plot differs significantly to the stress exponent determined by Langer *et al.* [63] in an electric field-assisted sintering and hot pressing of ZnO. Thus, the authors were unable to speculate or draw any conclusion on the FAST/HP sintering mechanism involved based on the stress exponent. However, the observed variations according to Bordia *et al.* [27] signifies that different experimental conditions influences different mechanisms. Consequently, Jesus and co-workers suggest that stress exponent >1 signifies presence of multiple mechanisms consistent to ZnO solid state sintering. Hydrothermal assisted CSP densification of $BaTiO_3$ has also been widely investigated but its mechanism understanding remains controversial even though diffusion reaction and dissolution-precipitation were proposed [21]. The later CSP path is assisted by epitaxial growth based on the observed chemical mapping that shows uniform distribution of Ti element in a glass phase.

The key synthesis parameters that influences CSP mechanisms and enable parameter-property-structure relationship to be established are the type of material, solvent and processing parameters [64]. Cong *et al.* [65] studied the effect of dwell time on cold sintered $0.9K_{0.5}Na_{0.5}NbO_3$-$0.1LiBiO_3$ (KNN-0.1LB) transparent ceramics. Haugh *et al.* [66] investigated the influence of aqueous phase pH, temperature and pressure on cold sintering densification of nanovaterites powdered particles using water to explain the underlying mechanisms of its uncommon densification. Li *et al*. [67] studied the effect of the amount of water on cold sintering process of NaCl which shows decrease in relative density and dielectric constant. The increase in Qf (Resonance behaviour of an underdamped harmonic oscillator) value was attributed to increased microstructural homogeneity with increase in water, responsible for the rapid mass transport of the water-mobilized dissolution-precipitation mechanisms. Hong *et al*. [41] revealed the influence of water during room temperature CSP of NaCl, suggesting pressure-driven plastic deformation contributing to cold sintering as the dominant mechanism of dry-pressed NaCl ceramic. This according to Hong *et al*. contributes also to the cold sintering dissolution-precipitation mechanism. Kang *et al*. [68] studied the influence of pressure, temperature, die sealing and concentration of ions in solution to unveil ZnO CSP densification mechanisms. The study highlighted particles rapid compaction, rearrangement of grains and subsequent dissolution-precipitation stages that largely described CSP. Tavari *et al.* [69] studied the influence of pH, soaking time and pressure on silica densification facilitated by preferential second phase precipitation driven by Ostwald ripening. Shen *et al*. [70] studied critical factors affecting the influence of CSP densification behaviour of hydroxyapatite, namely powder characteristics, pressure, temperature, time, and solvent type. According to Shen *et al*. [70], new mechanism contrary to the conventional CSP dissolution-precipitation mechanism plays a key role as hydrogen bonds were observed between hydroxyapatite particles that drives its densification. To date, several materials, and their composites were cold sintered to provide further understanding of the CSP mechanism and the influence of its variables. However, cold sintering fabrication of ceramic based composites thermal energy storage materials is less researched.

Presently, ceramic based composite PCMs with appropriate thermal and mechanical properties are required to meet the growing demand for high temperature thermal energy storage systems. Thus, appropriate structural support is required to provide a strong scaffolding to the PCMs over repeated cycles. Most fabrication studies focused on the use of high temperature conventional sintering approach which is energy consuming and limits materials integration due to mismatch in sintering temperature. In recent time, successful CSP densification of NaCl [41, 67] and Li_2CO_3 salts [36] which are potential PCMs was carried out to target properties for applications other than thermal storage. More so, direct use of salts as PCM is discouraged due to corrosion and low heat charging rate. The fabrication of ceramic based composite PCM by mixing method or infiltration of a porous ceramic structure with PCM [1, 71] as TES material for high temperature application have been proposed in several experimental studies. Porous ceramic materials characterized by unique properties namely low density, high surface area, low thermal conductivity, high thermal/chemical stability, and remarkably controlled permeability [72, 73]. The unique properties distinguished them as attractive material for structural support in porous metal oxide composite PCMs and functional applications [74] such as membranes, electric substrates, [75], catalyst and catalyst supports [76], filtration and separation materials [77] bio-ceramics, insulators of heat, hot gases and molten metal filters [74, 75, 78]. The need to develop high-quality porous ceramic requires unique and novel fabrication method to provide desired and unique grains as well as uniform microstructure [78]. Liu et al. (2014) suggested that novel technique is required to achieve the desirable balance between uniform distribution of mechanical strength and porosity. The discontinuous and non-uniform distribution of pore forming agent is responsible for the uneven distribution of pores and pore size distribution. Numerous techniques were employed to fabricate highly porous ceramic structures. These include use of the template methods [79, 80], pore-forming agents [81], gel-casting [78], freeze casting [82], electrochemical anodization [79, 83], sol-gel and freeze-dry processes [84]. The conventional sintering approaches are highly limited by high temperature requirement of about 50-75% of the ceramic's melting temperature for several hours or days [26, 36, 38].

However, several ceramic based fabrication methods have been reported [17] but, there are still some controversies surrounding their structural integrity and thermal properties. Until the first reported cold sintering process fabrication of TES material in our lab [49], no attempt was made to fabricate it using low temperature CSP since its discovery in 2016 by Randall and his co-workers. Though, significant progress has been made and further research efforts continue to unfold to provide an in depth understanding of its underlying mechanisms, but CSP is still at its early stage. Furthermore, cold sintering of the composite materials is also less researched requiring further attention to advance the scope of its mechanism understanding.

In this study, novel ceramic based composite phase change materials for thermal energy storage is fabricated by cold sintering process and characterized for its structure and property. The influence of its key synthesis parameters was also studied to further unveil its mechanism and establish parameter-structure-property relationship. A new novel approach to fabricate a porous structured material was developed and its structure and mechanical properties studied.

1.2 Statement of Problem

The enamours demand for thermal energy, its losses coupled with rapid global shift to renewable source of energy suggest the need for optimal energy storage materials performance and excellent fabrication method to address the 21st century TES material challenges. Efficient materials with tailored properties and cost-effective fabrication method are required for a successful delivery of both domestic and industrial energy requirement from renewable sources. The challenges of material compatibility, high cost and efficient fabrication method of TES material suggest the need for a low temperature fabrication method that could provide the flexibility of addressing challenges in material integration, high fabrication cost and high-performance demand for system reliability.

Attempts made to address these material challenges have led to the fabrication of different composite materials consisting of phase change material, composite phase change materials and PCM infiltrated porous structural support materials for latent heat thermal storage. Research emphasis is more for low temperature application compared to medium and high temperature. Several fabrication methods for low and high temperature composite TES materials have been used and reported. However, sintering approach remains the most widely used method despite high energy consumption, limited material integration to target specific properties for the desired TES system performance and reliability.

Novel and sustainable TES material fabrication strategy that will deliver efficient latent composite storage material with optimal performance over wide application temperature range are critical to address the future renewable energy and energy recovery material challenges. Therefore, development of fabrication strategy that could provide pathways capable of overcoming the enamours challenges faced by conventional and enhanced methods of TES material fabrication remain an important and strategic step towards addressing future renewable energy and energy recovery material challenges of the 21st century. To bridge this gap, a novel emerging cold sintering process (CSP) approach for efficient composite thermal energy storage material fabrication is investigated in this PhD project.

1.3 Aim and Objectives

The aim of this PhD project is to fundamentally explore the techniques of composite thermal storage material fabrication using a cold sintering approach.

The aim is to be achieved via the following objectives:

Experimental investigation the cold sintering mechanism of PCM and matrix material pair, consisting of:

i) to identify PCM and matrix material pair that are suitable for the fabrication of high temperature composite PCMs pellets using cold sintering approach.

ii) to characterize the microstructures, mechanical properties, and thermal properties of the composite PCMs and link the microstructures and properties with the sintering process parameters to establish parameters-structure-property relationships.

iii) to study the effect of cold sintering parameters namely pressure, temperature, dwelling time, and transient media on cold sintered ceramic based composite PCM

iv) to fabricate a porous structural ceramic support by CSP to encapsulate high temperature phase change materials

v) to propose and unveil cold sintering process (CSP) mechanism of a composite thermal storage material pair from fundamental chemistry understanding

The structure of the thesis is as follows:

The comprehensive literature review in Chapter 2 consists of four parts. The first section summarizes the shape stabilized composite phase change materials comprising of ceramics with organic and inorganic materials. Second section presents a detail description of the various fabrication methods of shape stabilized composite materials for thermal energy storage. The third part summarizes sintering processes describing its role and strategies developed to lower sintering temperature. The fourth section provides a detail background study on cold sintering process, ranging from sintered chemistries, sintered material properties, process conditions, fundamental stages, mechanism understanding, key operating variables and their influences.

Chapter 3 describes the experimental methods utilized in this investigation, which include materials preparation, CSP setup, detail experimental procedures for composite and porous alumina fabrication process, measurement, and analysis methods for related properties at different stages.

Chapter 4 demonstrate cold sintering technique using selected Alumina-NaCl composite powder. The influence of the main CSP processing variables such as temperature, pressure, amount of liquid, and dwelling time was investigated to establish parameter-structure-property relation.

Chapter 5 presents fabrication of porous structured alumina by CSP-post-annealing processes of cold Al_2O_3-NaCl composite. The effect of processing conditions on microstructure evolution and mechanical properties of Al_2O_3-NaCl composite were studied.

Chapter 6 unveiled the mechanism of cold sintering of the Alumina-NaCl from the perspectives of defect chemistry established from experimental and theoretical analysis.

The main findings of this study are concluded in Chapter 7. In this chapter, suggestions for future work on cold sintering process to further advance its process understanding and application is also presented.

CHAPTER TWO

LITERATURE REVIEW

2.1 Introduction

This chapter presents a detailed literature review regarding the shape stabilised organic-inorganic or inorganic-inorganic composite materials and their fabrication methods. The recent development in the fabrication of high temperature composites thermal storage materials is presented. The merits and demerits of the various fabrication methods are presented. Literature review on conventional sintering its limitation and development of new methods to lower the sintering temperature window is provided. Historical background of cold sintering process and its progress stages in terms of material compatibility, process mechanism understanding, and application is also presented.

2.2 Shape Stabilised Composite PCMs for Thermal Storage

The use of organic and inorganic phase change materials is becoming greatly important. PCMs are being used for thermal energy management systems [85, 86], solar energy utilization [87] and energy saving buildings [88, 89]. Presently, many organic and inorganic phase change materials have been proposed and significant number of these materials are being used as PCMs for latent heat energy storage. The most widely used are the organic but all have common drawbacks due to solid-liquid phase change. This causes leakage due to fluidity responsible for shape instability limiting the materials serviceable life and range of application [88, 90]. Other issues associated with corrosion, chemical incompatibility and poor thermal conductivity add up to these challenges. The common approach developed to provide solution to this drawback is the shape stabilization of the PCMs [90].

To date, organic based PCMs and their eutectics are the most widely used and reported PCMs tested for various applications such as in electronic devices, domestic heating, automobiles and in many space and food industries. They are characterized by congruent phase change and low melting point responsible for limited application at low temperature [91]. The shape instability due to high leakage tendency is being addressed by the use of compounding processes namely the use of porous structured support material, polymer blending technology, micro-macro encapsulation methods using organic or inorganic materials as shell or support [92]. The microencapsulated PCMs with polymer or inorganic shell as PCM container and PCM as core are widely investigated and sufficiently reported in recent reviews of experimental studies [93-95]. However, the approach suffers some setbacks from high cost of the process, low thermal energy transfer rate, and limited area of application due to low melting point.

The inorganic PCMs have large phase change enthalpy, stable thermal properties over repeated thermal cycles and wide range application temperature. However, inorganic PCMs such as molten salts are associated with subcooling, incongruent melting and phase segregation. The high melting point of inorganic PCM such as salts enables its utilization for high temperature thermal energy storage such as in concentrated solar power plants [96]. Though, corrosion of PCM metal containers in addition to poor thermal conductivity is another major concern preventing direct use of molten salts. To overcome this drawback direct use of highly conductive materials was proposed to improve thermal conductivity and prevent leakage of molten salts. This is largely associated with the non-wetting characteristics of the carbon materials by liquid molten salts responsible for leakage and clear separation between the molten PCM and carbon material [17]. The approach was ineffective producing mechanically weak structure to prevent salt leakage [1]. Similarly, in the case of inorganic PCMs further increase in the thermal conductivity material to overcome its inherent low thermal conductivity causes latent heat decrease [97]. In addition, Metal foam composite PCMs were also proposed but only reported in a very few studies for high temperature application largely because of severe corrosion problem [17].

Therefore, to fabricate shape stabilized composite phase change materials suitable for high temperature application, graphite composites, metal forms composites and porous metal oxides composites with inorganic salts PCMs were proposed and fabricated using different methods. The composites are characterized by good mechanical property, good wettability, and high temperature thermal stability [17]. The infiltration with/without vacuum, dispersion, compression, and electrospinning methods were used to prepare graphite composites. Meanwhile, three different fabrication methods namely sol-gel [18, 98-100], melting infiltration [20, 101] mixing and sintering [102-105] have been experimentally studied and reported to produce porous oxides composite PCMs for thermal energy storage.

2.3 Composite PCMs fabrication processes

Significant number of processes for the fabrication of composite PCMs have been developed and are reviewed to provide background understanding. Composite PCMs are fabricated using microencapsulation, infiltration/impregnation, electrospinning method, ultrasonic method, polymer blending process, mixing, and sintering method. Though, some of the processes are for both organic and inorganic based PCMs but the later mixing and sintering is only applicable to inorganic based composite PCMs.

2.3.1 Microencapsulation

Microencapsulation is another promising and advanced method employed to stabilize PCMs. Micron-sized particles of PCMs are enclosed in a variety of suitable polymer shells typically the melamine resin (MF) and poly (methyl methacrylate) providing an isolation cover against leakage during phase change [106, 107]. The microencapsulated PCMs are widely used because of good mechanical strength and micron scale size to enhance thermal storage capacity in building walls. Though, shell polymers have good mechanical property but usually are characterized by low thermal conductivity. The excellent mechanical strength and microscale size of microencapsulated PCMs have made them attractive for use in building walls to enhance their thermal storage capacity [108]. However, the shell polymers usually have low thermal-conductivity and to achieve complete coating, and good mechanical strength requires it to be in large quantity.

Several encapsulation methods have been used to prepare PCMs for thermal energy storage. The matured ones for real application such as the in-situ polymerization, interfacial polymerization, sol-gel, and spray drying method have delivered PCMs with the desired properties and prospects [95, 107]. The in-situ polymerization process consists of a soluble monomer and a catalyst situated outside or inside the PCM droplet core. The insoluble polymer is generated and deposited on the core from the surface reaction on the PCM droplet. Prior to the reaction PCMs are dispersed in form of emulsion and monomers or the low molecular weight prepolymer mixture are the predominant outer shell materials. Thus, enables polymer coating of the core material as the main process step. The method is quite matured and significant number of researchers in energy materials fabrication have used it to prepare latent heat energy storage materials. The in-situ polymerization reaction has been described as reaction between water soluble and oil soluble phases in a continuous suspension, emulsion or interfacial polycondensations phases. The four process routes involve preparation of oil-water emulsion, prepolymer mixture liquid, addition of prepolymer mixture into oil-water emulsion to encapsulate core material and washing followed by drying of encapsulated PCMs. Yu *et al.* [109] synthesized high density spherical phase change microcapsules for thermal energy storage using n-dodecanol as core material and melamine-formaldehyde resin as wall material. Two emulsifiers styrene-maleic anhydride (SMA) copolymer and polyoxymethylene octyl phenol ether-10 (OP-10) were used in a mass ratio 4:1, mixing speed of 4500 rpm, and 69% mass fraction of n-dodecanol with 167 J/g latent heat of phase change. High n-dodecanol encapsulation efficiency of 97.5% is observed and the phases transition temperature of 24°C recorded with average particle size around 30µm. Su *et al*. [110] modified melamine-formaldehyde resin with methanol to synthesized spherical and smooth surface microcapsules using paraffin as core material. This provides increased cross-linked structure in the wall material, reduced amount of excess formaldehyde, and promotes greater deformation resistance as well as wall material internal surface extrusion resistance. Pan *et al*. [111] synthesized a novel PCM microcapsule with melting point of 50°C from n-pentanol, palmitic acid, aluminium chloride hexahydrate, and ammonium bicarbonate. Meanwhile, using urea, melamine, and formaldehyde Zhang *et al*. [112] prepared n-octadecane, n-nonadecane, and n-icosane microcapsules. Boh *et al*. [113] prepared paraffin microcapsules with phase transition temperature of 25°C, 40°C, and 50°C using hexakis (methoxymethyl)-melamine-formaldehyde and trimethylolmelamine-formaldehyde prepolymer as wall materials.

To promote reaction rate, mild synthesis conditions, low purity monomer requirements and less raw material ratio strict requirement, interfacial polymerization was developed. It has been applied recently to produce phase change microcapsules energy storage materials. It is the polycondensation process involving two monomers with more than one functional group in two immiscible liquids. Zhou *et al*.[95] reported that Wei *et al*. produced mainly spherical thermoregulation phase change microcapsules with smooth surface for smart textiles with 10.6 µm average particle size by interfacial polymerization method. The authors further reported paraffin-based microcapsules prepared by Malfiet *et al.* using interfacial polymerization and studied its application potentials. The microcapsules prepared had paraffin fraction of 84% with phase change enthalpy of 118 J/g and temperature close to human body comfort range. Also, Lan *et al*. [114] prepared microcapsules of n-eicosane with 75% encapsulation rate of n-eicosane by interfacial polymerization. The reported phase change temperature was 36°C and corresponding enthalpy range of 29.34–63.55 J/g. The microencapsulated PCMs produced with polymer or inorganic shell as PCM container and PCM as core are widely investigated and sufficiently reported. However, the approach suffers some setbacks from high cost of the process, low thermal energy transfer rate to limited area of application [115].

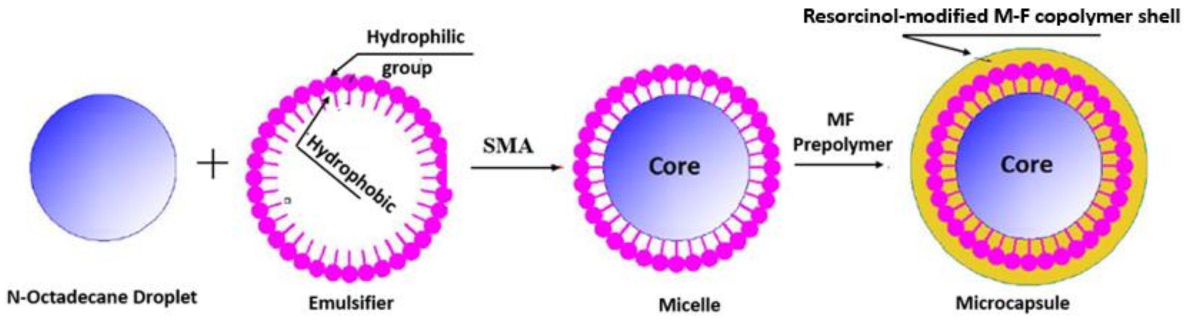

Figure 2-1 Microencapsulated PCM by in situ-polymerization [95]

2.3.1.1 Spray drying

To develop a low cost and simple microcapsules fabrication process in large scale, spray drying was innovated as microencapsulation approach. It has been used to produce powdered microcapsules by flash evaporation of atomized fluid containing bio-active compounds with very hot dry air [116]. The wall material is initially dissolved in an aqueous medium to which oil soluble core material is added to produce emulsion. The emulsion is loaded to a spray dryer to produce uniform microcapsules. Zhang *et al.* [116] fabricated β-Carotene by combined wet milling and spray drying with average diameter of 229.4nm after rehydration with 19.17 and 99.18% loading capacity and encapsulation efficiency respectively. The 13% β-carotene final crystallinity was achieved with some presence of amorphous phase. C_{18} microcapsule was prepared using C_{18} as core material and TiO_2 as wall material by spray drying with a phase change enthalpy of 92–97 J/g and particle size range of 0.1–5μm [117]. Hawlader *et al.* [118] used paraffin as the core material, gelatine, and gum Arabic as the wall material to produce uniform particle size paraffin microcapsules by spray drying suitable for solar energy storage with phase change enthalpy of 145–240 J/g.

2.3.1.2 Sol-gel method

Sol-gel method is being used to prepare polymer-based nanocomposites microcapsules for thermal energy storage. Metal-organic or inorganic compounds are subjected to sol-gel heat treatment to form oxides or other solid compounds. The reaction is generally considered to be mild with uniform phase dispersion. The possible changes in the reaction components provides greater advantage to target properties of interest using sol-gel fabrication method. However, long aging duration, material shrinkage are major limitations militating against the use of this method which affects morphology and service performance of the material. Zhang *et al.* [54] fabricated smooth surface phase change microcapsules for energy storage by sol-gel method with C_{18} core material and SiO_2 wall materials. Significant improvement in thermal conductivity was observed and forms a very compact body with good thermal stability. Zhang *et al.* [53] fabricated using tetraethyl orthosilicate and palmitic acid a nano-composite organic-inorganic by sol-gel process for thermal energy storage. The composite analysis shows adequate storage capacity, thermal stability over repeated cycles and is effective for solar energy utilization.

2.3.2 Infiltration / impregnation process

Porous materials are characterized by excellent properties such as high porosity, high pore volume and large specific surface area. The unique properties have made them applicable in various areas such as thermal energy storage, catalysis, battery, and in thermal insulation [119, 120]. The unique structure of porous material combined with a strong capillary attraction enables fabrication of composite PCMs currently receiving serious research attention [107, 115, 119]. It enables fabrication of composite organic or inorganic PCM on porous inorganic supports such as the metal foams (nickel, aluminium, steel), porous carbon (expanded graphite, carbon nanotube, graphene oxide, graphene aerogels), porous oxides (mesoporous silica, bentonite, expanded perlite, diatomite, sepiolite, attapulgite, vermiculite, fly ash, montmorillonite, TiO_2), porous polymers and metal organic frameworks (MOFs) supports [107, 115, 119]. The porous materials adsorption consists of fluid clearance from the pores and layer spaces by creating a vacuum which eventually forces melted PCMs such as salts to be sufficiently adsorbed into the pores.

Infiltration processes are used to prepare a composite porous structured support-PCM by immersion of the porous support at atmospheric pressure into a molten PCM or by vacuum impregnation method [121]. The vacuum infiltration approach achieves the largest incorporation of the PCM into the granular porous material in the range of pore diameter of 1μm to hundreds of micrometres. Therefore, vacuum conditions are the preferred choice that offers promising route to the fabrication of large thermal storage composite material [122]. Tian *et al.* [66] prepared paraffin/EVA composite phase change energy storage materials with paraffin as the PCM, ethylene-vinyl acetate (EVA) as the support material, one-dimensional graphite, and one-dimensional carbon fibre as the conductive filler. After testing, the phase change temperature was detected as 45.63℃, and the phase change enthalpy was 167.4 J/g. Li *et al.* [65] prepared nitrate mixture/SiC honeycomb ceramic (SCH) composite PCMs by vacuum infiltration. SEM showed that the nitrate mixture was dispersed and embedded into the porous structure of the SiC wall. The heat storage and release rate of the composite PCMs is increased with the elevated SCH mass fraction when SCH with different mass fractions is added into the composite PCMs. Compared to pure PCM, the melting temperature and solidification temperature of the composite PCM are altered slightly, while the heat storage and release time of the composite PCMs are also greatly reduced. do Couto Aktay *et al.* [123] prepared a composite of eutectic potassium and sodium nitrate salts PCM infiltrated into an expanded graphite. Other high temperature composites prepared by infiltration of KNO_3-$NaNO_3$ into natural graphite flake and expanded natural graphite are also reported [124, 125]. In a more recent study, Rathore and Shukla [126] prepared a composite PCM OM_{37} mixture with expanded graphite by ultrasonication and by vacuum impregnation into the expanded vermiculite a shape stabilizes composite phase change is produced.

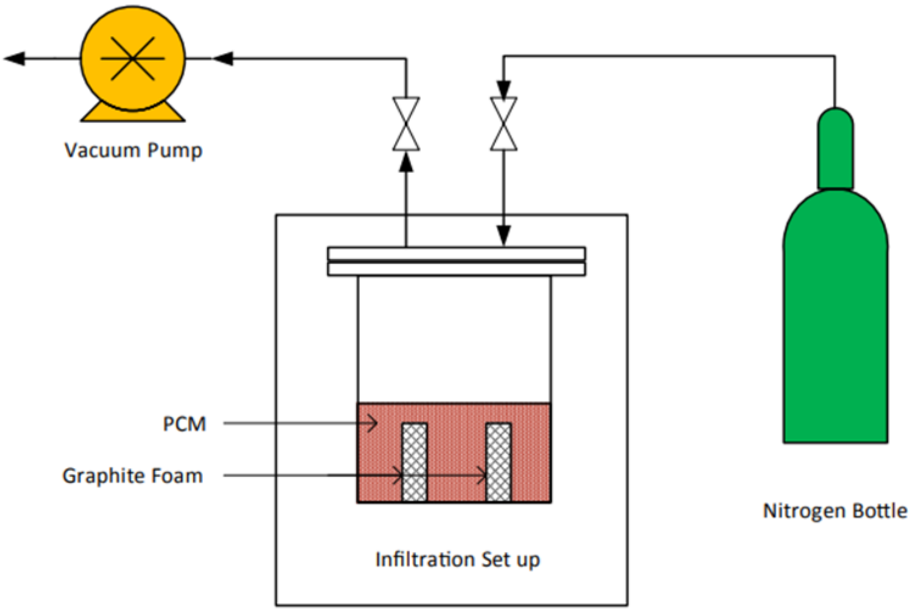

Figure 2-2 High pressure nitrogen and vacuum pump connection to infiltration device in an oven [127]

The fabrication of composite porous structured support-PCM could also be achieved by infiltration at atmospheric pressure. However, under vacuum conditions the largest PCMs loading into the granular porous structure in the range of 1µm to hundreds of micrometres pore diameter was achieved [121]. Therefore, vacuum conditions are the preferred choice that offers promising route to the fabrication of large composite thermal storage material [122]. The fabrication method is simple and suitable for large scale production at minimal cost without leakage [95, 119, 120]. The major drawback associated with this method is low thermal stability and short life span of the materials. Zhang and Fang [128] prepared composite phase change paraffin/expanded graphite (9:1) heat storage material. The paraffin was adsorbed into the expanded graphite without any significant change in its initial mechanically weak porous structure. In a related organic modification, Li *et al*. [129] modified bentonite layer spacing using paraffin to fabricate composite PCMs. The modification improves heat transfer rate of the composite paraffin/bentonite PCMs. Wang *et al*. [130] synthesizes composite PCMs using polyethylene glycol (PEG) PCM, SiO_2 molecular sieves and activated carbon. The composite with 80% glycol had the highest latent heat of 137.7 J/g. Comparatively, using porous SiO_2 and PEG as PCM, 21% increased thermal conductivity was observed with 137.7 J/g phase change enthalpy in a PEG to porous SiO2 mass ratio of 4:1. The composite offers competitive advantage of high storage performance, low subcooling and melting temperature. Furthermore, montmorillonite was used to absorb lauric acid PCMs to prepare composite for thermal energy storage. Feng *et al*. [131] fabricated lauric acid/ montmorillonite composite PCM. The organic modification of the porous material increases spacing of the montmorillonite layer by 3.6nm. Zhu *et al*. [132] prepared montmorillonite/polyethylene glycol (PEG) PCM with polyethylene grafted maleic anhydride added in a plasticizer as a compatibilizer to melt blend with the low-density polyethylene (LDPE). Thus, responsible for the formation of composite PCM with phase change temperature and enthalpy in the rage of 47.5–63.6℃ and 20.58–88.76 J/g respectively. Tian *et al*. [133] prepared composite phase change energy storage materials with paraffin as the PCM, ethylene-vinyl acetate (EVA) as the support material, one-dimensional graphite, and one-dimensional carbon fibre as the conductive filler. After testing, the phase change temperature was detected as 45.63℃, and the phase change enthalpy was 167.4 J/g. Li *et al*. [134] prepared nitrate mixture/SiC honeycomb ceramic (SCH) composite PCMs by vacuum infiltration. SEM showed that the nitrate mixture was dispersed and embedded into the porous structure of the SiC wall. The heat storage and release rate of the composite PCMs is increased with the elevated SCH mass fraction when SCH with different mass fractions is added into the composite PCMs. Compared to pure PCM, the melting temperature and solidification temperature of the composite PCM are altered slightly, while the heat storage and release time of the composite PCMs are also greatly reduced. do Couto Aktay *et al*. [123] prepared a composite of eutectic potassium and sodium nitrate salts PCM infiltrated into an expanded graphite. Other high temperature composites prepared by infiltration of KNO_3-$NaNO_3$ into natural graphite flake and expanded natural graphite were also reported [124, 125]. In a more recent study, Rathore and Shukla [126] prepared a shape stabilized composite PCM OM_{37} mixture with expanded graphite by ultrasonication and vacuum impregnation into the expanded vermiculite. The impregnation process involves mixing of the PCMs with the porous materials support. Thus, by mechanical stirring, melted PCMs influenced by good fluidity are impregnated gradually by surface adsorption and capillary forces into the pore structures of the porous material. This enables full encapsulation to be achieved [95, 120]. The composites PCMs made by this method are thermally stable making them suitable for medium and high temperature thermal energy storage.

Table 2-1 Composites PCMs fabricated by impregnation method

S/N	PCM	Porous media	Remarks	Reference
1.	Paraffin wax-polypropylene blend	Expanded graphite	High thermal conductivity and increases with expanded graphite	[135]
2.	Eutectic Adipic and Pimelic acid	Graphite	High thermal stability and adequate thermal conductivity of the composite	[136] [137]
3.	Binary fatty acid eutectic mixture	Diatomite		[138]
4.	Hydrated salts	Expanded graphite	Favourable thermal properties, low sub cooling and low cost of the hydrated salts/EG composite PCM	[139] [140]
5.	Potassium nitrate (KNO_3)	Porous alumina	KNO_3/SiO_2, KNO_3/Al_2O_3, and KNO_3/SiO_2-Al_2O_3 composites were produced. SiO_2 influences storage performance and prevent leakage	[141]
6.	Cementitious material incorporated with a solar salt	Diatomite	Increased thermal and mechanical properties without phase change material leakage	[142]
7.	Sodium nitrate	Expanded perlite	Good compatibility was observed with comparably high mechanical and thermal properties	[143]
8.	sodium nitrate	Expanded vermiculite	The expanded vermiculite had nitrate salt absorption capacity of 734.6%.	[144]
9.	Eutectic NaCl–$CaCl_2$	Expanded graphite	The composite with 20 wt% EG had higher thermal conductivity (4.937 W/m.K) than binary eutectic chloride by 701.1%.	[145]
10.	$LiNO_3$-KCl-$NaNO_3$	Expanded graphite	Strong linear relationship exists between thermal conductivity and density. Faster charging rate was observed in the composite than in the individual pure salts. Storage density of the composites is greatly reduced by increasing composite EG ratio	[7]

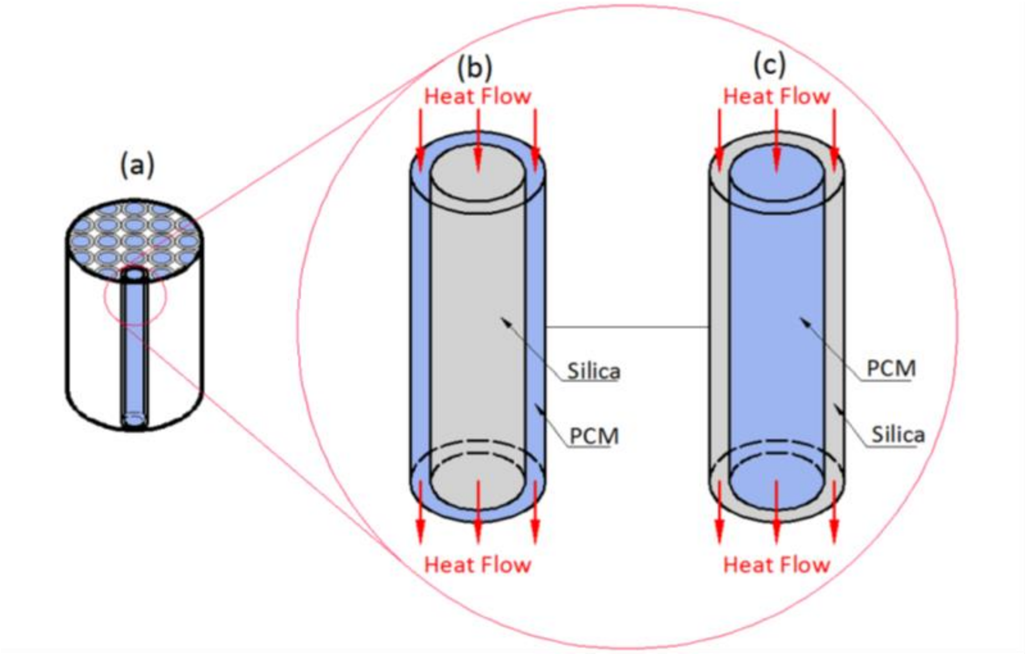

Figure 2-3 (a) melt-impregnated and mixing type PCMs package device showing the (b) tube and (c) shell side[95]

2.3.3 Polymer and melt blending processes

Polymers with higher melting temperature than that of paraffin or polyethylene glycol (PEG) are used as structural support materials, which include polyethylene [146-148], poly(propylene) [149], polyurethane [150], epoxy [151] etc. The supporting polymers provides the needed structural stability to maintain the structure and prevent leakage after PCMs changes phase from solid to liquid [152]. The hybrid paraffin/polyethylene PCMs morphology and blends behaviour was investigated with appearance of a co-continuous structure in all blends accounting for the leakage behaviour of molten paraffin [148]. The blending offers improved shape stability, but slow PCM leakage cannot completely be avoided. To effectively improve paraffin leakage-proof and achieve significant thermal conductivity, Xie *et al*. [97] prepared paraffin/high-density polyethylene (HDPE)/expandable graphite (EG) composite PCMs by melt blending method. The thermal conductivity was improved by 2.7 times higher than for paraffin with only 10% HDPE and 5% EG blend. Meanwhile, low paraffin leakage of 30% at 70°C was observed at a point when paraffin would have been completely leaked.

Recently, melt blending and mould processing method has been used to fabricate composite thermal energy storage materials made of PCM or eutectic mixture of PCMs with structural support. The PCM or its eutectic mixture is heated to melt and mixed thoroughly until it is uniform. Thermal conductivity enhancer playing a double role as shape stabilizer such as graphene and expanded graphite dispersed into the molten PCM. The mixture is transferred to a mould and allowed to cool down to room temperature to form a stabilized shape. Xu *et al.*[153] using melt blending approach produced a shape stabilized graphene/hexadecane/HDPE with high latent heat of 140.75 J/g, thermal storage capability of 62% and significant reduction in the loss of the heated organic PCM. Xie *et al.* [97] produced paraffin/high-density polyethylene (HDPE)/expandable graphite (EG) composite PCMs for low temperature thermal energy storage using melt blending and mould processing method. The HDPE efficiently lower paraffin leakage by 70% and EG improves thermal conductivity by 2.7 times that of paraffin at an optimized composite PCM mass ratio of 10 wt% HDPE – 5wt% paraffin. So far, this approach has only been deployed for low temperature thermal energy storage materials fabrication.

2.3.4 Electrospinning method

The electrospinning method is a fabrication technique employed in the manufacture of nano to micro-fibre materials from either nanoparticles, polymers, polymer blends and drug impregnated polymers [154, 155]. It utilizes electric field force to fabricate a composite phase change material for direct use with defined structure and specific application requirements. The process during fabrication involves droplet of polymer being stretched gradually to the Taylor cone. A jet of the material is ejected from the core surface when electric field force exceeded the melt or polymer solution surface tension. Cai *et al.* [156] using eutectic acid mixture of capric acid-lauric acid-palmitic acid (CA-LA-PA) fabricated by electrospinning method a thermally stable composite (CA-LA-PA)/SiO_2 phase change energy storage material with porous SiO_2 nanofiber as structural support. The spinning nanofiber measured porosity and specific surface area was high sufficient to absorb many eutectic PCMs. The SEM microstructural analysis shows clear boundary between the smooth cylindrical surface SiO_2 nanofibers and the PCMs except in few locations. The SiO_2 nanofibers stabilises the composite as it retains its shape and by capillary effect and surface tension between it and the eutectic acid it prevents leakage of the molten eutectic mixture. Chen *et al*. [155] prepared by electrospinning method a composite of a very fine polyethylene glycol as PCM and cellulose acetate as matrix support. Kuo *et al*. [157] fabricated thermo-regulating $LiNi_{0.5} + \delta Mn_{0.5} - \delta O_2$ nanofibers with reproducible thermal properties after 100 thermal cycle.

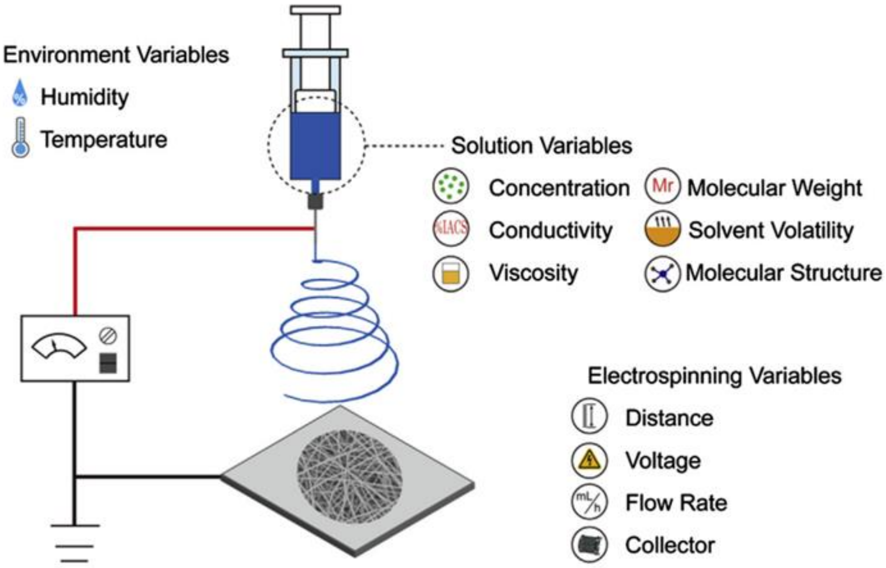

Figure 2-4 Conventional electrospinning setup, its environment, solution, and variables [158]

2.3.6 Ultrasonic method

The ultra-sonification method is the process in which the PCM is injected into the pores of the matrix support material. The major issues associated with this method is the uncertainty about complete filling of the pores by the impregnated PCM. [159] prepared beeswax/graphene composite phase change energy storage material and reported phase change enthalpy increase by 22.5%. In a related study, Rathore and Shukla [126] prepared a composite of OM_{37} and expanded graphite using ultrasonication method to study the influence of graphite on its thermo-physical properties. Xiao *et al*. [160] prepared a composite of eutectic $NaNO_3$ - KNO_3 (6:4) and expanded graphite to improve the PCM thermal conductivity which shows that composite is a good choice for both thermal conversion and storage respectively.

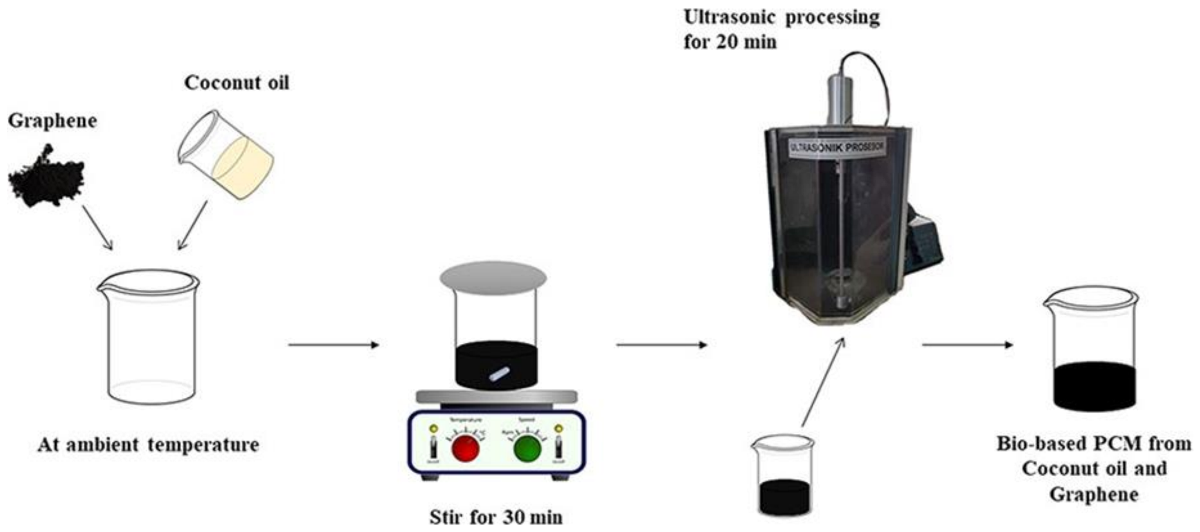

Figure 2-5 PCM composite preparation by ultrasonic processing [161]

2.3.7 Mixing and sintering Method

Two approaches were developed to fabricate composite thermal energy storage materials by mixing and sintering method. These were experimentally demonstrated. The first approach is shown in Figure 2-1, porous metal oxide was treated to modify its specific surface area and increase its absorption capacity. The amount of the salt PCM, porous structural support (SS) material and thermal conductivity enhancer required were measured and mixed thoroughly. The composite mixture was transferred into and compressed in a cylindrical mould (pressing die) at low pressure ≤45 MPa using hydraulic press [102, 162]. The second approach comprises of milling of the starting materials (support, PCM and conductivity enhancer) to achieve size matching, lower particle size and increase surface energy as shown in Figure 2-2. Thus, influences further ceramic sintering to form a denser microstructure that can provide a strong scaffolding to hold the salt PCM in position during phase change [163].

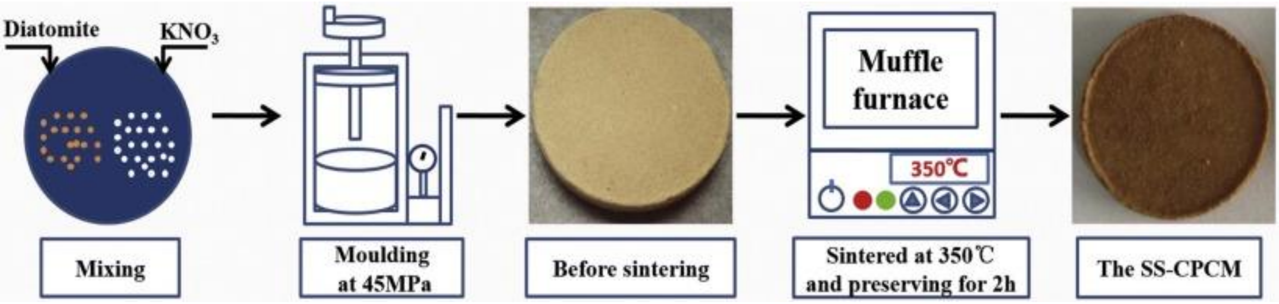

Figure 2-6. Direct mixing of PCMs with modified porous oxide materials a case study of KNO_3/diatomite [162]

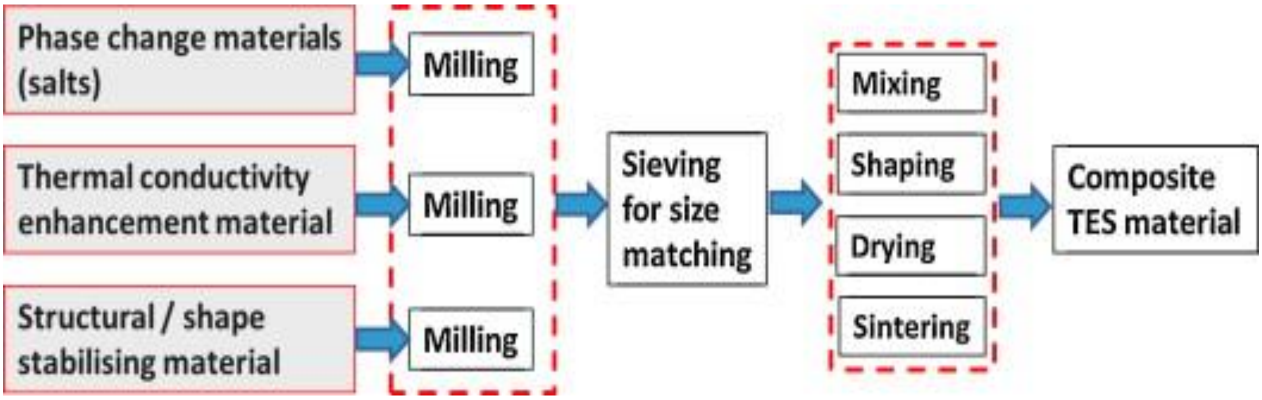

Figure 2-7. Formulation and fabrication procedure of composite PCM materials with particle size reduction and matching [163].

Several porous metal oxides-based composites for high temperature thermal energy storage fabricated by mixing and sintering method have been reported in previous literature, including silica [164], mullite-corundum [165], magnesium oxide [103, 166], alumina [105, 167] and diatomite [102, 162, 168, 169] oxide based supports. [10] using Li_2CO_3- Na_2CO_3 eutectic molten salt PCM, graphite as thermal conductivity enhancer and MgO as structural support produced a microstructured composite for thermal energy storage by sintering method. The MgO as structural support prevents salt leakage and serves a purpose of eliminating chemical incompatibility.

Table 2-2 Composites PCMs fabricated by mixing and sintering method

S/N	PCM	Structural support/TCE	Remarks	Reference
1.	Eutectic Li_2CO_3-Na_2CO_3	Graphite flakes	The dense composite shows better particles migration, rearrangement and MgO provide more salt containment. The strong correlation between structure and properties enables parameter-structure-properties relationship to be established	[104]
2.	K_2CO_3-Li_2CO_3-Na_2CO_3	MgO	Good composite chemical compatibility, mechanical strength, and thermal stability over 100 thermal cycles with no mass loss up to 1000 °C.	[170]
3.	$NaNO_3$	MgO/carbon conductivity enhancers (TCE)	Increased in TCE influences Thermal diffusivity decreases with TCE and salt leaked due to enhanced porosity depending on the type of TCE, and the amount used. Further loading of the PCM gives higher thermal energy storage capacity but influences salt leakage more pronounced in a composite with cylindrical carbon material	[171]
4.	Na_2CO_3, K_2CO_3, and Li_2CO_3 PCMs.	MgO	The composites thermal storage media performance test revealed prolong cooling time of the reactor catalyst bed by over 10 minutes	[172]
5.	Eutectic Na_2SO_4-NaCl	α-alumina and mullite	The 45:55 wt% composite ratio had the optimal thermal performance after 20 thermal cycles at 550 - 680 °C. The α-alumina composite had the lowest decrease in phase change enthalpy and its weight loss after 300 thermal cycles was only 4.6%	[167]
6.	Eutectic salt NaCl–KCl–$MgCl_2$ PCM,	α-alumina/expanded graphite (EG)	conductivity by more than 6-fold with increase in TCE. However, its energy storage capacity decreases with increase in both TCE and α-alumina support	[105]
7.	Eutectic NaCl–KCl–$MgCl_2$	α-alumina/expan	The composite storage capacity decreases with increase in TCE	[105]

		ded graphite (EG)	and alumina support. Meanwhile, its conductivity increases by more than 6-folds	
8.	KNO_3	Diatomite	The diatomite retained up to 65% KNO_3 salt without leakage and its crystalline structure preserved. The observed decrease in the phase change enthalpy during melt-freezing cycles is associated with the salt vaporization	[162]
9.	$NaNO_3$	Diatomite/EG	Excellent compatibility between the PCM and diatomite with 70% KNO_3 retention capacity observed in the diatomite pores and its surface. Presence of 6% graphite increases its conductivity by about 6-fold.	[169]
10.	Na_2SO_4	Diatomite	The composite was found suitable for application up to 980 °C and a composition with 45% diatomite had optimal and excellent chemical compatibility, storage density, mechanical strength, and minimal leakage	[168]
11.	Polyethylene glycol (PEG), $LiNO_3$, and Na_2SO_4	Mesoporous silica	The shape stabilized composite demonstrated excellent thermal storage capacity, and chemical compatibility between silica and the selected PCMs. It is thermally stable after 200 thermal cycles and no leakage was observed even at 70% maximum loading of $LiNO_3$ and Na_2SO_4 in the composite.	[164]

2.4 Sintering process

Sintering has been described as a process employing thermal energy under controlled conditions to bond particulate matter into a highly dense and mechanically robust solid object by lowering the surface free energy via a process of densification and atomic scale mass transport processes or coarsening [27, 173]. The minimization of surface energy as driving potential for sintering was related to annihilation of surface curvatures at early sintering stage. Meanwhile, flow of mass depends on the chemical potential gradient which is also proportional to the surface curvature. At later stage, interfacial energy minimization dominates as driving potential caused by pore size reduction and grain growth responsible for the replacement of higher interface energy with lower ones. The sintering rate decreases and at last stage the densification is regulated by temperature dependent diffusional processes. The conventional thermal sintering forms are the solid state, viscous and liquid phase sintering. The detailed mechanisms of the various forms are provided in the published literatures [27, 50].

Sintering from engineering perspectives, is a process of strengthening shaped particles that led to the fabrication of many industrial products like capacitors, transmission gears, cutting tools, watch cases and bearings mostly from metallic, polymer, ceramics, and carbide materials [174]. Prior to the discovery and application of sintering process, powders were shaped using different methods depending on the shape complexity. The die compaction, injection moulding, and extrusion process were applied to simple shapes, complicated 3-D shapes, and long thin objects respectively. Meanwhile, tape casting, slip casting and laser forming methods were successfully reported to have been used in powder shaping process into flat, hollow and a metal prototype structures [174]. The various forming processes mentioned are sintering processes producing weak bodies in terms of strength. However, when subjected to heating cycle peak temperature (sintering), a strong and robust sintered compact body is produced [27, 175]. Prior to the understanding of atomic structure concept, there was evidence of new materials development and detail phenomena of the processes. The emergence of better understanding of atom and atomic motion triggers a rapid development in sintering theory leading to a monumental increase in sintering application, literature volume and patents that led to the emergence of several new materials between 1940 to 1960‘s. Beyond this period and to date, more complex materials compositions and design are being developed and the fundamental process understanding is fast reaching its maxim level. This led to detail sintering theory documented in literature and good understanding of its application in complex processes [24].

Sintering provides an alternative route to produce a highly dense and robust compact from powder particles. This greatly affect the final compact properties depending on the density achieved [38]. The fabrication process of ceramic by mankind at very high temperature is historically documented to have started from the upper Palaeolithic time based on the proven discovery of Dolni Vêstonice archaeological sites found at Czech Republic where ceramic artefacts were assembled [23]. The practice now is to fabricate ceramics from powders that are sintered at temperature in the range of 50% to 75% of the material melting temperature (>1000 ^{O}C) to a density >95% of the theoretical [26, 38, 42]. To achieve improved properties and devices for various applications, integration of ceramic powders with metals, polymers or other ceramics is the common practice but limited by the differences in chemical and thermal stability, shrinkage temperature and high temperature physio-chemical incompatibilities [26, 38]. Ceramic materials have so far received the greatest research attention. However, traditional fabrication of these materials requires sintering at high temperature greater than 1400 ^{O}C [42]. Several literatures have reported the formation of dense natural ceramics formed in water at low temperature, or via biomineralization and geological formation processes [42, 176]. The chemical approach employing the strategy of biomineralization process has been used to push down the temperature window and densify inorganic materials at mild condition. However, the attempt yielded thin film and particles of inorganics at temperature much lower than 1400 ^{O}C for conventional technologies [176]. The natural geological approach to the densification of carbonaceous rocks material from inorganic sediment particles led to the fabrication of ceramic-like based material at lower temperature and pressure conditions respectively [177, 178]. The characteristic of this process involves pressure, temperature, and composition as variables to be manipulated. Thus, it is not as complex as biomineralization process strategy. It can be scaled up to a large scale using any of the cutting-edge technologies with potentials to reduce the long-time scale that characterize geological processes [42].

The high temperature requirement >1000 ^{O}C in conventional sintering to densify ceramics based composite PCMs was considered a large and substantial contribution to environmental and economic cost in addition to a limitation imposed on materials integration, synthesis, and desired shape fabrication [179]. The gradual shift is due to several observed defects such as the phase change (melting), crystal structure elements migration, chemical transformation, phase reactions and / or grain growth [28, 51]. There are three different broad classifications of approaches developed to lower the sintering temperature; these include novel sintering techniques, the role of sintering agents and powders optimization strategy [180, 181]. The later involves removal of the oxide's formation on non-oxide ceramics [180]. This is the starting powder material refining to further increase the sintering rate by minimizing mobile chemical species diffusion distance [181].

2.4.1 Role of novel sintering techniques

The use of novel advance technique is also appealing and has received remarkable research attention in recent time. The most recent appealing techniques achieved hundred degrees in temperature reduction using either pressure, field, or electric current. These are the Field Assisted Sintering Technology (FAST), Spark Plasma Sintering (SPS), Hot-pressing (HP), hot isostatic pressing (HIP) and flash sintering (FS). The latter is the most recent [182, 183] prior to the present discovery of cold sintering process (CSP) which is currently receiving growing research attention.

2.4.1.1 Field Assisted Sintering Technology (FAST)

Spark plasma sintering which is a field-assisted sintering technique (FAST) have been used to produce different formulations of ceramics at time intervals usually in a few seconds. It is characterized using processing parameters of low applied uniaxial pressure, direct current (DC) pulsed current activated and high intensity low voltage as shown in Figure 2-3 [183, 184]. Its comparative advantage to conventional sintering is its low temperature requirement and very short sintering cycle. The technique is rapidly gaining attention and a preferred choice for the very hard to sinter chemistries (metastable materials, nanocrystalline and refractories), metals, diverse ceramics as well as polymers. However, the complex nature of the process is the major setback militating against its scale up for large scale commercial fabrication requiring huge instrumentation expenses [53, 184]. Several studies on spark plasma sintering process have been reported. Takeuchi *et al*. [185] sintered nano BaTiO3 powder to 95% of its x-ray theoretical density with average grain size < 1µm and very high room temperature permittivity of ca. 10,000 associated to pellet inhomogeneity with resistive surface layer covering. Baraki *et al*. [186] studied the influence of AC electric field on the nano crystalline 8YSZ. Omori *et al*. [187] prepared innovative materials made from ceramics, metals, semiconductors and polymers involving sintering, reaction and crystal growth. Olevsky *et al*. [188] demonstrate theoretically the thermal run-away characteristics of flash plasma sintering and by experimental approach provides solution to un-controllable thermal conditions. Pournajaf *et al*. [189] fabricated a polycrystalline transparent MgO. Li *et al*. [190] prepared grain oriented single phase $Sr_2Bi_4Ti_5O_{18}$ ceramic. Huang *et al*. [191] prepared using spark plasma sintering (SPS) and investigate storage properties, microstructure and phase composition of a composite $Ba_{0.4}Sr_{0.6}TiO_3$/MgO electrical energy storage material. Tao *et al*. [192] prepared a dense SiCf/Ti_3SiC_2 composites with improved thermal transport properties by spark plasma sintering. Mistarihi *et al*. [193] prepared by spark plasma sintering a Mo-reinforced ZrO_2 composite to study its improved thermal conductivity with wire mesh interconnected Mo . Oliver *et al*. [194] reported the development and prospects in aluminium matrix composites consolidation by spark plasma sintering.

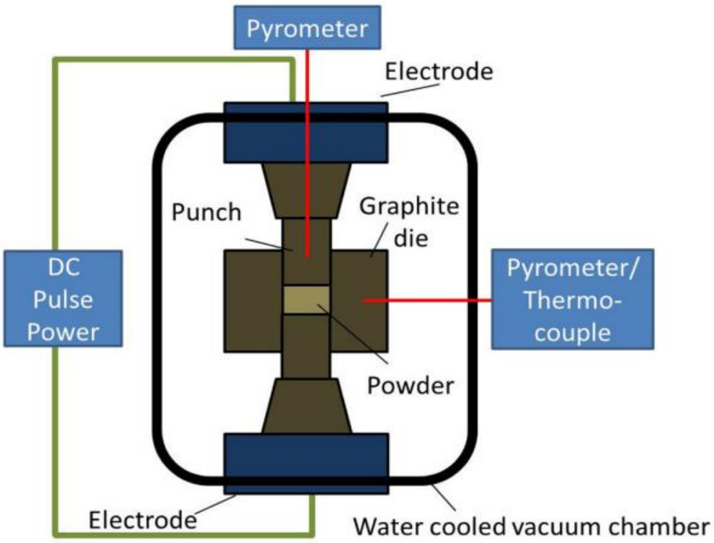

Figure 2-3. Schematic representation of FAST equipment [183].

2.4.1.2 Hot pressing

Hot pressing is a material synthesis process at high pressure and temperature lower than conventional thermal sintering method to form a dense compact body by direct hot pressing, induction heating or indirect resistance heating under uniaxial or isostatic pressing as shown in Figure 2-4 [53, 195]. The latter is employed as post sintering heat treatment to eliminate the final porosity with pressure uniformly applied in all directions. In general, the process of hot-press sintering method consist of initial particle rearrangement of the loose powder under pressure of ~80 MPa and temperature up to 2400 °C. Thus, HP has been widely used to fabricate metals, ceramics, and their composites into simple and complex shapes such as TiB_2 [196], ZrB_2-SiC-AlN composites [197], ZrB_2- and HfB_2 ceramics [198], SiC [199], SiC with magnesium additive [200], B_4C [201] , ZrC and its composite [202]. The HP mechanism is characterized by grain sliding, plastic flow and stress-enhanced diffusion [53, 195].

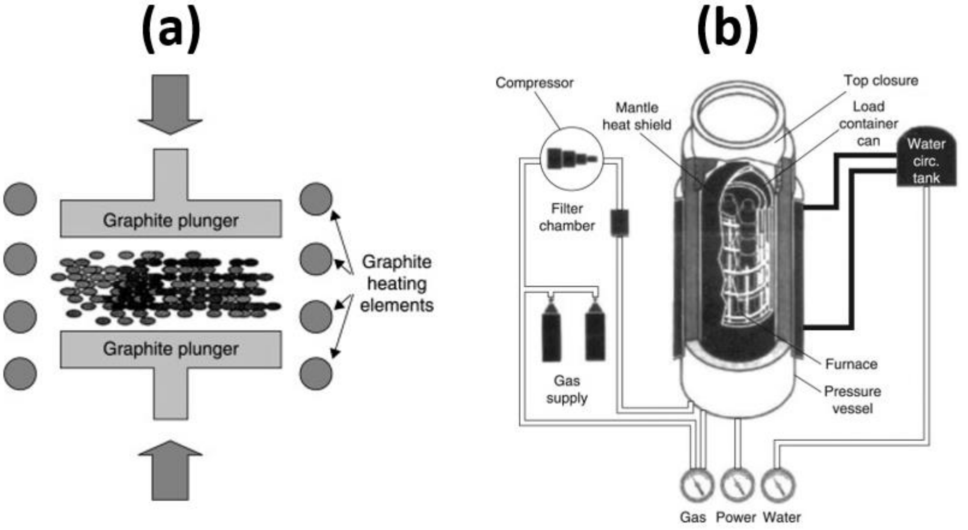

Figure 2 - 4 (a) Indirect resistance heating Hot pressing (b) Hot isostatic pressing [195]

2.4.1.3 Microwave sintering

Microwave sintering as shown in a schematic diagram in Figure 2-5 is a high thermal ramp rate heating process with potential economic savings, high product purity, sintering temperature reduction, selective and volumetric heating that drives fine microstructures. In comparison to the conventional sintering, microwave method has very minimal environmental hazard, and enhanced special, physical, and mechanical properties [203, 204].

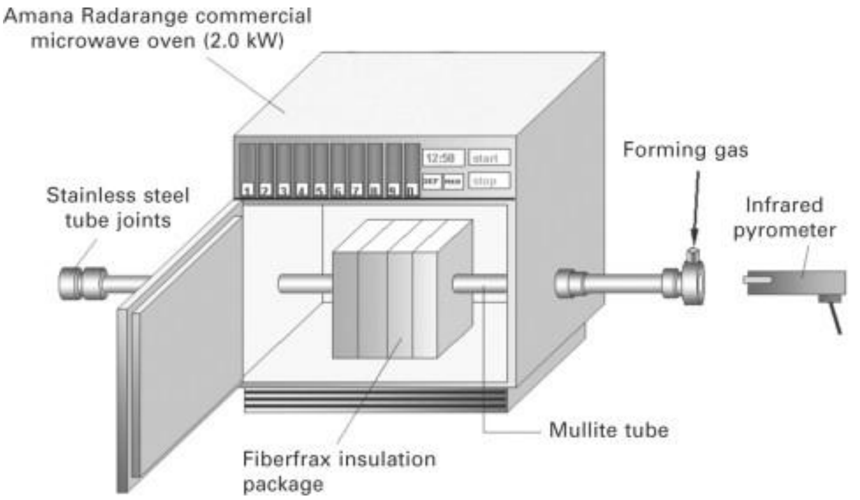

Figure 2-5 Schematic of 2 kW and 2.45 GHz multimode microwave processing unit [205]

Microwave sintering is characterized by uniform heat distribution associated with usually well controlled instruments and samples are also susceptors in addition to the modest thermal conductivity requirement. There has been a growing microwave sintering to synthesize and process materials as novel approach providing substantial reduction in energy, cost and improved diffusional processes [203]. Microwave sintering methos has been used to produced various ceramics and their composites such as Si_2N_2O [206], Yttria Reinforced Iron-Chromium Composites [207], Al_2O_3/TiC micro-composite ceramic [208], metals [209], WC/Co composites [204], ZrO2, $PbZr_{0.52}Ti_{0.48}O_3$(PZT), $BaTiO_3$, $Ba(Mg_{1/3}Ta_{2/3})O_3/Ba(Zn_{1/3}Ta_{2/3})O_3$, ZnO based ceramic varistors and micro-tubes, transparent ceramics, high temperature ceramic eutectics [210]   alumina [211-213], Nanostructured and Non-symmetrical NiO-SDC/SDC Composite Anode [214] and porous silicon carbide (SiC) foams [215].

2.4.1.4 Fast firing

According to Brook and his co-workers, non-isothermal conditions created during fast firing enable high densification with limited grain growth [53]. Figure 2-6 shows a schematic presentation of the continuous tubular and intermittent chamber furnace for fast firing reported by Garcia *et al*. [216]. Thermal gradients are intentionally introduced which drives diffusion to facilitate transport of mass to pore sites which are predominantly low-temperature regions within the microstructure [53]. Fast firing has been deployed for commercial scale production in many ceramic industries utilizing the roller kiln facility to produce products such as tiles and metal based $BaTiO_3$ ceramic capacitor [217].

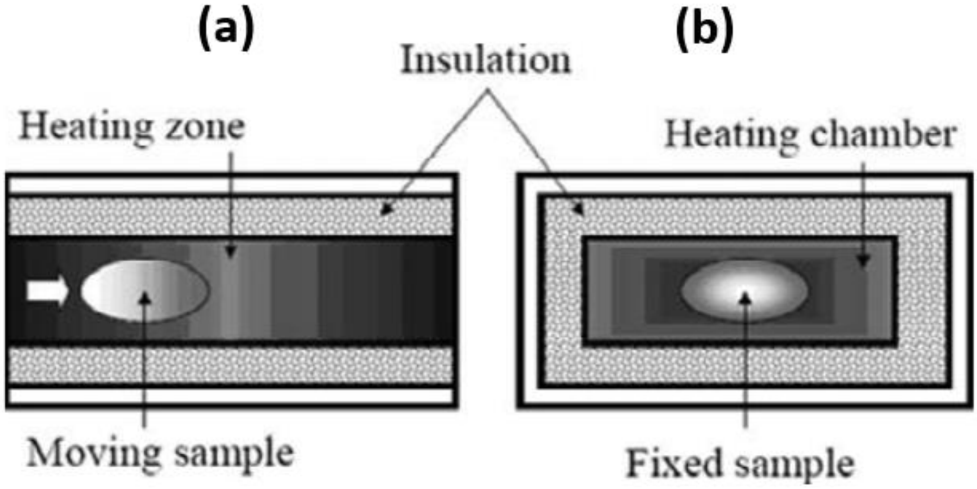

Figure 2-6 Schematic diagram of continuous tubular (a) and intermittent chamber furnace(b) [216]

2.4.1.5 Hydrothermal sintering

Hydrothermal sintering method was developed by Yamasaki and his co-workers to sinter ceramics at low temperature in the early 1980s [53, 218-220]. The HHP equipment details and the hydrothermal hot processing autoclave schematic representation is provided in Figure 2-7. Hydrothermal hot pressing was first reported in 1986 by Yamasaki but was made available in Japanese language in 1984 [52]. The concept of hydrothermal sintering was developed at the time when only ~80% of the theoretical density was achieved by the existing sintering methods but hydrothermal method is limited by longer processing time and limited densification in some cases where reactivity and solubility are influenced by the hydrothermal conditions [52]. The characteristics of this novel process are basically two comprising of powder compaction under continuous mode and space for water to pull out to reach its final densification. This depends on the amount of water present and processing conditions of pressure, temperature and dwelling time [50]. However, under hydrothermal conditions and much lower temperature <500℃ ceramics are sintered and can be termed as an artificial lithification based on sintering temperature comparable to those in Geology [52]. The approach has been extended to cover other forms of inorganic powders namely the refractories such as $CaCO_3$ [221-226], SiO_2 [218, 220, 227-235], $Ca_{10}(PO_4)_6(OH)_2$ [236-242], and TiO_2 [219, 227, 243, 244].

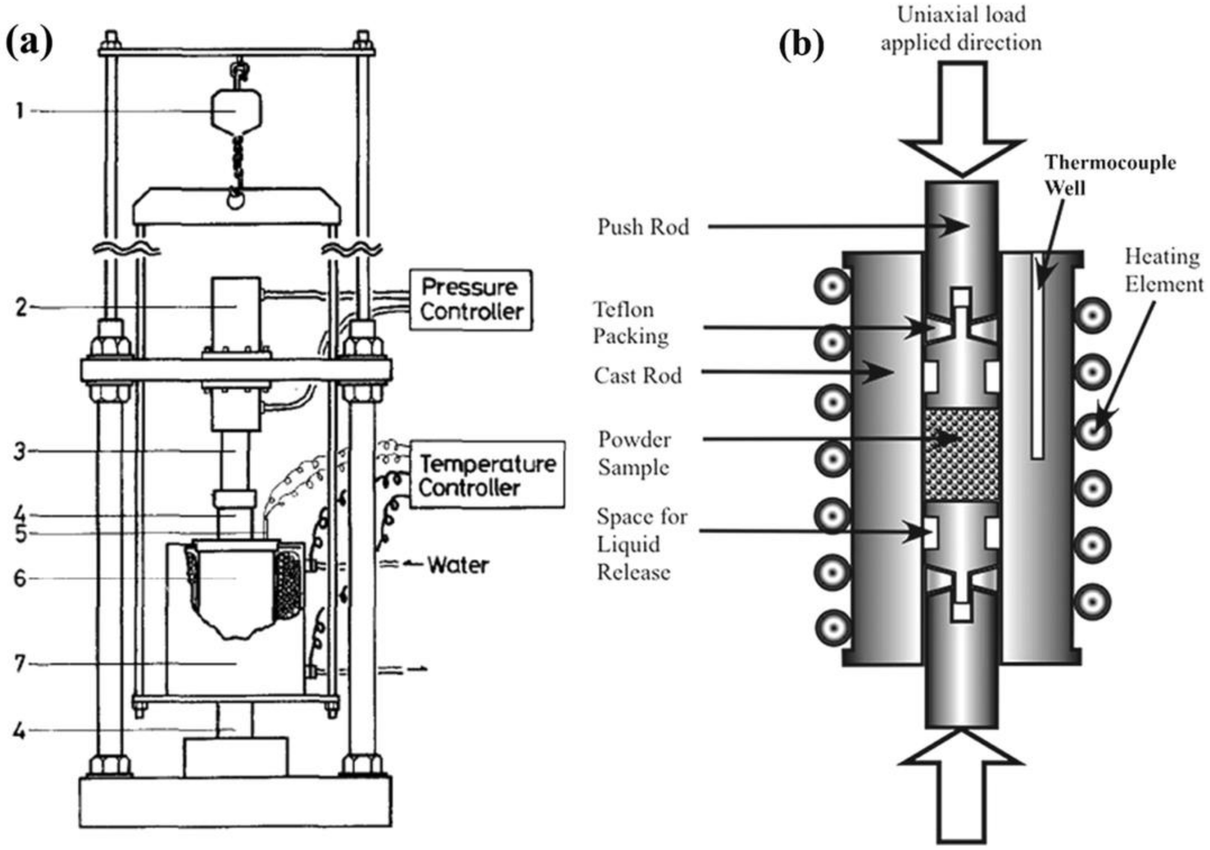

Figure 2-7 (a) HHP equipment details 1: crane for adjusting the furnace position, 2: pump, 3: ram, 4: autoclave push rod, 5: thermocouple, 6: autoclave, 7: induction furnace (b) hydrothermal hot pressing autoclave [50].

2.4.2 The role of densification aids

The addition of densification aids is another potential strategy established to lower the sintering temperature of ceramic materials. It can eliminate possible layer of oxides limiting densification on non-oxide surfaces of ceramics [35]. German *et al*. [35] described the characteristic behaviour of these aid materials virtually as a liquid phase change at high temperature in between the powder particles that results into capillary forces being generated. These forces provide an increased diffusion rate due to solid phase partial dissolution and its subsequent movement (transport) via the liquid phase. However, the use of water has always been contemplated due to its very low boiling point of 100 ^{O}C comparable to ceramics thermal sintering temperature of over 1000 ^{O}C. Though, several approaches have proven improvement in the densification of some material chemistries using water as sintering aid [51, 245]. The use of water as sintering aid reveals incomparable advantages such as environmental friendliness, availability, and low cost, safe and ease of handling.

The use of water as sintering aid was first reported by [245] in an isothermal hot processing of powder (borosilicate glass, silica, and amorphous titania) using externally heated autoclave. Water was added to the silicate powder and placed in between two piston arrangement providing uniaxial pressure under hydrothermal conditions. The piston opening is designed to allow removal of water trapped in the material pore volume that limits further densification. Steam was used to keep the autoclave pressure and the powder is heated and pressed by the pushrods continuously under hydrothermal conditions. Water is removed simultaneously from the powder interstices to the autoclave free space at pressure of 40 MPa, maximum temperature of 300 ^{O}C and heating rate of 10 ^{O}C/min for 2 hours. It was reported by Yamasaki *et al*. [245] at these conditions that water diffusion causes full densification of borosilicate glass particles but silica and amorphous titania remained a porous structure limiting densification process [227]. Li *et al*. [246] successfully reported a densified hydroxyapatite ceramics using hydrothermal hot pressing that facilitates hydrothermal reaction via precursor compounds incorporation. To consolidate the gains of hydrothermal hot pressing, the approach was used to densify zeolite compounds with 17 wt% water contents added with various amounts of 0.1 to 10 molar concentration of NaOH. The sintering mechanism understanding is predominantly a dissolution-precipitation process [247]. De Silva *et al*. [248] cold sintered $CaCO_3$ at room temperature and studied the combined influence of mechanical pressure (10 and 15 MPa), CO_2 gas pressure (1, 10 and 35 atm) and time (exposure and compact pressing time). The CO_2 gas pressure was used to improve the solubility of $CaCO_3$ in the sintering aid water. The exposure time of 0 - 90 minutes and pressing time of 10 to 60 minutes range were investigated. In the presence of very high CO_2 gas and high mechanical pressure, a new phase of the $CaCO_3$ is formed. The new phase acts as a binder and a facilitator of the powder particles agglomeration. The author's concluded that the efficiency of the entire formation process of carbonate binder depends on the increase in compressive (mechanical) strength which is determined solemnly by the available quantity of dissolved $CaCO_3$ for reprecipitation. In a related study by Schwarz *et al.* [249] using water as sintering aid and high heating rate of 100 ^{o}C/ min obtainable in the FAST/SPS technique, a humid nanocrystalline ZnO powder at temperature of 200 ^{o}C was densified under 50 MPa and temperature of 400 ^{o}C for 10 minutes to a relative density greater than 95%. In the air sintering media, the sintered dry powder consistently resists and proves difficult to be densified. Also, slow rate heating could not achieve more than 65% relative density as densification at lower heating rates results into a very little observed shrinkage. The differences can be attributed to the residual water trapped in the compact grain boundary promoting diffusion kinetics and further particles rearrangement. Dargatz *et al.* [250, 251] studied the effect of heating rate on ZnO densification in the FAST/SPS technique and high relative density of 99.5% was observed at 400 °C with average grain size distribution of 200 nm. Though, small optimal amount of water (1.6 wt%) was added in controlled manner directly into the sample powder but could not evaporate completely in the graphite die within the heating period, therefore, trapped at grain boundaries and the compact surface. The implications of this observed behaviour are the zinc (Zn^{2+}) and oxygen (O^{2-}) ions dissolution, particle surface carbonate removal, hydrogen, and hydroxyl ions diffusion into ZnO crystals and mass transfer via the liquid phase [250, 251]. However, none of these sintering modifications could achieve the desired low temperature for materials integration and desired properties improvement.

2.4.3 Room-temperature densification

In search for possibilities of sintering at low temperature, glasses and ceramics were reported to have been densified at room temperatures. A research group in Brazil for the first time at room temperature under very high pressure of 5.6 GPa densified nanosized γ-Al_2O_3 ceramics powder and silica-gel to form alumina translucent material and transparent SiO_2 [252]. The Al_2O_3 and silica relative densities of 92% and 82% were obtained with corresponding hardness values of 5.7 and 4.0 GPa respectively. Both consolidations mechanisms were referred to as cold sintering further supported by a study for the preparation of photoluminescence of silica monoliths [253]. Kähäri *et al*. [254] in a related study at Oulu University, densified monolithic lithium molybdate (Li_2MoO_4) at room temperature by compression under 130 MPa pressure in the present of small amount of water. Though, mechanism of the room temperature densification was not investigated in detail but observed microstructure similar to conventionally sintered at 540℃ and a very dense compact structure at room temperature was linked to the solubility of Li_2MoO_4 in water [254]. Subsequently, same group at Oulu studied the formation and application potentials in GPS antennas of Li_2MoO_4 ceramic composites with MnZn ferrite and TiO_2 [255-258]. In a more recent study, Bouville and Studart [259] sintered nanovaterites with water under uniaxial pressure of ~800MPa at room temperature. At room temperature and only 500MPa uniaxial pressure, a sintered relative density of 87% was achieved with corresponding compressive strength, flexural strength, and elastic modulus of 225 MPa, 50 MPa and 30 MPa higher than observed in most construction materials [259]. Interest in cold sintering continue to grow and many reported cold sintering processes differ from room temperature consolidations involving mild pressure and temperatures higher than the transient solvent temperature [50].

The conventional high temperature thermal sintering process is characterized by large grain growth at last sintering stage, limiting control to achieve desired and tailored microstructure such as the nano-structured materials. This challenge is being address by the advance low sintering temperature techniques developed based on the influence of pressure and electric current. However, none of this technique can lower the sintering temperature to a desired low level. The powder optimization process increases the sintering rate and the role of sintering liquid such as water is only observed in some chemistries specifically the nanoparticles of carbonate materials moderately soluble in it. This enables full scale densification of some of these chemistries at room temperature and high pressure such as nanovaterites [259]. Also, under hydrothermal conditions time scale is reduced and materials like borosilicate glass are fully densified but silica and others remain porous [227]. It is apparent that all the above-mentioned approach employed individually or combined to lower the sintering temperature window recorded some success but have either not been able to bring down the sintering temperature to the desired low level, pressure too high, sophisticated setup requirement or are compatible to few materials. Hence, cold sintering process is environmentally friendly and cost-effective process developed as an alternative route to lower sintering temperature.

2.5 Cold sintering process

The discovery of cold sintering process (CSP) is recognised as the long-awaited low temperature fabrication technique and the most sought for technique presently receiving greater research attention. The potentials of this process could provide the much-needed opportunity for researchers to address issues regarding high energy consumption, high cost and further explore all possibilities of integration and synthesis of different material chemistries that could revolutionize material industry [260, 261]. Its contributions to energy savings and manufacturing process are enormous and could provide more opportunities to discover novel materials [260]. The discovery of CSP has open an emerging and promising future research direction in search of novel materials for various applications. Several techniques were developed, and numerous research efforts have been made and reported in literature to fabricate materials at low temperature as highlighted in the previous sections. The emergence of cold sintering process can be traced to the series of research efforts made and reported in the literature to address the major challenges of high temperature and prolong sintering time requirement in the ceramic industries militating against the fabrication of tailored ceramics products with desired microstructure, properties, and optimal energy savings [51].

Randall and his co-workers in 2015 discovered cold sintering process (CSP) at state university of Pennsylvania using water as aqueous transient liquid. The presence of water aids ceramics materials densification to higher density at low temperature. Two methods of CSP were reported. The first powders are mixed with transient liquid using mortar and pestle in what is referred to as a conventional powder processing method [53]. The moistened powders were transferred and hot pressed into a compacts body in form of pellets under uniaxially pressure of 80 – 570 MPa and 25 to < 300 ^{O}C within few minutes (1 - 60) to a theoretical density between 80 - 99%. The pressure is applied to the powder in a heatable die by a simple hydraulic press and heating was carried out in a heater jacket as shown in the CSP experimental arrangement in Figure 2-8. Meanwhile, second method comprises of room temperature dry pressed powder pellets at low pressures usually between 30-70MPa stored in a humidity chamber maintained at constant relative humidity for a period of 10-360 minutes, an approach known as vapour transport process [53]. The resulting pellets are placed in a heatable die and hot pressed under pressure of 80 – 570 MPa at temperature between 25 to < 300 ^{O}C. The natural phenomena in geological and biological activities, sintering under hydrothermal conditions and a successful room temperature sintering of molybdates inspired the emergence of CSP [262].

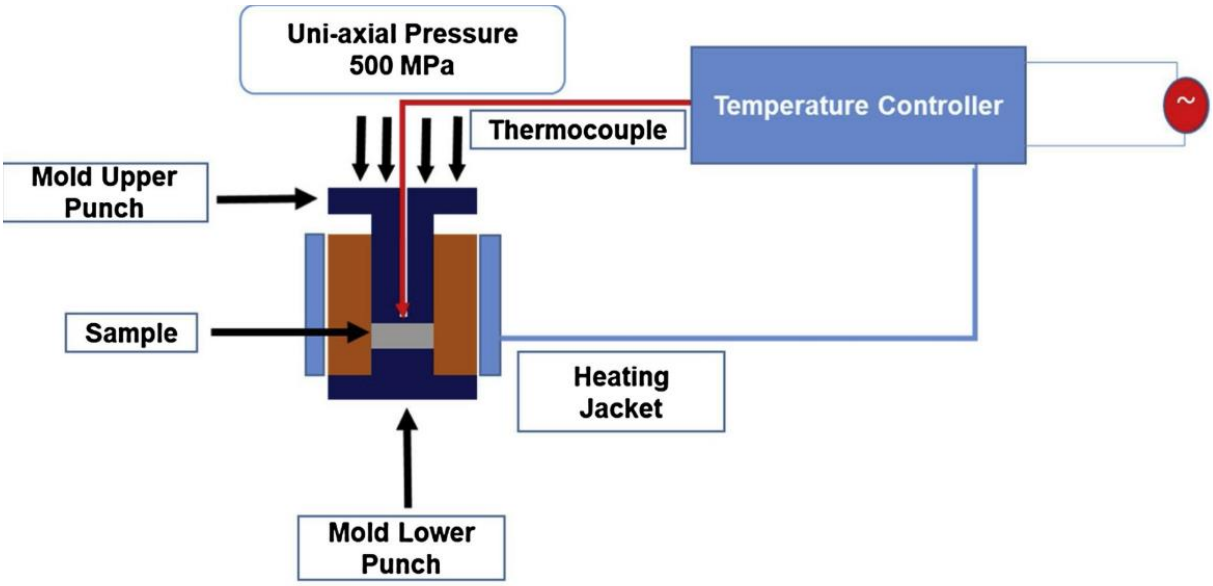

Figure 2-8. Schematic representation of cold sintering experimental arrangement [263]

The CSP temperatures could facilitate a single step co-sintering process of different materials chemistries such as ceramic with thermoplastic materials to provide novel composites with new functionalities. It is a borrowed terminology from powder metallurgy used over decades to refer to a process of compacting metal nanoparticles at ultra-low temperature below 400 ^{O}C at high pressure in GPa range by plastic flow mechanism [264]. According to Randall et al., the approach has reduced the sintering temperature window of several compositions to < 200 ^{O}C as evident in the Gibbs free energy reduction associated with cold sintering process as shown in Figure 2-9. Thus, the process has the potential to trigger fabrication of future advance novel materials from various chemistries with unique crystal structures for various applications. The properties of the selected materials fabricated using CSP have equal physical properties to those made via the traditional thermal sintering process [259].

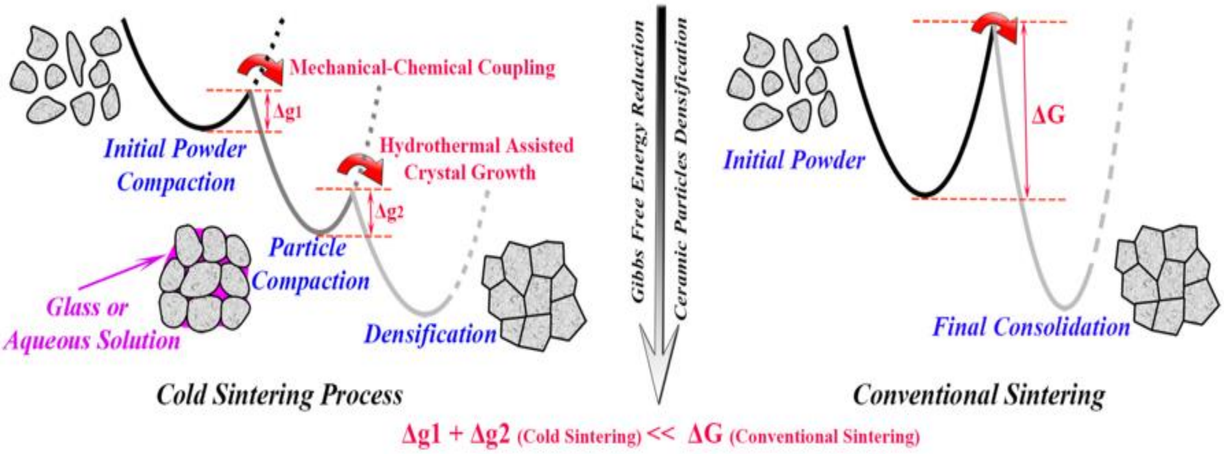

Figure 2-9 CSP Gibbs free energy comparison with conventional thermal sintering process [265].

Several inorganic chemistries with varying chemical composition and crystal structure ranging from binary to quinary compounds of phosphates, carbonates, iodides, fluorides, chlorides, and oxides have been cold sintered for various applications. These include dielectrics, thermoelectric, ferroelectrics, electrical, medical, structural, environmental, insulator, catalyst, energy storage and general applications [50]. Table 2-1 list the various materials cold sintered, areas of application and key properties investigated. Though, to date cold sintering is not compatible to some compositions such as zirconium oxides and carbides. Recently, the CSP of B_4C was reported with very low density of 57 - 62% but comparable to those made at temperature >2000°C by pressure less sintering [266]. The materials cold sintered for thermoelectric application include PbTe, $NaxCO_2O_4$, Bi_2Te_3, [36], $Ca_3Co_4O_9$ [40, 267] and ZnO [39, 40, 54, 68, 268-270]. The cold sintering of ZnO ceramics with acetic acid solution received the most research attention among ceramics. It was produced between 120°C - 305°C maximum temperature in the presence of small amount of acetic acid solution. In a recent study to demonstrate the influence of the ZnO nano-size particles, only deionized water was used and its theoretical density was above 99% [271]. Majority of the cold sintering studies reported ZnO conductivity of $\lambda = 12$ S/cm [50] lower than $\lambda = 41$ S/cm observed in $Ca_3Co_4O_9$ by

Funahashi, Guo [40] and $\lambda = 65$ S/cm by dos Santos, Thomazini [267]. Recently, Ndayishimiye *et al*. [272] compared the microstructural evolution and mechanism of cold sintered ZnO with those sintered using hydrothermal sintering method. Floyd *et al*. [273] cold sintered ZnO with crystalline zinc acetate dihydrate as transport phase to eliminate presence of aqueous solution. The high relative density of 96% observed shows that transport of mass is primarily by the adsorbed and structural water present in the crystalline transport phase and not by excess water which slow down densification unless it leaves the system by extrusion or evaporation. In a related study, Serrano *et al*. [274] studied the influence of microparticles (MPs) and nanoparticles (NPs) ratio of the starting powder on the morphology, structural properties and photoluminescence response of cold sintered ZnO. Kermani *et al*. [275] developed an innovative hybrid flash and cold sintering process combining water and electricity to sinter and preserve the defect structure of ZnO. In all the cold sintered ZnO studies, temperature between the range of 120℃ - 305℃ was used under pressure of 350 - 750 MPa. Several ZnO based composites were cold sintered for electrical applications with relative density >90% at temperature between 180 - 300 ℃ in the presence of acetic acid solution. These include ZnO-Ti_3C_2Tx [276], $InGaZnO_4$ [277], ZnO-PTFE [278, 279] and more recently are ZnO-$BaTiO_3$ [280]. The high relative density >95% of cold sintered ZnO-$BaTiO_3$ was obtained at low CSP temperature of 250 ℃ and $BaTiO_3$ was 10 wt% beyond which ZnO sinterability depreciates, grain size reduces, and dielectric properties drop. The ceramics compositions cold sintered for electrical applications with relative density ~90% using water as transient liquid are $K0_{.5}Na_{0.5}NbO_3$-NaCl [281], V_2O_5-CNF [282], and V_2O_5-PEDOT-PSS [283, 284]. Other materials cold sintered are Bi_2O_3, AgI, Na_2ZrO_3 [36], and V_2O_5 at 120℃ to 90% theoretical density but with low conductivity of $\lambda = 4.8 \times 10^{-4}$ S/cm [36, 285] lower than $\lambda = 16$ S/cm observed in the ZnO-Ti_3C_2Tx composites [276].

The number of dielectric materials reported in literature constitute majority of all cold sintered chemistries. These include TiO_2-Nb_2O_5 [286], Al_2O_3-NaCl, Al_2SiO_5-NaCl, $MgTiO_3$–NaCl [287-

289], Na_2WO_4 [290], $(Bi_{0.95}Li_{0.05})(_{.9}Mo_{0.1})O_4$-$Na_2Mo_2O_7$ [291], $K_2Mo_2O_7$ [292, 293], $(LiBi)_{0.5}MoO_4$ [293], $Li_{0,5x}Bi_{1-0,5x}Mo_xV_{1-x}O_4$ [36], (1-x)$(LiBi)_{0.5}MoO_4$-xPTFE [293], $Li_2Mg_3TiO_6$ [294], Li_2MoO_4, Li_2MoO_4-PTFE [293, 295], , Li_2MoO_4-$BaFe_{12}O_{19}$ [295], MoO_3[36, 296], $Na_{0.5}Bi_{0.5}MoO_4$-Li_2MoO_4 [297] and $Na_2Mo_2O_7$ [293]) shows that they are the most fabricated materials by cold sintering process. The dielectric materials were sintered at different CSP conditions between 120℃ - 250℃ with 4-25 wt % water except TiO_2-Nb_2O_5 and $Li_2Mg_3TiO_6$ cold sintered with 20-60 wt% 1M acetic acid solution and 20 wt% 4M LiOH solution. Similarly, the relative density obtained was >90 % except $(LiBi)_{0.5}MoO_4$ and (1-x) $(LiBi)_{0.5}MoO_4$-xPTFE with relative density < 90% and highest dielectric constant (ε_r) of 37.1 and ~ 40 respectively. The low temperature sintered Li_2MoO_4 dielectric ceramic on Nickel foil and PET film was tested as capacitor material in which CSP provides additional functionality and eliminates Nickel oxidation occurring at temperature above 300 ℃ as observed in conventional sintering techniques [298]

Cold sintered ferroelectrics at temperature between 120℃ - 300℃ were reported such as the $SrTiO_3$, $Gd_2(MoO_4)_3$, $Pb(Zr,Ti)O_3$, KH_2PO_4, $NaNO_2$, and $BaTiO_3$ using different transient liquids as shown in Table 2-1. The aqueous solution of the corresponding constituents of $SrTiO_3$ was used as transient liquid, lead nitrate solution for $Pb(Zr,Ti)O_3$ and Ba (OH)2/TiO_2 suspension for $BaTiO_3$ ceramic because of its incongruent dissolution. The water soluble $NaNO_2$ and KH_2PO_4 were cold sintered using water to a very high density >98%. Though, despite high relative density, amorphous phase appeared at the grain boundary of $BaTiO_3$ limiting its piezoelectric properties to meet application requirement. To address this challenge, CSP-post annealing process was carried out at 900℃ for 3 hrs to modify its crystal structure and improve properties [21, 37].

Significant number of materials for general, solid state battery materials [50] and few for medical [299], catalysis, insulation, biological [36] environmental [263, 300, 301], structural [302] and recently composite thermal energy storage materials have been produced by CSP.

The cold sintering of ceramic MgO and many ceramics for general application was only mentioned in literature without details regarding its CSP. MgO cold sintering was mentioned as unpublished data in literature [36, 38] until very recently reported in its low and medium temperature hydrate assisted sintering [303]. It was cold sintered at 180 °C with surface hydrate as sintering aid to a relative density of 93%. The final sintered MgO had significant amount of $Mg(OH)_2$ removed by further increase in the sintering temperature to 450℃ [303].

In recent time energy storage materials also dominates as evident in the rapid growing number of CSP fabricated solid-state battery materials. Significant number of these materials were cold sintered at low temperature between 120-180 ℃ to a very high theoretical density of 83 - 95% as depicted in Table 2-1. Some of the more recent battery materials cold sintered with water include NASICON-type $Li_{1.3}Al_{0.3}Ti_{1.7}(PO_4)_3$ (LATP) [304], $Li_{13.9}Sr_{0.1}Zn(GeO_4)_4$ (LSZG) [305]. Meanwhile, Sodium β-Al_2O_3 (SBA) [306] and $Na_3V_2(PO4)_3$(NVP)|$Na_3Zr_2Si_2PO_{12}$ (NZSP)-CNF with NaOH [307], LLZO-SM with dimethylformamide [308] and Fe_2O_3-doped 8YSZ with $Y(NO_3)_3$ solution [309]. To overcome the influence of aqueous solution in promoting proton exchange during cold sintering of battery materials such as garnet, a modified cold sintering process at 375 °C was carried out using fused hydroxide to replace the use of water or other sintering aids containing water [310]. In addition to battery materials for energy storage, three different composite phase change materials have so far been fabricated using cold sintering approach, namely $NaNO_3$-$Ca(OH)_2$ [49], Al_2O_3-NaCl [47] and $NaNO_3$/MgO [48]. In each of this attempts some successes have been recorded and the potentials of cold sintering to fabricate composite thermal storage materials at low temperature is demonstrated. Though, the understanding of the cold sintering is at early stage and composite systems made of insoluble ceramics requires details fundamental understanding to apply CSP to different composite phase change materials and overcome a major challenge of mismatch in processing temperature.

2.5.1 Composite fabrication by CSP

It is generally challenging via conventional sintering processes at higher temperature to fabricate a composite made of ceramics with polymer or nanoparticles due to mismatch in thermal expansion coefficient and processing temperatures of ceramics with metals, polymers, or nanoparticles [53, 279]. The low temperature cold sintering process provides not only opportunity to co-sinter diverse material chemistries but also provides significant reduction in thermal budgets [53, 279].

2.5.1.1 Cold sintering process of composite ceramic-polymer

CSP have been used to fabricate a dense composite made of organic-inorganic and few inorganic-inorganic composites. The ceramic-polymer composites have been reported in various studies as shown in Table 2-3 to 2-8. The use of polymers as fillers during cold sintering of ceramics provides opportunity to design and fabricate functional ceramics with enhanced mechanical, thermal and electrical properties [53]. Guo *et al*. [311] made the first attempt using CSP to fabricate a dense composite from different ceramics and polymers in a single step with surprised volume fraction. The study presents three diphasic to explain the CSP potentials in composite fabrication between organic and inorganic oxides namely Li_2MoO_4 – (–C_2F_4–) n (microwave dielectric), V_2O_5–poly (3,4-ethylenedioxythiophene) styrene sulfonate (semiconductor), and $Li_{1.5}Al_{0.5}Ge_{1.5}$ $(PO_4)_3$– (–CH $_2CF_2$–) $_x$[–$CF_2CF(CF_3)$ –] *y* (electrolyte) composites. The ceramics Li_2MoO_4 (LM), $Li_{1.5}$ $Al_{0.5}Ge_{1.5}$ $(PO_4)_3$ (LAGP), V_2O_5 and polymers PTFE dielectric material; PVDF-HFP electrolytes; and PEDOT: PSS conductors were cold sintered as composites respectively. The composites were cold sintered at 120 ^{O}C, 350 MPa for 20 minutes with exception of LAGP ceramics composite cold sintered in 60 minutes. The results obtained revealed a high relative density > 90 % for LM-PTFE and V_2O_5 – PEDOT: SS and 80-88 % for LAGP-(PVDF-HFP) composites respectively. The high relative density and pure two-phase system composites explains the level of compatibility of polymer-ceramic composite fabrication to the CSP process and its conditions. In addition, the low pH value of PEDOT: PSS (1.5-2.5) was observed to have influence on the V_2O_5 dissolution rate which further drives relative density increase of the PEDOT: PSS composite. The observed composite densification limit achieved demonstrated CSP potentials for greater densification improvement higher than 65% - 75% relative density achieved for LM, LAGP and V_2O_5 ceramics separately.

Table 2-3 Ferroelectric materials cold sintered, their processing conditions and key properties, and areas of application

Materials	Application	Processing conditions	Properties	R.D (%)	Ref.
$BaTiO_3$	Ferroelectric	430 MPa, 180 °C, 1–180 min, 25 wt% Ba $(OH)2/TiO_2$ suspension	$\varepsilon_r = 2332$, $\tan\delta = 0.01$ @ 10^{-3} MHz after annealing @ 900 °C	~80–97*	[265] [316], [21, 317]
$NaNO_2$	Ferroelectric	350 MPa, 120 °C,1–180 min, 7wt% water	Curie transition and melting enthalpies of ~34 and ~194 J/g	98	[265]
KH_2PO_4	Ferroelectric	350 MPa, 120 °C, 30 min, 7wt% water	N.A.	>98	[265]
$Gd_2(MoO_4)_3$	Ferroelectric	N.A.	N.A.	>94%	[36]
$Pb(Zr,Ti)O_3$	Ferroelectric	500 MPa, 300 °C, 150 min, 0.5 ml lead nitrate solution	d_{33} = 4 pC/N @ CSP, d_{33} = 197 pC/N @ 900 °C for 3 h	89	[318]
$SrTiO_3$	Ferroelectric	≤750 MPa, 180 °C, 60 min, aqueous solution of $SrCl_2$ mixed with TiO_2	N.A.	~96–97 after annealing @ 950 °C	[319]

Table 2-4 Optical and Dielectric materials cold sintered, their processing conditions and key properties

Materials	Application	Processing conditions	Properties	R.D (%)	Ref.
$AgVO_3$, $BaMoO_4$, CsBr and ZrF_4	Optical	N.A.	N.A.	N.A.	[36]
TiO_2-Nb_2O_5	Dielectric	300 MPa, 200 °C, 30-60 mins, 20-60 wt% 1M acetic acid solution, Microwave: 170 °C for 5mins	N.A.	>90	[286]
Al_2O_3-NaCl	Dielectric	200 MPa, 120 °C, 50 min, 4 wt% water	ε_r ~ 6.5, tanδ = 0.007 @ 1 MHz ε_r ~ 6.0, tanδ = 0.002 @ 5 GHz	96	[287]
Na_2WO_4	Dielectric	400 MPa, 240 °C, 2 wt % water, 1 hr.	permittivity = 5.80, Q × f = 22,000 GHz, TCF = −70 ppm/°C	92	[290]
$MgTiO_3$–NaCl	Dielectric	450 MPa, < 250°C, 30 min, water	Qxf= 29,500 GHz @ x = 0.2	N.A.	[288]
Al_2SiO_5-NaCl	Dielectric	200 MPa, 120 °C, 50 min, 4 wt% water	ε_r = 5.37, tanδ = 0.005, @ 1 MHz, ε_r =4.71, tanδ = 0.002, @ 1 MHz	N.A.	[289]
$(Bi_{0.95}Li_{0.05})(._{9}Mo_{0.1})O_4$-$Na_2Mo_2O_7$	Dielectric	200 MPa, 150 °C, 30 min, h 5–10 wt.% water	ε_r = 40–48, tanδ = 0.0012	95–96	[291]
$K_2Mo_2O_7$	Dielectric	350 MPa, 120 °C, 15–20 min, 4–25 wt.% water	ε_r = 9.8, tanδ = 0.00083	~94	[292, 293]
$(LiBi)_{0.5}MoO_4$	Dielectric	250–350 MPa, 25°C-120 °C, 20 min, 6-10 wt% water	ε_r = 33.7–37.1	~88–89	[293]
$Li_{0,5x}Bi_{1-0,5x}Mo_xV_{1-x}O_4$	Dielectric	N.A.	N.A.	N.A.	[36]
$(1-x)(LiBi)_{0.5}MoO_4$-xPTFE	Dielectric	Room Temp.-250–350 MPa, 120 °C,	ε_r ~ 10–40	>85	[293]

		20 mi6-10 wt% water			
$Li_2Mg_3TiO_6$	Dielectric	300 MPa, 180 °C, 1 h, 20 wt% 4 M LiOH solution,	ε_r = 15.51–15.68 after HT @ 800–950 °C	~90	[294]
Li_2MoO_4	Dielectric	37–74 MPa, 120 °C, 15–20 min, 6-10 wt% water	ε_r = 5.6	~96	[293]
Li_2MoO_4-PTFE	Dielectric	37–74 MPa, 120 °C, 15–20 min, 6-10 wt% water	ε_r = 5.8–2.9	>90	[293]
Li_2MoO_4-$BaFe_{12}O_{19}$	Dielectric	55–70 MPa, 120 °C, 10–40 min, 20 wt.% water.	ε_r = 5.6–5.8	94–97	[295]
MoO_3	Dielectric	100–150 MPa, 120–150 °C,10–30 min, 4 wt. % water	ε_r = 9.91 after HT @ 700 °C	77	[36, 296]
$Na_{0.5}Bi_{0.5}MoO_4$-Li_2MoO_4	Dielectric	200 MPa, 150 °C, 30 min, 5–10 wt % water	ε_r ~ 17.4, $\tan\delta$ = 0.0008	~93–96	[297]
$Na_2Mo_2O_7$	Dielectric	250–350 MPa, 120 °C, 15–20 min, 6-10 wt%	ε_r = 13.4	~94	[293]

Table 2-5 Electrical application materials cold sintered, their processing conditions and key properties

Materials	Application	Processing conditions	Properties	R.D (%)	Ref.
Bi_2O_3, AgI, Na_2ZrO_3, V_2O_3,	Electrical	N.A.	N.A.	N.A.	[36]
$InGaZnO_4$	Electrical	100–50 MPa, 25–180 °C, 10 min, 15 wt% ammonia solution	N.A.	~92–99 After annealing @ 1200 °C	[277]
V_2O_5	Electrical	350 MPa, 120 °C, 20 min, 4–25 wt.%	$\lambda = 4.8 \times 10^{-4}$ S/cm E_a ~ 0.25 eV	90.2	[36, 285]
V_2O_5-CNF	Electrical	350 MPa, 120 °C, 20 min, 12–22 wt % water	$\lambda = 10–10^2$ S/cm VC = 800 mAh/cm^3 @ ~0.2C-Rate	~89	[282]
V_2O_5-PEDOT-PSS	Electrical	300–350MPa,120–140 °C, 20–5 min, 11–17 wt%	$\lambda = 10^{-3}–10^{-2}$ S/cm E_a ~ 0.2 eV ρ = 6.34 Ωm	~90	[283, 284]
WO_3, ZnMoO4, ZnTe	Electrical	N.A.	N.A.	N.A.	[36]
ZnO-$Ti_3C_2T_x$	Electrical	250 MPa, 300 °C, 60 min, 17–20 wt% 1.5 M acetic acid	Hv ~ 2–5 GPa E ~ 60–110 GPa λ = 16 S/cm	92–98	[276]
$K_{0.5}Na_{0.5}NbO_3$-NaCl	Electrical	420 MPa, 120 °C, 60 min, 3 wt% NaCl in 20 wt% water	Tc= 448 °C, d33= 115 pC/N, kp= 32%	N.A.	[281]
ZnO-PTFE	Electrical	300 MPa, 285 °C, 60 min, 15-20 wt% acetic acid (2 mol/L)	α = 3–7 $E_b \leq$ 3225 V/mm E_a ~ 0.8 eV	>90	[278, 279]
ZnO-$BaTiO_3$	Electrical	66 MPa, 250 °C, 1h, 1M acetic acid solution	N.A.	>95	[280]
ScSZ	Electrical	350 MPa, 180 °C, 60 min, 20 wt% water	λ = 0.015 S/cm after HT @ 1200 °C, 0.11 S/cm @ 1400 HT	>70	[320]

Table 2-6 Thermoelectric materials cold sintered, their processing conditions and key properties

Materials	Application	Processing conditions	Properties	R.D (%)	Ref.
ZnO	Thermoelectric	20 MPa, 60 s, 20 V, 30A	N.A.	96.5	[275]
ZnO	Thermoelectric	750 MPa, 170 °C, 1hr, 20 wt% acetic acid solutions	N.A.	95	[274]
ZnO	Thermoelectric	530 MPa, 120 °C, 1 h, Crystalline $Zn(OAc)2\cdot 2H_2O$	N.A.	96	[273]
ZnO	Thermoelectric	155 °C, 320 MPa, <80 min, 15 wt. % acetic acid	N.A.	> 98	[321]
$Ca_3Co_4O_9$	Thermoelectric	350 MPa, 150 °C, 1h, 64 wt% acetic acid solutions	λ = 6459 S/m, λ_t= 0.672 W/m K	74	[267]
ZnO	Thermoelectric	50-300 MPa, 25°C, 1.6 wt. % water	N.A.	> 99	[271]
ZnO	Thermoelectric	0–530 MPa 25–305 °C, 5–300 min, 20 wt% 0.1-17.5 M acetic acid solution	λ = 12 S/cm σ_0 ~ 64.4 MPa m = 8.2	~65–99	[39, 40, 54, 68, 268-270]
PbTe, $NaxCO_2O_4$, Bi_2Te_3	Thermoelectric	N.A.	N.A.	N.A.	[36]
$Ca_3Co_4O_9$	Thermoelectric	350 MPa, 135–350 °C, 60 min, 5 wt% water and 1.0 mol /L acetic acid	λ = 41 S/cm	85–90	[40]

Table 2-7 Energy storage materials cold sintered, their processing conditions and key properties

Materials	Application	Processing conditions	Properties	R.D (%)	Ref.
Porous Zn electrode	Energy storage	10% acetic acid	N.A.	N.A.	[322]
$LiFePO_4$-CNF	Energy storage	240 MPa, 180 °C, 10 min, water vapor	VC = 373 mAh/cm^3 @ 0.1C (discharge rate)	~70	[323]
LAGP–LiTFSI and LATP–LiTFSI	Energy storage	LAGP–LiTFSI: 380 MPa, 130 °C, 2 h, 10 wt% water LATP–LiTFSI: 620 MPa, 130 °C, 2 h, 20 wt% water	$\lambda i = 10-4$ S cm^{-1} @ 20 °C	~90	[324]
$Li_{1.5}Al_{0.5}Ge_{1.5}(PO_4)_3$	Energy storage	400MPa, 25-160°C, 20 minutes, 30-39vol% water or 50-56vol% ethanol	$\lambda = 5.4 \times 10^{-5}$	80	[325]
$LiFePO_4$-PVDF-C	Energy storage	30–750 MPa, 240 °C, 30 min, 0.95 wt% LiOH	VC ~ 340 mAh/cm^3 @ 0.03–0.1C	~89	[326]
MoS_2-Graphite	Energy storage	520 MPa,140 °C, 1 h, water	SC = 950 mAh/g at 0.1 A/g	88	[327]
$Na_{3.256}Mg_{0.128}Zr_{1.872}Si_2PO_{12}$	Energy storage	300–780 MPa, 120–180 °C, 10–120 min, 30 wt % water	$\lambda \sim 1.4 \times 10^{-3}$ S/cm $\lambda_i = 0.88$ mS/cm after annealing @ 1100 °C	~83	[328]
$Li_4Ti_5O_{12}$-Carbon nanofibre (LTO-CNF)	Energy storage	500 MPa, 120 °C. 30 min, water vapour humidified for 30 min	VC~380 mAh/cm^3	87	[329]
$Li_{6.25}Al_{0.25}La_3Zr_2O_{12}$	Energy storage	510 MPa, 300°C, 15–60 min, water	$\lambda_i = 9.13$ µS cm^{-1}	N.A.	[330]
gc-$Li_{3.2}P_{0.8}Sn_{0.2}S_4$ SSE	Energy storage	N.A.	$\lambda = 1.21 \times 10-3$ S cm−1 @ RT	N.A.	[331]
Sodium β-Al_2O_3 (SBA)	Energy storage	360 MPa, 10 wt% solid NaOH, 350–375 °C, 3hrs	$\lambda \sim 10^{-2}$ S cm^{-1} @ 300 °C	>90	[306]

NASICON-type $Li_{1.3}Al_{0.3}Ti_{1.7}(PO_4)_3$ (LATP)	Energy storage	25 MPa, 200 ◦C, 5-30 min, 30 wt%	$\lambda = 3.0 \times 10{-}4$ S/cm		[304]
$Na_3V_2(PO4)_3$ (NVP)|$Na_3Zr_2Si_2PO_{12}$ (NZSP)-CNF	Energy storage	360 MPa, 350–375 °C, 3h, sodium hydroxide	$\lambda = 3.8 \times 10{-}8$ $S{\cdot}cm^{-1}$ (pure NVP), 5.81×10^{-6} $S{\cdot}cm^{-1}$ (60 wt% NZSP) and 1.31×10^{-5} $S{\cdot}cm^{-1}$ (5 wt % CNF)	>90	[307]
LLZO-SM	Energy storage	400MPa, 120 °C, 3 h, Dimethylformamide (DMF)	$\lambda = 10^{-4}$ S/cm	85–90	[308]
$Li_{13.9}Sr_{0.1}Zn(GeO4)_4$ (LSZG)	Energy storage	300 MPa, 120-200°C, 1 h, 30 wt% water	$\lambda_i = 3.0 \times 10^{-2}$ Scm^{-1} @ 400 °C	N.A.	[305]
Fe_2O_3-doped 8YSZ	Energy storage	350 MPa, 120 °C, 30 min, Y(NO3)3 solution	N.A.	95	[309]
$Na_3Zr_2Si_2PO_{12}$	Energy storage	350 MPa, 375 °C, and 3 h, 10 w/w fused NaOH,	$\lambda_i = 2 \times 10{-}4$ S/cm	>90	[310]
$BaCe_{0.8}Zr_{0.1}Y_{0.1}O_{3-\delta}$	Energy storage	125 to 500 MPa,180 °C, 30 min, 5 to 20 wt%	N.A.	94	[332]
$(Fe_{1.72}Mg_{0.8}Mn_{0.01}Ca_{0.02})^{2+}(Fe_{0.04}Al_{2.36})^{3+}Si_{2.93}{}^{4+}O_{12}$	Energy storage	450 MPa, 120–250 °C, 50 min, 15 wt% water	$\varepsilon_r = 6$–8, Q_ux f > 2000 GHz (f ≈10 GHz)	80–95	[333]
$NaNbO_3$-PVDF	Energy storage	550 MPa, 180 °C, 10 min, water	$E_b = 1345$ kV/cm	~97	[46]
LiCoPO4, LiVO3	Energy storage	N.A.	N.A.	N.A.	[36]
$NaNO_3$-Ca$(OH)_2$	Energy storage	500 MPa, 120 °C, 10 min, 10 wt% water	$\sigma_c \sim 20$–120 MPa $E_{es} = 59.48\%$	N.A.	[49]
NaCl-Al_2O_3	Energy storage	100-500 MPa, 80-140 °C, 10-90min, 0.15 g water	$L_V = 252.5$ J/g	98.65	[47]
$NaNO_3$/MgO	Energy storage	75 MPa, ≤180 °C, 6 wt% water	N.A.	>98	[48]

Table 2-8 General and other applications materials cold sintered, their processing conditions, and key properties

Materials	Application	Processing conditions	Properties	R.D (%)	Ref.
$Ca_5(PO_4)_3(OH)$	Medical	N.A.	N.A.	N.A.	[36]
Alumina-HA	Medical	500 MPa, 300 °C, 10 mins			[299]
Diatomaceous earth	Structural	300 MPa, 25-150°C, 12 min, 0.25-g NaOH	N.A.	90	[302]
$Ca_5(PO_4)_3(OH)$	Environmental	500 MPa, 200 °C, 10 min, dry pressed	H_v = 2.2–2.6, GPa, σ_c ~ 175 MPa	95–97	[263, 300, 301]
$Mg_2P_2O_7$	Biological	N.A.	N.A.	N.A.	[36]
Cs_2WO_4	Insulator	N.A.	N.A.	N.A.	[36]
Na_2WO_4, $CsSO_4$, Li_2WO_4, and $BiVO_4$	Catalyst	N.A.	N.A.	N.A.	[36]
$K_{0.5}Na_{0.5}NbO_3$	Piezoelectric	350 MPa, 120 °C, 30 min, 5 wt.% to 15 wt.%	d_{33} = 131 pC/N after HT @ 1115 °C	~65	[334]
CsH_2PO_4	Energy	300 MPa, 120–200 °C, 1 h	Ea = 0.38–0.4 eV $\lambda = 2.3 \times 10^{-4}$ S/cm at 200 °C	93–98	[43]
ScSZ	Electrical	350 MPa, 180 °C, 60 min, 20 wt% water	λ = 0.115 S/cm after HT @1200°C, 0.111S/cm @1400 HT	>70	[320]
ZrO_2	General	350 MPa, 180 °C, 30–180 min	Hv = 0.5 GPa @ CSP, Hv = 13.6GPa after annealing @ 1200 °C	~56–96	[36, 335, 336]
TiO_2	General	250–500 MPa, 150 °C, 30 min, 20-80 wt% water	SSA = 117 m^2/g	68	[30]
NaCl	General	300 MPa, 25–120 °C, 10 min, 4 wt% water	ε_r ~ 5.9	~93–99	[41, 67]
MnO	General	530 MPa, 100–300 °C, 30–60 min, dimethyl	N.A.	94	[268]

		sulfoxide solution			
CeO_2	General	500 MPa, 180 °C, 24 h, 7% wt. Malonic acid solution	Ea = 1.13 eV	~70	[337]
CeO2	General	500 MPa, 25°C-400°C, 10min, NaOH-KOH (51-49 molar ratio)	Ea = 0.49 eV	82-91	[338]
MgO, Li_2CO_3, KPO_3, CuCl	General	N.A.	N.A.	N.A.	[36]
MgO	General	500 MPa, 180 °C, 0-27 min 10 wt.% water	N.A.	93	[303]
$CaSO_4·2H_2O$	General	700 MPa, 25°C, 10 min, 15 wt% water	N.A.	89.6-96.8	[339]
PZT/Pb $(NO_3)_2$	General	500 MPa, 300°C, 15-180 min, 0.5 mL water	N.A.	66-80	[340]
Nano-to-macroporous TiO2	General	250-500 MPa, 150 °C, 30 min, 20-80% water and 60 wt% acetic acid solutions	ssa= 117 m^2/g,	60-68	[30]

The key processing parameter that influences cold sintered density is the transient solvent. Though, addition of soft materials such as polymers characterized by plastic shear could provide enhanced densification. However, comparative analysis between dry pressed and cold sintered using water clearly demonstrate enhanced densification benefits of cold sintering process of the composites. This is widely believed to be from its main dissolution-precipitation mechanism [312]. The following composites of an electrolyte $Li_{1.5}Al_{0.5}Ge_{1.5}(PO4)_3$ (LAGP)–PVDF-HFP (Poly (vinylidene fluoride-co-hexafluoropropylene)), dielectric $Li_2Mo_4O_4$ (LM)–PTFE (polytetrafluoroethylene), and V_2O_5–PEDOT: PSS (poly(3,4-ethylenedioxythiophene) polystyrene sulfonate) semiconductor were investigated. The relative density of all cold sintered was high between 80 – 98% and very low between 65-72% particularly at low polymer volume fraction of the dried pressed (Figure 2-10).

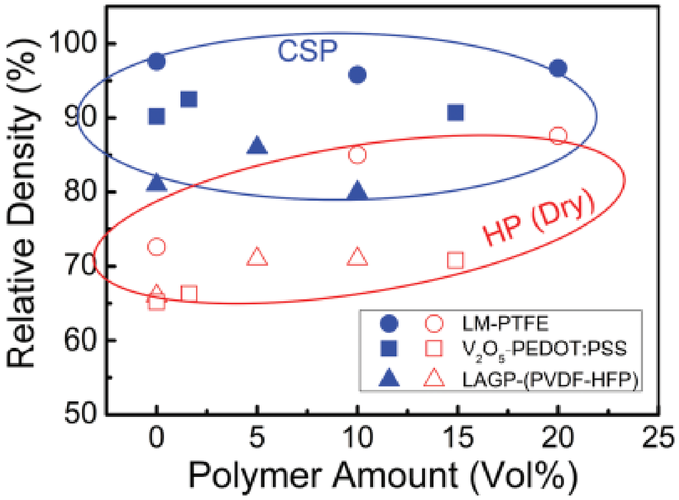

Figure 2-10 Relative density of cold sintered and dry pressed of (LM)–PTFE, LAGP-(PVDF-HFP), and V_2O_5-PEDOT: PSS composites at 120 °C and pressure 300–400 MPa [311].

The melting point of ceramics is much higher than the two transition temperatures namely the glass transition T_g and melting temperatures T_m of polymers and the polymer flow rate is a function of CSP temperature and pressure [313]. Thus, the CSP temperature of ceramic-polymer composite also plays a key role and determines the extent of densification, properties, and microstructural characteristics [313]. The role of temperature is demonstrated in the TEM images in Figure 2-11 of cold sintered composite $Na_2Mo_2O_7$ (NM) - polyetherimide (PEI) at temperature higher and lower than the PEI T_g temperature of 217 °C. It clearly shows that the region of PEI is made of large, segregated particles with clear polymers distribution at nanoscale in the intergranular boundaries. At cold sintering temperature $>T_g$ PEI flow easily into pores between ceramic grains with more PEI in the 90NM-10PEI composite grain boundaries cold sintered with water at 240 °C as shown in Figure 2-11b-c[312]. Meanwhile,

Figure 2-11d shows the presence of smaller particles of 1μm which influences uniform distribution to fill all the ceramic intergranular regions of the composite.

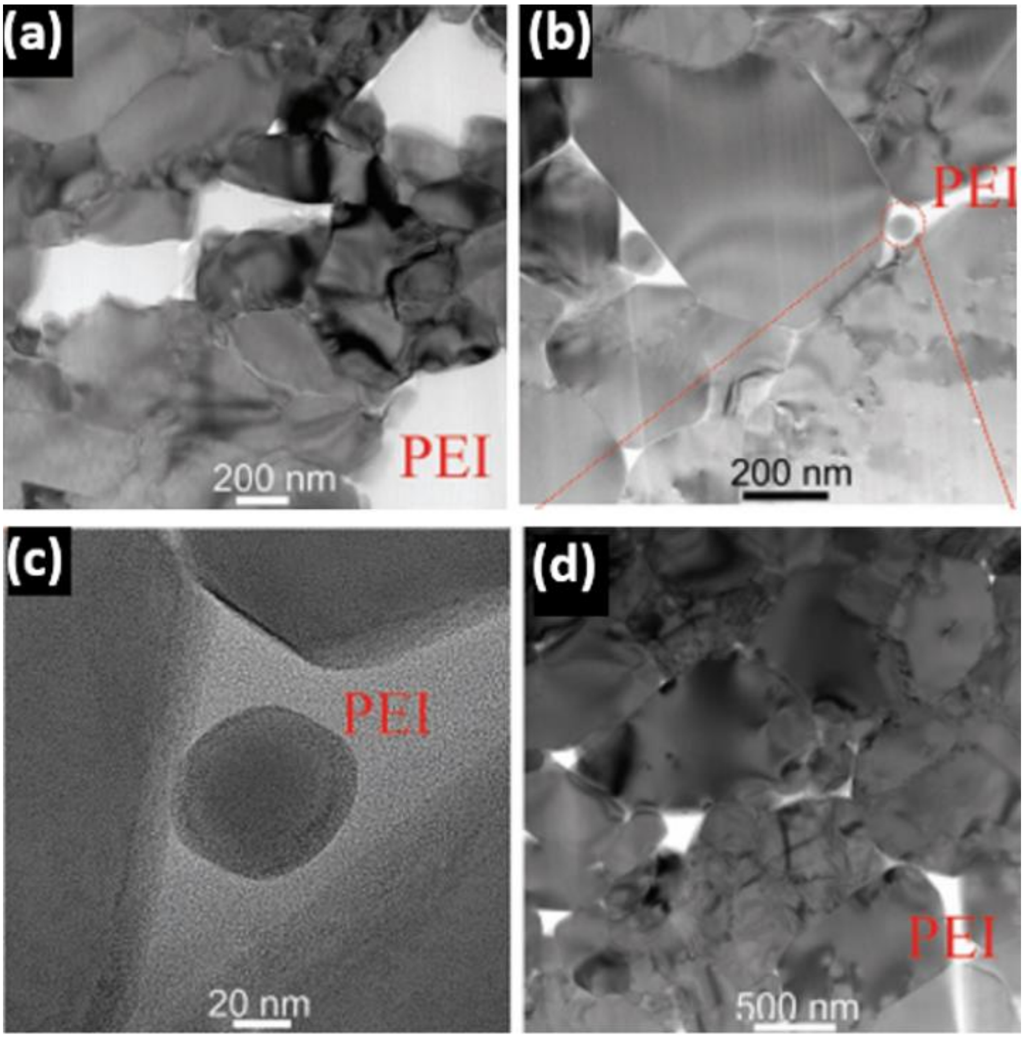

Figure 2-11 Cold sintered TEM images of NM-PEI composites using water under 300 MPa for composites containing (a) 90NM-10PEI (PEI: 15 μm) at120 °C (b-c) 90NM-10PEI (PEI: 15 μm) at 240 °C. (d) 90NM-10PEI (PEI: 1 μm) at 120 °C. The bright regions in TEM images belong to PEI [312].

The use of submicron and nano size starting powders during cold sintering process facilitate fabrication of ceramic-polymer nanocomposites as reported in the cold sintering of ZnO-PTFE nanocomposite using acetic acid solution (15 vol%–2 M) with ZnO and PTFE powder particle size of 40–100 and 500 nm [311]. TEM analysis of ZnO-PTFE shows a homogenous distribution of PTFE at 95ZnO-5PTFE composites grain boundaries with thin PTFE layer evenly distributed at the intergranular regions in a thickness layer of 1-10 nm at high TEM resolution of 5nm (Figure 2-12).

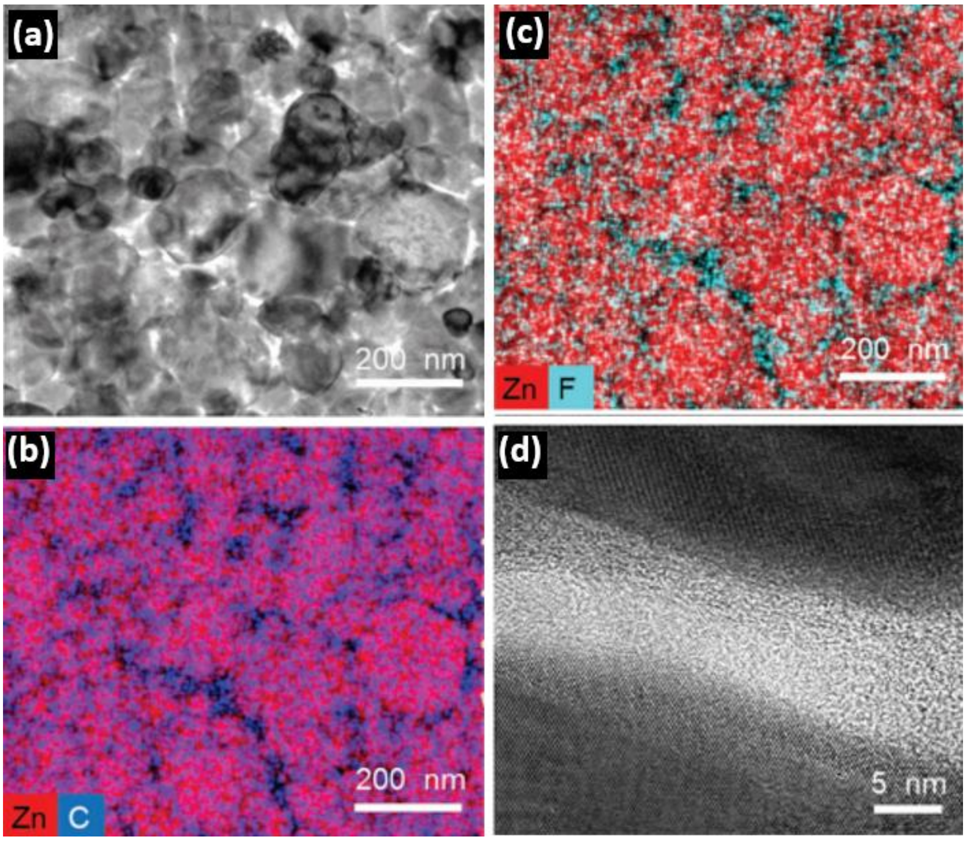

Figure 2-12 a) Cold sintered 95ZnO-5PTFE TEM image (b–c) EDS elemental distribution of cold sintered 95ZnO-5PTFE nanocomposite at 285 °C d) TEM of grain boundary interface of cold sintered 95ZnO-5PTFE. The letters C and F are for the PTFE [278]

2.5.1.3 Cold sintering process of composite PCMs

The fabrication of ceramic-PCM composite is being carried out using conventional sintering at high temperature or by PCM infiltration into a tailored porous ceramic [314]. These processes are energy consuming, prone to corrosion attack and high temperature sintering results into mismatch in the composite material melting temperature. Thus, this results into partial sintering of the ceramic support material because the PCM melting point is reached before its sintering temperature via conventional method [16]. Recently, innovative cold sintering process in the present of suitable transient liquid at temperature ≤300 °C under pressure has been proposed for the fabrication of composite materials for thermal energy storage. Yu *et al*. [315] cold sintered $NaNO_3/Ca(OH)_2$ composite phase change materials with $Ca(OH)_2$ salt as the matrix material encapsulating lower melting salt $NaNO_3$ instead of using high temperature ceramic material reported in previous studies. Though, attempt to use $CaCO_3$ as matrix has been made but the composite failed during thermal cycle test. The authors attributed the instability of the composite to insolubility of $CaCO_3$ in water limiting dissolution-precipitation process [315]. Structural analysis of the composite and elemental mapping shows a clear boundary between the constituent species and very good encapsulation of the $NaNO_3$ respectively. The region of the $Ca(OH)_2$ matrix revealed sintering of the $Ca(OH)_2$ particles triggered by pressure and temperature responsible for the coalescence of the particles by an epitaxial growth. This is evident by the appearance of grain boundaries between the $Ca(OH)_2$ particles. The phase change enthalpy after the first 100 thermal cycles was maintained near constant value of 94 J/g over the 400 repeated cycles. Further XRD analysis shows no new phase formation which demonstrate the composite chemical compatibility. The compressive strength increases significantly with pressure to a maximum of about 115 MPa at 400MPa pressure at which a plateau appeared beyond which further pressure increase has no effect on the composite compressive strength. Thus, this demonstrates the role of parameter-structure-property relation in the composite design and fabrication. Liu *et al*. [48] fabricated $NaNO_3$-MgO composite by cold sintering process using water as transient liquid at low temperature $\leq$ 180 °C under 75 MPa to >98% relative density. The authors investigation of the influence of key CSP processing parameters revealed 99%, 98%, 98.5% and 99% relative densities at pressure, dwelling time, amount of water and temperature of 200MPa, 10 minutes, 12 wt% and 120 °C respectively. Beyond these conditions a density plateau appeared and further increase in each of the variables has no effect on the densification of the composite expect in a preheated powder density decrease with increase in temperature. The phase change enthalpy of 109 J/g relatively maintained after 500 thermal cycles and good compressive strength >100 MPa demonstrate the potentials of CSP in the design and fabrication of composite phase change materials. Generally, understanding the mechanism of ceramics cold sintering will provide a guide to the fabrication of novel composite thermal storage materials.

2.5.2 Cold sintering process stages

The first description of the cold sintering process after its discovery by Randall group was reported by Guo *et al*. [26]. The authors [26] described CSP process as dissolution of the starting powder at particle interfaces with appropriate transient liquid. This result into dissolution of sharp edges of the powder particles by intentional liquid phase created at the particle interface. This eventually reduces an interfacial area that aids particle rearrangement, sliding and grain boundary creep in the next CSP stage as presented in Figure 2-19. The liquid phase present under appropriate temperature and pressure gradients is freely redistributed as it enters the pores between particles via diffusion. This influences monumental chemical driving force by solution-precipitation process responsible for solid-liquid equilibrium state to be achieved. The gradients further cause the excess liquid present to escape through the spaces between the punch and the die. The liquid is saturated by evaporation and drives precipitation process. During this process a higher chemical potential is created at the particle contact faces under capillary pressure. This paved way for ionic or atomic clusters to diffuse through the liquid and eventual precipitation on the particles stress free areas. This minimizes surface excess free energy and eliminates porosity of the material. After complete liquid evaporation, appearance of crystal nucleates was observed at the grain boundary and surface of very hygroscopic materials such as NaCl [341]. Though, some grain boundary points may be amorphous in the last sintering stage but solemnly depends on solute-liquid interaction and arrangement of atoms in crystalline solids.

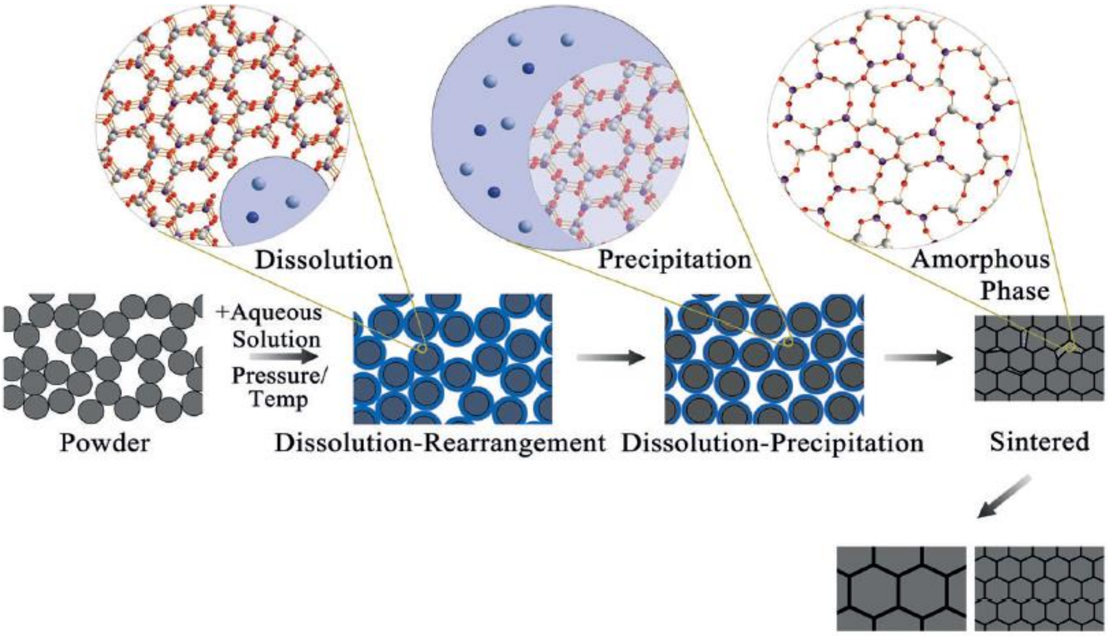

Figure 2-19 Schematic representation of powder compaction stages by cold sintering process [26].

Meanwhile, Guo *et al*. [265] presented further description of CSP at two levels namely macro and micro levels respectively. First, at the powder particle-particle interface, an appropriate amount of liquid phase solvent is introduced and homogenously wetted by mixing. Secondly, the powder is compacted by the application of uniaxial pressure. The liquid at the particle interfaces serves both as lubricant and solvent. The particles sharp edges dissolve into the solution under pressure and heat and precipitate into the pore spaces to drive sintering of the powder when the liquid phase solution is completely removed as shown in Figure 2-20.

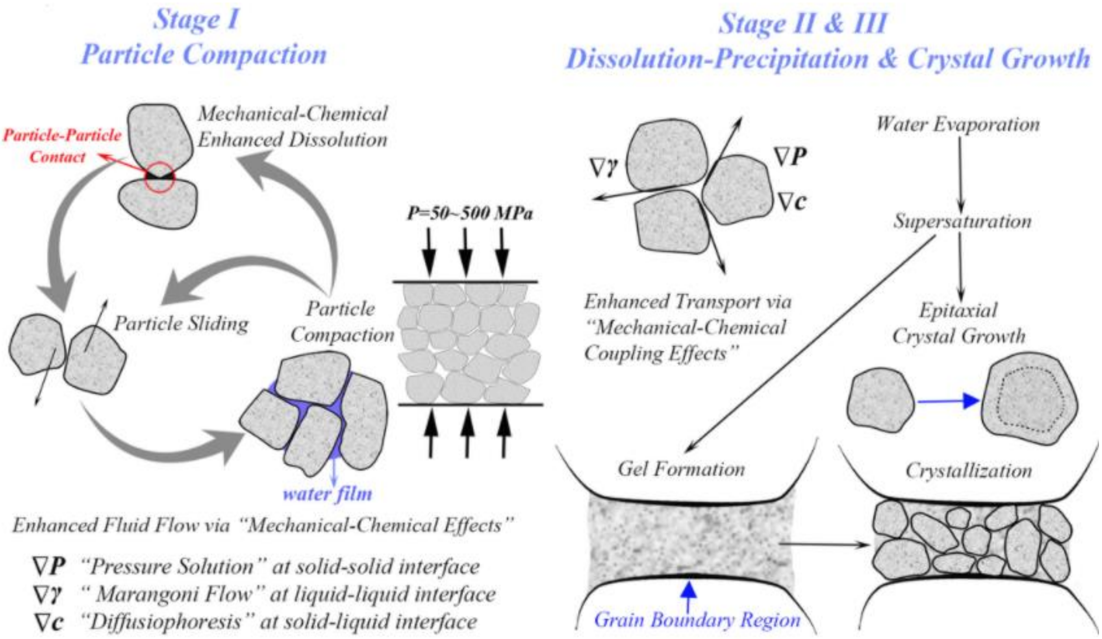

Figure 2-20 Schematic illustration of the three stages of CSP showing microstructure and major fundamental mechanisms of CSP [265].

More recent description by Maria *et al*. [36] describe cold sintering as two stage connected processes consisting of several speculated densification events as shown in Figure 2-21. At compaction stage, preferably nanosized ceramic powder with liquid is subjected to uniaxial pressure influencing particle rearrangement. The liquid provides some lubrications influencing particle sliding and is continuously discharged from the pressed powder through the punch-die clearance. Further increase in temperature under continuous pressing in the second stage, facilitates more solubility and dissolution-precipitation processes which dominates during the CSP in the heatable die. The liquid vaporises and escapes to form a supersaturated liquid necessary for densification. However, supersaturation of the liquid is necessary for densification to be achieved by dissolution of the powder particles in the solution or using either acidic or basic solution to influences dissolution to form saturated liquid.

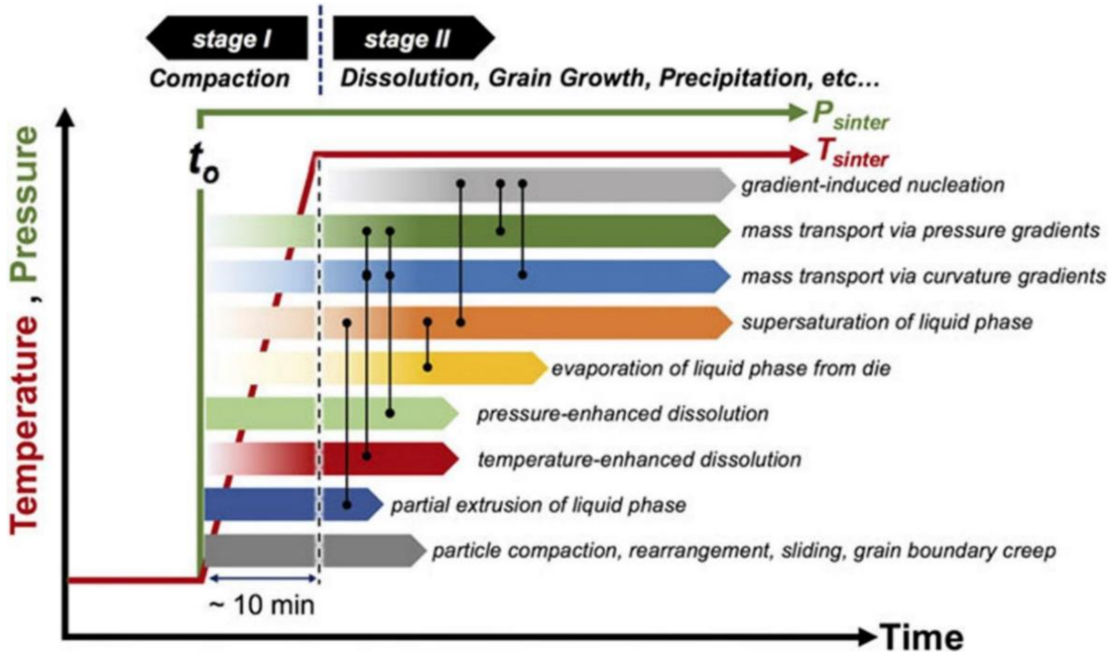

Figure 2-21. Schematic diagram of CSP process stages and mechanisms contributing to powder compaction, consolidation, densification and crystallization as a function of time [342].

2.5.3 Cold sintering process mechanism

The mechanism of different sintering processes ranging from solid state, viscous, liquid phase to pressure assisted sintering processes have been reported extensively from experimental and theoretical modelling perspectives [27]. In conventional solid-state sintering, viscous flow is the major rate controlling mechanism in amorphous and glass materials. Meanwhile, six (6) mechanisms were identified to characterize the solid-state sintering process of crystalline materials namely surface diffusion, vapour transport, lattice diffusion from particle surface, grain boundary diffusion, plastic flow and lattice diffusion from the grain boundary [27]. The later 3 mentioned mechanisms were identified as the densifying mechanisms encouraging neck growth and shrinkage while the former leads to neck growth and particle coarsening only, resulting into much undesired porosity for most applications. In liquid phase sintering process, particle rearrangement, dissolution-precipitation and Ostwald ripening are the three overlapping stages and the latter two are the densification mechanisms. The solution-precipitation and Ostwald ripening densification mechanism could both be diffusion control mechanisms or phase boundary reaction rate control mechanism in the case of solution-precipitation [27, 28].

However, in most hot-pressing processes, externally applied pressure provides enhancement to the existing or trigger the emergence of new pressure assisted mechanisms namely the lattice diffusion, grain boundary diffusion, plastic deformation, viscous flow, grain boundary sliding and particle rearrangement mechanisms [27]. The controlling mechanism of pressure assisted sintering could be diffusional or plastic deformation depending on the densification rate under the applied stress. Several approaches were reported to have been used to identify and establish the sintering mechanism, such as the method of determining the grain growth exponent (m) in solid state sintering, stress exponent (n) in pressure assisted sintering processes [27] and stress stepping method reported during uniaxial compaction creep study of a wet granular calcite [55]. These methods put together within their limitations are being used to identify the main underlying and rate controlling mechanisms. They form the basis of which most theoretical models were proposed and extensively studied to model sintering process with varying assumptions at various stages.

The mechanism of cold sintering process developed recently by Randall group at Penn State University have been described by the group as dissolution-precipitation process as shown in Figure 2-21. This is supported by evidence from various ceramic and polymeric materials cold sintered. It is the most important cold sintering mechanism as reported [292]. The significance of this process was demonstrated in the cold sintering of Al_2O_3-NaCl to high relative density of 96% associated with the hygroscopic NaCl present [287]. The case is different as observed in the CSP experimental analysis of some materials such as the $BaTiO_3$ characterized by appearance of secondary phases. This is associated with limited solubility or incongruent dissolution as reported for $BaTiO_3$ in many cold sintering studies [21, 265, 316, 317, 342].

Thus, final CSP-post annealing heat treatment is required to facilitate the formation of $BaTiO_3$ in order to achieve complete crystallization to remove the secondary phase present as impurity. With the aid of water suspension containing $BaTiO_3$ constituents for hydrothermal synthesis, the $BaTiO_3$ nanoparticles are uniformly wetted, and the liquid is self-redistributed into pore spaces between particles. This causes sliding, rearrangement, and compaction. Under the influence of pressure, temperature rise promotes hydrothermal synthesis reactions to form glass phase and expedite up the partial dissolution of the $BaTiO_3$ surface into solution. This results into a round shape crystallite formation and at ≥100 °C a dynamic non-equilibrium environment is established until the water present is completely consumed. When water vapour goes off the $BaTiO_3$ ensemble under applied uniaxial pressure, more compaction is achieved over the CSP dwell time and the nano $BaTiO_3$ particles are tightly cemented by the glass phase and a dense $BaTiO_3$ crystalline (~ 93 % relative density) to reach equilibrium. At this state, thermodynamics favours the glass phase atomic clusters and /or ionic species to precipitate on the $BaTiO_3$ crystallites with lower chemical potential. Further precipitation gives a rounded crystallite configuration when glass phase dominates and a flat faceted polyhedron manifest when glass phase substantially reduced. The precipitation process is accompanied by large mass transport which minimizes its surface area free energy, eliminate porosity and surfaces to create more contacts between crystallites. Thus, a rigid skeletal of the particles is formed with significant relative density increase to about 95%. Randall *et al.* [342] reported two contradictive mechanisms of hydrothermal synthesis of $BaTiO_3$ from CSP experiments. The first is the diffusion reaction (In-situ transformation) proposed based on the chemical reaction initiated at TiO_2 particles surface and cause heterogenous nucleation [37]. This triggers the formation of continuous $BaTiO_3$ layer when barium dissolve and diffuses into TiO_2 until the latter is totally consumed. The second is the dissolution-precipitation mechanism which suggest initial formation of amorphous hydroxy titanium complexes ($Ti\ (OH)^{n-}$) from dissolved TiO_2 in an aqueous solution. The complexes react with the dissolve barium to homogenously precipitate

$BaTiO_3$ from the glass phase. This is also evident in the chemical mapping of the glass phase that shows uniform Ti distribution suggesting that the main CSP mechanism is the dissolution-precipitation mechanism aided by $BaTiO_2$ epitaxial growth. The densification of $BaTiO_3$ using CSP has been reported in many studies but its hydrothermal assisted cold sintering approach mechanism understanding remains controversial. Guo *et al.* [21] in a hydrothermal CSP assisted process of $BaTiO_3$ suggested dissolution-precipitation as the sintering path assisted by epitaxial growth based on the observed chemical mapping that shows uniform distribution of Ti element in a glass phase.

Inspired by the natural geological compaction of sediments, nanovaterites particles were cold sintered at room temperature [42]. The authors suggested CSP mechanism as the dissolution limited kinetics widely reported for pressure solution creep in geological materials. In addition, the room temperature cold sintering process (CSP) of geological materials such as the carbonate rocks that takes place in nature is governed by dissolution-precipitation mechanism through diffusion and plastic deformation mechanism via dislocation motion and/or viscous flow at sufficiently high pressure [42]. The authors suggest that the cold sintering mechanism is dissolution limited kinetics as widely reported for pressure solution creep in geological materials.

To further unveil the CSP mechanism understanding, Guillon and his co-workers cold sintered ZnO using water and concluded that the Randall group proposed solution-precipitation mechanism for CSP is not adequate to activate the process of ZnO densification [39]. According to Gonzalez-Julian *et al.* [39], high concentration of defect potentials at the cold sintered ZnO grain boundary was observed because of H^+ and OH^- diffuses into crystal of the ZnO. The population of defects site created substantial diffusion path was formed that aids mass transport and sintering at extra ordinary low temperature. The subsequent substitution of the additive water with zinc acetate causes changes in the concentration of ionic species on ZnO surface responsible for large crystal growth [39]. It was observed that in the absence of heat ZnO powder can be sintered at room temperature to ~98% theoretical density by increasing the specimen conductivity >10 000 times using absorbed water vapour to trigger flash assisted sintering [343]. The mechanism of cold sintered ZnO-PTFE was proposed to explain the transient distribution of PTFE polymer driving densification and grain growth. The composite grain growth was found to be anisotropic at crystal and microstructural level consistent to electrical analysis [279]. The proposed mechanism involving PTFE influence on liquid flow direction responsible for ZnO grain growth is consistent to the conductivity increase in-plane compared to pure ZnO cold sintered [279]. ZnO/HAc/water interface kinetics was investigated during cold sintering of ZnO to understand the dissolve Zn ions adsorption behaviour from experimental and computational analysis [344]. The Zn cations recrystallization under different acid concentrations shows that their surface adsorption is a limiting factor in CSP. The analysis confirms presence of surface hydroxylation which do not constitute any barrier to start recrystallization. Surprisingly, instead hydroxylation aid initial adsorption of ion on the surface of ZnO and influences further surface diffusion. Thus, this revealed a new CSP mechanism of water-mediated and accelerated surface diffusion responsible for accelerated recrystallization. The mechanism is influenced by the structure of surface hydroxylation and dissolve species hydration energy which are functions of temperature, pressure, and acid concentration.

The existing CSP data and knowledge available shows that dissolution-precipitation processes are the main CSP mechanisms consistent to those observed in a liquid phase sintering [36, 292, 345]. In a case study of ZnO cold sintering, only ~4 vol% of 0.8 M Zn-acetate solution is required for full scale densification at temperature of ~ 100 °C. It is obvious that converting all Zn in the acetate to ZnO and transporting it to occupy the interstitial space of the green body, only few % relative density could be achieved. Thus, to achieve near 100% densification, redistribution of the materials comes mainly from the dissolution transport of the parent ZnO particles. However, dissolution-precipitation processes are surface events encouraging coarsening not densification creating much doubt about the authenticity of dissolution-precipitation model as the main CSP mechanism when only mass transport vehicle available is surface-surface. This suggest that pressure creates a stress gradient at grain-to-grain contact points and play a key role in the densification as evident in the observed material pressed under 200MPa generating Hertzian stress of more than 20 GPa. The liquid present at this zone that can dissolve the ceramic will generate chemical potential gradient associated with the stress gradient [53]. The authors concluded that the driving force for mass transport is from the contact zones that forms grain boundaries and brought particle centres even more closer [53]. The Kingery and colleagues' model for liquid phase sintering was adopted to unveil CSP fundamental mechanism based on their similarities. The model describes liquid phase sintering as two stage process namely particles rearrangement and subsequent dissolution-precipitation all characterized by unique densification rates. The densification rates are diffusion control dependent consistent to those observed during CSP that characterize it as multistage process. However, at different pressures each stage is defined by unique rate encouraging either particle grain rearrangement or dissolution-precipitation events [53]. In a related cold sintering study, it was suggested that dissolution-precipitation mechanism of CSP is in three stages comprising of particle rearrangement-dissolution, dissolution-precipitation and Ostwald ripening that dominates the microstructure [26]. These are based on the previous CSP research, the current understanding of liquid phase sintering theory and microstructural observations made in many systems cold sintered to date.

CSP similarities to LPS was compared based on the liquid-surface interface behaviours to gain more CSP fundamental understanding. The inorganic powder particles surface interaction with a liquid phase used as solvent during CSP is complex and approaches such as ReaxFF has been used to gain insight into the chemical interaction occurring at the particles grain boundary [344]. The complexity of liquid-surface interaction could be explained by the presence of hydrolysis, dynamic chelating reactions, and cluster formation whose details and dynamics are key to advance the level of cold sintering mechanism understanding [346, 347]. The understanding of these reactions will guide the choice of appropriate solvent to cold sinter any ceramic and its composites. This was demonstrated in the cold sintering of KH_2PO_4 (KDP) using heavy water which suggest a mechanism that the liquid phase acts on the particle phase and redistribute it under pressure. The liquid residual preferentially resides in the new grain boundary consistent to observation in a liquid phase sintering [53].

The understanding of grain growth behaviour of materials during sintering is necessary. In this regard, Funahashi *et al*. [54] made the first attempt to unveil CSP mechanism of ZnO by determining the grain growth exponent of cold sintered ZnO and its subsequent comparison to values reported for conventional solid-state sintering. The values were found to be like the reported values for conventional solid-state sintering. However, limited understanding of the CSP and absence of literature reported grain growth exponent of the same system under CSP limits their conclusion on the rate controlling mechanism. Meanwhile, availability of ZnO sintering data made Jesus and his co-workers to unveil the mechanism of cold sintering of ZnO sintered at 250 °C via KPFM boundary characterization and varied applied external stress [51]. Gonzalez-Julian *et al*. [51] determine the strain rate at three different close pressure and temperature range to ensure constant grain size is maintained. A point density was selected by the authors and densification around this point was determined and plotted as a function of effective stress. The stress exponent (n) determined as the slope of the plot was compared with stress exponent determined and reported from conventional solid-state sintering process. Though, Langer *et al*. [63] in an electric field-assisted sintering and hot pressing of ZnO presented microscopic analysis of the sintering behaviour from which the stress exponent (n) was determined from a similar plot of strain rate as a function of effective stress. The n-values reported are different and according to Bordia *et al*. [27] leading mechanism(s) could be different under different conditions of experiment. However, Lagner *et al*. were unable to speculate or draw any conclusion on the FAST/HP sintering mechanism involved. Consequently, to bridge the gap of Funahashi and Langer and their co-workers in ability to draw any conclusion regarding the mechanism, Gonzalez-Julian and co-workers revealed from the stress exponent >1 obtained that the mechanism of ZnO CSP is not only one but a combination of different mechanisms, a scenario reported for ZnO solid state sintering. Jiang *et al*. [348] demonstrated grain growth mechanism of cold sintered ZnO with acetic acid solution. In terms of grain growth mechanism, CSP differs from CS as evident in the low temperature solution as source of ion in CSP and fusion liquid phase at high temperature in CS process [349].

Hong *et al*. [41] proposed a echanism during CSP of NaCl and its dry pressing to study the behaviour of the NaCl under the influence of applied uniaxial pressure. The relative density of cold sintered NaCl (88.4% - 93.1%) is higher than observed in dried pressed NaCl (80.0% - 89.8%) at low pressure between 50-100 MPa. This indicates that within this region of pressure dissolution-precipitation dominates. Meanwhile from 150 MPa, relative density of dry pressed begin to exceed cold sintered relative density and more significant mechanical deformation of dry pressed than cold sintered was observed between 200 – 300 MPa. This was attributed to the NaCl low mechanical hardness making it possible to be rearranged and reshaped under pressure due to plastic deformation mechanism contributing also to the cold sintering process. The authors [41] identify amount of liquid as the key variable ranging from 100 % dry powder to maximum wetness. This allowed the choice of mechanism to be activated from complex possibilities of CSP to aid fabrication of all kinds of materials and their composites. In another cold sintering study, NaCl with high solubility in water was cold sintered without influence of external pressure to high relative density depending on the exposure time in a constant relative humidity chamber [292]. This demonstrate a close CSP similarity with liquid phase sintering whose fundamentals understanding has been expensively reported [60]. The Randall group study on NaCl revealed present of sufficient amount of water provides adequate capillary pressure and enables multiple channels of mass transport in the sintered compacts. Thus, it was speculated that transport by dissolution and capillary forces acting are the main densifications mechanisms responsible for the NaCl sintering at room temperature without external force acting. Conclusively, significant experimental studies and proposed theories have been reported on the CSP of different chemistries and composite particularly ceramics, but cold sintering process mechanism is still not fully understood and is at its very early stage. Therefore, detail study of other material systems is required to fully unveil CSP mechanism to meet the current and future challenges of application requirement limited by fabrication challenges. Thus, understanding the influence of key operating variables is important.

2.5.4 Cold sintering process variables

Three fundamental aspects of CSP (materials, solvents and processing parameters) and their associated variables that determine crystallization and densification of particles have been highlighted and discussed to a large extent [341]. These are basically the internal characteristics namely composition, crystal structure, particle size, solubility in water [38, 53] and the external characteristics comprises of the aqueous medium which depends on pH value, quantity, and solute type [38, 53]. Thirdly, the choice of appropriate physical variables comprising of pressure, temperature, time, ramp rate and atmosphere as shown in Figure 2-22 [38, 53]. The influence of some key parameters has been established in many cold sintering studies. This can be traced starting from Li_2MoO_4 room temperature densification [254, 256] to studies of properties and densities of several chemistries cold sintered for various applications as shown in Table 2-1. Some of the key variables are highlighted and discussed in detail:

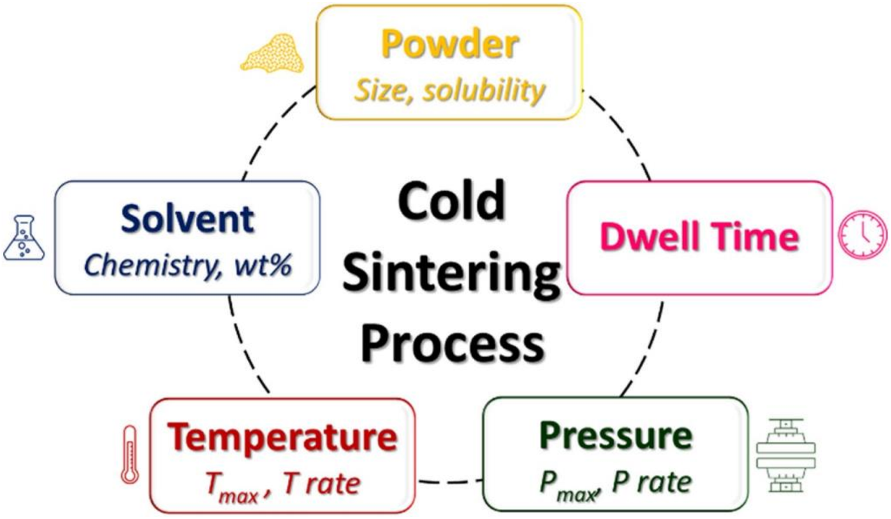

Figure 2-22 Key CSP synthesis parameters flowchart [350]

2.5.4.1 Aqueous solution (solvent)

The first most significant step in CSP is to determine a proper solution and its limiting amount (2-20 wt%) in a proportion required to facilitate non-equilibrium environment for chemical interaction that significantly lower sintering temperature until it is completely evaporated [341, 350, 351]. The role of the solvent is in two stages, providing lubrication to reduce friction and enhance particles rearrangement in the initial CSP stage, and its chemistry interaction with the powder to promote dissolution and diffusion processes in the final sintering stage. The aqueous solution causes materials dissolution which varies with powder specie and is responsible for the different CSP scenarios [21, 352]. Significant number of CSP studies have shown that transient aqueous solution provides increased densification as much as 10% increase in the sintered relative density in comparison to the dry pressed under same CSP operating conditions [36, 41, 42, 50, 66, 326]. However, limited densification is observed during CSP of NaCl at pressure higher than 150 MPa when dry pressed exceeds cold sintered density due to plastic deformation [41]. This is consistent to the observation during geological events in which pressure-solution is accompanied by plastic deformation caused by Joffe effect [353], a mechanism observed in ionic crystal and the dominant in halite structures [41]. The cold sintering of hygroscopic materials such as KH_2PO_4 [38] proceeds directly and smoothly to desired densification.

However, in the case of incongruent dissolution such as in cold sintered $BaTiO_3$, amorphous layer appeared limiting precipitation and densification processes [38]. The approach developed to solve this problem is to prepare a saturated solution in an appropriate stoichiometry ratio that can facilitate rearrangement of particles, growth, and final densification to desired density. This approach is also employed when the material has limited solubility by deliberately preparing aqueous solution containing the powder constituent chemical species [352].

In solid state conventional sintering process, mass transfer is solely driven by high temperature [354]. The transport of mass in CSP is aided by an aqueous solution that lowers activation energy, greater defects generation at particle faces and favourable reaction environment. Preparation of appropriate aqueous solution that satisfy a given nature of solute at given pH value and concentration provides a more favourable environment for chemical interaction that can induce defects at grain boundary and lower activation energy to facilitate atomic diffusion at early CSP stage [355]. The increase in mass transport in liquid phase is due to the increase diffusion in liquid phase more than solid phase i.e DLδL >> Dgbδgb, where DL and Dgb are diffusion coefficients of atoms in liquid and solid phase, δL and δgb are the widths of liquid and solid bridges respectively [354]. Inherent in hygroscopic substances such as the alkali molybdates [26] $NaNO_2$, KH_2PO_4 [356] and NaCl [41, 42] is the congruent dissolution and large solubility in water. This is responsible for a density >90 % from room temperature to 120 ^{O}C [26]. The hygroscopic nature of these materials allows their structures to readily interact with transient liquid water to facilitate efficient and fast dissolution-precipitation to achieve its maximum final densification at low temperature [38]. The material product solubility constant K_{sp} in water according to Lewin [357] provides insight regarding its solubility in water and for insoluble substances (electrolyte) in water equilibrium is established according to Equation 2-1. and an amorphous TiO_2 layer forms and wraps around the inner part of the particle

$$A_aB_b \rightleftharpoons aA^{n+}bB^{m-} \qquad (2\text{-}1)$$

The K_{sp} in equation 2-2 is for system in Equation 1 comprised of two chemical species A and B with dissociated ions concentrations $\lfloor A^{n+} \rfloor^{a}$ and $\lfloor B^{m-} \rfloor^{b}$ respectively.

$$K_{sp} = \lfloor A^{n+} \rfloor^{a} \lfloor B^{m-} \rfloor^{b} \qquad (2\text{-}2)$$

The solubility of the substance according to Equations 1and 2 increases with concentration of dissociated ions leading to increase in K_{sp}. Lewin clearly suggests that a low K_{sp}values indicate materials resistance to dissolution in water and dissolving this insoluble substance requires changes in the equilibrium condition by reducing the concentration of $\lfloor A^{n+} \rfloor$ or $\lfloor B^{m-} \rfloor$ ions to values lower than K_{sp}in order to favour the reaction in Equation 1 to proceed from left to the right.

Cold sintering of some solid electrolytes materials using water such as $Li_{1.5}Al_{0.5}Ge_{1.5}(PO_4)_3$ (LAGP) and $Li_{1+x+y}Al_xTi_2$–xSi_yP_3–yO_{12} (LATP) results into a formation of amorphous grain boundary responsible for limited Li ionic conduction of only 10^{-5} S/cm after CSP-post annealing at 650°C above its onset crystallization temperature [325]. Also, cold sintering of a NASICON-type $Na_{3.4}Sc_{0.4}Zr_{1.6}Si_2PO_{12}$ solid electrolyte using NaOH and KOH solutions enables cold sintering between 82% - 87% relative densities. However, the sintered compacts were characterized by low conductivities in the range 10^{-5} - 10^{-6} S/cm to 10^{-4} after CSP-post annealing at 800 °C consistent to the result obtained by [328]. NZSP dopped with Mg conductivity was only improved after annealing at 800°C from 10^{-5} S/cm to greater than 10^{-4} S/cm with relative density > 90% achieved at 1100°C [358]. Further modification of the transient liquid containing water, Bi_2O_3 sintering additive and binding agent enables conductivity of 10^{-4} S/cm after annealing at 850°C-1200°C at which Bi_2O_3 melts to initiate a liquid phase sintering [359]. Li ion batteries cathode [282, 327], anode [329] and another NASSICON type electrolyte $Li_{1.5}Al_{0.5}Ge_{1.5}(PO_4)_3$ [324] materials were cold sintered using low boiling temperature aqueous solutions. The later electrolyte requires addition of salt to improve conductivity to10^{-4} S/cm. To avoid the use of aqueous solution responsible for low conductivity observed in all studies reported, a fused NaOH obtained by heating at temperature >312 ℃ during CSP was used as transient solvent extruded contrary to evaporation observed in using aqueous solution [360]. In another study [308], a non-aqueous dimethylformamide (DMF) was used as a transient liquid to cold sinter LLZO-SM $Li_7La_3Zr_2O_{12}$ -SM composite to achieve conductivity of 10^{-4} S/cm. Generally, Li based garnets undergoes proton exchange encourage by present of aqueous media militating against the electrolyte material conductivity.

The addition of other materials such as acid or alkali to react with one of the ions is the approach employed to reduce the ionic concentration that could influence the dissolution of insoluble materials. The material interacts and forms a weak electrolyte such as water characterized by a low dissociation tendency. The detail of the mechanism of this process was reported using HCl as an additive to insoluble Mg $(OH)_2$. Mg $(OH)_2$ dissociate slightly into Mg^{2+} and OH^- in water and in the presence of HCl, OH^- reacts with dissociated H^+ from the acid to form water [355]. The mechanism explained how HCl drives continuously dissociation of Mg $(OH)_2$ to form $OH^-$to enhance solubility. Thus, this establishes the basis of using acid or alkali as an additive during CSP to modify solution and enhance solubility of insoluble materials. Several materials particularly ZnO have been cold sintered in different aqueous solutions of $ZnCl_2$, $ZnSO_4$ and acids such as HCl and H_2SO_4 [68]. The formation of second phase using $ZnCl_2$ solutions and in solutions containing SO_4^{-2} and NO_3^- was observed limiting final relative density to a range of 70-75%. These are addressed using acetic acid solution to prevent hydroxide or cement formation and prevent die materials corrosion [68]. The acetic acid solution have been used widely to cold sinter ZnO to a relative density of 85 - 99% [39, 40, 54, 68, 267-270, 274, 321] and its composites such as $ZnO-Ti_3C_2T_x$ [276], $ZnO-BaTiO_3$ [280] and ZnO-PTFE [278, 279]. Also cold sintered using acetic acid is $Ca_3Co_4O_9$ [267].

Similarly, alkalis solutions, fused and dry form such as the NaOH, LiOH and eutectic NaOH-KOH have been used to increase solubility and cold sinter different materials. NaOH solution was used to sinter diatomaceous earth [302], $Na_3V_2(PO_4)_3$ (NVP)|$Na_3Zr_2Si_2PO_{12}$

(NZSP)-CNF [307]. Meanwhile, $Li_2Mg_3TiO_6$ [294], $LiFePO_4$-PVDF-C[307] were cold sintered using LiOH. The mixture of molten NaOH-KOH solvent was used to cold sinter $CeCO_2$ [338]. Meanwhile solid and fused NaOH was used as sintering agent of Sodium β-Al_2O_3 (SBA) [306] and $Na_3Zr_2Si_2PO_{12}$ [310] to a relative density >90% respectively. Liu *et al*. [277] prepared by cold sintering method a high-density InGaZnO4 target using ammonia solution as solvent. Lead Zirconate Titanate (LZT) ceramic was prepared using lead nitrate solution [361]. In a different CSP route, Yang *et al*. [362] fabricated zirconium tungstate ceramic (ZrW2O8) with hydrothermal suspension made from $ZrOCl_2 \cdot 8H_2O$ (120 mL, 0.3 mol/L) and $Na_2WO_4 \cdot 2H_2O$ (120 mL, 0.5 mol/L) as sintering aid. Chi *et al*. [281] prepared $K_{0.5}Na_{0.5}NbO_3$-NaCl (KNN-NaCl) ceramics by cold sintering using NaCl aqueous solution as transient solvent. Thus, choice of aqueous solution for cold sintering process depends not only on the solubility but also the pH, nature of the solute and solvent concentration. Therefore, solubility data and pourbaix diagrams are critical.

In addition to large solubility in aqueous environment at low temperature, congruent dissolution plays a critical role during cold sintering. Some compositions such as the perovskites and spinels with close packed structure whose atoms strongly bonded have very limited solubility or have incongruent dissolution in water such as the $BaTiO_3$. Thus, a new cold sintering route was developed and named a modified hydrothermal synthesis cold sintering process using precursor solution as demonstrated during cold sintering of $BaTiO_3$ [38]. The $BaTiO_3$ shows incongruent dissolution in water due to its thermodynamic instability in an aqueous solution with pH value <12. Ba ions leached out, leaving a surface layer rich in Ti with amorphous layer of TiO_2 formed as shown in Figure 2-23. This results into a decrease in crystal growth and variation of the chemical stoichiometry of the product generated from the separation of saturated solution and crystal surface containing active sites. Thus, the covering of the active sites by the layer resulting from the incongruent dissolution prevents nucleation and hinder mass transfer between aqueous liquid and crystalline phases. Guo *et al*. [38] prepared 25-27 wt% Ba $(OH)_2/TiO_2$ suspension to overcome the incongruent limitation of $BaTiO_3$. It shows that relative density of ~ 93 % of the sintered $BaTiO_3$ prior to post sintering treatment was achieved at low temperature < 200℃. The high relative density obtained indicates choice of appropriate transient liquid and CSP route. In addition to $BaTiO_3$, another perovskite material $Pb(Zr,Ti)O_3$ was cold sintered at 300 °C and 500 MPa using $Pb(NO_3)_2$ solution to a relative density of 89% [318]. The use of $Pb(NO_3)_2$ solution helps to overcome the ceramic PZT incongruent dissolution in water and on heat treatment at 900℃ increases the relative density to 99% and relative dielectric permittivity from 200 – 300 at RT and 100kHz. Huang *et al*. [363] cold sintered bismuth titanate sodium $(Na_{0.5}Bi_{0.5}TiO)_3$ nanoparticles powder to 74% relative density using hydrothermal precursor solution containing $Bi(NO_3)_3 \cdot 5H_2O$ and $Ti(OC_4H_9)_4$ and NaOH as source of Na^+. Ozmen *et al*. [364] Studied the rate and degree of pure KNN cations dissolution in both alkaline, acidic and a neutral media solution. It was observed that K dissolution rate value differs and higher than observed in potassium which suggest that KNN undergoes incongruent dissolution in the selected aqueous solutions. The dissolution of KNN in water shows two layers h1 rich in Nb and h2 rich in Na and Nb respectively. The unreacted part provides a shield against A-site cation diffusion. The optimal properties of cold sintered KNN in water transient medium were observed when the amount of Na exceeds K present. This, suggest that NaCl solution could provide additional Na to supplement cation losses. In a related study, $K_{0.5}Na_{0.5}NbO_3$-NaCl ceramics was prepared using NaCl aqueous solution to reduce sintering temperature, improve its electrical properties, tailor microstructure and minimize volitization of alkali metals [281].

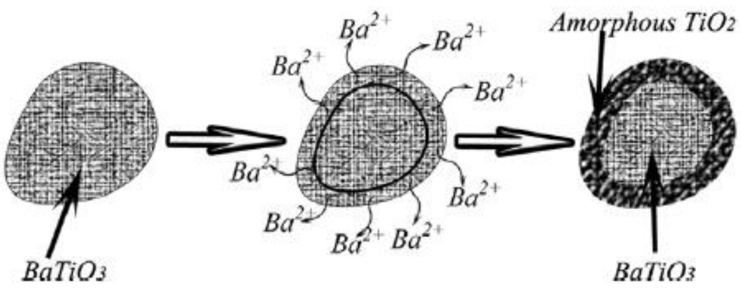

Figure 2-23. Schematic illustration of the incongruent dissolution of BaTiO3 in aqueous solution [38]

Furthermore, non-aqueous organic solvents with low boiling temperature <200°C such as ethanol, ethanolamine and glycerol are being used as potential transient solvents during cold sintering process. To demonstrate the use of organic solvents as replacement for water, [325] cold sintered solid electrolyte $Li_{1.5}Al_{0.5}Ge_{1.5}(PO_4)_3$ using ethanol as transient liquid. The authors recorded a relative density of 80% and $5.\ 4 \times 10^{-5}$ S/cm ionic conductivity after thermal treatments 650°C consistent to the result obtained using water as transient liquid. Other organic solvents with long-pair electrons orbital and proton donor site such as glycerol, ethanolamine, propylamine, formamide, and ethanol were tested as solvents of Zr-based ceramics [365]. Thus, these are projected as potentials organic solvents for CSP of materials like ZrO_2 [355]. Conclusively, it is apparent that most of the studied systems cold sintered using selected solvents as highlighted, a relative density ≥90% dominates the process and signifies the extent of densification achieved and appropriateness of the selected solvents. However, to further understand CSP mechanism, more studies are required to further investigate parameter-structure-properties to fully unveil CSP fundamental mechanisms.

2.5.4.2 Pressure

Pressure is an important and critical CSP parameter that first influences sintering liquid distribution followed by a particles reorientation, subsequent sliding, and compaction at rapid rate with controllable grain size unlike in conventional sintering [355]. It provides the main driving force when applied within a scale of hundreds of MPa [350] contrary to thermal energy in conventional sintering [24, 50]. Nur *et al*. [271] recently studied the influence of applied uniaxial pressure during cold sintering of ZnO between 50-300 MPa in the presence of different water contents (1.6 wt% and 3.2wt%) at constant temperature. The increase in pressure significantly improves the final relative density from ~79% at 50MPa to 92.37% at 300 MPa when the amount of water used as solvent was 1.6 wt%. Further increase in the amount of water to 3.2 wt% only increases the relative density to 93.9% as shown in Figure 2-24. Hong *et al*. [41] studied the influence of applied uniaxial pressure on the relative density of dry pressed and cold sintered NaCl. The relative density of cold sintered NaCl at 50MPa is 88.4% and increase to 93.1% and 93.9% at 100MPa and 150MPa. Beyond 150MPa negligible density increase between 94.3% to 94.6% was observed. Surprisingly, the relative density of dry pressed NaCl was only 80.0% and 89.8% at 50MPa and 100MPa but rapidly increase between 100-200 exceeding cold sintered relative density from 150MPa. Between 200-300MPa the relative density increases from 98.5%-99.3% which is 4.3%-4.7% higher than observed in cold sintered. Thus, uniaxial pressure in the dry pressed NaCl induced plastic deformation densification mechanism responsible for its higher relative density than cold sintered. Leng *et al*. [328] reported the influence of pressure on the density evolution of cold sintered Mg-doped NASICON ($Na_{3.256}Mg_{0.128}Zr_{1.872}Si_2PO_{12}$) at 140 °C. At 310 MPa, relative density of about 69.8% of cold sintered NASICON was observed and rapidly increases to about 82.8% when the applied uniaxial pressure increases to 780MPa. Gonzalez-Julian *et al*. [39] unveil the influence of applied uniaxial pressure between 100-150 MPa on the densification behaviour of cold sintered ZnO in air, water, and acetic acid solution media. The result shows that cold sintered green density of ZnO composition containing water from RT to 250 °C is higher than observed in air and acetic acid solution with relative density of 59.5% (Figure 2-25). Though, details of the effect has not been thoroughly investigated but this is attributed to less friction between powder particles at low pressures as previously reported in literature [366]. Meanwhile, air pressed samples densification is low and only 52% final relative density achieved at 100 MPa. This is lower than in composition densified with water to final relative density of 84.1% at 100 MPa. However, cold sintered in the present of acetic solution under hot pressing demonstrate faster sintering rate and higher final relative density of 88.3% than cold sintered using water with 84.1% relative density. Two separate cold sintering studies of ZnO nanoparticles using 20 wt % 2M acetic acid solution at temperature of 285 °C under 300 MPa [278] and 250 °C under 320 MPa [272] demonstrate the relevance of pressure over temperature in driving densification. At lower temperature of 250℃, Ndayishimiye et al. achieved cold sintered relative relative density of 98% higher than 94% by Zhao et al due to 25MPa pressure increase. Gonzalez-Julian *et al*. [39] shows that increase in pressure from 50MPa – 150MPa reduces the ZnO onset densification temperature from 130℃ to 89℃. However, presence of acetic acid further pushed down the onset densification temperature to as low as room temperature at all pressures. Thus, consistent to the observation made in ZnO [39] and NaCl [41] CSP studies. Thus, the modifications in the transient liquid under the influence of applied pressure demonstrates its potentials to achieve the final relative density at extra ordinary low temperature.

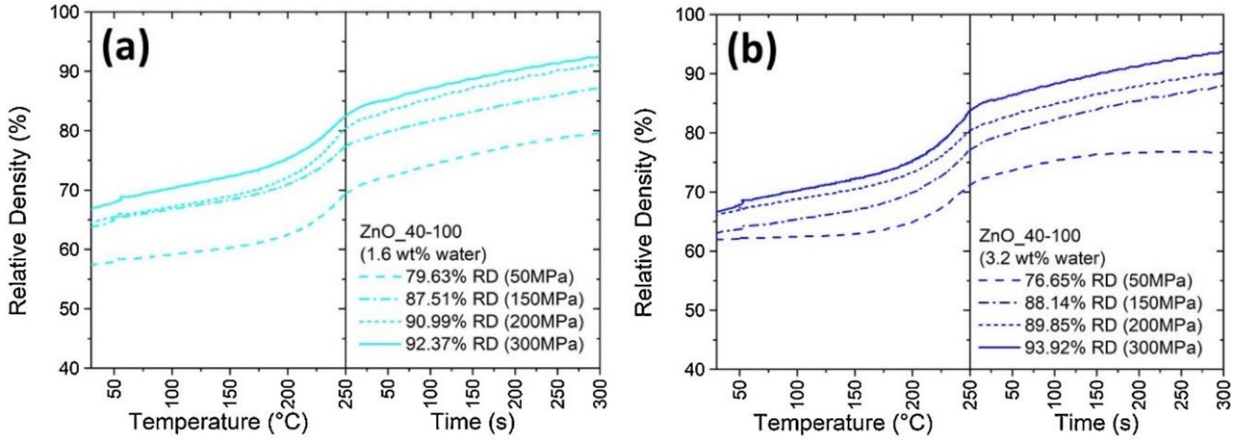

Figure 2-24. Density evolution of ZnO (40–100nm) during cold sintering at 250 ℃ for 5 min dwelling time influenced by external pressure between 50-300 MPa in (a) 1.6 wt. % (b) 3.2 wt. % water content [271]

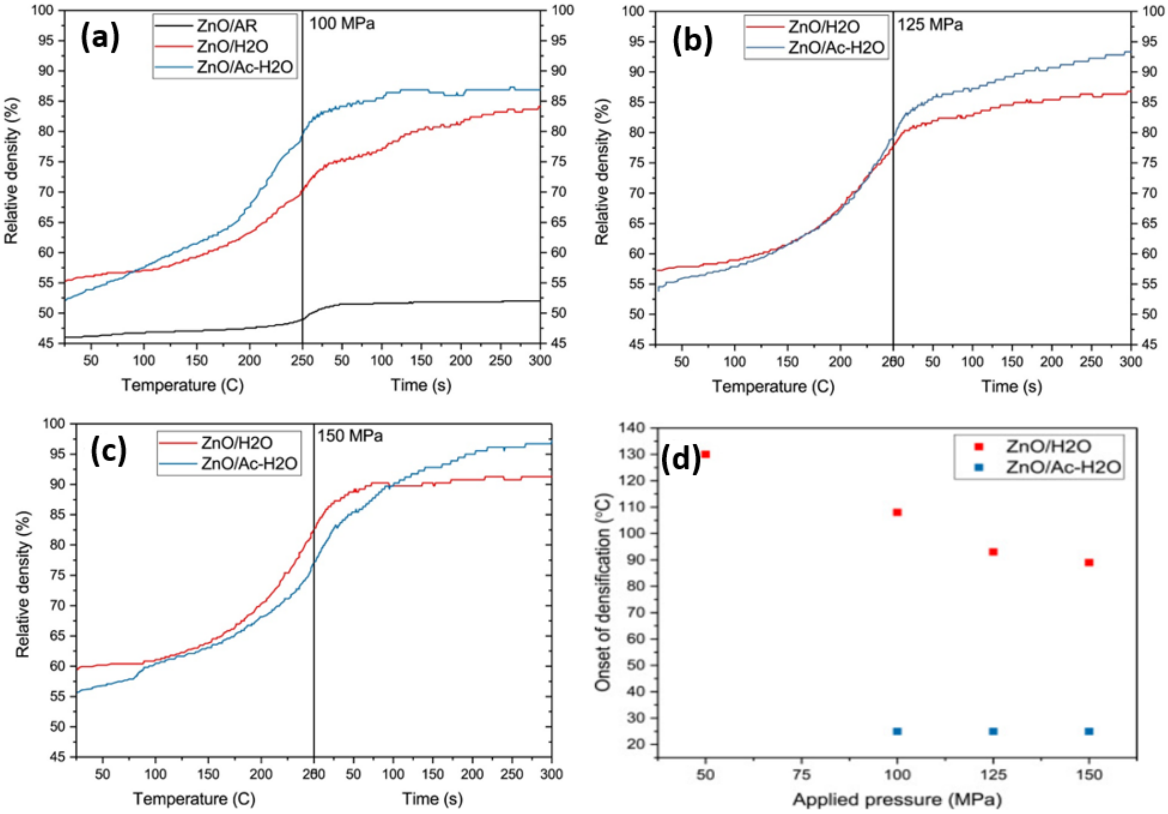

Fig. 2-25 Cold sintered ZnO densification curves under uniaxial pressures of a) 100 MPa, b) 125 MPa, and c) 150 MPa (d) Onset temperature of densification as a function of the applied pressure in the FAST/SPS for ZnO/H_2O [39, 366]

2.5.4.3 Temperature

Cold sintering temperature increase provides more energy required for an effective mass transport. At more elevated temperature, more dissolution and precipitation process take place. The temperature increase improves densification during CSP as reported in some cold sintering studies but its influence is less effective than observed in pressure [350]. The CSP temperature is expected to be at least higher than the liquid solvent boiling temperature to ensure it is removed completely to avoid pore formation leading to decrease densification. The maximum reported limit is between 350 – 400 ℃ [311, 342]. It causes the solvent to evaporates and escapes from the die through the clearance spaces between the punch and the die [355]. At final sintering stage higher temperature influences grain growth. Berbano *et al*. [325] reported density evolution of cold sintered $Li_{1.5}Al_{0.5}Ge_{1.5}(PO_4)_3$ (LAGP) as a function of temperature from RT to 160°C. The density profile revealed fast densification rate at initial sintering stage which stabilizes and maintain constant with further increase in temperature from 60 to ~ 80% relative density consistent to its microstructural evolution of cold sintered LAGP (Figure 2-26). It is also consistent to ~70% relative density of cold sintered ceria ceramics by [337]. The authors combined CSP with two step sintering method at elevated temperature to achieve ~98% relative density. Kang *et al*. [68] studied the effect of CSP temperature between RT to 140℃ on ZnO cold sintering process with acetic acid solution under constant uniaxial pressure of 530 MPa for 30 minutes. A relative density increase with temperature was observed (Figure 2-27) and reaches its 98% peak value at 120℃. The maximum increase was observed between 50 and 90℃ which is associated to the solubility increase and destabilization of the zinc hydroxide [68]. In some cold sintering studies the temperature at some range has no influence on the densification such as observed in the cold sintering of Mg-doped NASICON ($Na_{3.256}Mg_{0.128}Zr_{1.872}Si_2PO_{12}$) [328]. However, slow heating to reach CSP temperature prolong sintering time and provides more contacts between the powder and the solvent to enhance dissolution [367].

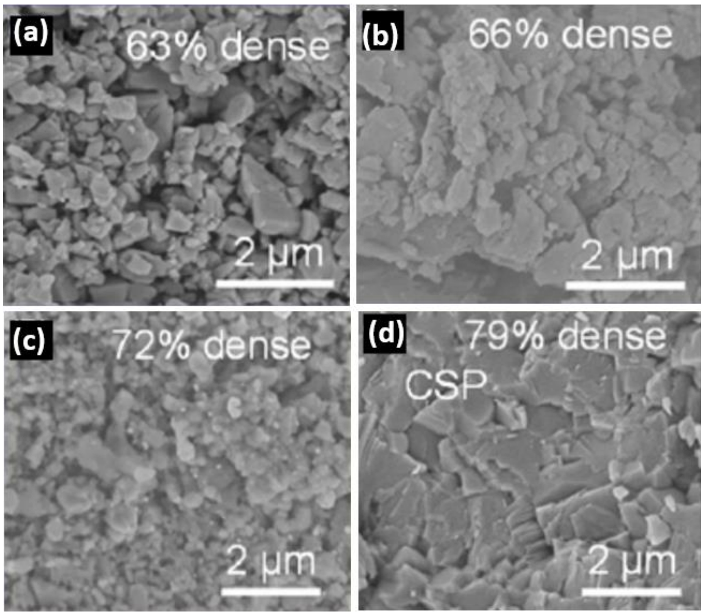

Figure 2-26 (a) SEM micrographs of LAGP dry pressed at (a) 25°C (b) 120°C and cold sintered with water at (c) 25°C and (d) 120°C under 400MPa for 20 minutes [368]

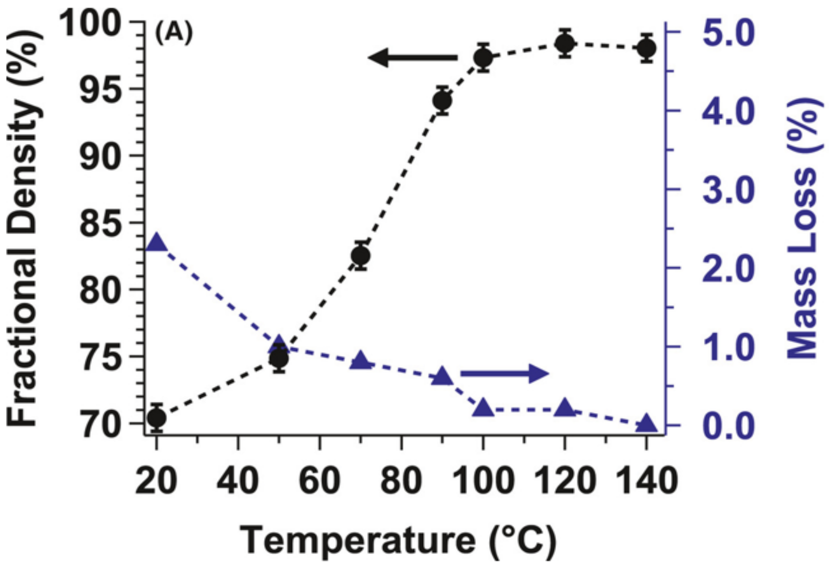

Figure 2-27 Relative density of cold sintered ZnO pellets and as pressed pellets mass loss after drying as a function of temperature [68]

2.5.4.4 Amount of liquid

Cod sintering process requires transient liquid solvent in which the powdered material to be sintered has congruent dissolution and present in sufficient quantity to facilitate desired densification. Nur *et al*. [271] studied the influence of the amount of the aqueous solution during cold sintering of ZnO to determine its optimum amount of water as aqueous phase. Two different amounts of water 1.6 wt% and 3.2 wt% were used. It was observed that using 1.6 wt%, cold sintered final relative density was 92.37% and further increase in water to 3.2 wt% results into 93.92% final relative density representing 1.5% increase. Guo *et al*. [303] cold sintered MgO and studied the influence of the amount of transient $Mg(OH)_2$ liquid generated in an in-situ reaction of MgO with water during pressure less heating. The rapid evaporation of water during pressure less heating requires it in excess and 160 wt.% of the starting powder was introduced as the starting liquid. A final relative density of 99 wt% was achieved when the $Mg(OH)_2$ residual was 30.9 wt% at CSP temperature of 450 °C under uniaxial pressure of 500 MPa hold for 30 min. The high relative density achieved is also attributed to a high stress gradient at interparticle faces and pores driving densification. However, high pressure as well slows down $Mg(OH)_2$ decomposition and therefore, requires sufficient dwelling time of ≥30 min at 450℃ to achieve pure MgO as final product. The authors also revealed that the extent of the densification and purity of the final product without additional phase is determined by the time pressure is applied. In a CSP densification of NaCl, the influence of the amount of water as transient solvent was studied [67]. According to the author, present of water influences not only the final relative density but also determines the structural homogeneity. Presence of up to 1 wt% water creates no difference in the cold sintered NaCl relative density and microstructure compared to dry pressed samples. The cold sintered NaCl relative density increases to ~99.7% when 2 wt% water was used. Beyond 2 wt% cold sintered NaCl relative density decreases. Though, microstructural homogeneity as shown in Figure 2-28 increases with increase in the amount of water but relative density of dried samples after CSP generally decreases and more rapidly from 99% to 95% when amount of water was increased from 0 - 3 wt%. It slows down to 93% when amount of water was increased from 3 wt% to 10 wt%. The observed density decrease of cold sintered at 300 MPa with increase in amount of water reaffirm the earlier observations made in a related NaCl cold sintering study [41]. Hong *et al*. [41] reported increase in cold sintered NaCl density at low pressure (50-150MPa) higher than dried pressed NaCl. Meanwhile, at higher pressure (200-300MPa) no appreciable increase in density was observed and dried pressed density begins to exceed cold sintered density from 150 MPa. This shows that presence of water limits the final relative density of the cold sintered NaCl at higher pressure. Thus, further increase in the amount of water beyond a specific limit will continue to lower the density as observed by *Li et al*. [67]. Yang *et al*. [369] cold sintered ZrW_2O_8 ceramics at 180 °C under uniaxial pressure of 340 MPa and studied the influence of the amount of the liquid phase solvent (0 - 35 wt%) on the sintered density and microstructure. The sintered density and hardness increase with increase in the amount of liquid and forms a plateau at 25 wt% as shown in Figure 2-29. This is maintained constant with at appearance of a homogenous microstructure observed at 25 wt% threshold values as depicted in Figure 2-30.

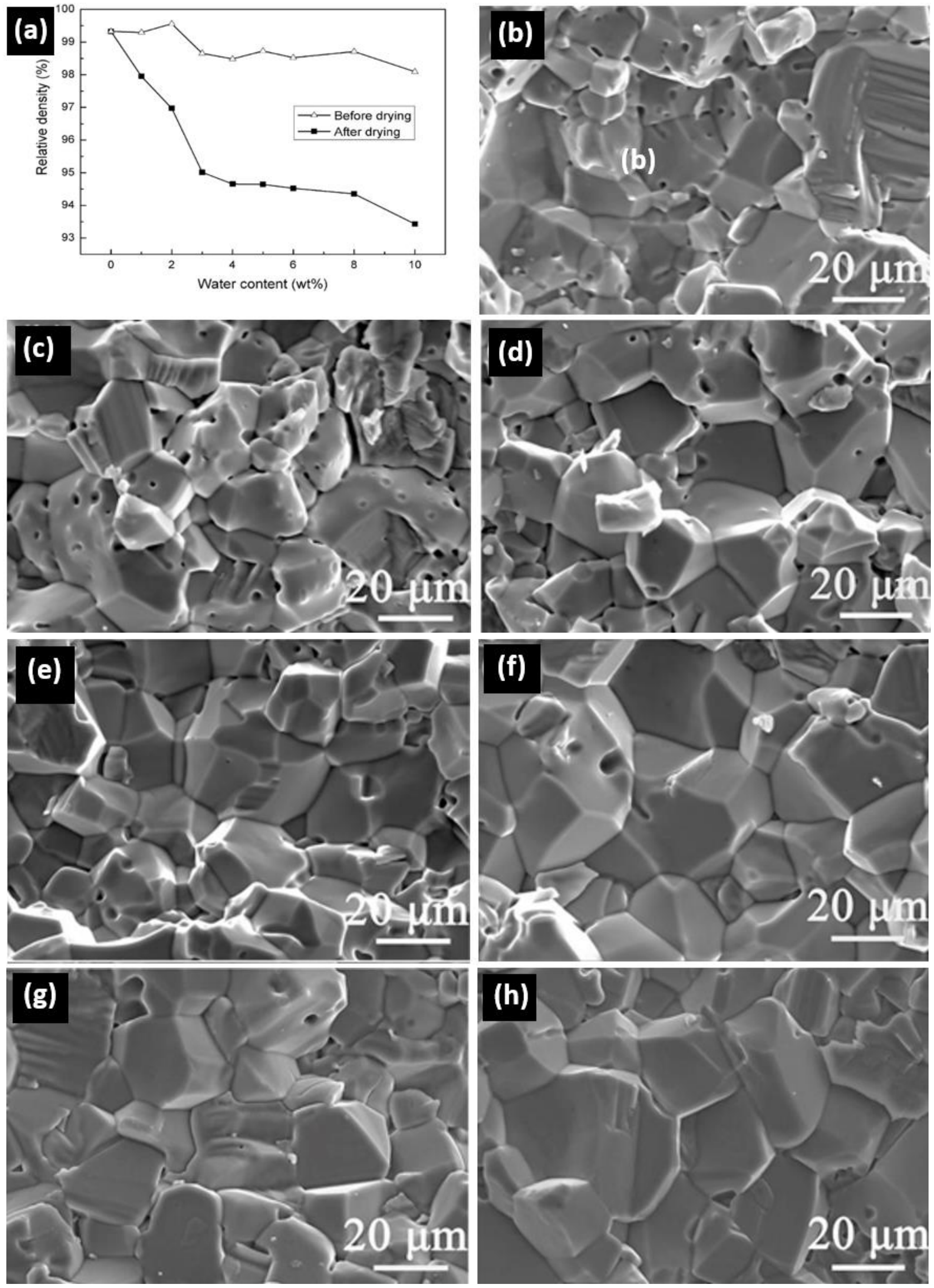

Figure 2-28 Room temperature cold sintered NaCl ceramics relative density as a function of water content (a) Room temperature cold sintered NaCl fractured surface SEM images with (b) 0, (c) 1, (d) 2, (e) 3, (f) 4, (g) 5 and (h) 10 wt% water content [67]

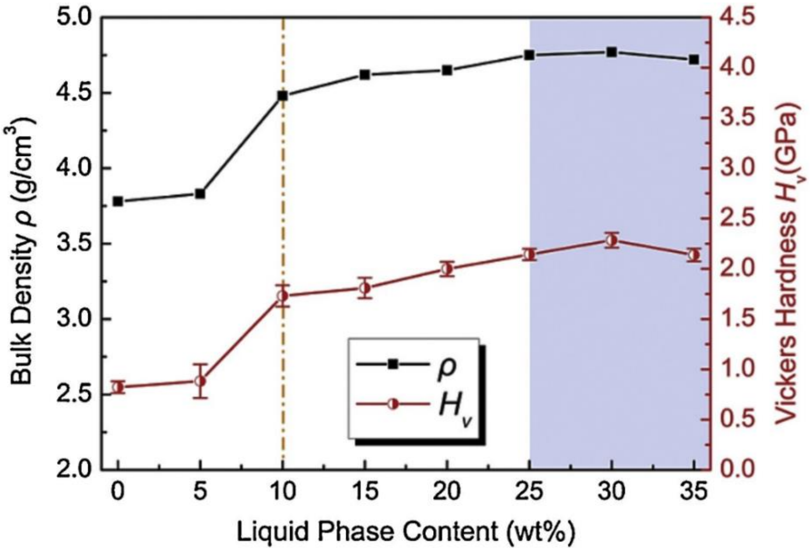

Figure 2-29. Evolution of cold sintered ZrW_2O_8 bulk density ρ and Vickers hardness Hv as a function of the liquid phase content cold sintered at 180 °C and 340 MPa.

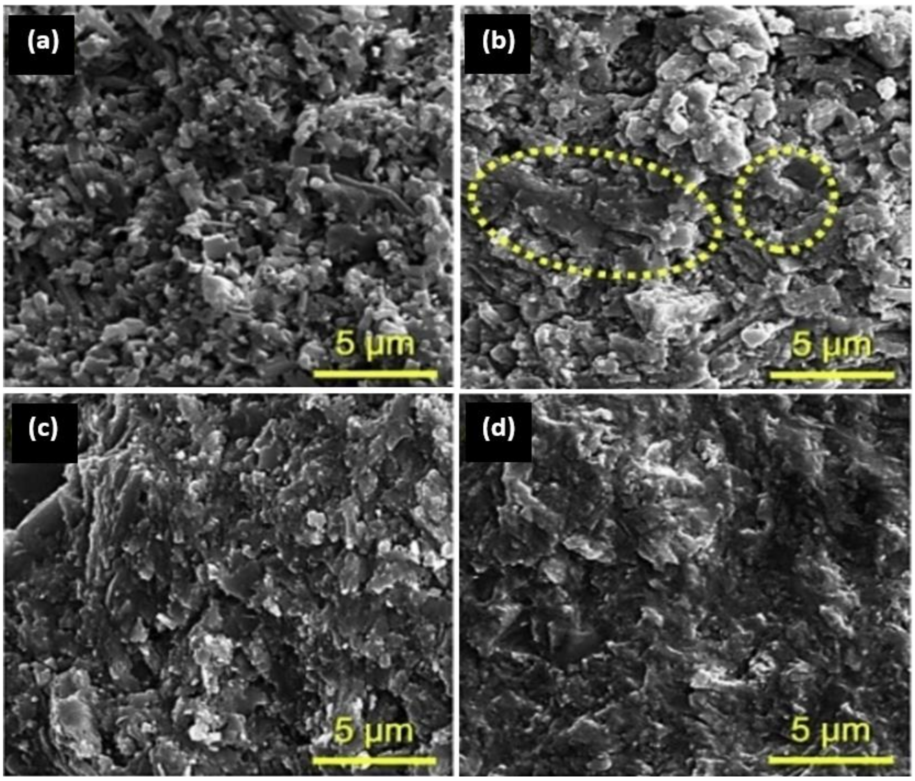

Figure 2-30 SEM micrographs of ZrW2O8 cold-sintered at 180 °C, 340 MPa with (a) 0 wt %, (b) 10 wt %, (c) 20 wt %, (d) 30 wt % water contents. The yellow dashed ellipses indicate partial glass phase [369].

2.5.4.5 Dwelling time

The measurement of various sintering responses such as hardness, strength and density are determined as a function of independent parameters that can be adjusted such as time or maximum temperature [370]. According to German [370], sintering generally at higher temperature is responsible for the density increase but densification is a function of the dwell time with limited impact. CSP is characterized as a very fast sintering process usually within few minutes, mostly ≤60 minutes. This is because pressure-solution creep is the main CSP mechanism and when the solvent completely evaporates, no dissolution is observed, and temperature is usually low to cause diffusion. The dwell time is an important parameter contributing significantly to the cold sintering process of several ceramics and their composites with metals, polymers, and other chemistries. The influence of dwell time has been reported in various cold sintering studies. Ndayishimiye *et al*. [321] compared the influence of dwelling time (0 - 80 mins) on cold sintering and hydrothermal sintering of ZnO at 155°C in an open and closed system. Under uniaxial pressure of 320 MPa and at time 0, relative density of cold sintered was >98% higher than in hydrothermal sintered specimen by 2%. A non-linear density evolution manifest, it decreases from 98% at 0 mins to 97% after 20mins in CSP and 97.8% at 40mins in HS (Figure 2-31). Subsequently, it increases in a non-linear form to near full density in CSP and ~99% in HS. Meanwhile, the grain size evolution of HS and CSP sintered specimens increases from 166 to 229 nm and forms a plateau after ~ 40 mins and sustained amidst relative density increase with time. The continuous grain size increase with time from 131 to 334 nm observed in cold sintered ZnO with time signifies decrease in the population of small grains converted to larger ones over the sintering period. In a related study, ZnO was cold sintered at 250 °C using water in a vacuum and studied the influence of dwell time from 5-60 mins [271]. It shows significant improvement in the ZnO density from 93% after 5mins to 99% after 60 mins (Figure 2-32). Jiang *et al*. [348] reported density evolution of cold sintered ZnO at 150 °C under 200 MPa using acetic acid solution at different isothermal dwell times. The relative density increases form ~86% at 0 mins to 97.4% after 30 minutes beyond which the density remains constant and forms a plateau. The structural evolution (Figure 2-33a-d) of the cold sintered ZnO shows clearly that prolonging the dwell time the population of small grains decreases and are converted into larger ones which reduces the spacing between the grains an indication of enhanced densification consistent to the density evolution in Figure 2-33e. [277] in a cold sintering study, hold $InGaZnO_4$ pellets for 6hrs at 180 °C but reaches its theoretical density after an 1hr lower than 5hrs for conventional sintering of a similar composition at 1200°C. Therefore, prolong sintering beyond the limit of its theoretical density possible do not contribute to the material densification during CSP. In the case of ZnO CSP using acetic acid, dwelling time of 30 minutes is required to achieve theoretical density at 300 °C under uniaxial pressure of 350 MPa. Beyond 30 minutes, no additional densification could be achieved. Thus, Hérisson de Beauvoir *et al*. [279] cold sintered ZnO using acetic acid in 30 minutes at 300°C against 60 minutes at 305°C reported in a previous study [40]. Generally, hygroscopic substances readily soluble in the chosen solvent cold sinter within a short time due to fast dissolution-precipitation process [38]. Near fully dense cold sintered KH_2PO_4 and $NaNO_2$ [38] were reported within ≤ 5 minutes consistent to fully sintered NaCl [41, 67].

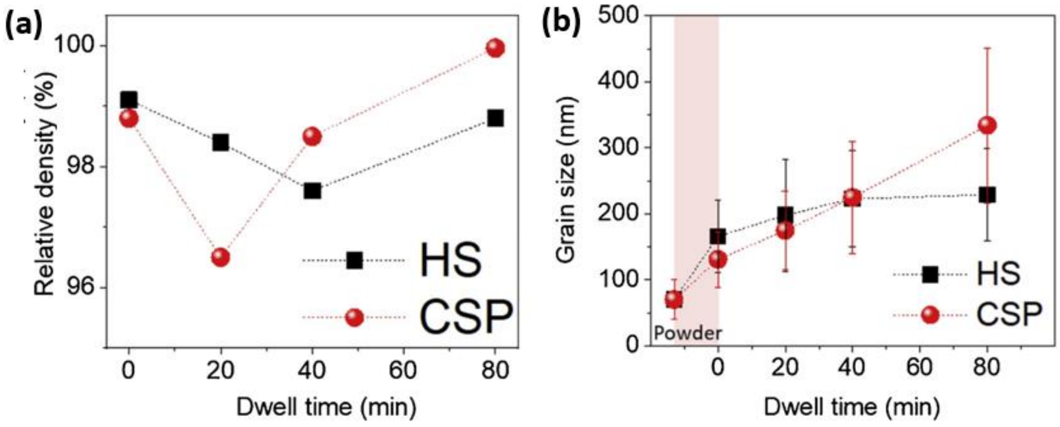

Figure 2-31. (a) Relative density and (b) grain size evolution of ZnO cold sintered and hydrothermally sintered at 155 °C as a function of dwell time [321]. The red band corresponds to the heating.

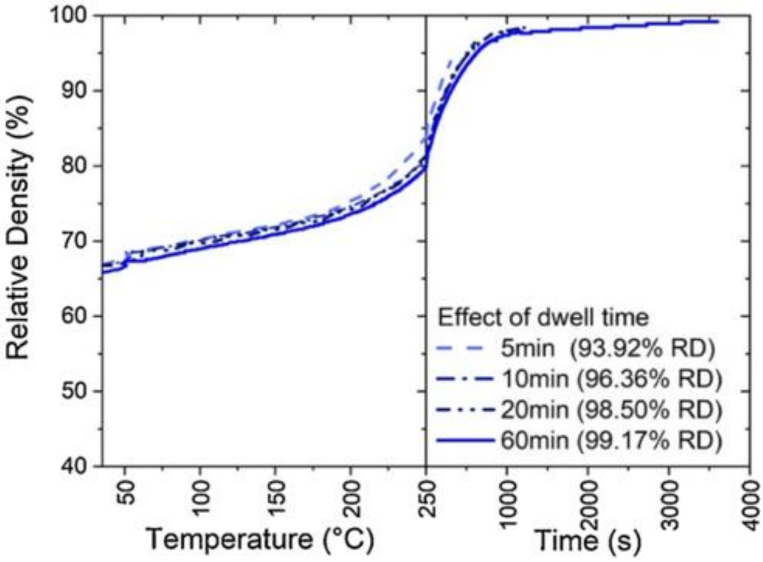

Figure 2-32 ZnO cold sintered at 250 °C, 300 MPa, using 3.2 wt. % water content for a dwelling time of 10 min, 20 min and 60 min in a vacuum atmosphere [271].

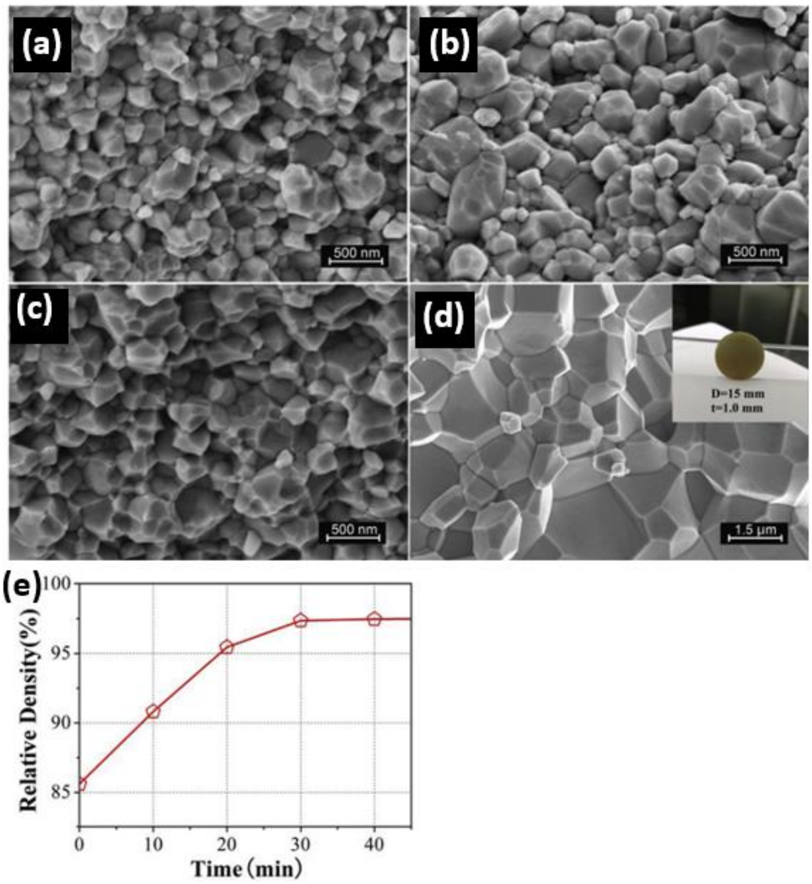

Figure2-33 Microstructures of pre-sintered ZnO at 150 °C for (a) 10 min, (b) 20 min, (c) 30 min and complete sintered ZnO at 200 °C for (d) 30 min (e) cold sintered ZnO density evolution at 150 °C under 200 MPa [348].

2.5.4.6 Powder characteristics

The size of the powder particles plays a key role in cold sintering process. [38] demonstrate the role of nanoparticles in an experimental CSP study of $BaTiO_3$ ceramics. The nanoparticle size enables total surface Gibbs free energy minimization and its advantage over coarse particles could be attributed to the higher chemical reactivity derived from its large surface area to volume ratio enabling greater dissolution events. The presence of more crystal lattice sites available in nanoparticles promote precipitation events that lower CSP temperature [371]. Thus, the possibility of altering the Gibbs free energy by nanoparticles suggest its critical role in the cold sintering process either during precipitation or crystal growth by Ostwald ripening [37]. The thermodynamic concept of Gibbs free energy minimization explains further in more details the contribution of using nanoparticles to aid sintering process. The Gibbs free energy reduction of a given system with coarse particle subdivided into clusters is quantitatively described in Equation 2-3. Replacing the coarse particles with nanoparticles, the change in the Gibbs energy of the system containing molar surfaces $\bar{s}_{nm}$ and $\bar{s}_{\mu m}$ of nanoparticles and coarse particles is given by Equation 2-4 [37].

$$\Delta G = \frac{2}{3}\overline{\gamma s} \qquad \text{2-3}$$

where $\bar{\gamma}$ is the mean free surface energy and $\bar{s}$ is the molar surface

$$\Delta G = \frac{2}{3}\bar{\gamma}\,\Delta\,\bar{s} = \frac{2}{3}\bar{\gamma}\left(\bar{s}_{nm} - \bar{s}_{\mu m}\right) \qquad \text{2-4}$$

If a given bimodal system is in a weight ratio of 1:1 has 50nm and 0.4μm particles, the ration of $\bar{s}_{nm}/\bar{s}_{\mu m}$ gives 8 suggesting that surface area gain is 7 times the 0.4μm coarse particles. This change quantitatively represents a change in the Gibbs free energy associated with non-uniform surface energy and localized energy gradient responsible for thermodynamically unstable system that drives Ostwald ripening crystal growth. Thus, this drives the entire system to reach equilibrium through surface energy minimization. The nanoparticles are in higher energy state and by Ostwald ripening coalesces to form sub-micron meter size particles. Further heat treatment at higher temperature results into the overall system surface energy reduction responsible for the coalescing of sub-micrometre grains to micrometre-size as shown in Figure 2-34. Thus, selection of appropriate ratio of surface energy $(\bar{s}_{nm}/\bar{s}_{\mu m})$ could provide opportunity to tailor the desired final microstructure of sintered specimen [37].

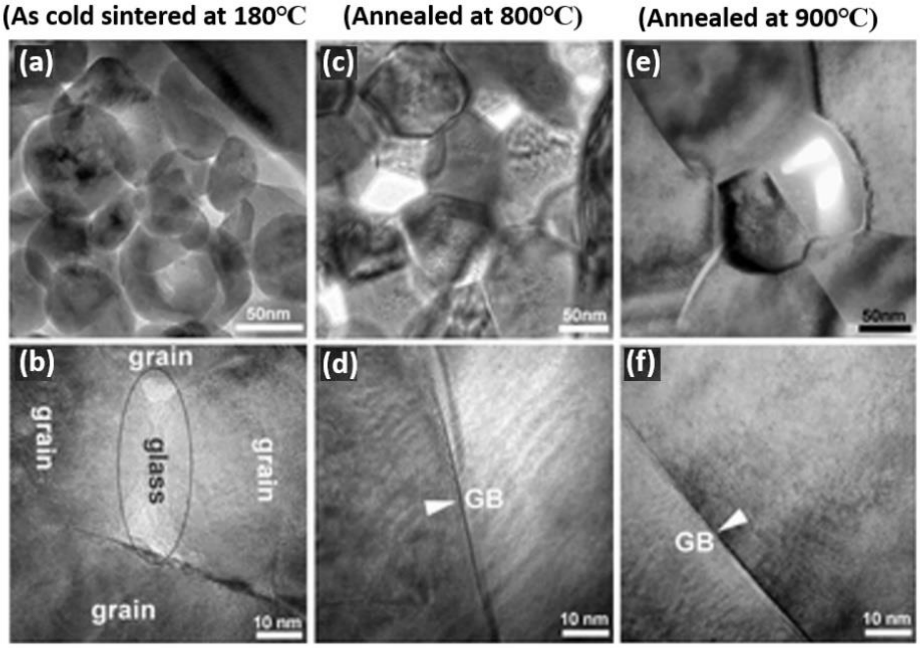

Figure 2-34 (a) Cold sintered BaTiO3 microstructural evolution TEM bright-field images at (a) 180℃, (b) CSP-post annealed at 800 °C (c) and CSP-post annealed at 900 °C. The GB are indicated by the white triangles [37]

The sintering processes of nano particles of Y_2O_3-doped ZrO_2 (8Y-YSZ) have been widely reported in literature [186, 372-377]. The reaction of water with the Zr-O-Zr bond triggers growth of the ZrO2 particles in a water vapour atmosphere [365, 378]. This was utilized recently to densify 8Y-YSZ nanoparticles using water [45, 335, 336, 379]. Huang *et al.* [363] cold sintered bismuth titanate sodium $(Na_{0.5}Bi_{0.5}TiO)_3$ nanoparticles powder to 74% relative density using hydrothermal precursor solution containing $Bi(NO_3)_3 \cdot 5H_2O$ and $Ti(OC_4H_9)_4$ and

NaOH as source of Na^+. The nanoparticles cold sintered are characterized by high surface energy, specific surface area, and chemical reactivity responsible for higher densification.

However, nanoparticles are characterized by large particles defect concentration responsible for limited electrical and mechanical properties of the materials. This is attributed to the properties dependence on particle size as observed in the $BaTiO_3$ permittivity peaks at ~1µm [380, 381] and conductivity of ZrO_2 limited by grain boundary [382, 383]. It was observed that grain boundary conductivity increases generally with increase in grain size irrespective of the powder material porosity, purity, and its thermal contribution history [371]. Thus, a strategy employed to counter this defect is to develop a bimodal composite size made of nm and µm size particles. [318] cold sintered a bimodal lead zirconate titanate at 300 °C and 500 MPa using $Pb(NO_3)_2$ solution to a relative density of 89%. The use $Pb(NO_3)_2$ solution helps to overcome the ceramic PZT incongruent dissolution in water and on further heat treatment to 900℃, the relative density increases to 99% and relative dielectric permittivity from 200 – 300 at RT and 100kHz. [265] and [316] used of bimodal composite particle size to demonstrated the improved dielectric properties performance of cold sintered $BaTiO_3$. Serrano *et al*. [274] prepared ZnO ceramics by cold sintering of its powder containing 1-10wt% nanoparticles at 170℃ and 750 MPa using acetic acid as transient solvent to study the influence of nanoparticles and microparticles fraction. The study revealed that the sintered morphology, physical properties, and microstructure are functions of the number of nanoparticles present. The nanoparticles present influences reduction in the average valence suggesting oxygen deficiency as observed in the conventional thermal sintering of ceramics. In addition, structural disorder, and lattice modifications of ZnO responsible for intrinsic defects associated with zinc and its vacancy diffusion was observed.

2.5.4.7 Post CSP-annealing

It is impossible in just a single step cold sintering process to achieve the desired full-scale densification of some materials particularly the ceramics with limited solubility or incongruent dissolution. This is particularly responsible for the different pathways of cold sintering including those observed but not very common as shown in Figure 2-35. Majority of ceramics have limited dissolution or incongruent dissolution with characteristic amorphous or secondary phase present in their grain boundaries. These include ZrO2 [384], $Pb(ZrTi)O_3$ and $BaTiO_3$ [21, 317] ceramics. Thus, a second stage post annealing heat treatment is required at a specific temperature and time scale depending on the materials glass crystallization temperature to eliminate the secondary phase and achieve the desired increased densification. This phenomena was first observed in the $BaTiO_3$ CSP study [21]. The reaction between $Ba(OH)_2$ (Ba^{2+}) and CO_2 in air forms $BaCO_3$ at grain boundaries between $BaTiO_3$ particles. The CO_2 stabilizes the amorphous phase but kinetically restrict further sintering until the $BaCO_3$ is decomposed. Post CSP-annealing of this sample was carried out first at 700℃ lower than 800℃ decomposition temperature of $BaCO_3$ to remove the glass and second phase formed along the grain boundaries as impurities. This only removes significant part of the glass phase but virtually eliminated after CSP-post annealing at 900℃ which facilitate $BaTiO_3$ formation and impurity removal as shown in Figure 2-36. In a related study, a secondary phase formation was observed after cold sintering of $Pb(Zr,Ti)O_3$ to a relative density of 89% at 300 °C and 500 MPa [318].The second phase is eliminated at the second stage heat treatment after 3hr CSP-post annealing as shown in Figure 2-37. This not only increase the relative density from 89% to 99% but also significantly improve the relative dielectric permittivity a key application property from 200 to 1300 at RT and 100 kHz. Leng *et al.* [385] cold sintered Mg-doped NASICON ($Na_{3.256}Mg_{0.128}Zr_{1.872}Si_2PO_{12}$) ceramic at 140 ℃ to a relative density of about 83% with appearance of minor secondary phases. CSP-post annealing at 800℃ of cold sintered sample had conductivity >0.5 mS/cm and higher than <0.1 mS/cm observed in conventionally sintered specimen at 1000°C. Further annealing at 1100°C, cold sintered sample relative density significantly increases and doubled the conductivity of a dry pressed sample sintered at same temperature. This can be attributed to increased densification of cold sintered after annealing than the dry pressed as shown in Figure 2-38 and Figure 2-39. Though, sintered NASICON materials are characterized by small secondary phases [358, 386] but appearance of unknown phase at 1000°C and 1100°C annealing temperatures in the XRD pattern suggests further investigation to understand the underlined mechanism involved and why it disappeared at 1200°C.

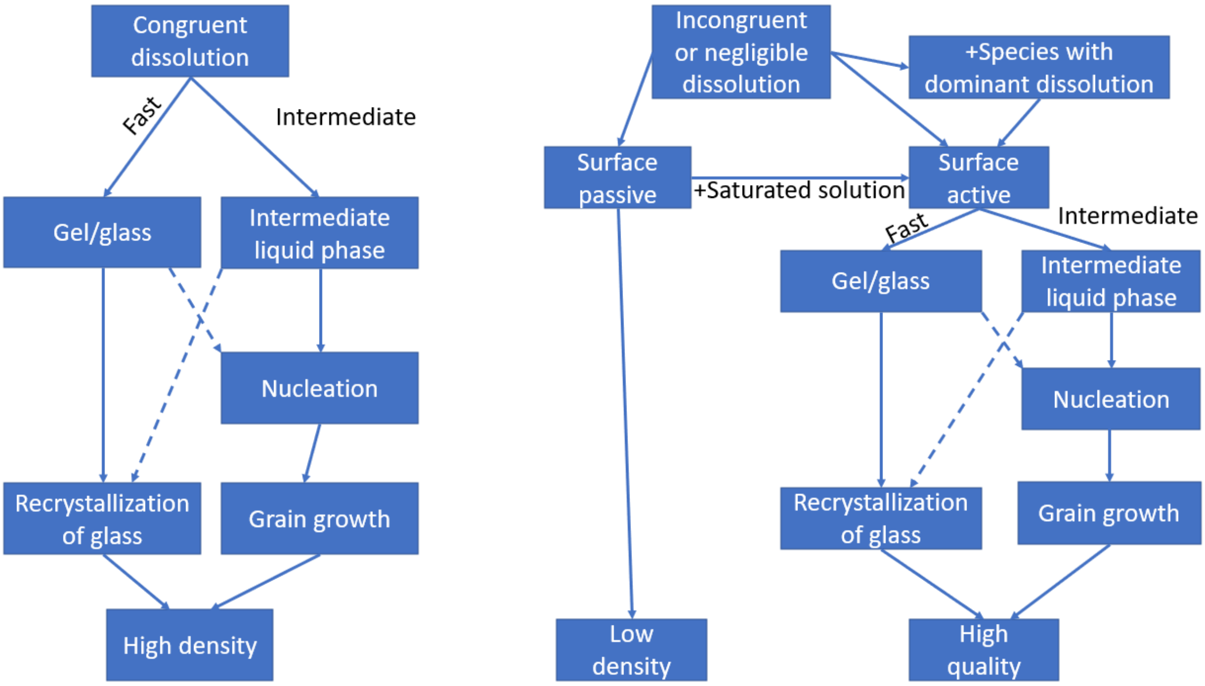

Figure 2-35 Cold sintering pathways for the densification of materials under different conditions with solid lines representing common pathways and the dashed for pathways observed but not common[53].

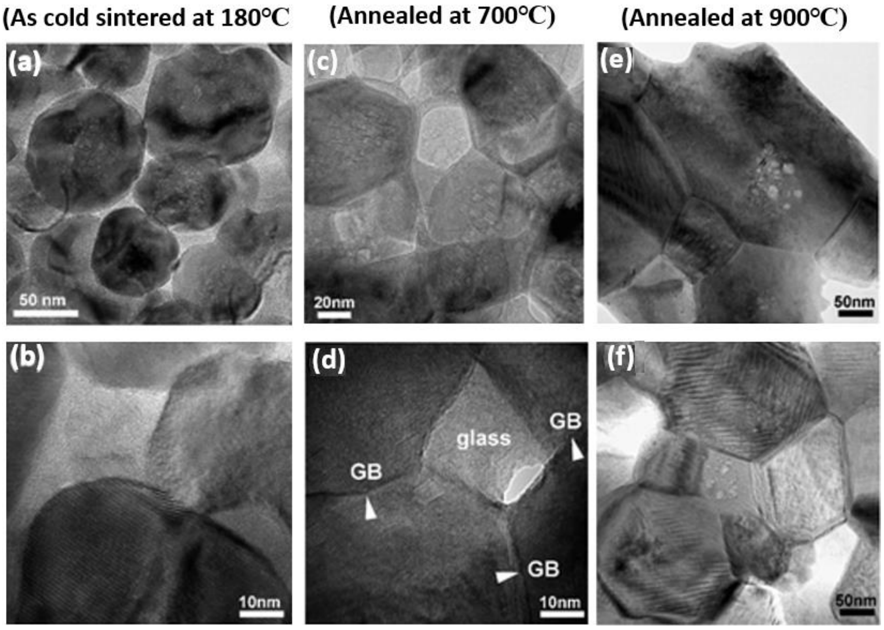

Figure 2-36. TEM images of cold sintered BaTiO3 microstructural evolution after (a-b) cold sintering at 180 °C (a-b), annealing at 700 °C (c-d), and 900 °C (e-f). Bright triangles represent grain boundaries (GB) [21]

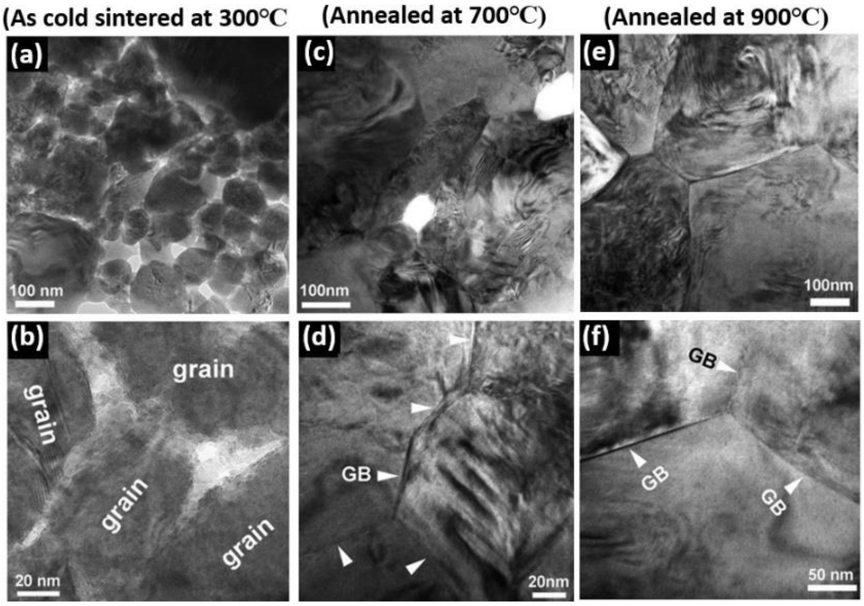

Figure 2-37. TEM images of cold sintered Pb(Zr,Ti)O_3 microstructural evolution after (a-b) cold sintering at 300 °C (a-b), annealing at 700 °C (c-d), and 900 °C (e-f). Bright triangles represent grain boundaries (GB) [318]

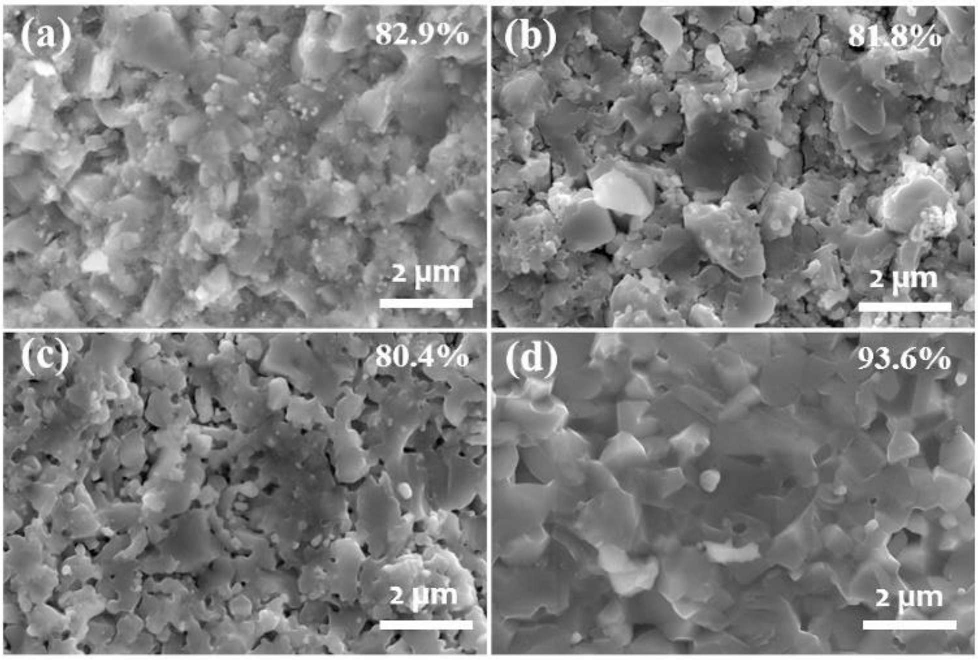

Figure 2-38. Fractured surface SEM micrographs of microstructural evolution of Mg-doped NASICON ($Na_{3.256}Mg_{0.128}Zr_{1.872}Si_2PO_{12}$) after **(a)** cold-sintering at 140 °C and annealing at **(b)** 800 °C for 6 h, **(c)** 900 °C for 6 h, and **(d)** 1100 °C for 48 h [385].

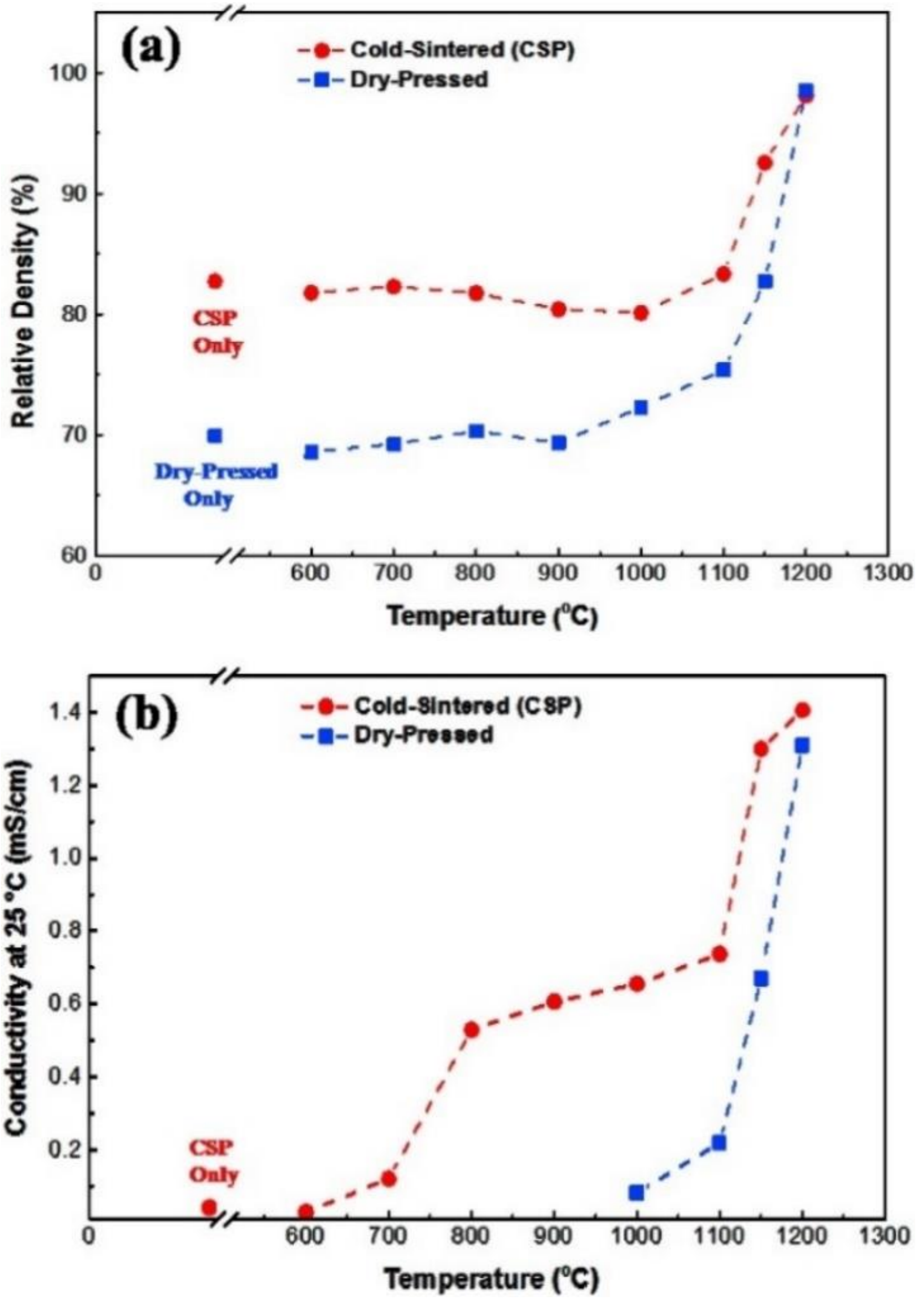

Figure 2-39. The cold-sintered and dry-pressed Mg-doped NASICON ($Na_{3.256}Mg_{0.128}Zr_{1.872}Si_2PO_{12}$) **(a)** relative density and **(b)** total ionic conductivity at room temperature as a function of annealing temperature for 6 h [385].

2.6 Summary

The reported literature has shown that the demand for thermal energy storage will continue to increase as the future energy utilization from renewable sources continue to grow. It also presents the need for need for novel energy storage materials and their current fabrication methods. Literature has clearly shown that fabrication methods currently used including the most practiced sintering process at high temperature using conventional approach to prepare medium to high temperature composite thermal storage materials is still not effective highlighting major limitations arising from mismatch in processing temperature. The report has put forward the various sintering modifications made to develop new methods and use strategies such as powder refining and addition of sintering aids that lower the sintering temperature. More specific, it has also provided the trend of various research efforts made to develop new processes and processing routes to address the diverse challenges associated with composite PCMs fabrication. It also points out successes made with respect to each sintering method but none of them was able provide the desired low temperature requirement. The new innovated cold sintering process developed recently by Randall and his co-workers has been reviewed and presented in an up-to-date literature in this report. The detail process description, its similarities to room temperature consolidation and liquid phase sintering, materials system cold sintered and the progress made to unveil its fundamental mechanism understanding has been presented. Moreover, the influence of key processing variables has been reviewed and presented. The few efforts made to use cold sintering process for composite thermal energy storage materials fabrication have been provided. Therefore, cold sintering study has enormous gasps to fill in the literature particularly its underlying mechanism in relation to single material system and composites fabrication to realise its potentials.

CHAPTER THREE

EXPERIMENTAL PROCEDURES

3.1 Introduction

This chapter provides detail experimental procedure caried out to fabricate a composite thermal storage material using alumina as structural support material and NaCl as phase change material. It consists of five sections, three experimental and one theoretical. Section 3.2 consist of details of materials, experimental approach to determine CSP parameters and their influences, and subsequent thermal, mechanical, and structural characterization of the fabricated samples. Section 3.3 accounts for the experimental procedure for the structural and mechanical properties study of cold sintered porous alumina ceramic fabrication. Details of materials, fabrication route and characterization of cold sintered composite and porous alumina were provided. Meanwhile, section 3.4 provides details regarding experimental and theoretical approach for the proposed mechanism of the Al_2O_3-NaCl composite cold sintering from the perspectives of defect chemistry.

3.2 Materials

Raw analytical grade aluminium oxide alpha phase solid powders (purity: 99.95% purity; size: 0.2-0.45 micron) and sodium chloride solid powders (purity: 99.5% average size: 1.2 microns) were all purchased from Alfa Aesar, UK. The deionized water was obtained in the lab and used for the fabrication of Al_2O_3-NaCl composite by CSP. NaCl was grounded, sieved to ≤ 45 μm sizes. The NaCl and Al_2O_3 powder were fully dried in Lenton air-drying oven (model WF 120) overnight at 120 ℃ and cooled down to room temperature.

3.3 Sample preparation

The composite Al_2O_3-NaCl in a mass ratio of 1:1 was cold sintered in stages. Firstly, dehydrated NaCl powders (0.6g) were mixed uniformly with deionized water (25 wt% of NaCl). Al_2O_3 powders were added to the NaCl mixture, mixed and ground in a mortar for about 5 min to form a uniform semi-solid paste. The Al_2O_3-NaCl paste was then transferred into a cylindrical mould with a dimeter of 13 mm and pressed under a uniaxial pressure P and heat at temperature T as shown in the CSP schematic diagram in Figure 3-1. The composite was first fabricated at CSP temperature of 120 ℃ under uniaxial pressure of 200 MPa for a dwelling time of 50 minutes with 0.04g water (0.067wt% of NaCl). The amount of water was increased gradually from 0 to 0.21g (35 wt% of NaCl) under the same temperature and pressure until density plateau was establish as a function of amount of water. At constant amount of water of 0.15g (25 wt% of NaCl), the pressure was varied from 100 MPa to 700MPa to determine pressure influence. Pressure of 400MPa was maintained under 50 minutes holding time to investigate the influence of temperature using 25 wt% of NaCl as water. The dwelling time under uniaxial pressure of 400MPa in the presence of 0.15g water at 120 ℃ was studied from 10-110 minutes.

Secondly, Al_2O_3-NaCl composite was cold sintered under constant uniaxial pressure of 400MPa, 250℃ temperature and dwelling time of 90 minutes with different amount of water between 0 – 0.21g. At constant amount of water of 0.18g (35 wt% of NaCl), composite samples were fabricated to investigate the role of pressure (200-600MPa), time (10-90 minutes) and temperature (80-250℃) on mechanical strength and density of cold sintered composite. At room temperature, Al_2O_3-NaCl was dry pressed and cold sintered with 0.18g water respectively to study the role of plastic deformation under different applied uniaxial pressures. All composite fabricated samples were dried overnight in an oven maintained at 120℃. Samples were selected and subjected to thermal cycle, post-CSP annealing and volatilization study. In the thermal cycling test, the composite pellets were arranged in high temperature aluminium oxide square crucible of 12 cm × 12 cm size, which were then placed inside furnace and subjected to 30 heating-cooling cycles between 750 °C (1 hr dwelling time) and 850 °C (1 hr dwelling time) at heating and cooling rate of 10 and 1 °C /min respectively. Some selected CSPed pellets were annealed in air at 1100 - 1500 °C for 30 minutes to form complete porous Al_2O_3 structure. Meanwhile, dry pressed and cold sintered composite pellets with 20 wt% and 35wt% water before and after first thermal cycle were placed in water for a period of 4 weeks. The undissolved sintered pellets were identified and selected for further structural analysis.

3.4 Sample Characterization

The dried composite pellets were characterized for their simple sintering monitors (density, and grain size), phase composition, microstructure, thermal and mechanical properties. The bulk density was determined by dividing the measured pellets mass by its volume obtained from its dimensions. Meanwhile, relative density is the ratio of the measured bulk density of the pellet to the theoretical density of the composite which is 2.9082 g/cm^3 determined from Equation 3-1 below:

$$\rho_T = \frac{W_1 + W_2}{\frac{W_1}{\rho_1} + \frac{W_2}{\rho_2}} \qquad (3\text{-}1)$$

where ρ_T is the theoretical density of the composite, W_1 , W_2 , ρ_1 and ρ_2 are respectively the weights and densities of NaCl and Al_2O_3. Meanwhile, the porosity P of the porous alumina fabricated according to schematic procedure shown in Figure 3-2 was computed as $P = \left(1 - \frac{\rho_b}{\rho_t}\right)$, where ρ_b and ρ_t are bulk density and theoretical density, respectively. The porous samples surface area and pore analysis after CSP-post annealing were carried out using Brunauer-Emmett-Teller (BET) process using N_2 gas in a Micro Active TriStar II Plus BET analyzer.

The phase constitution of the starting powders, CSPed and post-annealed pellets was detected by using X-ray diffraction (XRD D8 Advance, Bruker, Germany). The microstructure of cold sintered samples was observed using scanning electron microscopes (XL30 FEG E-SEM and TM 3030 Plus). The fractured surfaces from Al_2O_3-NaCl pellets were observed using scanning electron microscope (SEM, XL30 FEG E-SEM) equipped with energy-dispersive spectroscopy (EDS) for elemental distribution analysis. EDS spectrum and elemental mapping of annealed dry pressed and CSP-post annealed composites was carried out using scanning transmission electron microscopy (STEM) (FRI TECHNI F20 (OXFORD AZTEC). Samples specimens for the TEM were prepared using a standard procedure including thinning, polishing, and dimpling. Ar-ion mill (Gatan PIPS II) was used to further thinned the dimpled specimens to form an electron transparent perforation. The specimen was cooled down to liquid nitrogen temperature during ion milling using cryogenic stage to lower artefacts and structural defects. In addition to SEM analysis, microstructure of both as-CSPed and post-annealed Al_2O_3-NaCl composite were examined using high resolution X-ray tomography (XRT). The composite samples were scanned using Micro-CT (Bruker Sky-scan 1172) with acquisition parameters as follows: 5.95 µm pixel size, 80 kVp, 100 µA, 90º rotation and 4 frames averaging. The scan data sets were reconstructed using NRecon software (v1.7.1 Bruker) with correction parameters as follows: 5%, for smoothening, 52% ring artefacts and 20% beam hardening, respectively. The data sets of the reconstructed scans were exported and saved in the BMP file format. The image segmentation and volume calculation were carried out using CTAn software (V1.5 Bruker). Region of interest (ROI) is selected from the original image and converted into binary for analysis. Thresholding was carried out and its upper and lower global limits were selected by adjusting sliders under the histogram. The images were visually segmented and threshold values recorded for each sample with white part of the binary images as solid objects for 2D and 3D analysis. The total porosity was calculated using the CTAn software. The thermal properties were studied using simultaneous thermal analysis with NETZSCH STA 449 F3 Jupiter®.

Mechanical strength test of the composite pellets at ambient temperature was performed using universal testing machine (LS100 plus, Lloyd Instruments) according to the Brazilian method reported [370]. The splitting tensile strength of the cold sintered composite and the porous Al_2O_3 pellet discs were determined by breaking the pellets using 10 kN load cell universal testing machine (LS100 plus, Lloyd, UK) at 0.5mm/min displacement speed. Standard Vickers hardness tests were conducted on polished Al_2O_3-NaCl composite samples using a diamond indenter (INDENTEC Vickers Macro hardness Tester 5030SKV). The 50 kg load was held for 15s for each test. The hardness data were determined as an average of ten test results. The tensile strength measured and computed as in Equation 3-2 was analysed using Weibull statistical approach by linear fitting of ln [ln $(\frac{1}{P_S})$] in a strength relation in Equation 3-2 as a function of ln (σ_t). P_S is defined as the probability of survival determined by samples ranking in an increasing order of strength using a relation P_S= 1- $\frac{n}{N+1}$ with n = 1, 2, ⋯, N being the samples rank and N their total number. The Weibull statistical analysis of the measured strength allowed determination of the Weibull modulus (m), as the slope of the straight line of the linear plot of ln $(\frac{1}{P_S})$ versus ln (σ_t) and characteristic strength (σ_o). It allows an estimation of the measured strength result dispersion, where low m means high scattering of the data and high m corresponds to low data scattering, indicating narrow size of the flaws distribution in the test material samples. Meanwhile, characteristic strength σ_o is the survival probability of $\frac{1}{e} \approx 0.37$ reported. Measurements regarding mechanical strength and hardness, an average result from 12 samples were taken from which standard deviation was determined and used to estimate standard error.

$$\sigma_t = \frac{2P_f}{\pi D t} \qquad (3\text{-}2)$$

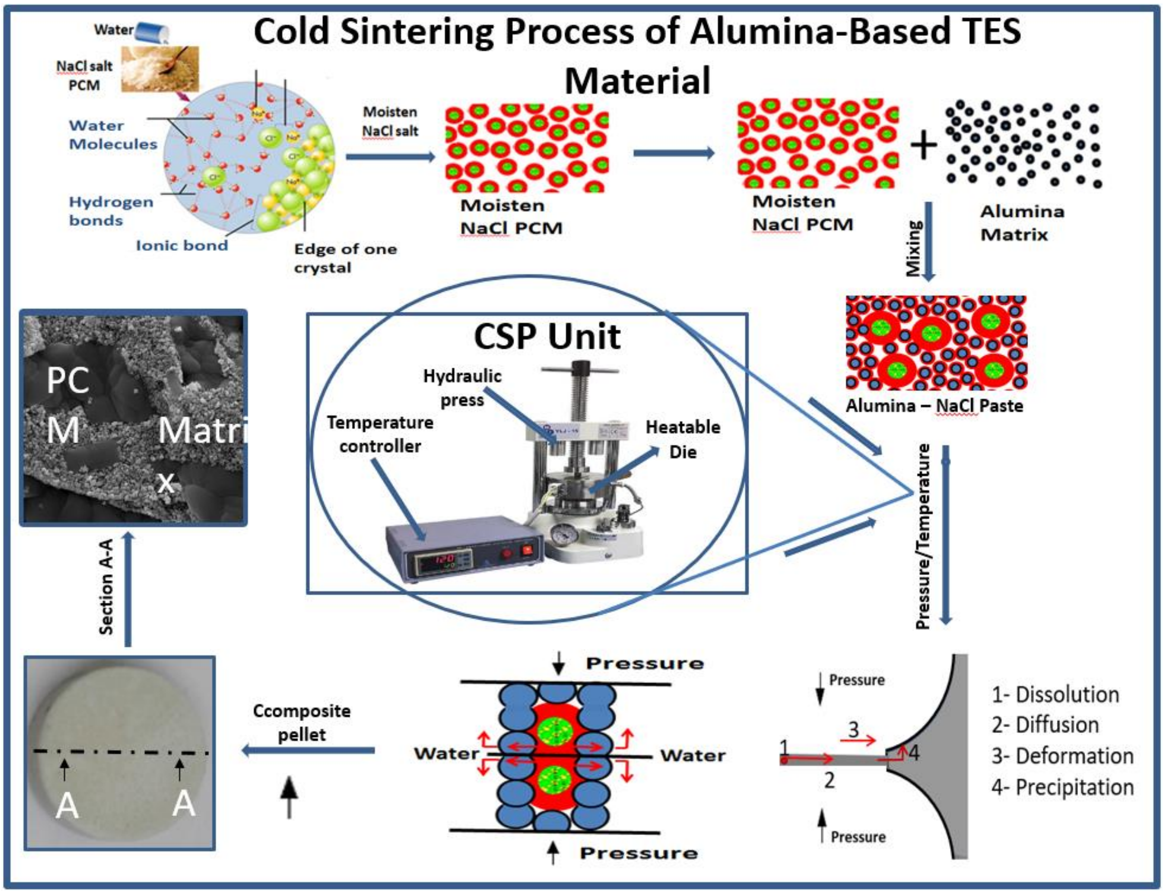

Figure 3-1 Cold sintering process schematic diagram

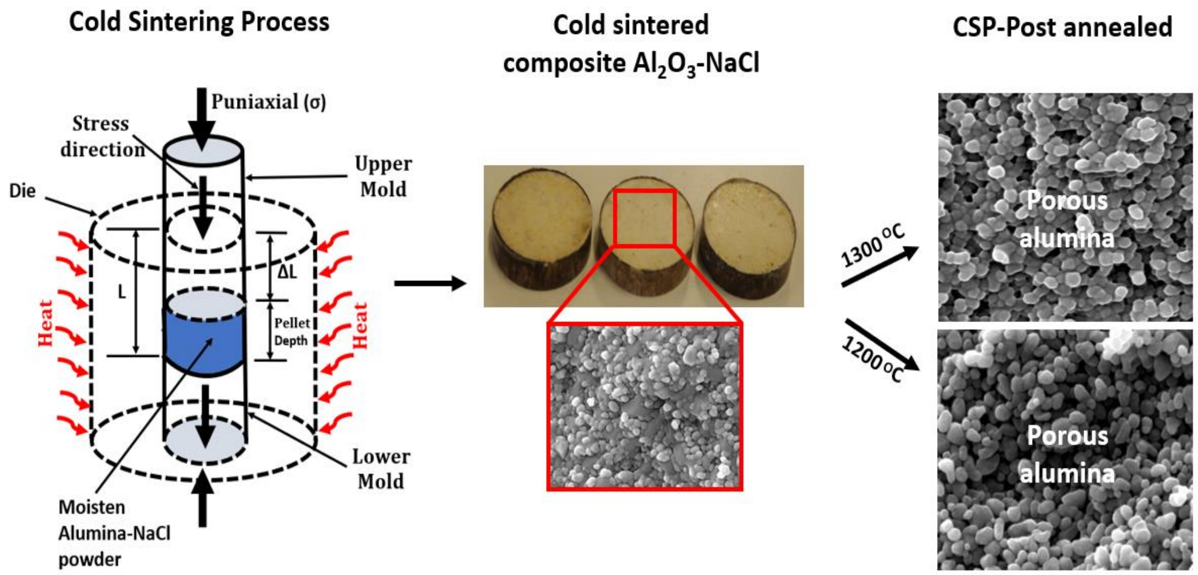

Figure 3-2 Schematic diagram of cold sintering and CSP- post annealing stages for the porous alumina fabrication.

3.5 Mechanism analysis at CSP and CSP-post annealing stage

The defect chemistry mechanism of Al_2O_3-NaCl CSP was proposed based on the experimental observations made from the initial sintering test, phase, and structural characterizations. All CSP-ed and dry pressed composite at T≤250 °C were placed in water. The composite dissolution over time was observed for dry pressed and cold sintered composites with 25 wt% and 35 wt% water. The composites which remain undissolved in water was selected for subsequent characterizations at various stages. It was characterized at CSP stage, after annealing and when placed in water. XRD phase analysis and structural analysis using TEM, SEM and SEM-EDS elemental mapping was carried out for as CSPed and selected annealed composite samples.

The process mechanism was proposed at both CSP stage and CSP post annealing stage. At CSP stage, water was introduced to the NaCl, and ions are created which interact with alumina under pressure and heat to produce $Al = O$ defects and Na_2O. The mixture of Al_2O_3 left over, Na_2O and deficient $AlO_h\cdot$ after CSP were subjected to thermal cycle heating to facilitate two kinds of interaction responsible for sintering. Interaction between similar $AlO_h\cdot$ and $AlO_h\cdot$ with Na_2O at 850°C application temperature of NaCl as PCM. The sample was held at 850°C for the period of 1 hr. At this temperature and based on experimental observations different possible interactions were speculated and led to the formation of $Al - Al\ and\ Al - ONa$ bonds respectively. Firstly, *oxygen* lone pair in the ONa_2 was shared to the empty P_x orbital of the defect $AlO_h\cdot$. It creates positive charge on oxygen with 2 electrons in the Aluminium Pz orbital. At this high temperature, the Pz electrons were shared to Alumina and after atomic rearrangement $Al - Al\ and\ Al - ONa$ bonds were created. Secondly, ONa_2 reacted with $AlO_h\cdot$ and the oxygen lone pair electrons in ONa_2 were shared by the defect $AlO_h\cdot$ via its empty Px orbital. Partial positive was formed on oxygen in the ONa_2 with two lone electrons in the

Pz orbital of AlO_h•. These were shared with another AlO_h• to form $Al - Al\ and\ Al - ONa$ bonds after atomic rearrangement. Thirdly, ONa_2 reacted with AlO_h• differently in which lone pair oxygen created partial positive charge on oxygen of ONa_2 causing cleavage of the defect $Al - O$ double bond. Subsequently, it interacted with another defect AlO_h•., and electrons in the ONa_2 were deposited into the empty Px orbital of the aluminium. After atomic rearrangement $Al - O - Al$ and $Al - Na$ bonds were formed. Finally, limited amount of water (20 wt% water) was used as transient liquid responsible for very limited defects. Thus, richer in Alumina particles than its defects (Alumina >> AlO_h•). It caused a very slow reaction speculated to be like when excess water was used to cause defect solvation.

CHAPTER FOUR

FABRICATION OF AL_2O_3–NaCl COMPOSITE FOR THERMAL ENERGY STORAGE (TES)

4.1 Introduction

Conventional sintering method have been used to prepare composite thermal energy storage materials consisting of PCM, thermal conductivity enhancer and structural support material. However, high temperature structural support ceramic materials require high temperature more than the PCM melting point to sinter, usually above 1000°C. Therefore, limits the fabrication process potentials to achieve desired support with required mechanical properties to withstand high temperature repeated cycles. This chapter presents an attempt to fabricate a composite Al_2O_3–NaCl thermal storage material using an innovative cold sintering process at low temperature $\leq$250°C. The cold sintering process variables namely temperature, pressure, amount of water and dwelling time were determined and the influence of each was investigated. In addition, the role of post annealing process was also studied and reported.

4.2 Results and discussion

4.2.1 Experimental CSP parameters determined by single variable optimization to fabricate a composite Al_2O_3-NaCl

Figure 4-1 shows the phase structure analysis using XRD to investigate both chemical compatibility and thermal stability before (Figure 4-1a) and after thermal cycling (Figure 4-1b). It shows that the phase purity of CSP fabricated sample before thermal cycling contains only the phases of Al_2O_3 and NaCl like the phases in the starting powder. The peaks correspond to the peaks of NaCl and Al_2O_3 phases respectively. The NaCl and Al_2O_3 peaks are indexed to the cubic and hexagonal systems respectively. Thus, absence of new phases in the cold sintered composite before and after thermal cycle shows chemical compatibility and thermal stability of the phases at low temperature during CSP and after 30 thermal cycles at high temperature of 850℃ as shown in Fig. 4-1b. Therefore, increase in sintering temperature, pressure, and amount of water in this study enhances the densification of the Al_2O_3 ceramic based composite as shown in Figure 4-2 and 4-3. Thus, the key parameters were determined from experiment based on single variable optimization study.

Figure 4-2a shows cold sintered Al_2O_3-NaCl composite density evolution as a function of amount of water at 120 °C under 200MPa and 50 minutes dwelling time. In a composite Al_2O_3-NaCl mass ratio of 1:1, the density increases with increase in the amount of water until it reaches its peak and begins to form a plateau when the amount of water reaches 0.15g and fully at 0.18g water. Using 0.15g water, the relative density increases sharply as a function of applied uniaxial pressure of 100 – 700 MPa. Figure 4-2b shows that it increases from ~83% at 100MPa to 92% at 200 MPa and ~96% at 400 MPa. Further increase in pressure beyond 400 MPa in the presence of water $\geq$0.18g shows increase in relative density. However, samples fractured during thermal cycle when the amount of water exceeds 0.18g or when undehydrated powder used has excess water present in it. This suggest that at CSP stage, the pores in between alumina particles are fully filled by precipitated NaCl but alumina was not sintered. Therefore, did not form a strong alumina scaffolding that can accommodate NaCl during phase change which contribute to the pellet fracture failure. Thus, the choice of 400 MPa as maximum pressure limit to fabricate a failure free composite pellet for a repeated stable thermal cycle.

To determine appropriate choice of sintering time, at 120℃ and under 400MPa pressure using 0.15g water Alumina-NaCl was cold sintered and the relative density trend as a function of time between 10 – 90 minutes as shown in Figure 4-3a. The relative density increases with time from 96% in just 10 minutes to >98% after 90 minutes dwelling time. The influence of the dwelling time is not as significant as the pressure and the amount of water, but majority of the densification was achieved at the early sintering stage reaching 98% after 70 minutes dwelling time. Figure 4-3b shows the influence of sintering temperature on the relative density of cold sintered Al_2O_3-NaCl composite under 400MPa for a period of 50 minutes. The density increases with increase in temperature to ≥99% at 220 °C and maintained constant up to 250 °C maximum temperature. Surprisingly, at 80°C and 100°C, the relative density was >97 and >98% respectively. This is comparably higher than reported relative density of 96% at 120°C under 200 MPa [287]. This shows that the amount of water and pressure plays the most significant role than the temperature particularly at the early sintering stage when the major densification required is achieved as clearly depicted in the microstructural analysis in Figure 4-4 and 4-5 respectively.

Figure 4-4 shows the SEM microstructural changes of cold sintered Al_2O_3-NaCl composite as a function of amount of water. In a limited amount of water between 0.02-0.08 gram, the fractured surface structure appears porous with limited precipitation of NaCl. With further increase in the amount of water, NaCl precipitation increases filling spaces in between alumina particles to form a denser structure as shown in Figure 4-4(f-h) using sufficient water of 0.15 to 0.18g. However, the precipitation of the salt in between alumina particles suggests absence of sintered bonds between alumina particles making the entire structure unstable. Meanwhile, cold sintered composite with a limited amount of water shows a more stable structure without precipitation but weak in terms of structural integrity.

Figure 4-5 shows the influence of applied uniaxial pressure on the cold sintered composite microstructure before and after thermal cycle. In the presence of 0.15g water, increase in pressure at constant CSP temperature of 120°C influences dense structure with increase NaCl precipitation to the surface. The preserved dense structure of cold sintered composite under low pressure of 100 - 200 MPa was weak and porous after 30 repeated thermal cycles. A more robust and stable surface structure begins to appear after thermal cycle in a cold sintered sample under 300 MPa. Further increase in pressure, causes more NaCl surface layer formation responsible for greater mass loss after few initial cycles. However, after several repeated cycles, pellets cold sintered at 400 MPa appeared robust even though has appearance of surface volitization. Hot pressing during CSP above 400 MPa with ≥0.18g water causes fracture failure during thermal cycle. Furthermore, towards a theoretical limit, the densification process is favored by time and temperature responsible for mainly microstructural rather than bulk property changes. Thus, further increase in temperature only results into a very slight density changes as observed in the density profile in Figure 4-3b and in a related study in literature [287]. The changes in density were observed up to 220 ℃ and maintained constant to 250 ℃ maximum temperature. Though, density increases with temperature and time slightly, but its microstructural changes are evident in Figure 4-6. This suggests that temperature up to 250 ℃ and dwelling time of 90 to 110 minutes could be selected for the composite CSP. The temperature increase promotes structural integrity of the composites, but significant precipitation of the salt with temperature influences greater NaCl volatilization as shown in the surface SEM microstructure of cold sintered composite after first thermal cycle in Figure 4-7.

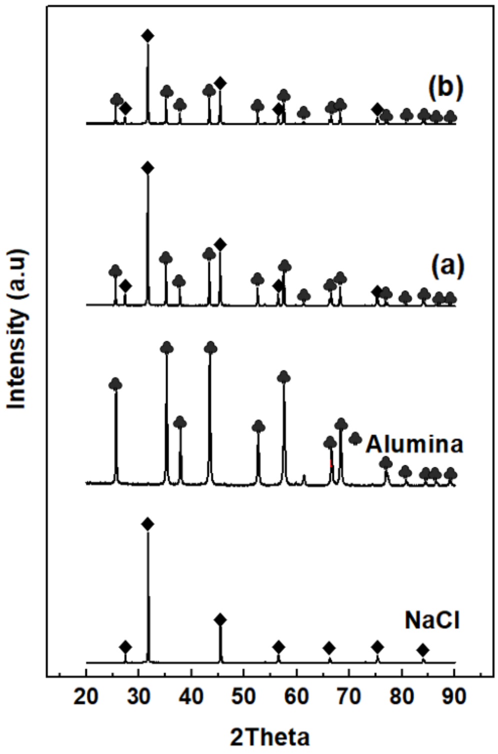

Figure 4-1 XRD Pattern of pure powders and NaCl- Al_2O_3 composites before (a) and (b) after thermal cycling

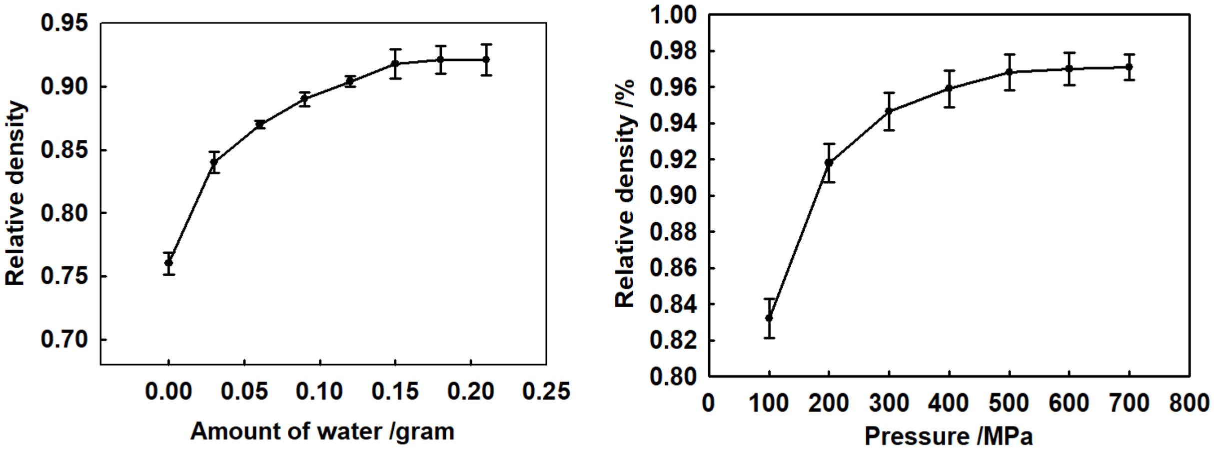

Figure 4-2 (a) Relative density of cold sintered Al_2O_3-NaCl composite (1:1) at 120°C, 200MPa, for 50 minutes as a function of amount of water (b)Relative density of cold sintered Al_2O_3-NaCl composite (1:1) with 0.15g water at 120°C, for 50 minutes as a function of pressure

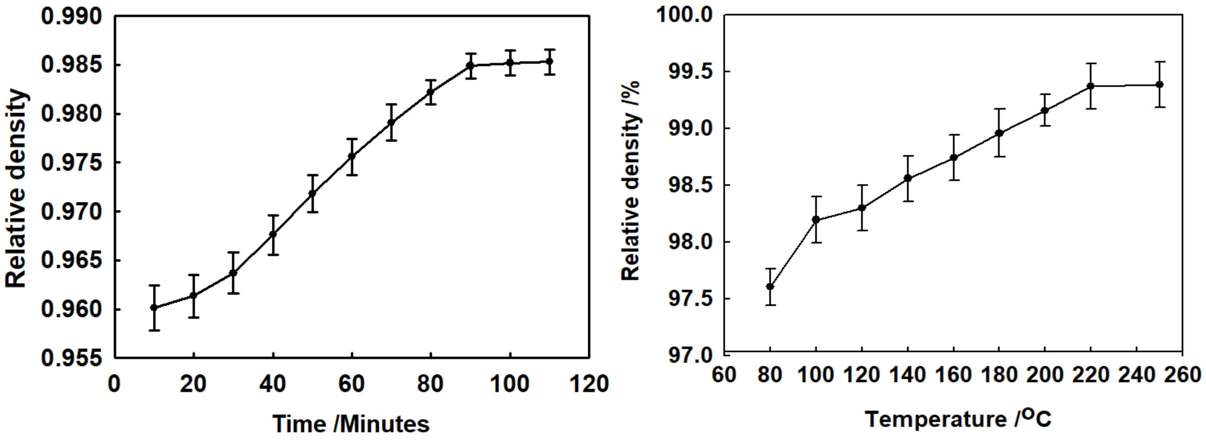

Figure 4-3 (a) Relative density of cold sintered Al_2O_3-NaCl composite (1:1) with 0.15g water under 400MPa, for 50 minutes as a function of temperature (b) Relative density of cold sintered Al_2O_3-NaCl composite (1:1) with 0.15g water at 120℃ under 400MPa as a function of dwelling time.

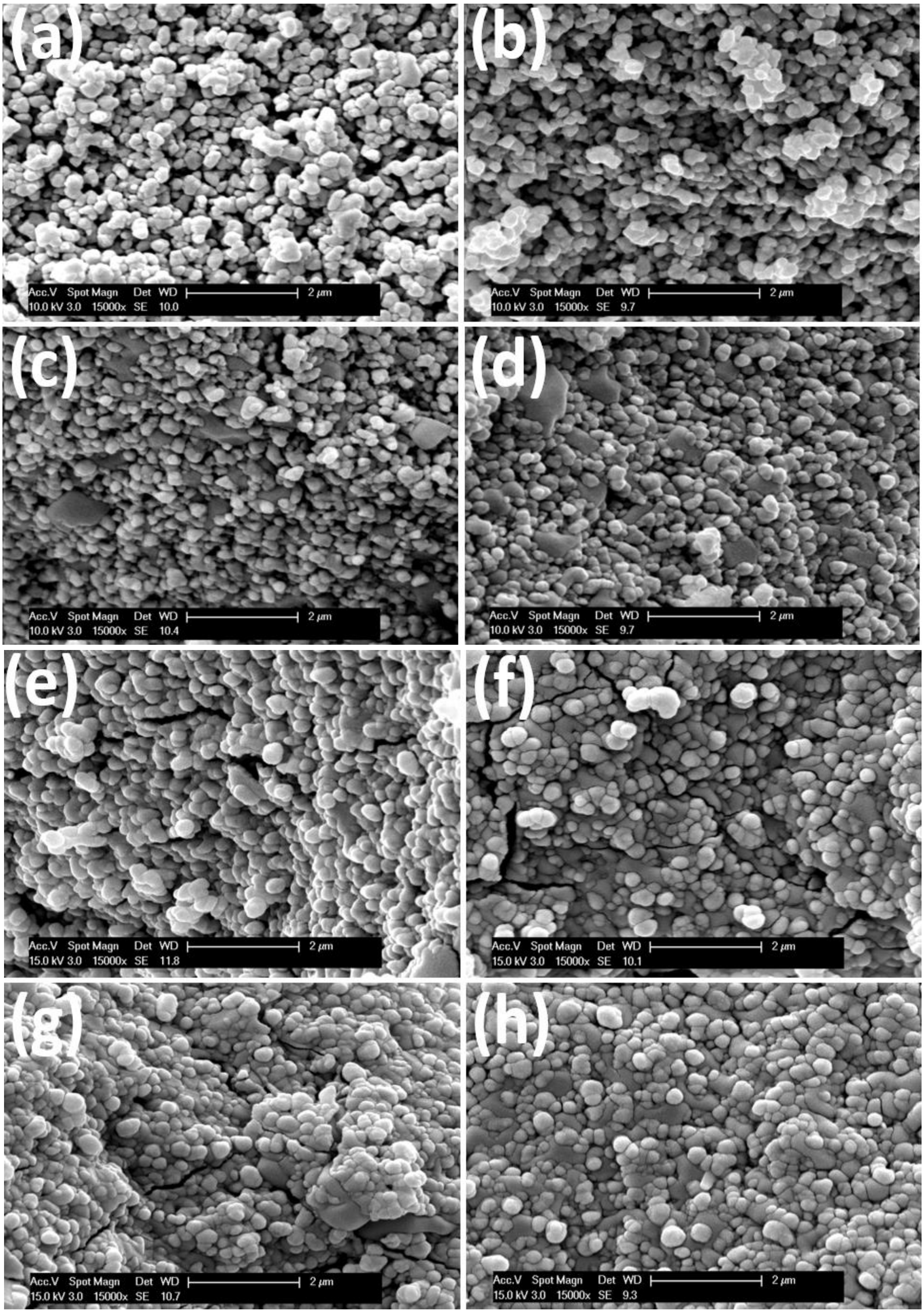

Figure 4-4 SEM images of cold sintered Al_2O_3-NaCl at 120 ℃ as a function of amount of water (a) 0.0 (b) 0.04 (c) 0.06 (d) 0.08 (e) 0.12 (f) 0.15 (g) 0.18 (h) 0.21g water under 400MPa.

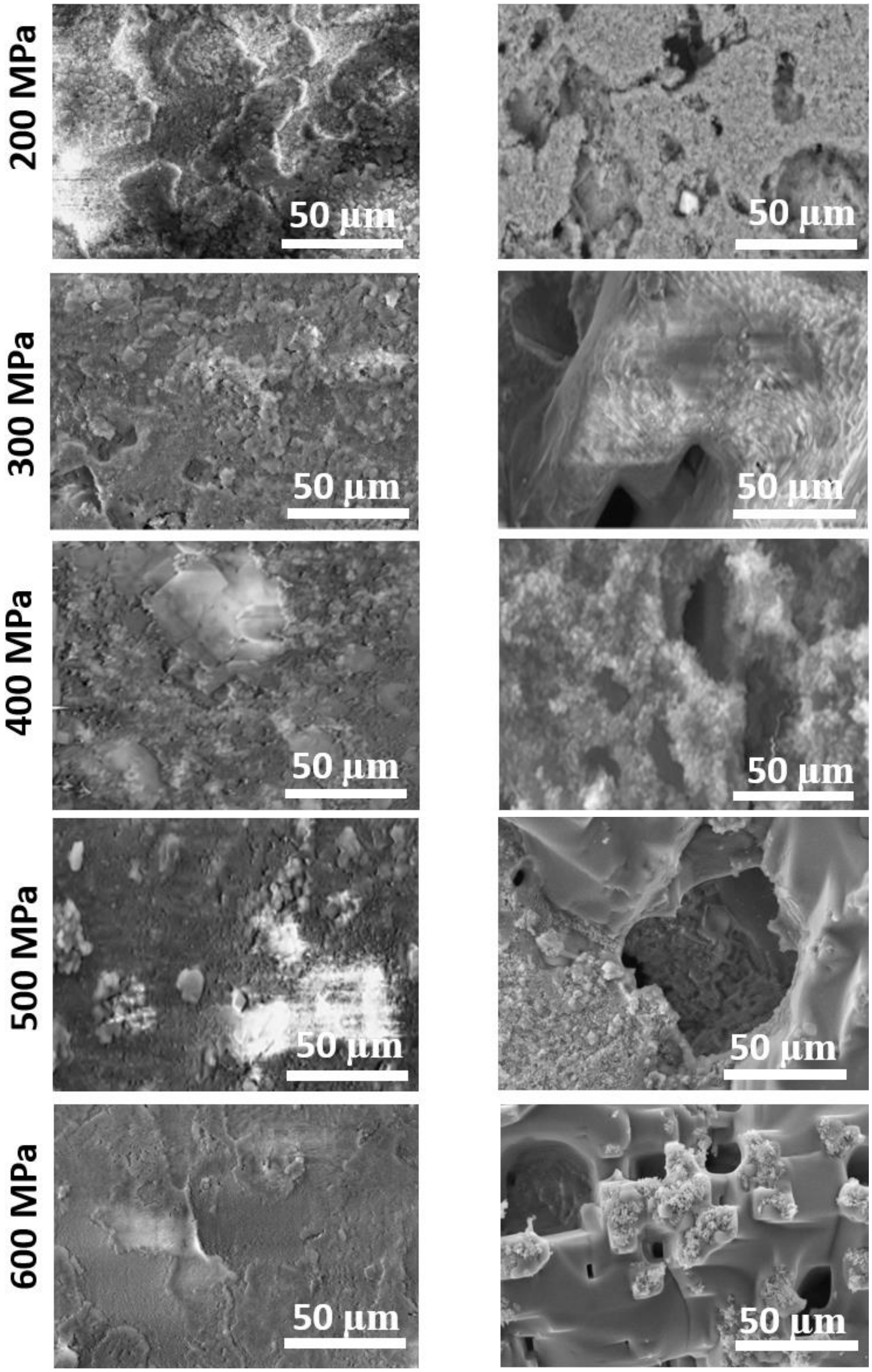

Figure 4-5 SEM microstructure of cold sintered Al_2O_3-NaCl at 120 °C with 0.15g water for 50 minutes as a function of pressure

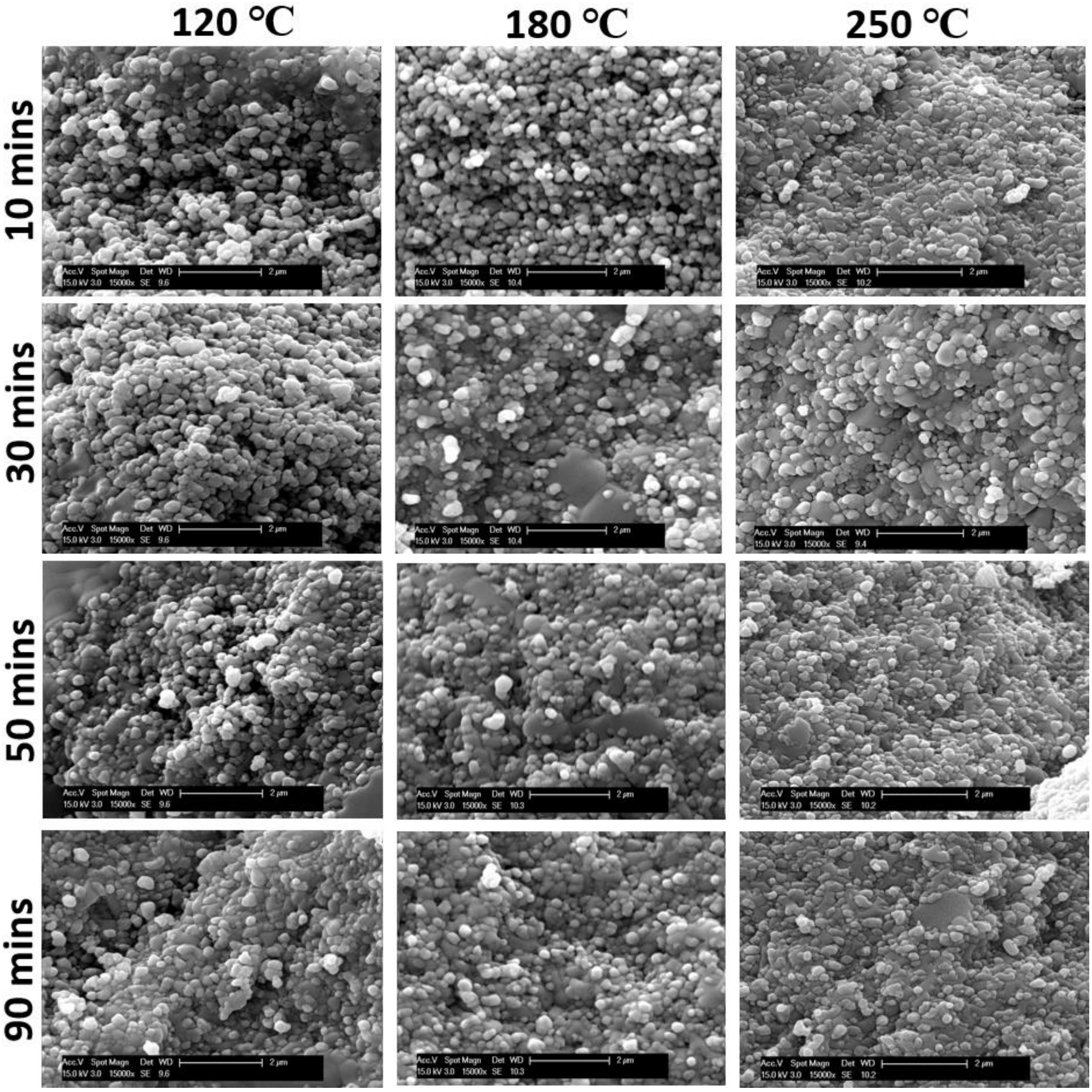

Figure 4-6 Fractured surface SEM microstructure of cold sintered Al_2O_3-NaCl with 0.15g water, under 400 MPa for 50 minutes as a function of temperature.

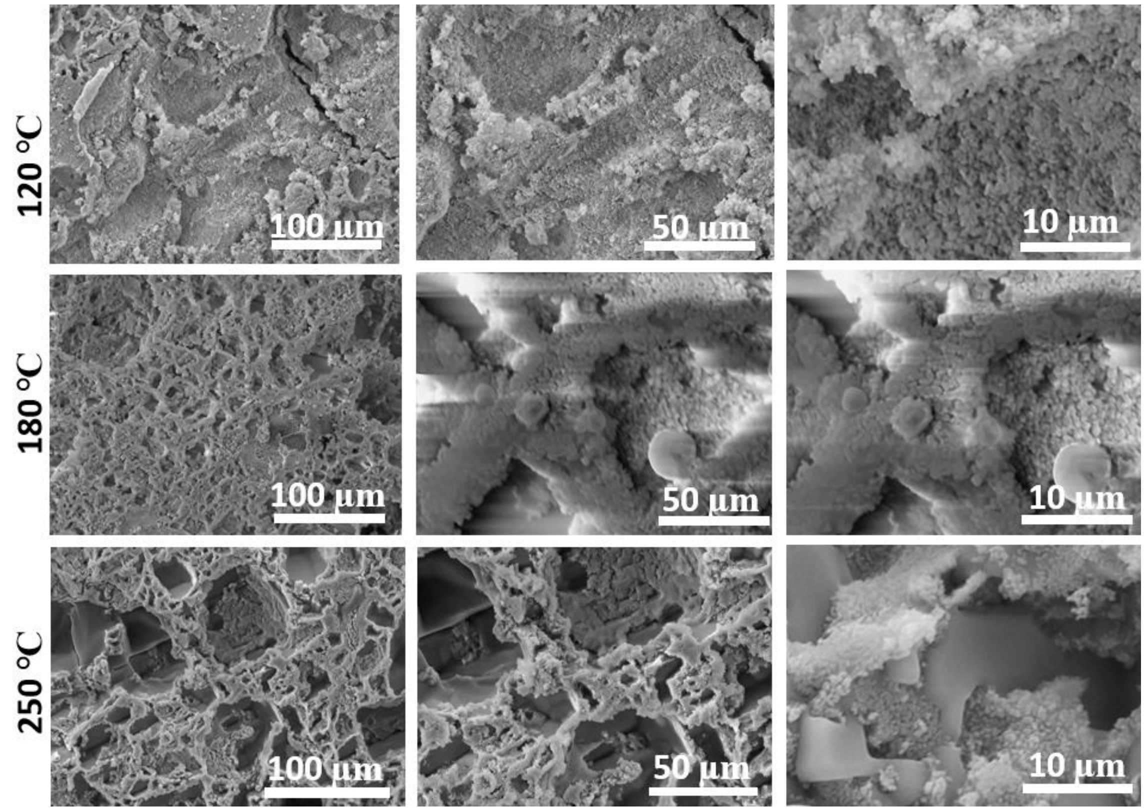

Figure 4-7 Surface SEM microstructure of cold sintered Al_2O_3-NaCl with 0.15g water, under 400 MPa for 50 minutes after thermal cycle.

It is interesting to note that irrespective of cold sintering temperature, pressure, amount of solvent (water) and dwelling time, the composite pellet morphology in Figure 4-8 shows no sign of leakage. However, mass changes continue to evolve due to the NaCl high volitization at its melting point. Figure 4-9 shows volatilization analysis of pure NaCl and composite Al_2O_3-NaCl heated over a temperature range of 800 - 950°C at constant heating rate of 10 °C /min and dwell time of 30 minutes. The result of this study is consistent and the trend is similar to the reported volatilization study of NaCl and NaCl- Al_2O_3 composite made by one-step chemical synthesis method [387].

The comparative analysis of both studies shows that between 800 - 900℃, the mass loss in the composite pellet was small compared to pure salt at 800 - 900 °C. However, it is apparent that the magnitude of the volitization ratio and a range of temperature for which composite and pure salt have minimum volatilization differs. The mass loss observed in the composite is smaller than observed in pure salt up to 850 °C. Beyond this it gradually loses its capacity of minimizing exposed contact surface area with surrounding at high temperature. Thus, the increased volatilization at 900 °C in this study is higher than observed by Zhu *et al*. [387] which is attributed to the 30 minutes dwell time allowed at each temperature to investigate the salt volitization. Surprisingly, both studies have shown that at 950 °C, the mass loss of pure salt was lower than observed in the composite pellet. This is because the specific surface area of pure salt is smaller than the composite surface area. In terms of its application potential, the composite NaCl-Al_2O_3 composite revealed its greatest resistance to volitization between 800 - 850 °C which is therefore, a preferable working temperature range. The composite application potential is further revealed by its high phase change enthalpy shown in Figure 4-10. It shows the composite STA curves containing 50 wt% NaCl with melting and solidification phase change enthalpy of 252.5 J/g and 256.7 J/g respectively. The result reveals that the phase change enthalpy, on set and end temperatures are quite close with 4.2 J/g difference between the phase change enthalpy of melting and solidification. The phase change enthalpy is consistent to the theoretical NaCl phase change enthalpy and even higher than observed in the composite made from one step chemical synthesis method with a reported phase change enthalpy of 362 J/g at 75.1 wt% NaCl composition [387]. This clearly demonstrates CSP compatibility to TES material fabrication for wide temperature application. In terms of chemical compatibility, thermal stability, and storage capacity, CSP appears competitive and could achieve higher performance than existing methods via material integration at low temperature. Conclusively, the key influencing CSP variables determined are the temperature, pressure, amount of water and dwelling time keeping other parameters constant. It is apparent that the composite sintering at temperature up to 250℃ under 400MPa in the presence of only 0.15g water in a fully dehydrated powder is not adequate to achieve full scale densification or cause alumina particles to sinter. This is evident in the observed dissolution of all cold sintered composite material when placed in water. Thus, the influence of pressure and amount of water is greater requiring further investigation.

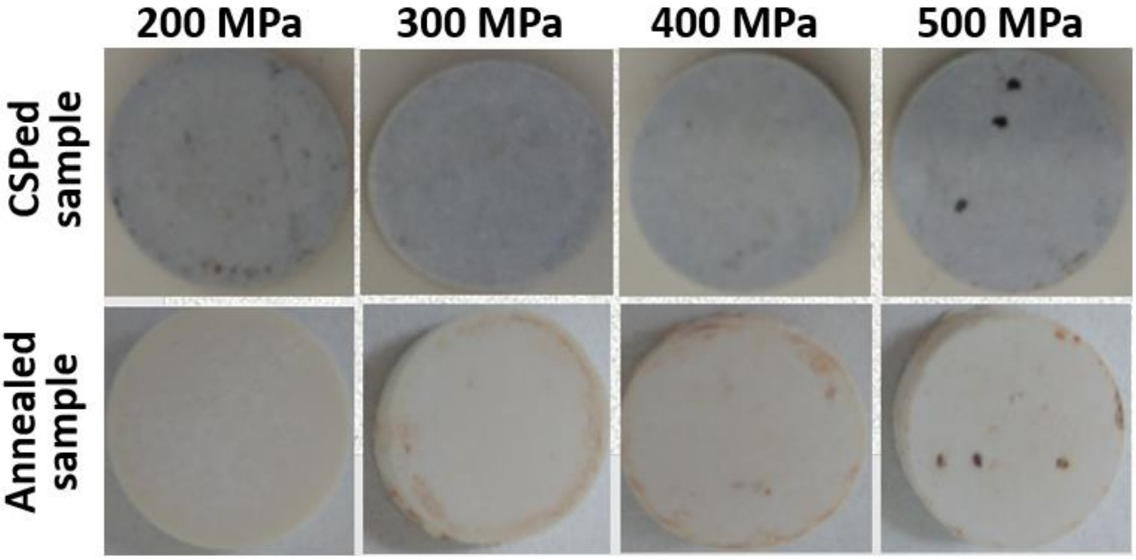

Figure 4-8 Pellet morphology before and after thermal cycle of cold sintered Al_2O_3-NaCl composite fabricated at 120 °C with 0.15g water for 50 minutes under different pressure.

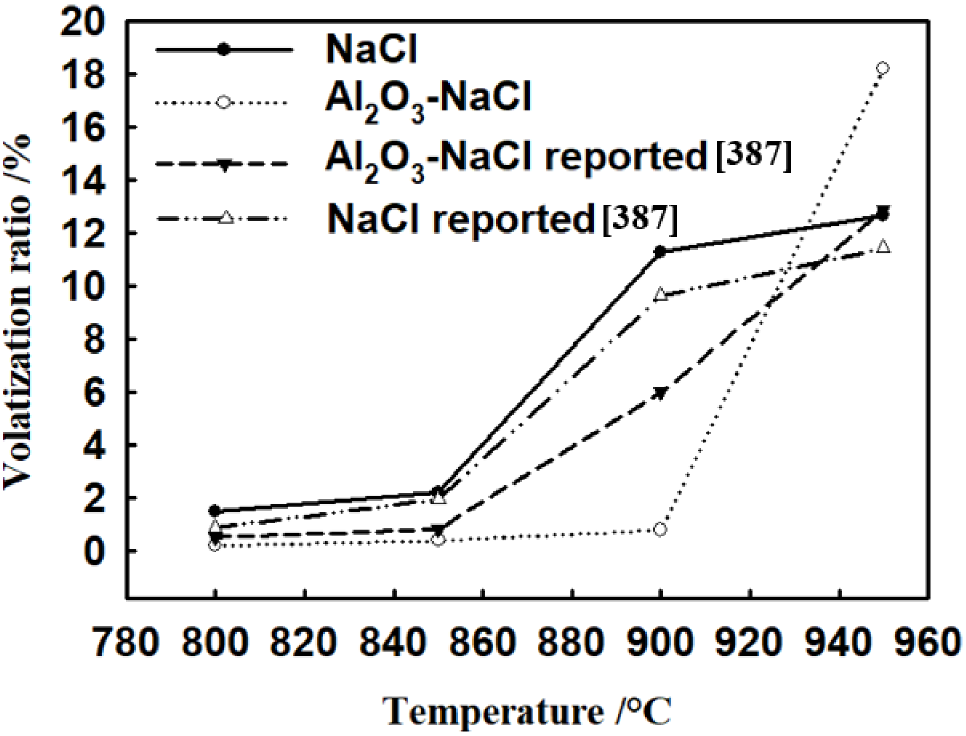

Figure 4-9 Pure NaCl and NaCl- Al_2O_3 composite volatilization ratio at different temperatures

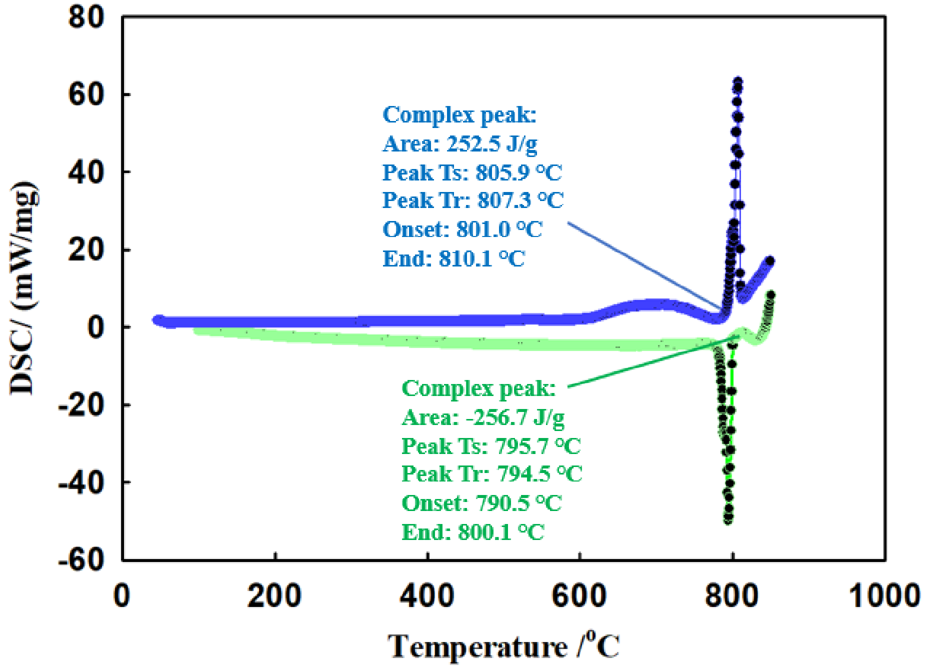

Figure 4-10 STA melting and solidification segment curves of Al_2O_3-NaCl (50-50 wt%) composite material fabricated by CSP.

4.2.2 Influence of pressure induced plastic deformation and amount of water in low temperature cold sintering of Al_2O_3-NaCl

The influence of pressure induced plastic deformation and amount of water was studied during cold sintering of composite Al_2O_3-NaCl and compared with NaCl. Figure 4-11 shows the XRD pattern of the raw alumina, NaCl powder and cold sintered alumina-NaCl composite as a function of amount of water and applied uniaxial pressure, respectively. The starting alumina and NaCl powder peaks intensity and position on the XRD pattern are clearly shown and could be indexed to aluminium oxide corundum structure (PDF card 00-042-1468) and sodium chloride halite structure (PDF card 00005-0628) respectively. The raw starting powder is made up α-alumina and NaCl only. The position of the alumina and NaCl diffraction peaks in the cold sintered composite are identical to those of the starting powder. The XRD pattern of NaCl specie in the cold sintered composite shows near constant peak intensity. This is consistent to the dry pressed and cold sintered NaCl reported by [41].

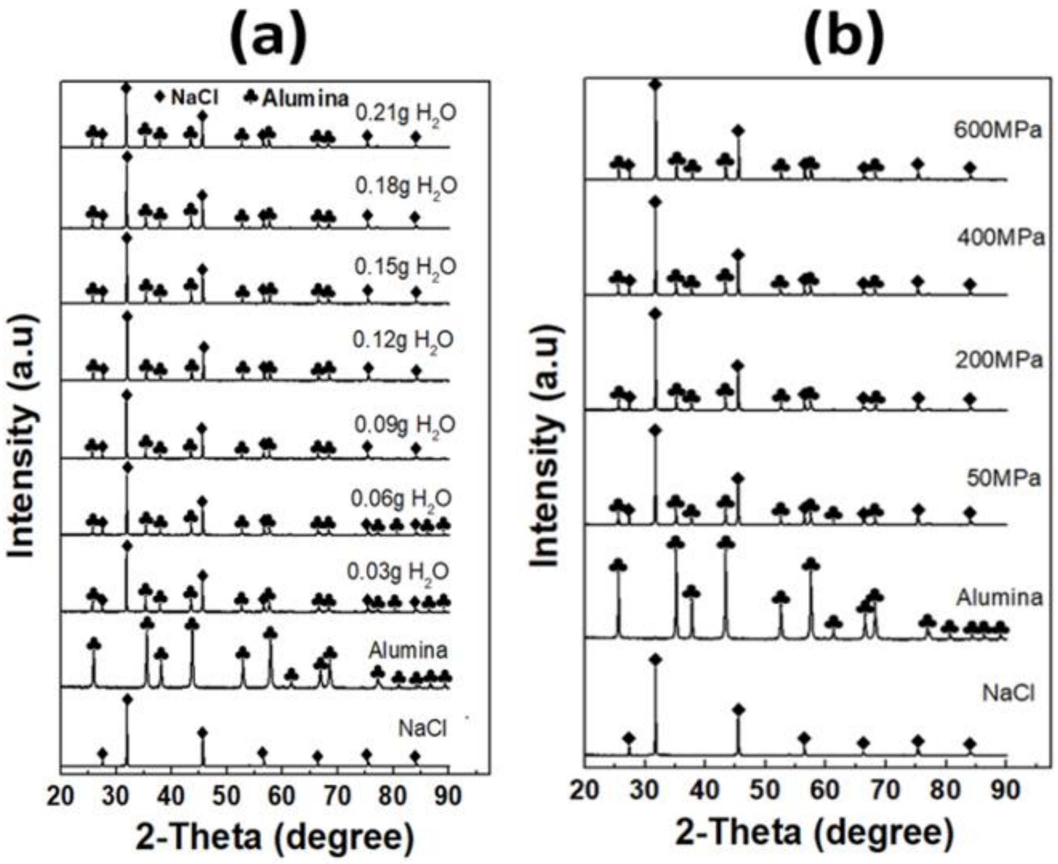

Figure 4-11 (a) XRD patterns of dehydrated starting powders, and as-CSPed composite pellets at 250°C, 400MPa as a function of water content (b) Figure 4-12 XRD patterns of dehydrated starting powders, and as-CSPed composite pellets with 0.18g water at 250 as a function of pressures

Generally, the intensity of the peak’s decrease with increase in water. However, the peaks near 90 of 2 theta are very weak, and they are easily covered by the background due to the presence of sodium chloride. Figure 4-11a shows no appearance of new peaks in the cold sintered composite different from the starting alumina and NaCl powder species, an indication that under the cold sintering conditions used, water was not incorporated, and no other phase or impurity is present. This is one of the most striking observations as increase in the amount of water up to 0.21g has no effect on the phase purity. The observation made in this study differs significantly to the observed appearance of hydrated Lithia phase at high water content during cold sintering of lithium molybdate ceramic [388]. Meanwhile, Figure 4-11b shows the XRD pattern of cold sintered composite as a function of applied uniaxial pressure. In the presence of 0.18g water, pressure has little or no influence on the lumina peak intensity changes during CSP. The peak intensity changes under 50MPa are like those observed between 200-600MPa, suggesting that in the presence of sufficient amount of water, a very low pressure is required to trigger alumina interaction with NaCl. Therefore, it is apparent that there was interaction between the composite species requiring further study.

Figure 4-12a-g shows the relative density of dry pressed NaCl, cold sintered NaCl and Alumina-NaCl composite as a function of applied uniaxial pressure. Figure 4-12a shows that relative density of air pressed NaCl at low pressure of 50 MPa was 80.4 % and increases beyond cold sintered NaCl samples at applied uniaxial pressure ≥150 MPa. The limited densification of cold sintered at pressure >150MPa can be attributed to trapped pores at room temperature limiting its final relative density at higher pressure. This is consistent to the dry pressed NaCl relative density reported [41] as shown in Figure 4-12a. The relative density of cold sintered NaCl according to Hong *et al*. was 88.4% at uniaxial pressure of 50 MPa and increases to 93.1% at 100MPa and 93.9% at 150 MPa. Beyond 150 MPa, only slight increase was observed as shown in Figure 4-12b. In contrast to the observed cold sintered NaCl, dry pressed NaCl density shown in Figure 4-12c is consistent to the reported relative density of 79.6% and 87.9% at low applied pressure of 50 and 100 MPa respectively [41]. Figure 4-12c revealed that increase in applied uniaxial pressure >300MPa enables high relative density of dry pressed NaCl close to theoretical value at uniaxial pressure of 400 MPa [41]. Beyond 400 MPa, no significant increase was observed up to 600 MPa. Interestingly, a high relative density of 98.3% to 99.4% of the dry pressed NaCl was observed at applied uniaxial pressure of 200 – 300 MPa. This represent 4.0 to 4.8% higher relative density than cold-sintered NaCl at the same uniaxial pressure and is consistent to 4.3% to 4.7% reported by Hong *et al*. [41]. Thus, pressure induced plastic deformation is the dominant mechanism of dry pressed NaCl and contributes to its cold sintering process mechanism.

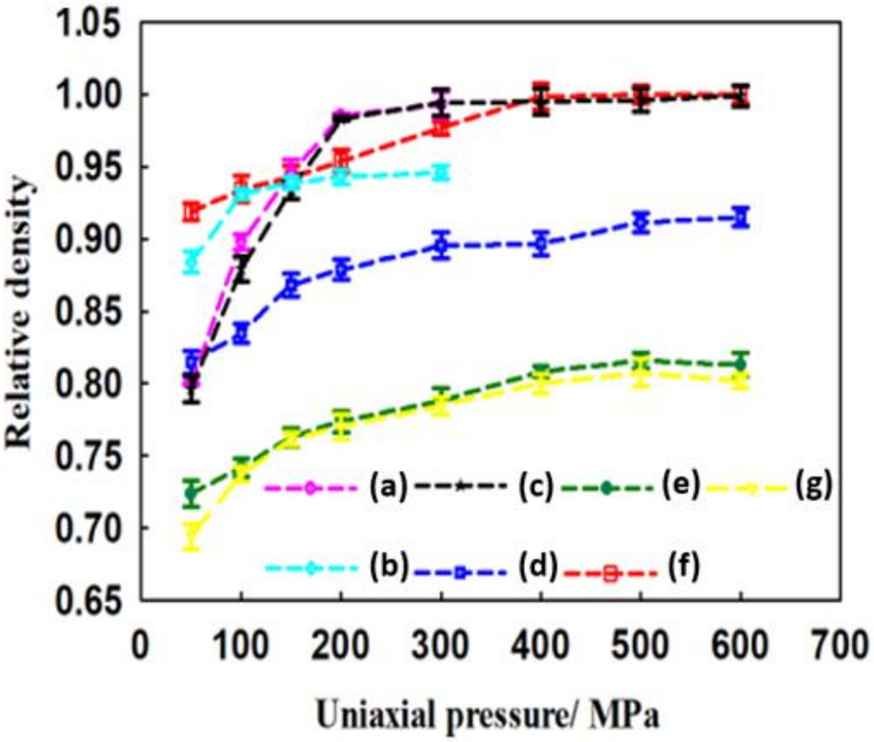

Figure 4-12 Relative density as a function of applied uniaxial CSP pressure of (a) dry pressed NaCl at 25 °C reported [41] (b) cold sintered NaCl at 25 °C reported (Hong et al., 2018) (c) dry pressed NaCl at 25 °C (d) cold sintered Alumina-NaCl at 25 °C (e) dry pressed Alumina-NaCl at 250 °C (f) cold sintered Alumina-NaCl at 250 °C (g) dry pressed Alumina-NaCl at 25 °C

Surprisingly, and in contrast to the earlier reported [41] and observed limited densification of cold sintered NaCl in this study, relative density of cold sintered composite Alumina-NaCl at room temperature (Figure 4-12d) increases with increase in pressure from 81.5% to 91.5% higher than dried pressed by 12% (Figure 4-12e). At higher CSP temperature of 250°C (Figure 4-12f), it increases from 91.9% to 99.9% at 250°C when uniaxial pressure increases from 50 - 600MPa. Figure 4-12d shows clearly higher densification of cold sintered than dry pressed. This clearly shows influence of water in promoting mass transport, thereby reducing inter-particle diffusion distance to achieve rapid densification as it facilitates grain boundary diffusion responsible for low CSP time scale reported by German [389]. Differently from dry pressed and cold sintered NaCl (Figure 12-3e and 3g), cold sintered composite had higher relative density than dry pressed by 19% at 250℃ when pressure increases from 50 – 600 MPa. This shows how water promotes mass transport, thereby reducing inter-particle diffusion distance to achieve rapid densification which facilitates grain boundary diffusion responsible for low CSP time scale reported by German [389]. The dry pressed NaCl high density greater than observed in cold sintered samples at higher pressures could be attributed to NaCl low Mohs hardness value of 2 [390]. It enables NaCl particles rearrangement and shaping under mild mechanical strength. Thus, the observed pressure influence suggests that plastic deformation mechanism in dry pressed NaCl contribute significantly to the overall mechanism of the composite cold sintering and dry pressing.

It is also pertinent to note that, temperature has influence on cold sintered composite but little or no influence on the dry pressed relative density. The slight increase in relative density observed in Figure 4-12e above 400 MPa at 250 ℃ can be linked to the pressure increase and appears to be elastic which is reversible. Figure 4-12f shows that increase in CSP temperature from room temperature to 250 ℃ influences a dramatic increase in relative density from 82 % to 92 % under 50 MPa and 91% to ~99% under pressure of 400 - 600 MPa. It represents 10 % and 8% increase in relative density from room temperature to 250 ℃ at 50MPa and 400 MPa, respectively. Though, according to Rahaman [28], the monumental increase in cold sintered density from room temperature to 250 ℃ could be attributed to hot-pressing mass transport densification mechanisms. These could be either a particle rearrangement, grain boundary and lattice diffusion, viscous flow, grain boundary sliding or both.

The variation in relative density and microstructure between cold sintered and dry-pressed Al_2O_3-NaCl composite significantly contribute to the phase change enthalpy of the composite as a function of pressure as shown in Figure 4-13. The latent heat of phase change increases with increase in the apply pressure and is higher for cold sintered than the dry pressed. The variation is consistent with the composite relative density shown in Figure 4-12e and f. The phase change enthalpy difference between cold sintered composite at 250 °C under 200MPa and 400MPa was 21.24J/g equivalent to 8.3% increase for cold sintered. Meanwhile, increase under similar pressure increase and holding temperature, the phase change enthalpy increase of the dry pressed composite was 12.56 J/g representing 6.1% increase. It is very clear that present of water increase structural homogeneity due to dissolution-precipitation and higher densification. This is responsible for the observed higher increase in latent heat of phase change with increase in pressure than observed in the dry pressed.

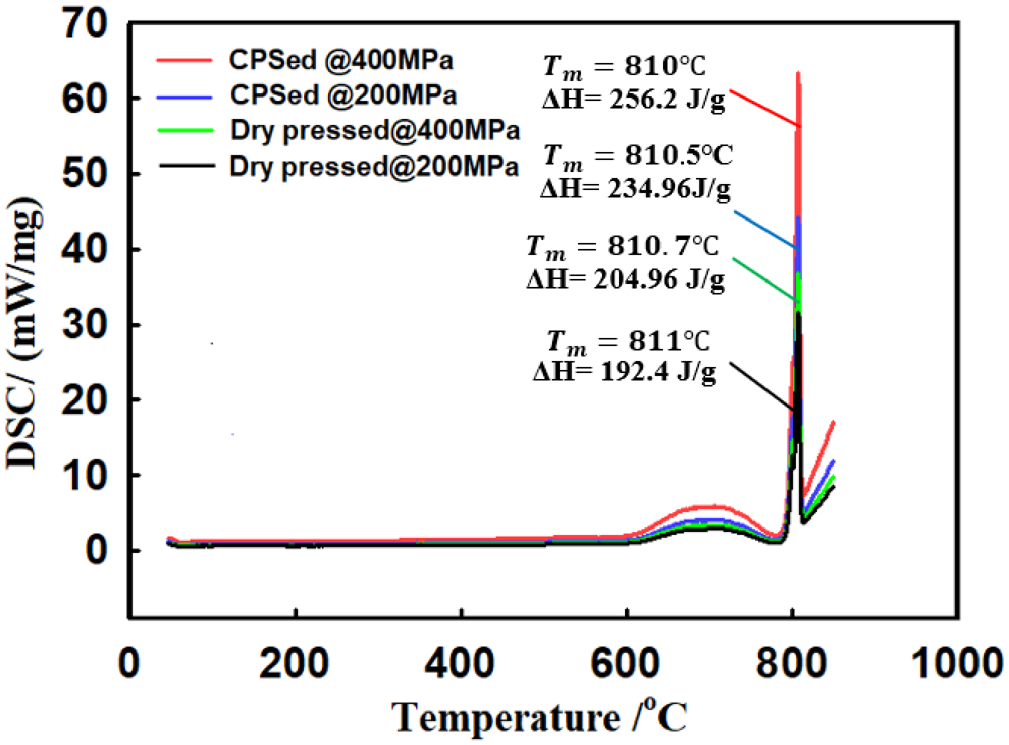

Figure 4-13 STA melting curves of Al_2O_3-NaCl composite cold sintered with 0.18g water and dry pressed at 250°C for 90 minutes under 200 and 400MPa.

Figure 4-14 shows the relative density and mechanical strength as a function of water content and applied pressure during cold sintering of alumina-NaCl composite at 250°C under 400MPa for 90 minutes. Figure 4-14a shows that the increase in relative density with increase in water content was linear and more pronounced between 0.06 – 0.18g water. It increases from 81% relative density and 0.66 GPa rupture strength when fully dried to maximum of 99.8% and ~14.4 GPa rupture strength. From 0.18g water, density and strength plateau appeared. With further increase in water beyond 0.21g (35 wt% of NaCl), it is impossible to hold the mix as it spills from the die under pressure, a situation responsible for density measurement variation. Generally, the composite density continues to increase with increase in the amount of water under pressure even at room temperature comparably much higher than dry pressed. Presence of water promotes mass transport, thereby reducing inter-particle diffusion distance to achieve rapid densification. Thus, it facilitates grain boundary diffusion responsible for low CSP time scale reported by German [389].

Figure 4-14b shows relative density and mechanical strength of Al_2O_3-NaCl composite as a function of applied uniaxial pressure. It shows a 4-fold rupture strength of cold sintered Alumina-NaCl composite at 250 °C from 200 - 400MPa compared to cold sintered composite between 400-600 MPa. Generally, ruptured strength of the composite pellet increases with pressure, and is more between 200 to 400MPa. It slows down above 400MPa where the density plateau first appeared. The mechanical rupture strength correlation in CSP is a strong function of uniaxial pressure and it tends to plateau beyond 500 MPa at constant temperature and dwelling time. It also shows that at early stage of the composite cold sintering, the applied uniaxial pressure is amplified between the contacting particles as contact zone become small. This is consistent to the reported effective pressure which is several time the applied pressure [391]. The applied pressure enhances driving force for faster densification of the composite materials because of the major pore elimination during sintering responsible for mechanical strength and density boost [391]. According to German, internal sintering stress pulling the particles together is supplemented by the applied external pressure amplified at the particle contacts, influencing greater inherent sintering stress. Thus, pressure in this study contributes to the in-built sintering stress responsible for low CSP sintering temperature. However, the influence of water in promoting densification of the cold sintered composite is incomparably much more significant than the pressure influence at all CSP temperatures.

Figure 4-15 shows the densification rate as a function of applied uniaxial pressure and the relative density variation as a function of dwelling time at different temperatures. According to German [391], densification rate is an instantaneous change in relative density of dry powder in case of conventional sintering or moisten powder in liquid phase assisted sintering such as in CSP. At constant temperature of 250 ℃ and 90 minutes dwelling time, Figure 4-15a shows that the rate of densification of the Alumina-NaCl is linear and is rapidly influenced by uniaxial pressure at constant temperature. The appearance of non-zero densification rate in Figure 4-15a at zero applied stress emanating from surface energy effect is consistent to the observed and reported applied external pressure influence on the densification of 3 µm alumina at 1630 ℃ by German [391]. Figure 4-15b shows that the densification rate is faster and higher at the early stage of the sintering and subsequently slow down at longer time with no appreciable increase in densification. Therefore, bulk transport mechanisms dominate CSP densification of Alumina-NaCl composite responsible for the observed maximum densification within the first 20 minutes. This according to Coble [392], it is a creep dominated period for pressure assisted sintering. Beyond this it is controlled by the surface mechanisms as shown in Figure 4-15b and corroborated by the densification rate. It shows that at the beginning of the sintering, porosity is high and drives faster densification rate which declines as porosity is annihilated.

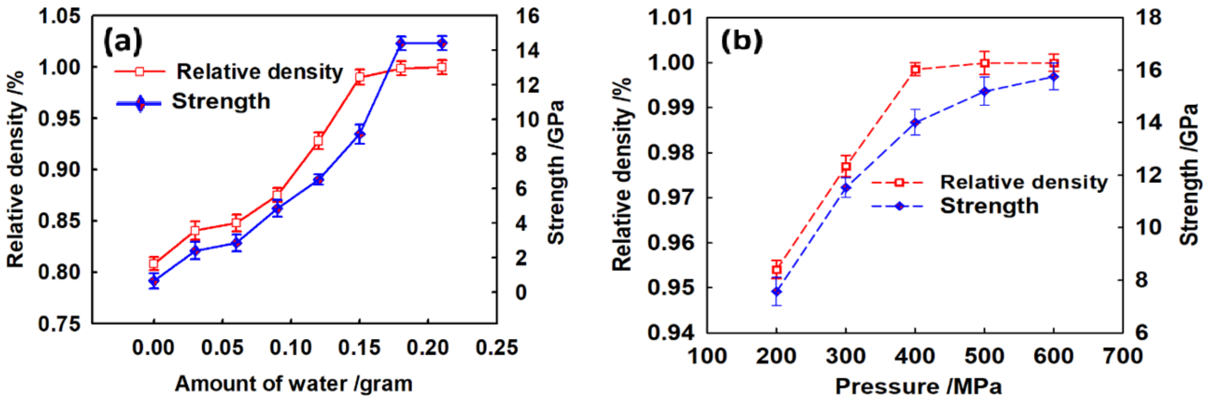

Figure 4-14 Relative density and mechanical strength as a function of (a) amount of water content and (b) applied uniaxial pressure of cold sintered Al_2O_3-NaCl at 250 °C under uniaxial pressure of 400 MPa of cold sintered Al_2O_3-NaCl at 250 °C.

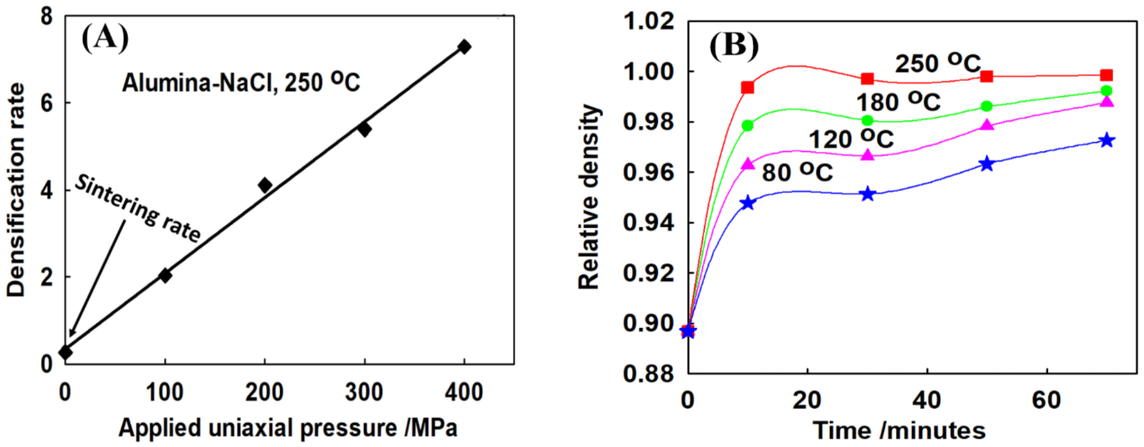

Figure 4-15 (a) Influence of externally applied uniaxial pressure on relative densification rate enhancement for Alumina-NaCl composite (50wt%:50wt%) cold sintered at 250 °C. (b) Relative density as a function of dwelling time for Alumina-NaCl at 400 MPa pressure and four different hold temperatures

The physical observations of the influence of amount of water and applied uniaxial pressure on the composite thermal cycle was carried out. When limited amount of CSP water $\leq$ 25 wt% NaCl was used, no fracture or any form of structural failure was observed during thermal cycle irrespective of CSP temperature, pressure, and dwelling time. Further increase in water content to 30 wt.% limits the applied pressure to maximum of 400MPa beyond which composite fracture failure occurs. Though, further increase in water is possible at low applied pressure but beyond 35 wt.% the powder spills out and cannot be hold in the die. To prevent failure during thermal cycle, the amount of water is regulated and appropriate CSP variables (P, T, and t) are selected to achieve desired toughness. Trade-off between highly strong and ductile composite pellet is required for the salt circulation and expansion during phase change [393].

However, observations made from the initial sintering test, shows that all cold sintered and dry pressed composites dissolves when placed in water. After annealing at 850 °C, cold sintered pellet remain undissolved over time and its stability in water without dissolution increases with increase in the amount of water, processing temperature, pressure, and dwelling time. The appearance of undissolved pellet in water was first observed when cold sintered with ≥ 25 wt.%. It stabilizes and remain fully undissolved when cold sintered with 30 wt.% water in a dehydrated powder under 400 MPa pressure and 250°C. In contrast to the cold sintered, dry pressed composite dissolves in water irrespective of the number of thermal cycles, dwelling time and thermal cycle temperature up to 1300 °C. This shows that dry pressed composite pellets sintered through the salt only by plastic deformation. Also, alumina particles expected to provide structural support were not sintered because key dissolution-precipitation mechanisms at low temperature were not activated in the absence of water. NaCl diffuse in between alumina particles during cold sintering step with water and help the alumina sintering somehow in a liquid phase sintering and thus stabilize the structure at high temperature compared to the samples in which NaCl does not diffuse at the alumina boundary [41, 394]. Figure 4-16 shows fractured SEM images of room temperature dry pressed NaCl (Figure 4-16a-d) and Alumina-NaCl at room temperature (Figure 4-16e-h). It also shows the SEM image of the dehydrated starting powder of NaCl (Figure 4-16i) and alumina particles (Figure 4-16j). Meanwhile, Figure 4-17 shows the fractured SEM images of cold sintered NaCl (Figure 4-17A-D) and Alumina-NaCl at room temperature (Figure 8E-H). At room temperature and under very low uniaxial pressure of 50 MPa, dry pressed NaCl (Figure 4-16A) and alumina-NaCl composite (Figure 4-16E) are characterized by porous and heterogenous microstructure, and the particles arrangement appears like a simple random filling of the preserved original NaCl and alumina particles in Figure 4-16i and j respectively. Meanwhile, cold sintered NaCl (Figure 4-17A) and Alumina-NaCl (Figure 4-17E) at room temperature shows unique and homogenous microstructure with disappearance of original particles and appearance of new grains, grain boundary and few pores on sintered NaCl. This is consistent to the observed relative density in Figure 4-12b and d, respectively. Though, NaCl in the sintered composite precipitate in between alumina particles during cold sintering, but pores appeared between alumina particles at low applied pressure of 50 MPa. This limits its final relative density lower than observed for cold sintered pure NaCl in Figure 4-12b. Further increase in applied pressure to 150 MPa at room temperature enables more particles densification and disappearance of original particles in both dry-pressed NaCl and alumina-NaCl composite. The increase in pressure to 150 MPa triggered dry pressed NaCl final density (Figure4-12c) to be equal to cold-sintered NaCl density (Figure 4-12b) by plastic deformation mechanism. However, cold sintered NaCl microstructure differs significantly to the dry pressed. Cold sintered NaCl grains grow better and well faceted with clear boundaries. Beyond 150 MPa, dry pressed NaCl is further densified, but cold sintered density is limited and maintain a near constant value due to trapped water pores. This agrees well to the earlier findings by Hong et al. [41]. Cold sintered maintained lower density than dry pressed as evident in the observed few larger pores associated with trapped water. When the applied pressure reaches 300MPa at room temperature, original particles of dry pressed NaCl disappeared and well faceted grains and clear boundary appeared with small pores spotted inside the grains as shown in Figure 4-16c and d. Surprisingly, unlike pure NaCl, dry pressed Al_2O_3-NaCl composite density is always less than cold sintered density under all pressures as shown in Figure 4-12d and e. The density evolution is consistent to the observed increase and higher structural densification with increase with pressure from 150 to 400MPa (Figure 4-17b-d). Also, absence of any traceable identity of original particles contribute to higher density of cold sintered than dry pressed. This is attributed to the high structural densification and presence of nor or very few tiny spotted pores under 300 MPa (Figure 4-16g) and 400MPa (Figure 4-16h) pressure. It shows that presence of alumina in the composite has influenced the plastic deformation of the NaCl in the structure.

Generally, influence of the pressure manifest in both cold sintered and dry pressed composite microstructural homogeneity and grain appearances. Cold sintered composite structure appeared more dense, homogenous and its NaCl grain visibility progressively increase with pressure (Figure 4-17E-L). Conclusively, composite densification and structural homogeneity increases with increase in pressure, and cold sintered relative density is higher than dry pressed at all pressures as shown in the density profile in Figure 4-12. Secondly, dry pressed composite sintered through the salt only by pressure induced plastic deformation mechanism of the salt. Thirdly, plastic deformation of the salt significantly contributes to the main CSP dissolution-precipitation mechanism of the cold sintered composite. The presence of water enables NaCl dissolution-precipitation process responsible for pore filling between alumina particles, a process described as low temperature liquid phase sintering. Finally, we speculate that precipitated NaCl enables chemical interaction with alumina responsible for the speculated defect formation during CSP and subsequent sintering at annealing temperatures lower than conventional alumina sintering temperature. It is important to note that choice of appropriate CSP temperature is key and necessary to achieve the desired densification. This is consistent to the observed variation in relative density at 250 ℃ and room temperature in Figure 4-12f and d, respectively.

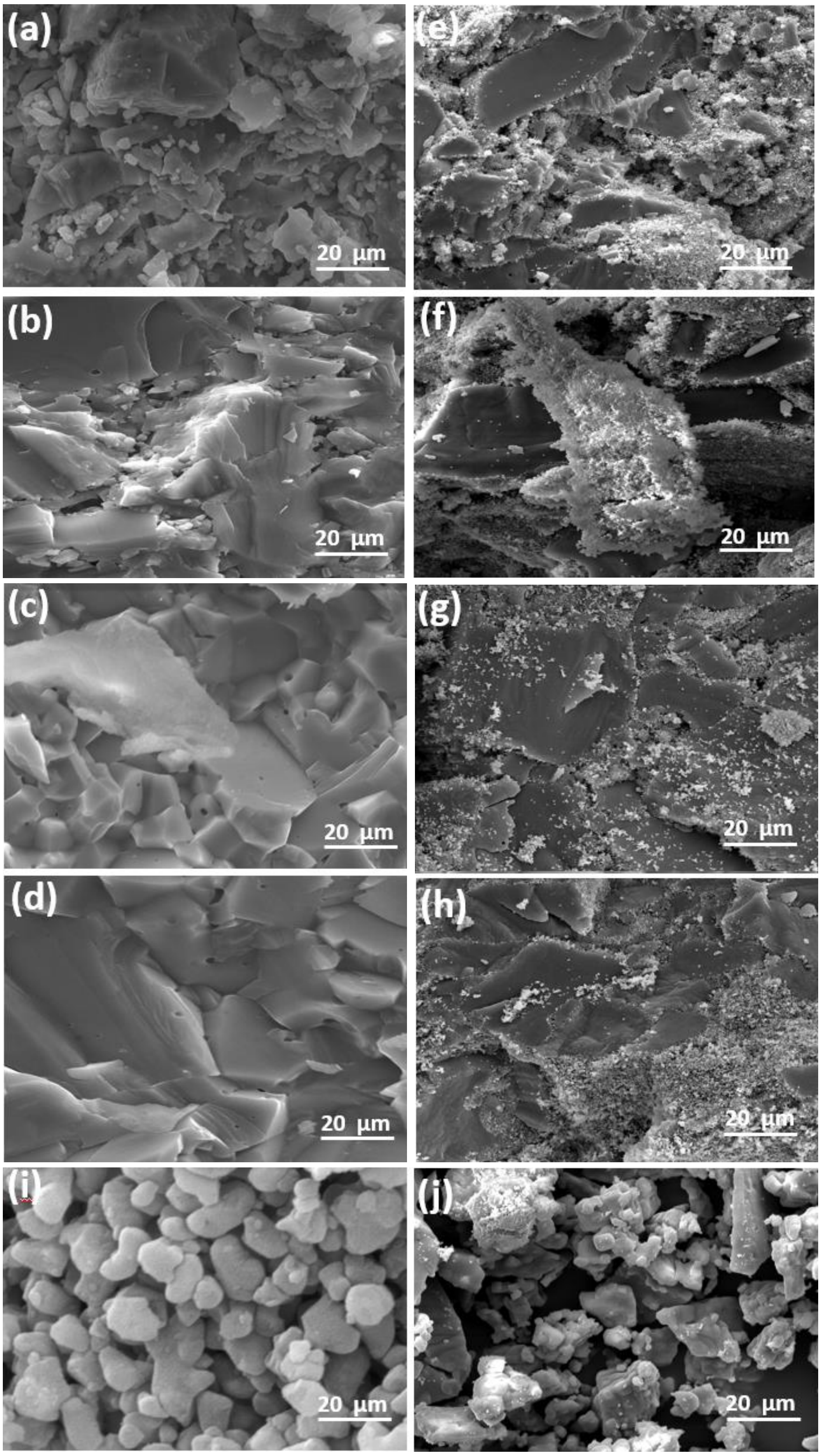

Figure 4-16 SEM images of dry pressed NaCl under uniaxial pressure of **(a)** 50 MPa **(b)** 150 MPa **(c)** 300 MPa **(d)** 400 MPa and Al_2O_3-NaCl composite under uniaxial pressure of **(e)** 50 MPa **(f)** 150 MPa **(g)** 300 MPa and **(h)** 400 MPa and at room temperature. The starting powders are (**i)** NaCl and **(j)** alumina.

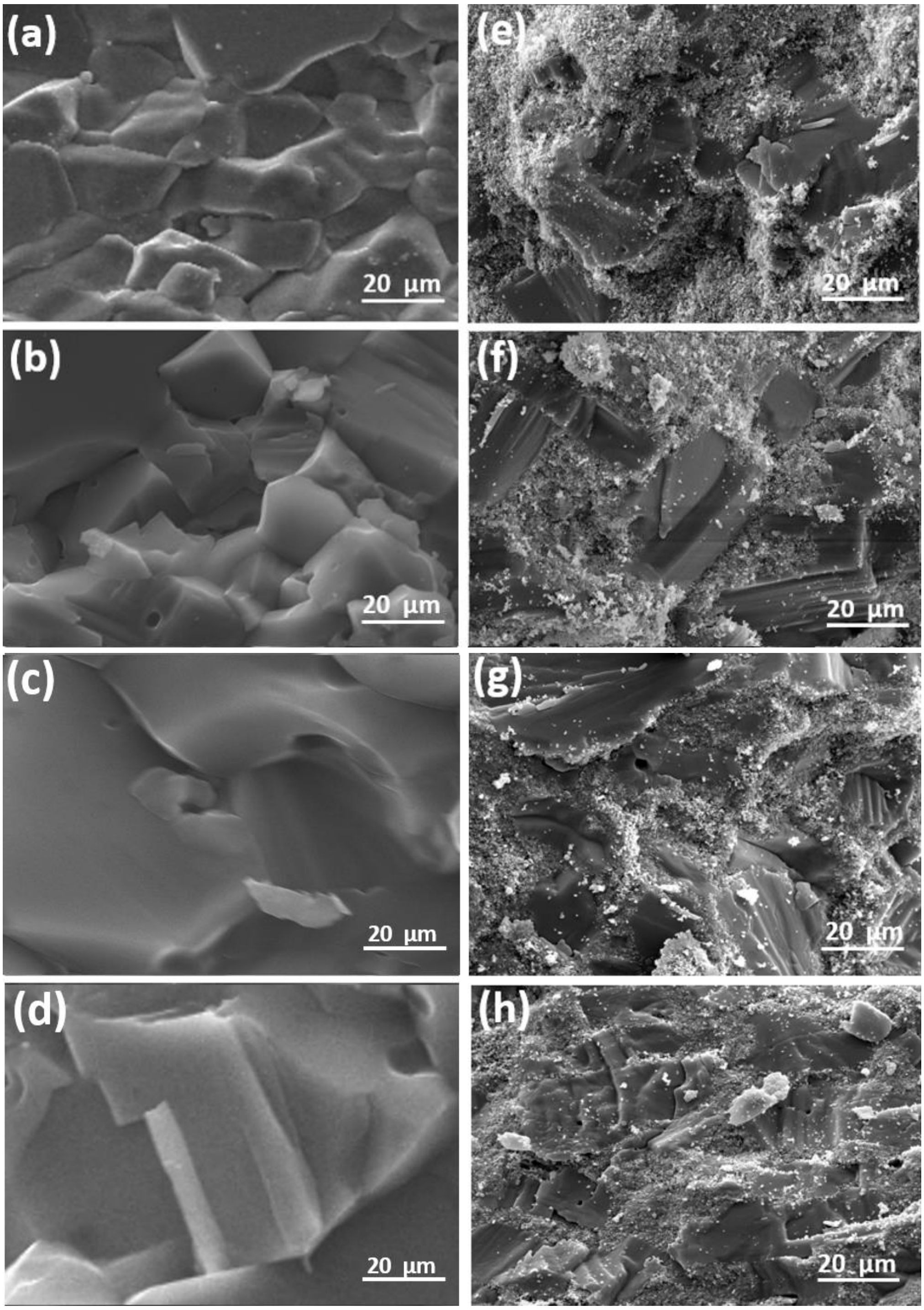

Figure 4-17 SEM images of cold sintered NaCl under uniaxial pressure of **(a)** 50 MPa **(b)** 150 MPa **(c)** 300 MPa **(d)** 400 MPa and cold sintered Alumina-NaCl composite TES material under uniaxial pressure of **(e)** 50 MPa **(f)** 150 MPa **(g)** 300 MPa **(h)** 400 MPa

4.2.2 Influence of temperature and dwelling time on relative density and mechanical strength of cold sintered Al_2O_3-NaCl

Figure 4-18 shows the relative density response of cold sintered Al_2O_3-NaCl under constant pressure of 400MPa as a function of temperature for different dwelling time. The density increases with increase in temperature and dwelling time. The highest increase was observed at CSP temperature of 100°C, a temperature at which the water begins to boil encouraging fast vaporization and escape from the die. This suggest that the densification rate was very fast at the early sintering stage consistent to the reported fast densification of cold sintered $Li_{1.5}Al_{0.5}Ge_{1.5}(PO_4)_3$ [325]. The density progressively increased with both temperature and time. The density approaches its plateau at 220°C for 30- and 50-minutes dwelling time. When the dwelling time was 90-minute, density plateau appeared at 220 °C and maintained constant at 250 °C maximum heater temperature. This shows that temperature promotes fast dissolution-precipitation and lowers the sintering time to achieve higher densification. The situation is observed when the liquid phase solvent completely evaporates without further dissolution and increase in CSP temperature up to 250°C is not adequate to cause diffusion. The density increase is accompanied by corresponding increase in sintered mechanical strength response with increase in CSP temperature as shown in Figure 4-19. It shows that with increase in time and temperature, the mechanical strength increases. In contrast to the density profile, no strength plateau was observed at all temperatures and dwelling time investigated. This suggest that increase in temperature will further cause greater mass transport responsible for enhanced mechanical strength.

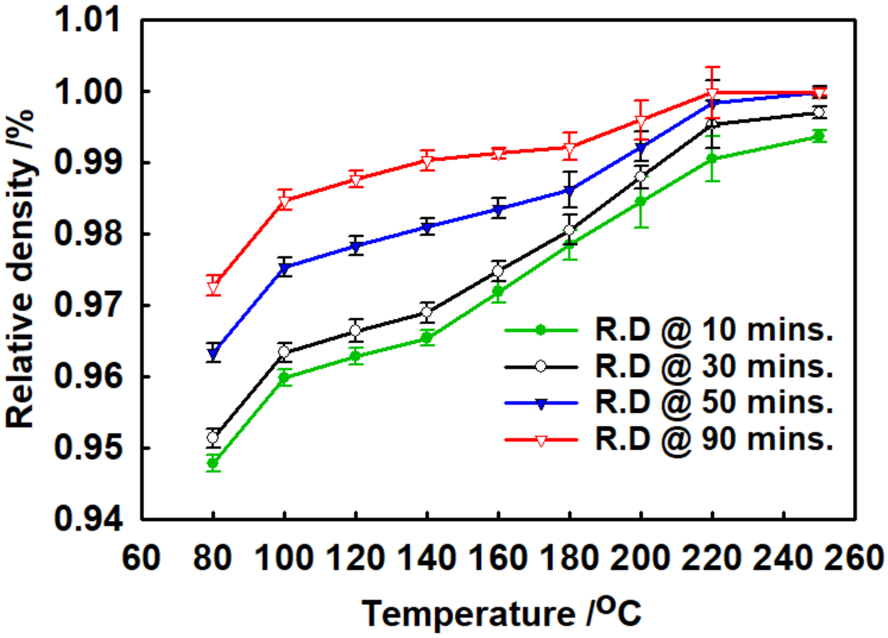

Figure 4-18 Relative density evolution of cold sintered composite Al_2O_3-NaCl with 0.18g water under 400 MPa pressure as a function of temperature at different dwelling time.

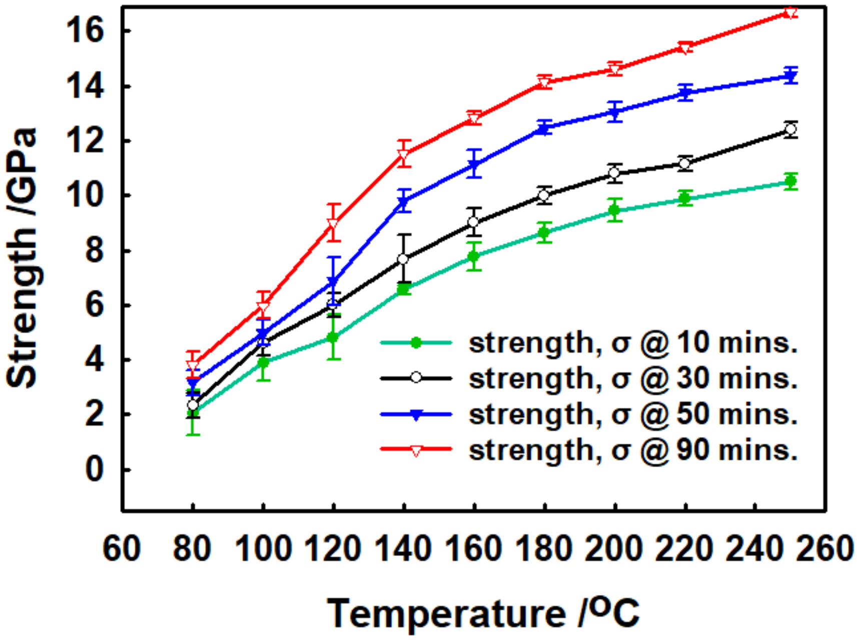

Figure 4-19 Mechanical strength evolution of cold sintered composite Al_2O_3-NaCl with 0.18g water under 400 MPa pressure as a function of temperature at different dwelling time.

4.2.2 Influence of CSP-post annealing on cold sintered Al_2O_3-NaCl composite structure

Fig. 4-20 shows the XRD patterns of the starting powders (dehydrated NaCl and Al_2O_3 powder), as-CSPed Al_2O_3-NaCl composite, and pellets after post-annealing at thermal cycle temperature of 850℃ and 1000℃. All the diffraction peaks of the starting powders can be indexed by NaCl (JCPDS No 5-0628) and α-Al_2O_3 (JCPDS No 00-042-1468), respectively. Both NaCl and α-Al_2O_3 were present in as-CSPed sample. Compared with XRD patterns of the starting powders, all the peaks correspond to the peaks of alumina and NaCl only without appearance of any new specie after cold sintering. Though, it is apparent that the alumina peak intensity around 90 of 2 theta are very weak and completely disappeared due to NaCl background cover. The diffraction peak of CSP post-annealed samples at 1000 ℃ shows that the intensity of NaCl peaks significantly reduced because of volatilization, consistent to previous reported studies [47, 287, 387]. However, it is to note from the XRD that Al_2O_3 and NaCl species co-exist when cold sintered composite was annealed for 30 minutes at temperature up to 1000℃ in different proportions by weight due to NaCl mass loss.

Figure 4-21 shows the surface and fractured surface SEM microstructure of cold sintered and dry pressed Al_2O_3-NaCl composite after annealing at different temperatures. Figure 4-21a and b shows the presence of precipitated NaCl in between Alumina particles after first thermal cycle annealing. The NaCl precipitated just like in cold sintered composite sample. Though, all cold sintered and dry pressed composites dissolve in water but cold sintered remain undissolved for four weeks after first cycle annealing at 850℃. The process of annealing after CSP enables removal of glass phase and second phase at the grain boundary of cold sintered materials. These are particularly observed in cold sintered $BaTiO_3$ [21], Pb(Zr,Ti)O_3 [318] and Mg-doped NASICON ($Na_{3.256}Mg_{0.128}Zr_{1.872}Si_2PO_{12}$) ceramic [385]. Though, only densification via dissolution-precipitation process was achieved at CSP stage and no glass phase or second phase formation was observed from phase and structural analysis. Surprisingly, annealing of cold sintered Al_2O_3-NaCl at temperature between 850-1200°C enables sintering of alumina particles. The annealing temperature of 850°C is far less than Al_2O_3 conventional sintering temperature of ≥ 1600°C [395], suggesting that cold sintering stage has influenced alumina characterises. At high temperature ≥850°C, atomic rearrangement takes place and formed sintered bonds. Figure 4-21c and d shows that further increase in the annealing temperature to 1000°C causes the salt to accumulate during internal circulation at specific locations. In contrast to the precipitated salt in Figure 4-21a and b, the salt was held and encapsulated by the alumina particles as shown by the inset in Figure 4-21c. However, Figure 4-21d shows pores between alumina particles and appearance of few sintering bonds. The pores are due to the migration of the salt to the new locations leaving pore spaces between alumina particles.

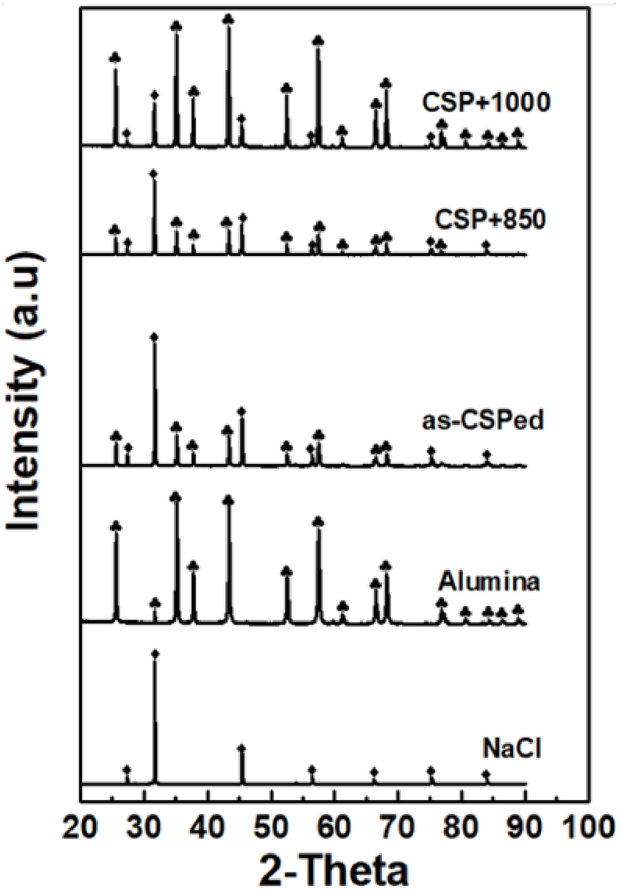

Figure 4-20 XRD patterns of dehydrated starting powders; as-CSPed and CSP-post annealed Al_2O_3 - NaCl composite at 850°C and 1000°C different temperatures.

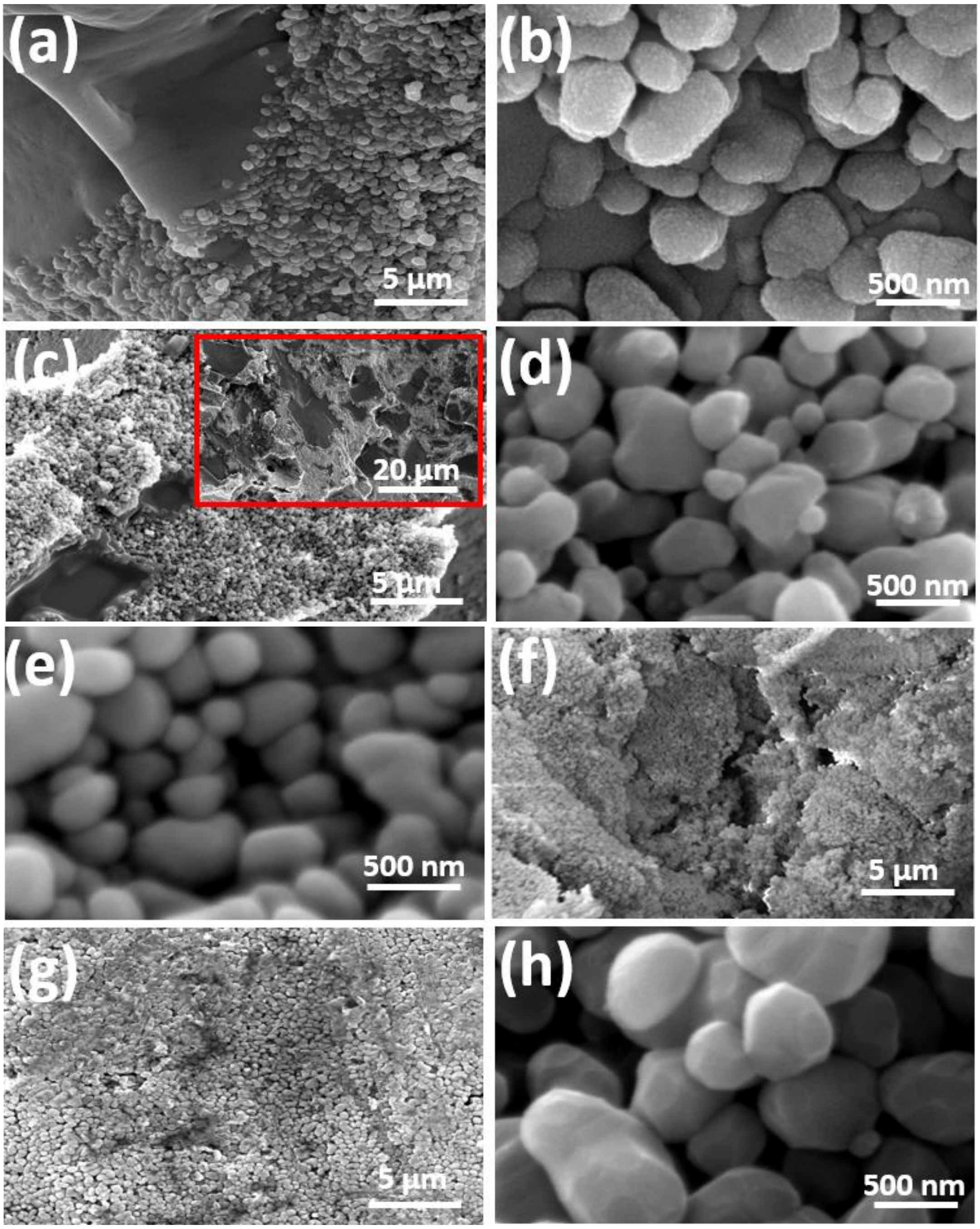

Figure 4-21 Surface and fractured CSPed Al_2O_3-NaCl composite (at 250°C, 400MPa, 90 minutes) annealed at (a -b) 850°C thermal cycles for 1hr (c-d) 1000°C (e-f) 1200°C and annealed dry pressed composite at (g) 1200°C for 30 minutes.

Figure 4-20e shows a porous alumina fractured surface at 1100°C annealing temperatures without appearance of NaCl in between alumina particles. It shows sintered bonds with rounded shape particles present, an indication that some particles were only in contact and not sintered.

At temperature ≥ 1200°C and even higher dwelling time, dry pressed composite structure was weak and destroyed after annealing as shown in Figure 4-20f. It clearly shows that simple shaping of the composite powder and subjecting it to heat will not cause sintering of the alumina particles in the molten salt. It is apparent that insolubility of alumina in water and absence of driving force for shape modification without external pressure present two limitations. First, limited densification and interaction between the composite species in the absence of any of the CSP processing step or conditions. Secondly, pure alumina system in the present of water under all cold sintering conditions will not sinter because of insolubility [396]. This further reaffirm the role of cold sintering process which in the presence of water, NaCl serves as sintering agent and a pore forming agent for the fabrication of porous alumina.

However, surface, and fractured surface SEM images in Figure 4-20g and h show good sintered porous alumina particles structure after annealing of cold sintered composite at 1200 °C. A complete volitization of the salt and a well sintered alumina to alumina bond with neck growth was observed. The absence of any trace of the salt in the SEM microstructure is also consistent to a quantitative measurement of phases present at CSP and CSP-post annealing temperatures in Figure 4-21. Figure 4-21 shows that the composition of alumina and NaCl was 49 and 51 wt% which conform with the initial 50:50 mass composition of alumina and NaCl phases during CSP. At 850 °C, 18 wt% was loss and NaCl was only 38wt%. Further increase in temperature to 1000°C and 1100°C the NaCl reduces to only 14.6 and 8.5 wt% respectively. At temperature of 1200°C, only alumina phase was present with constant zero mass change.

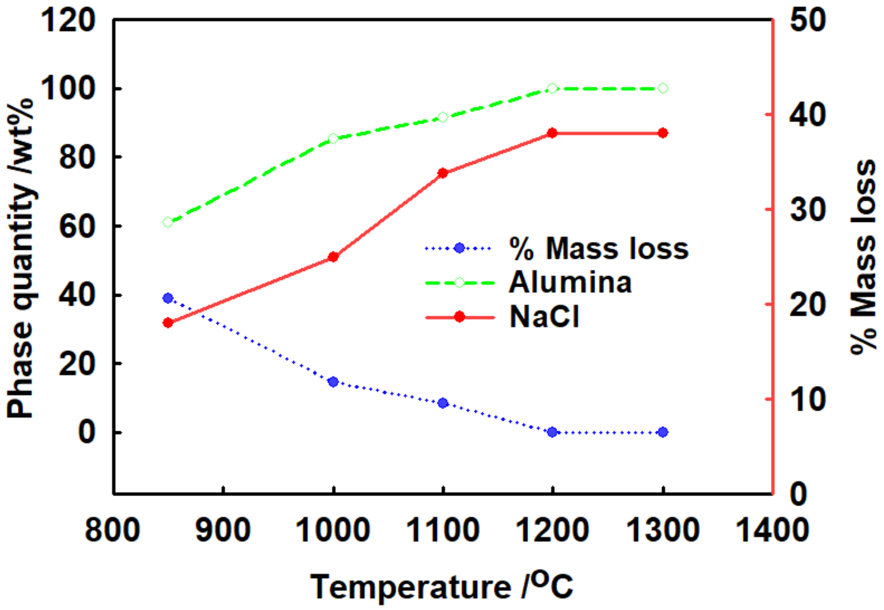

Figure 4-22 Phase content and mass loss of samples at different heat treatment temperatures for 30 minutes

Alumina is strongly hygroscopic, but the raw dry powder TG in Figure 4-23 shows little or no residual water present in it. Therefore, the mass loss observed in Figure 4-22 is largely due to the NaCl volitization and small losses of the starting materials during sample preparation and processing at CSP stage. The constant mass change observed in the TG analysis of the raw alumina sample differs significantly to the 14 wt% loss linked to the boehmite dehydration reported by [397] at temperature between 400 - 1200 °C. In a related study by Induja and Sebastian [287], prior to 790 °C moisture escape was observed, and beyond this the weight loss is associated to the NaCl decomposition. The alumina thermal behaviour reported by the authors significantly differs from the observed constant mass change in this study associated with boehmite dehydration by Induja and Sebastian [287].

4.3 Summary

It is apparent that cold sintering of composite Al_2O_3-NaCl and its CSP-post annealing between 800 to 1100°C could not produce a sintered alumina structural scaffolding to support the NaCl salt for a repeated thermal cycle at 850 °C. More so, the composite is characterized by high volatilization of the salt which increases with increase in temperature starting from the NaCl melting point of 801°C. The high densification at cold sintering stage and interaction of alumina with NaCl enables sintering of the alumina particles at 1200°C lower than its conventional sintering but NaCl volatizes to form an alumina porous structure. Thus, this provides a new fabrication route of porous ceramic support for possible infiltration of salts to produce a high temperature composite thermal storage material with requisite mechanical properties to withstand repeated high thermal cycles.

CHAPTER FIVE

MICROSTRUCTURE AND MECHANICAL PROPERTIES OF COLD SINTERED POROUS ALUMINA CERAMICS

5.1 Introduction

Cold sintering process at ≤250 °C only enables fabrication of a very dense composite Al_2O_3-NaCl near its theoretical density by dissolution-precipitation process. CSP-post annealing of the composite activates alumina sintering from 850°C but NaCl continue to volatilize up to 1000°C limiting the process potential to fabricate the required shape stabilized composite materials for thermal energy storage. Porous materials have been reported as potential materials for the encapsulation of PCMs by vacuum impregnation method. This chapter presents the effects of CSP and post-annealing temperature on microstructure and mechanical properties of a porous alumina fabricated using an innovative CSP process at low temperature and subsequent CSP-post annealing at 1200°C lower than conventional alumina sintering temperature.

5.2 Results and discussion

5.2.1 Phase and microstructural characterization

Figure 5-1 shows the XRD patterns of the starting powders (dehydrated NaCl and Al_2O_3 powder), as-CSPed Al_2O_3-NaCl composite, and pellets after post-annealing at different temperatures. All the diffraction peaks of the starting powders can be indexed by NaCl (JCPDS No 5-0628) and α-Al_2O_3 (JCPDS No 00-042-1468), respectively. Both NaCl and α-Al_2O_3 were present in as-CSPed sample. The highest diffraction peak was from NaCl, which suggests its high-volume fraction within as-CSPed Al_2O_3-NaCl composite. Compared with XRD patterns of the starting powders, all the peaks correspond to the peaks of alumina and NaCl only without appearance of any new specie after cold sintering. Though, it is apparent that the peak intensity of both species decreases after CSP and at higher 2θ around 80-90, alumina peaks completely disappeared due to NaCl background cover. The diffraction peak of CSP post-annealed samples at 1100 ℃ shows that the intensity of NaCl peaks markedly reduced to a large extent due to volatilization. Similarly, at 1200°C only Al_2O_3 was present after annealing. The intensity of diffraction peaks of α-Al_2O_3 greatly increased at higher temperatures after NaCl volitization and slightly becomes sharper, suggesting better Al_2O_3 particles crystallization. The gradual disappearance of NaCl phase with increasing post-annealing temperature can be attributed to NaCl volitization at temperature higher than its melting point (801 ℃) which is consistent with the previous studies [47, 287, 387].

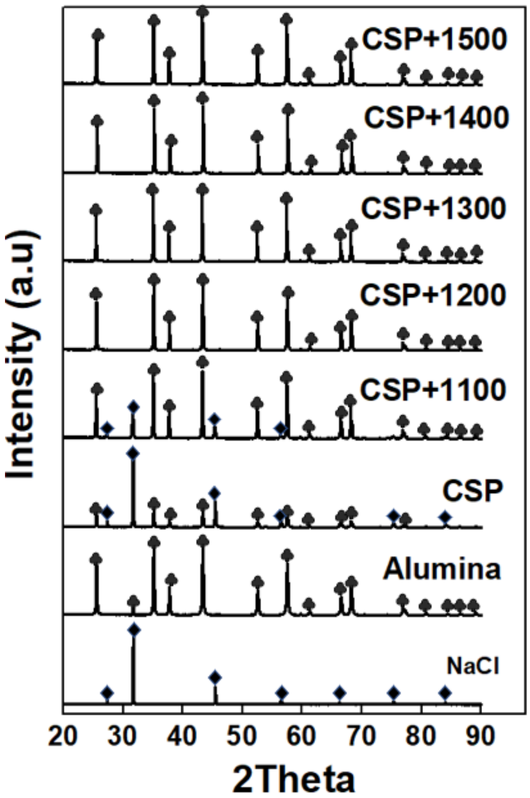

Figure 5-1 XRD patterns of dehydrated starting powders; as-CSPed and CSP-post annealed Al_2O_3 - NaCl composite at different temperatures

Figure 5-2 shows the bulk density evolution as a function of CSP and post-annealing temperature. Both Al_2O_3 and NaCl were present in the as-CSPed sample, and the bulk density of sample is 2.92 g/cm^3. After the sample was post-annealed at 1100 °C for 30 minutes, most of the NaCl was lost due to volitization. This is responsible for the observed drop in the bulk density to 1.96 g/cm^3. When annealing temperature is further increased to 1200 °C, NaCl was absent completely and the density increased up to 2.04 g/cm^3 due to bulk volume shrink. With further increase in the annealing temperature from 1300°C to 1500 °C, the bulk density increases from 2.34 to 2.85g/cm^3.

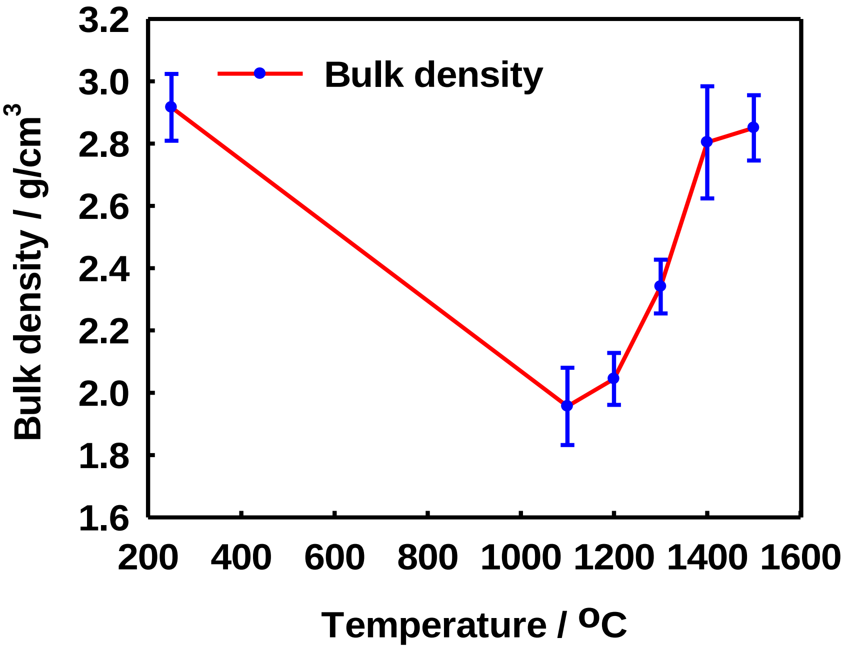

Figure 5-2 Bulk density evolution of samples as a function of CSP temperature (250 °C) and post annealing temperature.

The microstructure of as-CSPed and post-annealed samples were studied by observing their fractured surface via SEM, as shown in Figure 5-3. Figure 5-3a shows that small Al_2O_3 particles were uniformly separated by coarse NaCl precipitates in as-CSPed sample. This is contrary to the dry pressed composite morphology in Figure 5-3b which shows a clear boundary without NaCl precipitation between Alumina particles, sintering through the NaCl only by plastic deformation, a mechanism reported for dry pressed NaCl cold densification in recent studies [41, 67]. Figure 5-3c and d show the sample morphology changes as a function of post-annealing temperature. After as-CSPed sample was post-annealed at 1100 °C (Figure 5-3c), the content of NaCl reduced significantly due to the volitization during annealing. Further increase in annealing temperature of the as-CSPed sample to 1200°C, a complete porous structure was formed, as shown in Figure 5-3d. The formation of porous Al_2O_3 can be attributed to both low degree of densification of Al_2O_3 and greater surface volitization associated with chloride salts at high temperature [398]. According to Kubaschewski [399], the volatilization of NaCl is evident at temperature above 804°C because of its high vapour pressure of 66.69 kPa at 800°C. This is consistent with the XRD patterns in Figure 5-1, which shows that the intensity of NaCl peaks decreases after the sample was post-annealed at 1100 °C. From Figure 5-3d, the round grains with uniform size distribution and limited neck formation can also be observed. Figure 5-3e-g shows that the microstructure with increase in annealing temperature from 1300 °C to 1500 °C. The obvious neck connection between Al_2O_3 grains was visible after the sample was post-annealed at 1300 °C with an average grain size of 0.68 μm. With further increasing post-annealing temperature from 1400 °C to 1500 °C, the grain coarsening occurred, and the porosity reduced dramatically. Figure 5-3h shows the grain size variation as a function of post-annealing temperature. The grain size increased from 0.5 μm to 5.7 μm when the post-annealing temperature increased from 1200 °C to 1500 °C.

To accurately characterise the spatial distribution of polycrystalline grains and pores, 3D–tomography images of samples are constructed using XRT technology. Figure 5-4 shows the XRT images of as-CSPed Al_2O_3-NaCl sample and the samples post-annealed at different temperatures. Figure 5-4a shows a relatively dense microstructure with small pores in as-CSPed sample. The as-CSPed dense samples are also characterized by the appearance of few, and uniformly distributed pores represented by the tiny black spots presumed to be in a nano scale. This suggests uniform distribution of NaCl within as-CSPed Al_2O_3-NaCl sample.

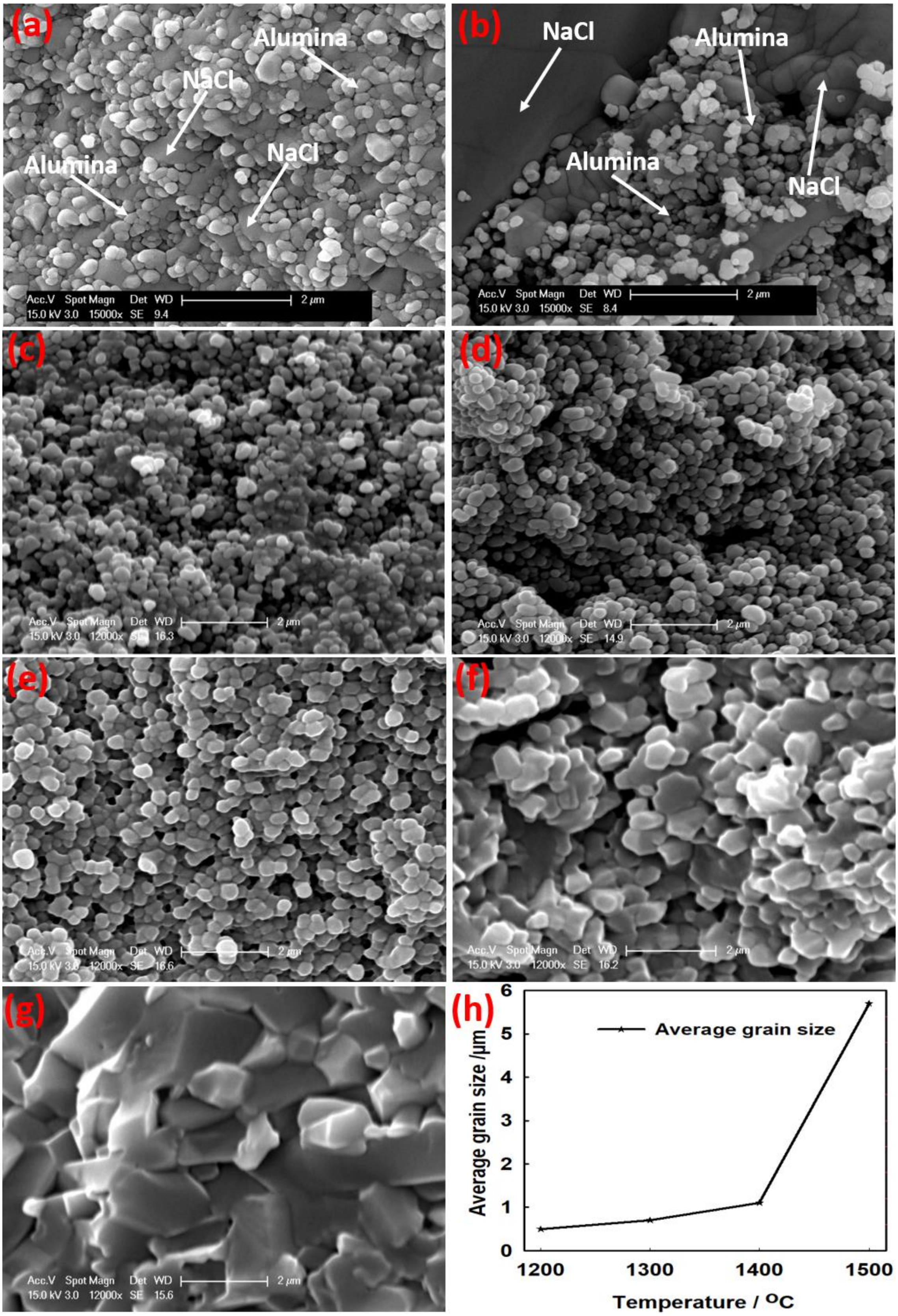

Figure 5-3 SEM micrographs of fractured sample surface of Alumina-NaCl: (a) As-CSPed; (b) Dry-pressed; and annealed samples at 1100 ℃ (c); 1200 ℃ (d); 1300 ℃ (e); 1400 ℃ (f); 1500℃ (g); and their corresponding average grain size distribution (h).

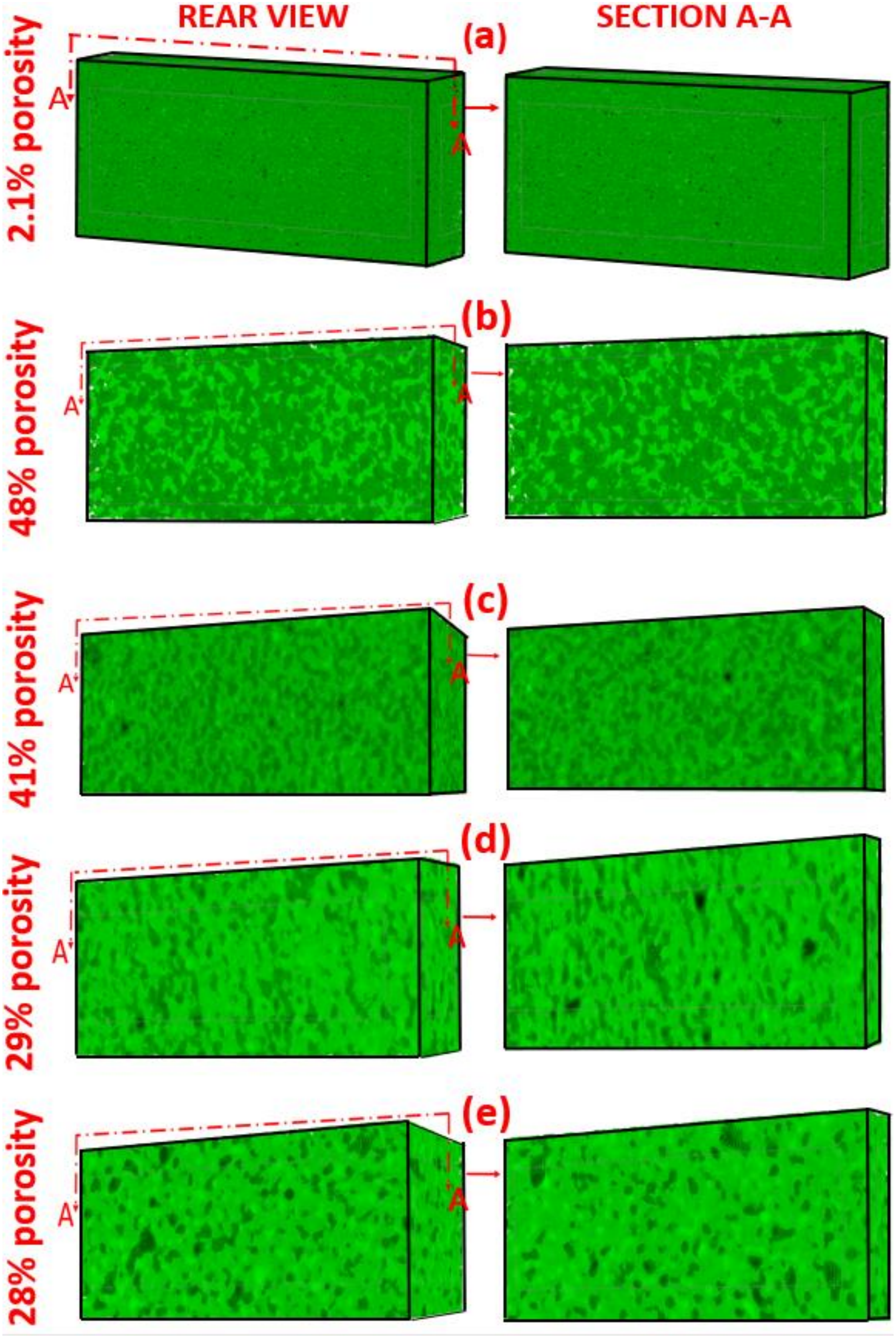

Figure 5-4 XRT 3D-images of (a) as-CSPed sample and the samples after post-annealing at temperature of 1200 °C (b); 1300 °C (c); 1400°C (d); and 1500°C (e).

Figure 5-4b-e show both the rear view and a cross section of the XRT 3D images to provide details on pore size changes at different annealing temperatures. The porosity increased up to 48% after the sample was post-annealed at 1200 ℃ as shown in Figure 5-4b, because of NaCl volitization and poor densification of Al_2O_3 ceramics. The porosity then decreased with the increasing post-annealing temperature from 1300 ℃ to 1500 ℃, as shown in Figure 5-4c-e, which is in good agreement with SEM observation. After annealing at 1200 ℃, complete salt volitization was observed, creating more pores (black holes) and greater interconnectivity between the pores with maximum average porosity of 48%, as shown in Figure 5-4b. Figure5-4c shows that the porosity decreases to 41% with increase in annealing temperature to 1300℃. This is evident by the decrease size and connectivity of the pores because of pores coalescence and closure resulting from alumina particles sintering. Further increase in annealing temperature to 1400 ℃ and 1500 ℃ enhances more alumina sintering and grain growth, closing more to few small size and less interconnected pores. However, the pore sizes from the XRT images at temperature of 1400 and 1500 ℃ are not much different, which is consistent to the measured average porosity of 29 and 28% respectively.

The specific surface area of the porous alumina measured according to the BET method and summarised in Table 5-1. The highest specific surface area of 4.2684 m^2/g was observed for 1200 ℃ with corresponding average pore size of 15.04 nm. The surface area and average pore size diameter decreased with temperature to 0.1903 m^2/g and 8.5nm at 1500 ℃. The nitrogen adsorption-desorption isotherms of porous alumina fabricated by CSP-post annealing at 1200 ℃, 1300℃, 1400℃, and 1500℃ are shown in Figure 5-5. With reference to the IUPAC isotherms classification, the porous alumina isotherms at temperatures between 1200-1400 ℃ are consistent to the type IV, exhibiting mesoporous nature that varies with annealing temperature [400]. The initial characteristic feature of the type IV isotherms is monolayer formation followed by multilayer adsorption and pore condensation. The micropore filling mechanism clearly appeared in the 1200°C isotherms at low relative pressure [401]. This shows presence of micropores at 1200°C beyond which mesopores and macropores dominate the porous structure as it sintered. At 1400°C - 1500 °C it appears more consistent to the type II isotherm characteristic for macropores and non-porous materials.

Table 5-1 Comparison of pore texture data obtained from different temperatures

CSP-post annealing Temperature (^{O}C)	Specific surface area (m^2/g)	Average pore size (nm)	Pore volume (cm^3/g)
1500	0.1903	8.50	0.0001
1400	1.0093	12.43	0.0006
1300	1.4255	13.04	0.0008
1200	4.2684	15.04	0.0024

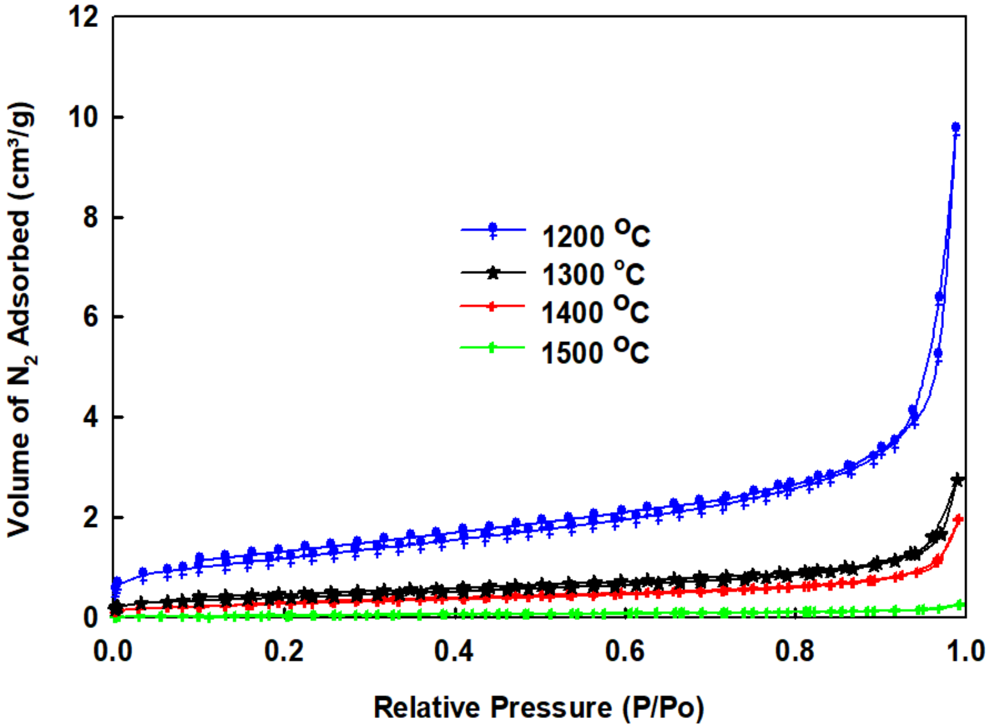

Figure 5-5 BET pore size distribution of porous alumina fabricated at 1200 ^{O}C, 1300 ^{O}C, 1400 ^{O}C and 1500 ^{O}C.

The porous alumina isotherms exhibit similar patterns and shapes. It shows presence of hysteresis loop of type H3 decreasing in size with temperature to near no hysteresis at 1500 °C. Thus, it is an indication of a complex pore structure [402]. The size (width) of the hysteresis loop is quite small, signifying limited pore condensation. The H3 nature of the material shows that the microstructure comprises of aggregates of plate like particles, responsible for slit-shaped pores [400, 402]. It has no saturation adsorption platform which shows that the pore distribution is irregular. Generally, the hysteresis loops close similarity to both type H3 and H4 hysteresis indicates that it is a mixture of micropores, mesopores and macropores alumina. The micropores and mesopores are more between 1200°C - 1300 °C. No hysteresis loop was observed in the isotherm of 1500 °C porous alumina sample. Thus, increase in annealing temperature influences closure of all micropores and mesopores, leaving majorly macropores of a dense non-porous structure. The lower part of the loop represents the incremental N_2 gas in take, and the upper part shows incremental withdrawal of the gas. Though, gas initial uptake is low, indicating that the pores are not filled with the condensate.

The major uptake observed is at higher relative pressure in the range (P/P^O) 0.8-0.99. This phenomenon supported the filling of mesopores in the 1200°C and 1300 °C annealed samples. Though, hysteresis starts at very low relative pressure $< P/P^O = 0.38$ supporting micropores filling. Figure 5-6 shows the BJH based pore size distribution plot with the aid of the adsorption part of the isotherm. The pore distribution shows that the micropores and mesopores are eliminated and larger macro pores sizes continue to decrease towards meso size as it gradually closes with increase in annealing temperature. The pore distribution curve of porous alumina fabricated at 1200 °C exhibit unimodal distribution with a pore diameter in the mesoporous range as shown in Figure 5-6. However, analysis of the entire pore distribution data range shows average pore size of around 15.04 nm of the porous alumina at 1200°C. Further increase in temperature results into a broad distribution, decrease porosity and closure of macro to meso pores which dominates the structure.

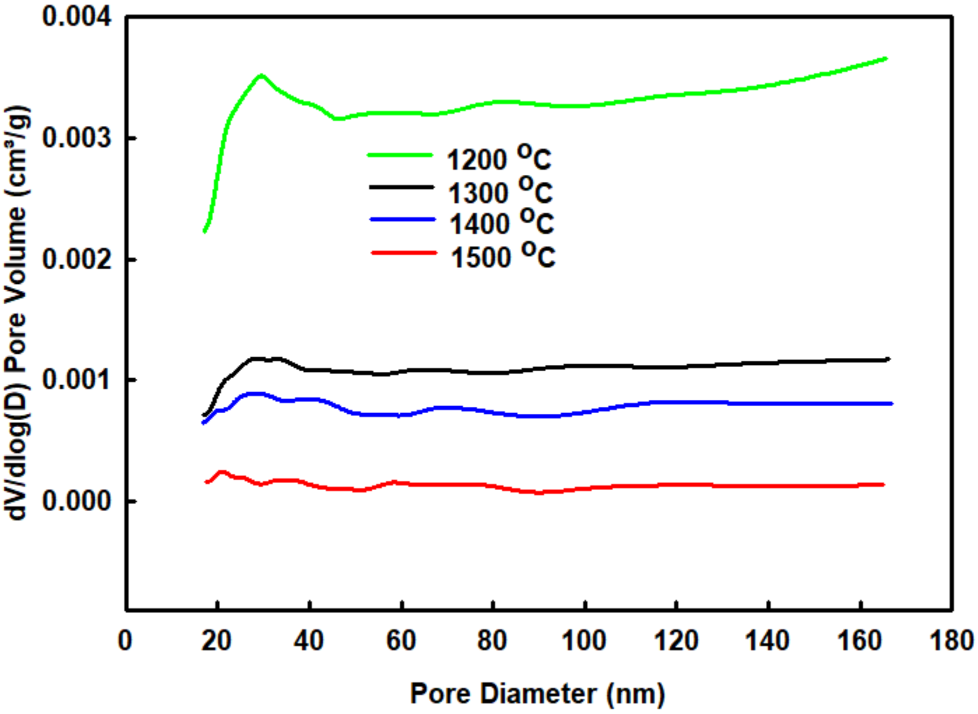

Figure 5-6 Pore size distribution curve of porous alumina fabricated at 1200 ^{O}C, 1300 ^{O}C, 1400 ^{O}C and 1500 ^{O}C.

5.2.2 mechanical properties of post-annealed Al_2O_3

To study the effect of post-annealing on mechanical properties of Al_2O_3, only the samples after post-annealing at temperature of 1200 °C and above were considered due to their NaCl-free structure. The crushing strength, hardness, and porosity as a function of post-annealing temperature between 1200 to 1500 °C were presented in Figure 5-7. It showed that with increasing post-annealing temperature, both tensile strength and hardness greatly increased.

The Weibull statistical analysis distribution plots of the Brazilian test of Al_2O_3 ceramic after post-annealing at temperatures from 1200 to 1500 °C were presented in Figure 5-8. Meanwhile, Table 5-2 showed the Weibull statistical analysis parameters of Al_2O_3 obtained from the Brazilian test method namely, the characteristic strength (σ_0) and Weibull modulus (m). The highest m value of 15.93 was obtained at post-annealing temperature of 1400 °C followed by 12.35, 12.36 and 9.64 at 1300 °C, 1500 °C and 1200 °C, respectively.

Table 5-2. Weibull parameters, porosity, and mechanical strength of the porous alumina

Temperature (°C)	Number samples	Total Porosity (vol%)	strength $\boldsymbol{\sigma_t}$(MPa)	Modulus (m)	Effective strength $\boldsymbol{\sigma_0}$ (MPa)
1200	30	0.48	17.63	9.64	19.36
1300	30	0.41	36.57	12.35	38.13
1400	30	0.29	111.47	15.93	114.67
1500	30	0.28	137.21	12.36	141.17

The results indicated that the empty pore spaces accommodating stress concentration was responsible for the cumulative reduction in the effective surface area of load application [397]. A model developed by Gibson and Ashby in below Equation 5-1 used in previous porous alumina study [397] relating porosity P to the mechanical strength, has been used in this study to model the strength data as a function of the porosity of the porous alumina.

$$\boldsymbol{\frac{\sigma}{\sigma_f} = c\left(\frac{\rho_b}{\rho_t}\right)^n} \tag{5-1}$$

where σ_f is the modulus of rupture of the solid skeleton from which the porous material is made, ρ_t is the theoretical density, ρ_b is the bulk density, c is a geometrical dimensionless constant, and the exponent n is 1.5 and 1 – 1.5 for an open cell and closed cell structure, respectively.

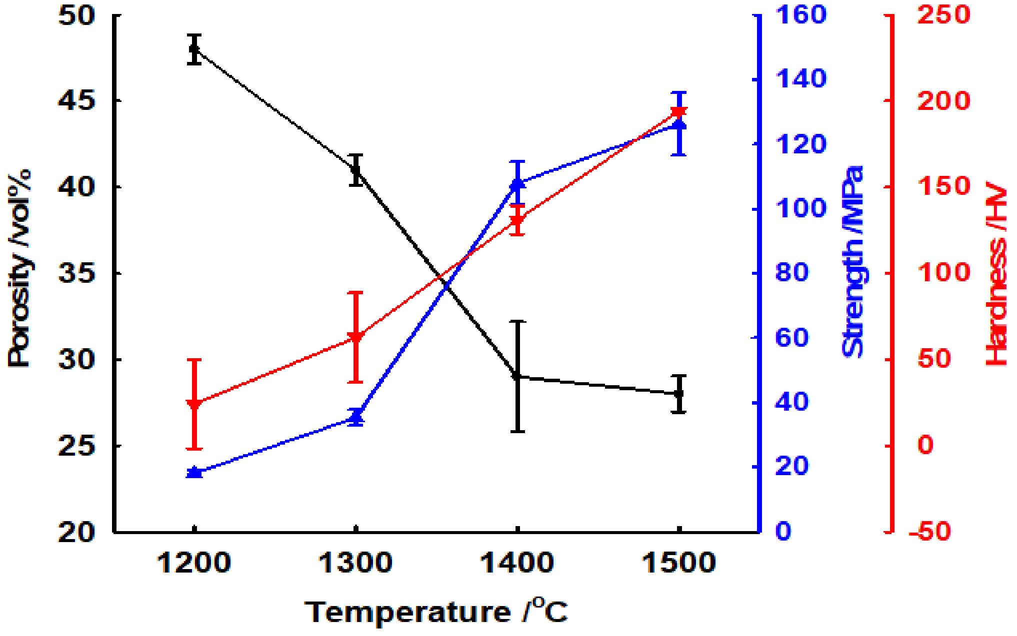

Figure 5-7 Porosity, tensile strength, and hardness as function of cold sintered Alumina-NaCl (3:2) composite post CSP-annealing temperature

The linear fitting of the strength and relative density data obtained in this study into Equation 5-1 using excel regression tool box is shown in Figure 5-8, which gives n = 5.998, c = 1.42 and R^2= 0.996 at flexural strength σ_f value of 400 MPa reported by Alzukaimi and Jabrah [397] for the porous alumina. The model fitting parameters n, c and R obtained in this work are and near two times higher than reported in literature [397]. The exponent n value of 5.998 is higher than the extreme range of closed cell characteristics of 1 – 1.5 but more closer to n = 1.5 that describes the minimum characteristics of an open cell based on the GA model as reported in literature [397]. It is also higher than 1-3 reported in some literatures [403-405]. Thus, it generally exceeded GA theoretical limits which has been linked to non-uniform loading responsible for inhomogenous microstructure, presence of un-accounted pore distribution by the model, and intrinsic brittleness of ceramics responsible for defects during loading . The major cause is due to random mixture of both close and open cells. This manifest as discrepancy between the theoretical and experimental values [404].The presence of holes and windows in the pore walls connecting different pores add to this variation [404, 405].

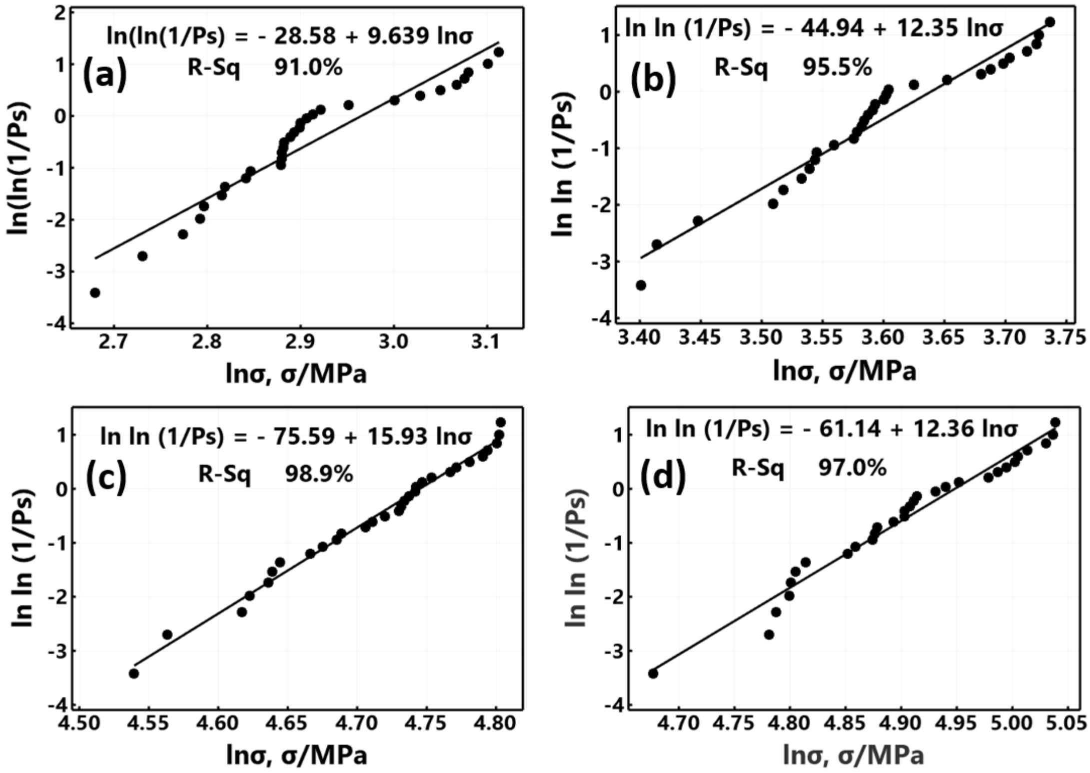

Figure 5-8 Weibull distribution plots of the Brazilian test data for sample post-annealed at various temperatures: (a) 1200 °C; (b) 1300 °C; (c) 1400 °C; (d) 1500 °C

This means the porous alumina fabricated is characterized by an open cell porosity with the exponent value of 5.998. This is further confirmed by the the interconnectivity of the pores in SEM and XRT images in Figure 5-3 and 5-4 respectively. This eliminates doubts about the possibility of closed cells to behave like open cells as observed commonly in man made foams particularly those made using liquid phase [406]. In order to further validate the result obtained from the GA model, a similar approach used and reported by Azukaimi and Jabrah from literature [407, 408] was empolyed in this study. The splitting strength obtained from Brazilian test of the prepared porous alumina in this study as a function of its porosity and the corresponding compressive strength predicted from GA model for both open (n=1.5, c= 0.2) and closed (n=1, c=1) porous alumina ceramic structure using similar porosity are compared as presented in Figure 5-9. It is important to note that the strength data used in the Gibson and Ashby (GA) model was obtained for the tensile strength indirectly measured using Brazilian test method but not a compressive strength data involved in the GA model that use fracture mechanics analysis to predict cellular structure tensile strength according to Equation 5-2.

$$\frac{\boldsymbol{\sigma}}{\boldsymbol{\sigma_f}} = \boldsymbol{c'}\sqrt{\frac{\boldsymbol{L}}{\boldsymbol{a}}}\left(\frac{\rho_b}{\rho_t}\right)^{\mathbf{1.5}} \tag{5-2}$$

where L is the foam cell size, $\boldsymbol{c'}$ is a geometric constant and $\boldsymbol{a}$ is the macroscopic (or critical) flaw size subject to $L \leq a,$ with $L = a$ when the foam is flaw-free or intact. The factors c and c' were reported approximately the same value c = $c' = 0.2$ [407, 409, 410] suggesting that for an open foam that is intact compressive strength is equivalent to the tensile strength. Thus, the experimental tensile strength obtained in this study is comparable to the theoretical compressive strength obtained using the GA model as only slight differences in the strength exists at different relative densities for an open porous structured material shown in Figure 5-9. Therefore, the engineered porous alumina structure fabricated via combined cold sintering- post annealing is quite intact, and its characteristics are that of the open pore structure. Though, according to [397], the theoretical basis of GA relies on a model that assumes a uniform cellular structure characterized by uniform and definite size of cell. It is apparent from the SEM images in Figure 5-3 that the porous structured alumina fabricated in this study do not have a well-defined cellular structure but are characterized by interconnected pores. Hence, the fabricated structure is complex, making it extremely difficult to fully explain the result with the aid of cellular ceramics GA model. Hence, speculated to be responsible for the large, calculated exponent *n* value of 5.998. However, the tensile strength values obtained compares well with the theoretical compressive strength anticipated from the GA model. This is largely in conformity with the findings reported in a recent related study [397] and concluded based on reported studies [410, 411] that the tensile streangth is always less than compressive strength by at least one order of magnitude.

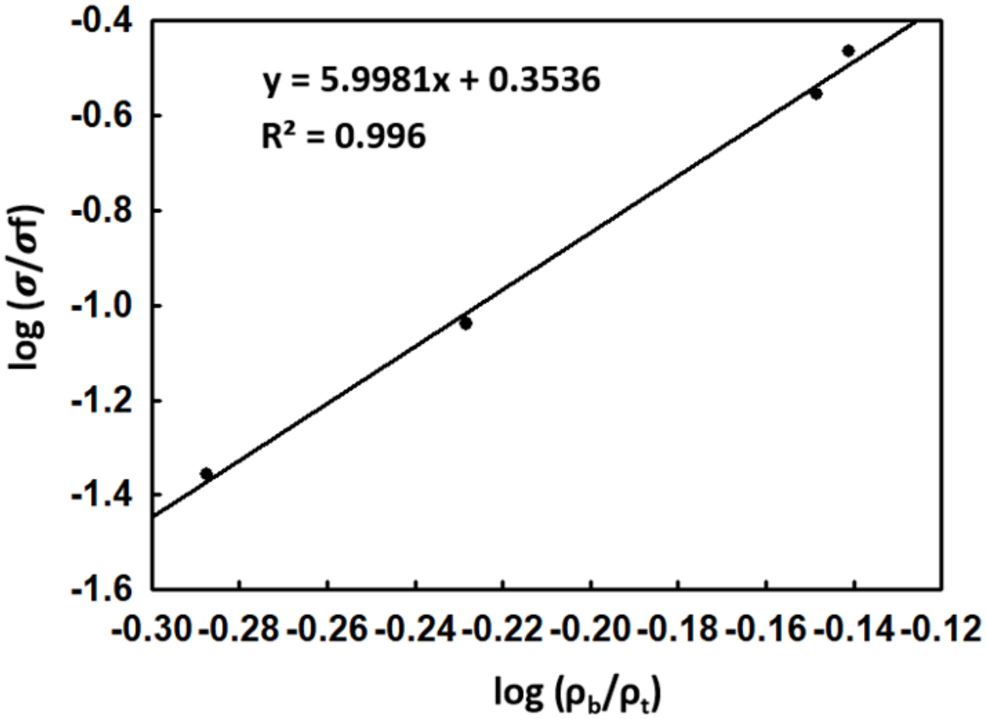

Figure 5-9 Splitting tensile strength of porous alumina fitted with Gibson and Ashby model

The use of minimum solid area models to account for porous structured materials properties such as the mechanical properties (strength and hardness) dependence on porosity have been reported in various studies and more recently in the fabrication of porous alumina ceramics [397, 412]. This model describes an exponential function (e^{-bP}) relating porosity and property of porous material. It was proposed on the basis that porous structures are made of two idealized identitical features: (1) spherical particles partially bonded; and (2) spherical pores embedded in a solid matrix; or both [413]. The relationship gives good approximation of all developed minimum solid area models for various structures which are characterized by the b values obtained. In addition to strength and elastic modulus, the exponential relation was recently extended to mechanical property hardness of a porous structure of alumina multilayers by [412]. The exponential function is as shown in Equation 5-3.

$$y = y_0 e^{-bP} \tag{5-3}$$

where P is the porosity, y and y_0 are the corresponding porous structure mechanical properties at porosity P and $P = 0$, respectively, and b is an emperical costant describing a porous structure characteristics parking (b=5 the structure is acubic stacking of solid spheres, b= 3 is a cubic stacking of spherical pores, and b= 9 is a rhombohedral stacking of solid spheres) obtained as a slope of the function on a semi-log plot. In this study, fitting of the minimum surface area (MSA) model in Equation 5-3 on semi-log plot with tensile strength and hardness data obtained using brazillian and vickers hardness test methods gives b = 9.579, R^2 = 0.99 for mechanical strength at $\sigma_0 = 220$ MPa [397] and b = 9.288, R^2 = 0.96 for hardness at an assume $H_0 =$ 250 HV as presented in Figure 5-11 and Figure 5-12, respectively. The two properties fitting gives close stacking characteristics within the range of 9 for rhombohedral solid spheres with R value > 0.9 in each case.

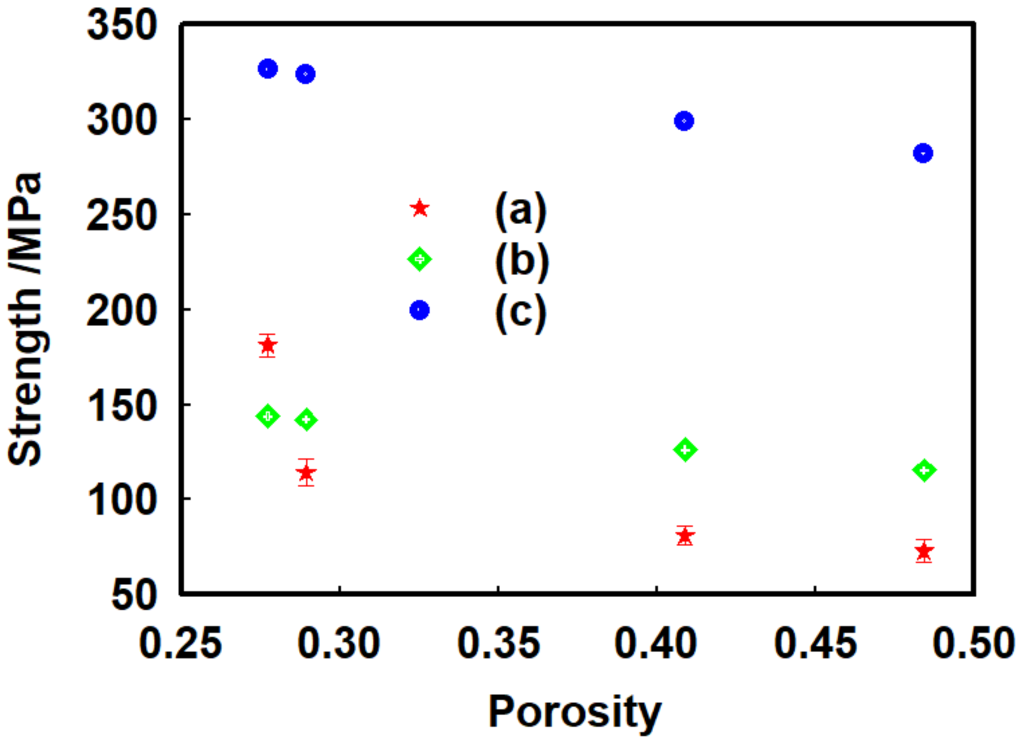

Figure 5-10 (a) The splitting tensile strength of the porous alumina fabricated via CSP - post-annealing process as a function of their porosity; (b) theoretical compressive strength predicted using GA model for open porous ceramic (c) theoretical compressive strength predicted using GA model for close porous ceramics evaluated at the same experimental porosity values.

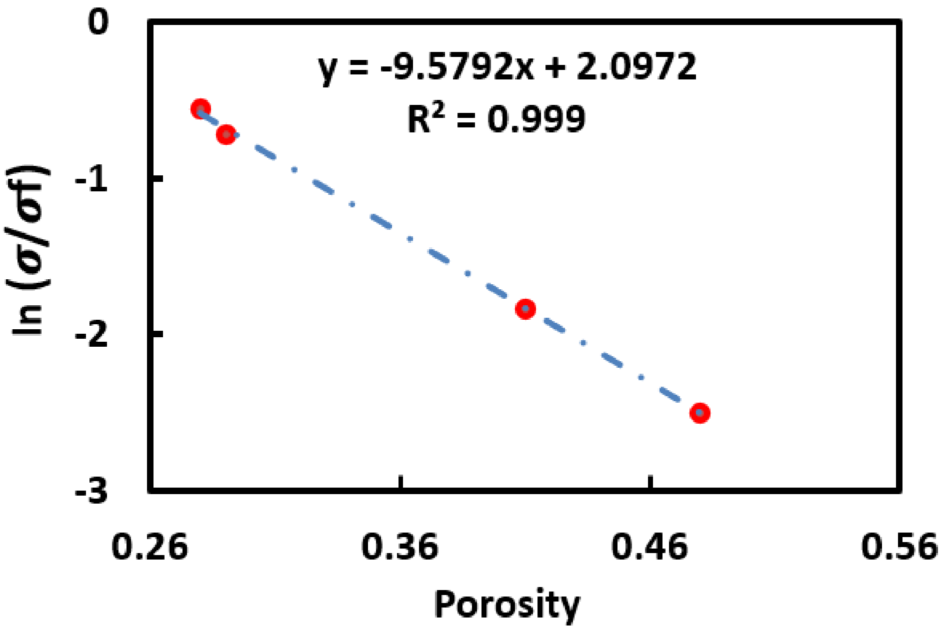

Figure 5-11 Porous alumina measured tensile strength data as a function of porosity fitted using an exponential expression of Minimum surface area (MSA) model

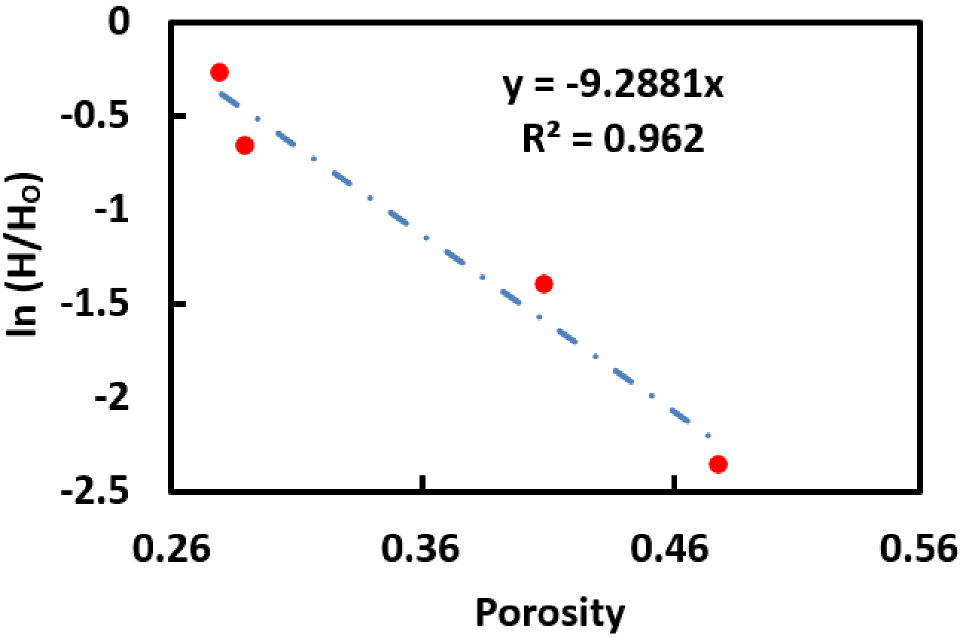

Figure 5-12 Porous alumina measured hardness data as a function of porosity fitted using an exponential expression of Minimum surface area (MSA) model.

Conclusively, porous alumina ceramics were successfully fabricated using cold sintering approach with sodium chloride as pore forming agent. The CSP lowers the overall thermal budgets than the conventional or modified sintering approaches, overcomes the limitation of insolubility of metal oxide materials in water as major limitation militating against compatibility to CSP. The effect of the CSP and post-annealing temperature on the pore distribution, structure and mechanical properties were investigated. At cold sintering stage, the sample consisted of both Al_2O_3 and NaCl. Increase in the post-annealing temperature to 1200 ℃ could completely make NaCl phase volatized to obtain 48 vol% porous alumina structure. The mechanical properties, including hardness and strength, increased with increasing post-annealing temperature from 1200 to 1400 ℃. The grain growth and rapid pore closure also occurred between 1400 – 1500 ℃. The mechanical strength and hardness fitting using an exponential minimum surface area (MSA) model showed a satisfactory fitting result with close stacking characteristics range of 9 and R value > 0.9. The average good mechanical property, structural characteristic and controlled higher micro and meso porosity have made porous Al_2O_3 fabricated at 1200 ℃ the most competitive and a good candidate for applications in various areas such as energy storage, adsorption, building insulation, filtration, and catalysis fields.

5.3 Summary

New innovative approach to fabricate porous alumina ceramics by cold sintering process (CSP) is presented using NaCl as pore forming agent. Al_2O_3-NaCl composite with bulk density of 2.92 g/cm^3 was compacted firstly using CSP and then a porous structure was formed using post-annealing at 1200℃ to 1500℃ for 30 minutes. Brazilian test method and Vickers hardness test were used to determine the indirect tensile strength and hardness of the porous alumina, respectively. Meanwhile, the phases and the microstructure were respectively examined using X-ray diffractometer and scanning electron microscope (SEM) complemented by the 3D image analysis with X-ray tomography (XRT). SEM structural and XRT image analysis of cold sintered composite showed a dense structure with NaCl precipitated between Al_2O_3 particles. The NaCl volatilization from the composite was observed during the annealing and then complete porous Al_2O_3 structure was formed. The porosity decreased from 48 vol% to 28 vol% with the annealing temperature increased from 1200 °C to 1500 °C, while hardness and mechanical strength increased from 14.3 to 115.4 HV and 18.29 to 132.82 MPa respectively. The BET analysis also showed a complex pore structure of micropores, mesopores and macropores with broad pore size distribution. In conclusion, the approach has provided a new route to fabricate porous ceramic that can be used for various applications but fundamental mechanism understanding of the composite cold sintering that aids alumina sintering at temperature lower than its conventional sintering temperature needs to be investigated.

CHAPTER SIX

UNVEILING COLD SINTERING PROCESS (CSP) MECHANISM OF ALUMINA-NACL COMPOSITE FABRICATION

6.1 Introduction

To unveil sintering mechanism, an established approach is used that links sintered material changes to its governable variables and processes. These are realized from experimental measurement or theoretical modelling of sintering process behavior [414]. Several attempts to unveil CSP mechanism has been made in recent studies, but its fundamental mechanism is still not very clear. The major CSP mechanism reported since its discovery by Randall is the dissolution-precipitation process. However, CSP is complex process influenced by the nature of materials, media, and processing conditions. In this chapter, the mechanism of cold sintering process of Alumina-NaCl composite has been proposed from experimental and theoretical analysis. The chapter presents experimental observations and proposed mechanism based on the experimental studies and theoretical basis of defect chemistry. It provides details of the mechanism at both CSP and CSP-post annealing in molten salt from the perspectives of defect chemistry.

6.2 Results and Discussion

6.2.1 Experimental observations

As earlier observed in Figure 5-1 XRD pattern the phase structure evolution of as-CSPed and CSP-post annealed Alumina-NaCl composite revealed that the initial characteristic peaks intensity of as-CSPed composite alumina species decreases, and completely disappeared at some 2-theta positions. Unlike sodium chloride, alumina is insoluble in water and do not meet the key congruent solubility requirement for cold sintering. Therefore, prone to densification and primary bonds are not formed [52]. The characteristic peak changes during CSP shows that presence of water activates chemical gradient between Alumina and NaCl. This caused decrease and disappearance of some alumina low intensity peaks of as-CSPed. The influence of CSP-post annealing helps to rebuilt alumina peaks at 850 ℃ and its intensity increases at 1100 ℃ with large increase in NaCl volatilization. This is consistent to the reported NaCl volatilization with temperature in recent studies [47, 387]. According to Ye et al. [398] rapid volatilization of NaCl at 1100℃ is attributed to the NaCl high vapor pressure of 66.69 Pa at 800℃, accounting for about 90 wt.% loss of the salt at 1000℃ [398]. Further increase in annealing temperature to ≥1200 ℃ for 30 minutes causes complete removal of NaCl out of the structure. At this temperature, the alumina peaks intensity increases and reappeared at some 2-theta. The volatilization of NaCl is also attributed to the presence of volatile Na specie at higher temperature. This influences not only volitization but also variation in chemical stoichiometry of the final product [38].

Figure 6-1 shows the FTIR analysis of the composite Alumina-NaCl. Its peak intensity decreases from dry pressed to the mix and to the CSP pressed pellet. This confirms chemical interaction activated by the presence of water and triggered by the applied uniaxial pressure. Thus, a reason to speculate that alumina defects species are created at CSP stage with water consistent to the observed decrease and disappearance of some XRD peaks in Figure 5-1. Interestingly, presence of water up to 30wt% of the NaCl during composite powder CSP shows no presence of second phase in the XRD pattern in Figure 5-1 consistent to the FTIR analysis in Figure 6-1. However, it is contrary to the observations made in some cold sintered materials such as the appearance of hydrated Lithia second phase caused by trapped water during room temperature CSP fabrication of Li_2MoO_4 and amorphous phase due to incomplete re-precipitation during LiFePO4 composite CSP using LiOH solution [326, 394].

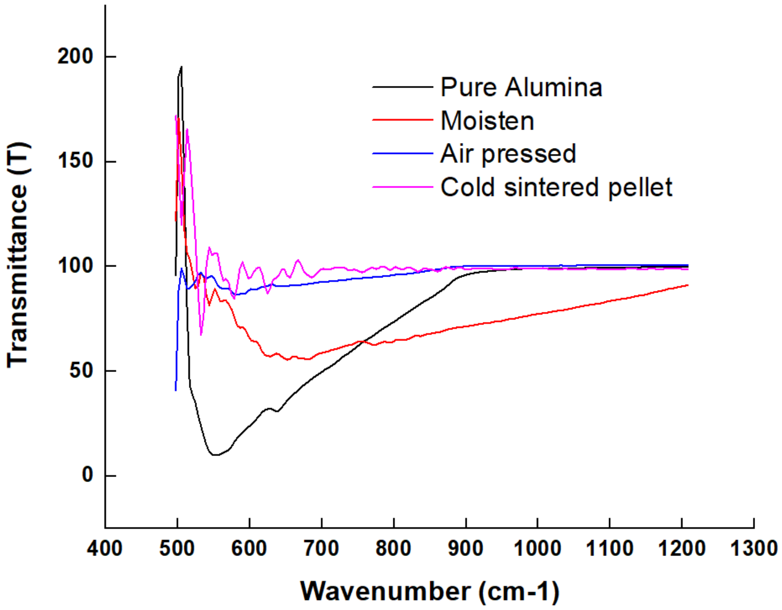

Figure 6-1 FTIR spectrum of Pure Alumina and NaCl dry starting powders, moisten powder, air pressed and cold sintered composite pellets superimposed

Figure 6-2a-f shows the fractured surface SEM microstructure of cold sintered and dry pressed composite Alumina-NaCl with their corresponding measured relative densities. Meanwhile, Figure 6-2g and h show the composite representative micrograph and EDS spectrum. A very high relative density of ~99.6% of the cold sintered composite with 30 wt.% water was obtained as shown in Figure 6-2a-b. This is significantly higher than 92.6% and 80.8% relative density observed for cold sintered with 20wt% water (see Figure 6-2(c-d)) and dry pressed composite (Figure 6-2e-f) respectively. The SEM images of cold sintered composite in Figure 6-2(a-d) shows dense microstructure and increases with water content. It shows that in the presence of 30 wt.% water, NaCl dissolve and precipitate to form a matrix in between alumina particles that facilitate pore removal. This is responsible for a dense structure formation without presence of easily observable pores in the fractured surface microstructures (see Figure 6-2(a-b)). The dissolution and precipitation of NaCl demonstrate CSP similarities to the characteristics of a liquid phase [38, 51]. In the presence of only 20 wt.% water, the salt dissolution-precipitation processes are limited, and the structural density (see Figure 6-2(c-d)) decreases with appearance of clearly open pores consistent to the observed decrease in theoretical density. The SEM microstructure in Figure 6-2(e-f) shows that dry pressed composite sintered through the NaCl only by plastic deformation mechanism. The microstructure is characterized by well define boundary between NaCl and alumina particles. It shows very high alumina porosity, but a more stable structure free from NaCl precipitation. Thus, alumina particles sintering requires high temperature and therefore, not suitable for the composite.

Further analysis of as-CSPed composite microstructures in Figure 6-2(a-d) shows that the composite mechanical strength would not really come from the cold sintered alumina but from the precipitated NaCl. This clearly indicates absence of sintered bonds between alumina particles and therefore, may not provide the desired strong structural scaffolding to encapsulate the salt at its thermal storage application temperature of 810 - 850°C. To unveil CSP fundamentals of Alumina-NaCl, initial sintering test carried out for as-CSPed, and dry pressed composites shows that all pellet samples dissolve immediately when placed in water. It clearly shows that NaCl is responsible for the composite binding. Though, higher structural densification is observed but the dissolution behavior reveals that composite Alumina-NaCl CSP is more of compaction than sintering. Thus, it requires higher temperature thermal treatment to fully crystallize the composite alumina particles consistent to the reported Zirconia CSP requiring further heat treatment to fully crystalize [51, 368].

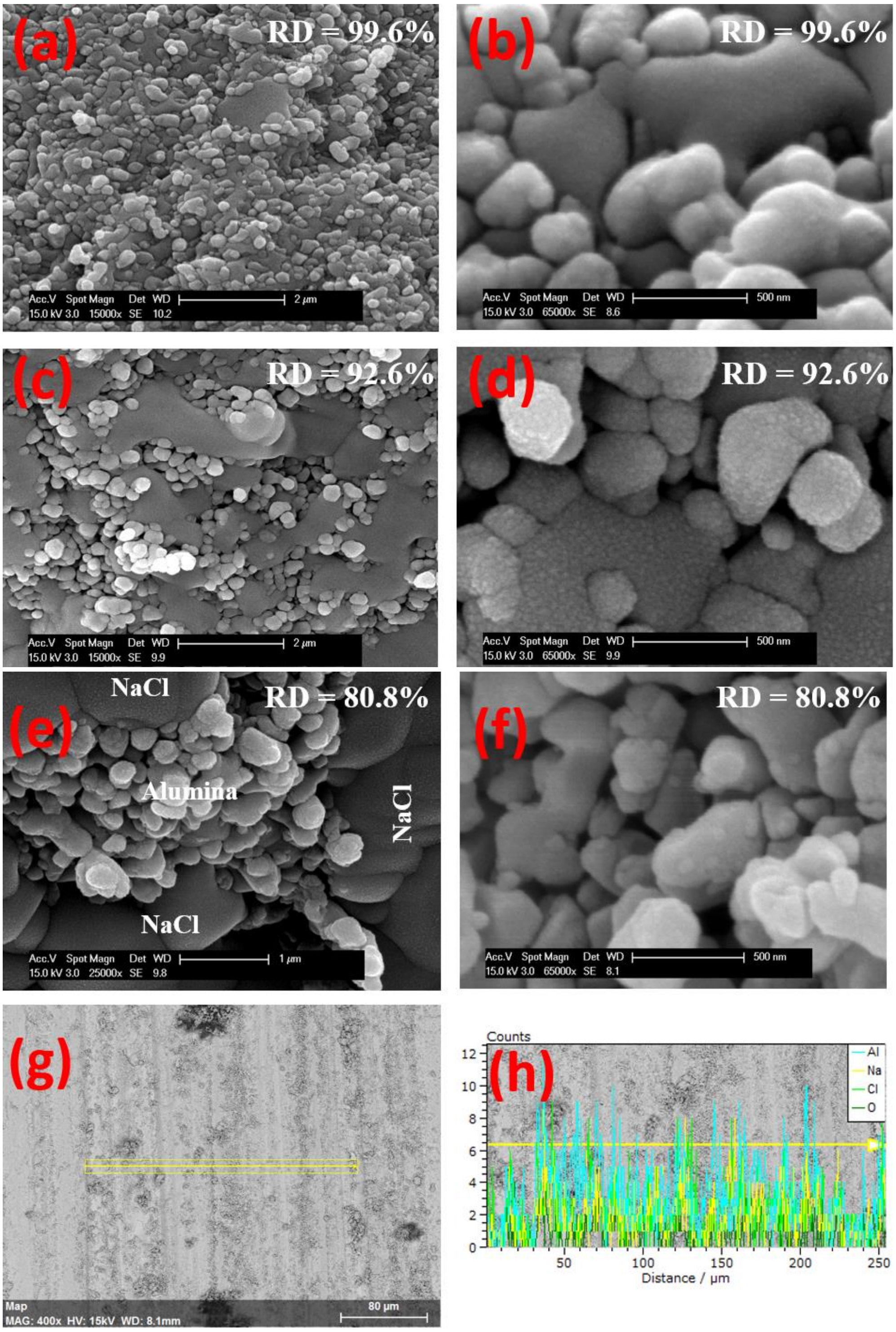

Figure 6-2 SEM images of as-CSPed Alumina-NaCl composite at 250 °C, 400 MPa with (a-b) 30 wt% H_2O (c-d) 20 wt% H_2O (e-f) air pressed and (g-h) representative micrographs and EDS spectrum of as-CSPed composite with 30 wt% H_2O.

Interestingly, the beginning of alumina sintering at 850 °C heat treatment temperature reveals the role played by CSP responsible for alumina sintering at temperature lower than its conventional sintering temperature of ≥1650 °C. The initial sintering test of cold sintered composite with 30 wt.% H_2O shows that it remains undissolved over a period of four weeks when placed in water after first thermal cycle. The bulk SEM and EDS spectrum analysis of the undissolved sample after drying in Figure 6-3a shows that only alumina was present and NaCl gradually dissolve leaving a relatively weak porous alumina structure. Further increase in the annealing temperature to 1000°C for 30 minutes still shows that NaCl was substantially present in the composite despite volatilization. The precipitated salt undergoes internal circulation, rearrangement and accumulate at different spot that appeared to be supported and encapsulated by alumina as shown in the SEM imaging in Figure 6-3 (b and c). These shows cold sintered composite microstructural rearrangement after annealing with appearance of a clear boundary between alumina and NaCl. It shows that annealing helps to stabilizes the structure like the dry pressed composite structure, but the composite mechanical strength is mainly from the partially sintered alumina structural support. In addition to the SEM microstructural changes, species present after CSP-post annealing were analyzed using SEM-EDS. The EDS spectrum reveals presence of Alumina and NaCl consistent to the XRD and FTIR result in Figure 5-1 and 6-1. Figure 6-4 shows the microstructural evolution and phases present in the composite examined by TEM imaging and elemental mapping after CSP-post annealing at 850 °C (see Figure 6-4). The high magnification TEM images in Figure 6-4(a-b) shows the presence of sintered bonds between alumina particles. The elemental mapping in Figure 6-4(c-f) at high magnification shows distribution of Al, O, Na and Cl and clearly indicates alumina species network. At low magnification images in Figure 6-3(b-c), clear boundary exists between the composite species. However, within the region of alumina matrix some NaCl in small quantity are present on its surface. The present of uniform distribution of Na and Cl on alumina surface can be linked to the deposited salt due to internal circulation during CSP-post annealing and the likely residuals between alumina particles. Thus, fair distribution of NaCl after CSP-post annealing demonstrate CSP compatibility to composite thermal storage material fabrication. The major limitation remains full sintering of alumina at CSP stage or after annealing prior to NaCl melting point.

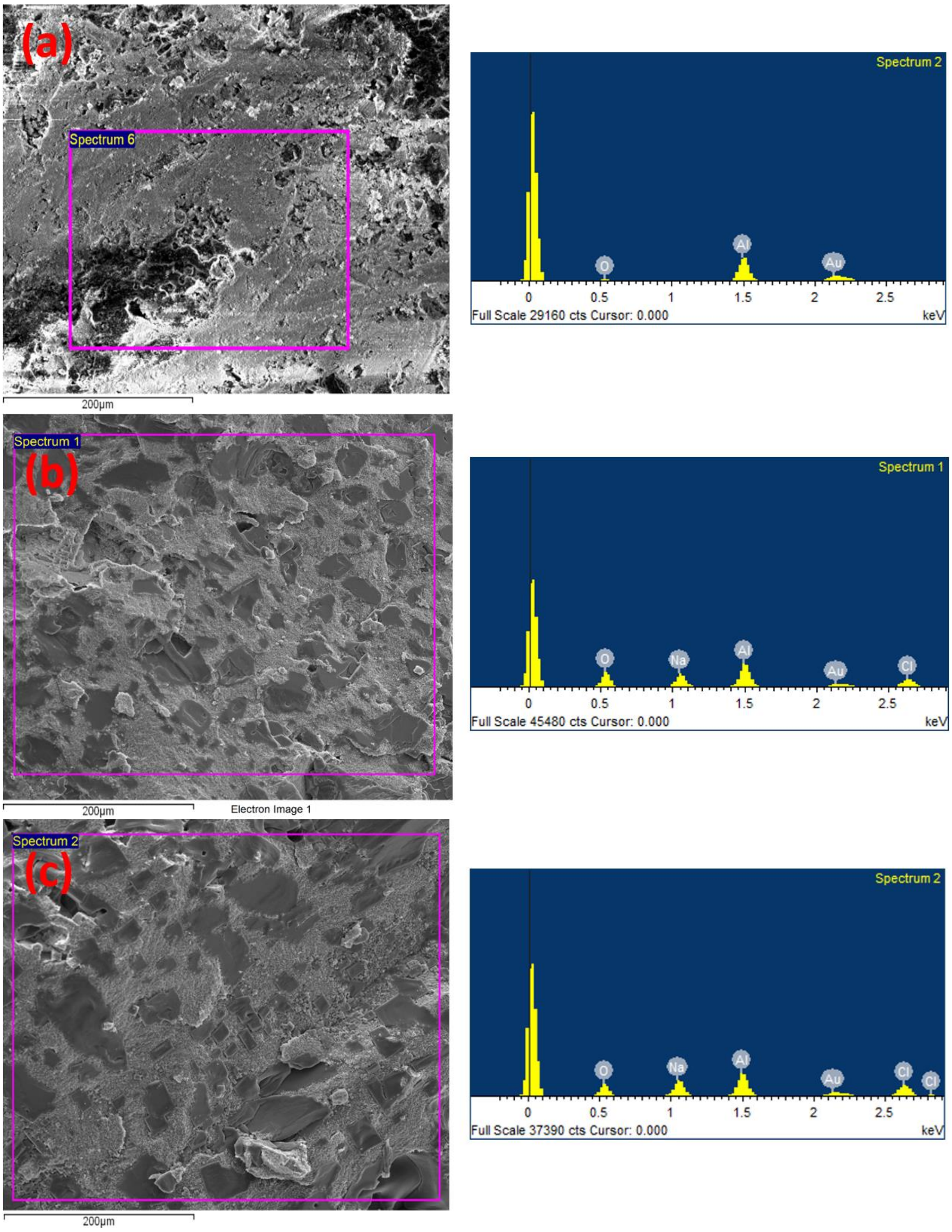

Figure 6-3 SEM-EDS spectrum of CSP-post annealed Alumina-NaCl composite (A) at 850 °C (B) 1000 °C (C) at 850°C after four weeks sintering test in water

In contrast to the cold sintered, we further understand from the TEM images and elemental mapping in Figure 6-5 that plastic deformation of NaCl does not influence alumina sintering. It is apparent in Figure 6-5a and b that alumina particles are either not in contact or just in contact without sintering bond formation after annealing. Though, it gives a more stable structure in which alumina-alumina particles contact is maintained without NaCl precipitation. However, it requires higher sintering temperature as it dissolve in water after annealing between 850℃-1300 ℃.

To fully understand the mechanism of Alumina-NaCl CSP and the role of CSP-post annealing process, a more detail analysis of the grain boundary using EDS provides better understanding of the grain boundary and the mechanism responsible for alumina sintering. Figure 6-6 shows the representative EDS spectrum and elemental composition at several alumina particles grain boundary after CSP-post annealing at 850℃. NaCl which precipitates alumina particles grain boundary during CSP, interacts with alumina as evident in Figure 5-1 XRD and Figure 6-2 FTIR intensity decrease. Thus, the composite undergoes atomic rearrangement to sinter after annealing. This is responsible for the appearance of only Al, Na and O at many grain boundaries without chlorine as represented by the EDS spectrum in Figure 6-6c.

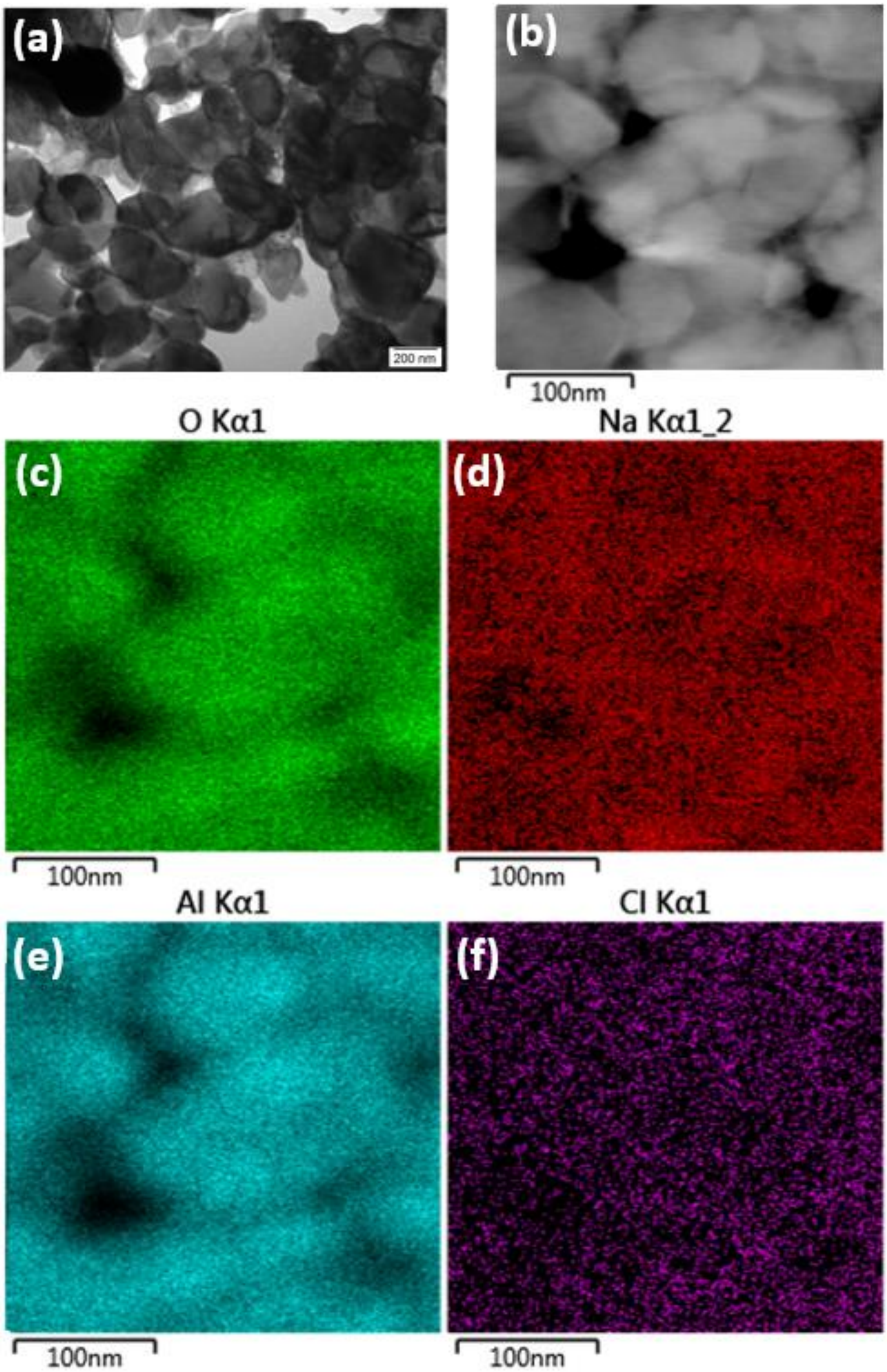

Figure 6-4 (A) Representative TEM micrographs of CSP-post annealed Alumina-NaCl composite at 850℃ (B) High resolution TEM image of the area outlined for EDS elemental mapping (C-F) corresponding EDS chemical mapping

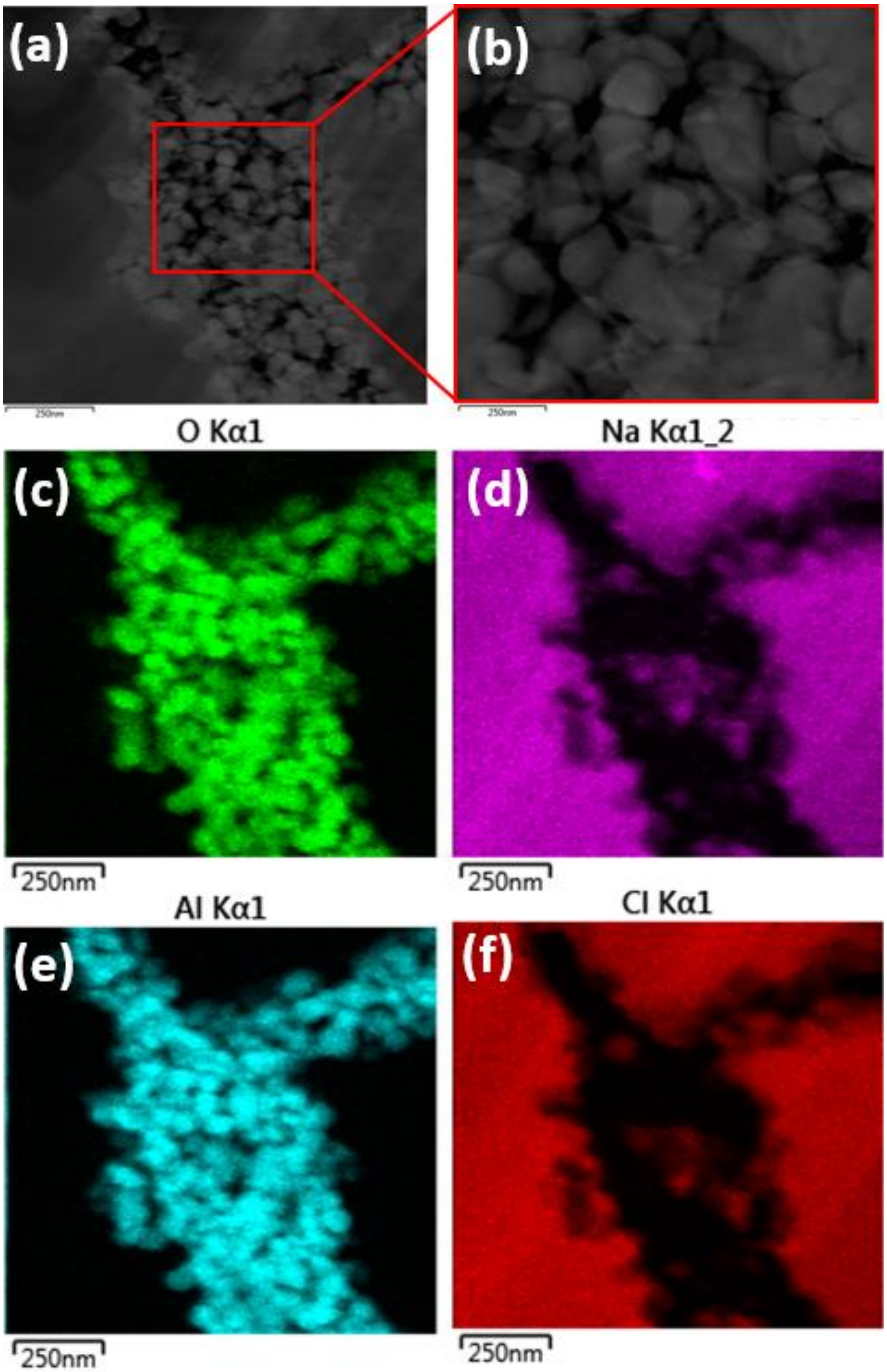

Figure 6-5 (a) Representative TEM micrographs of dry pressed annealed composite at 850°C (b) High resolution image of the area outlined by the red square to show absence of sintered bonds between alumina particles (c-f) corresponding EDS chemical mapping

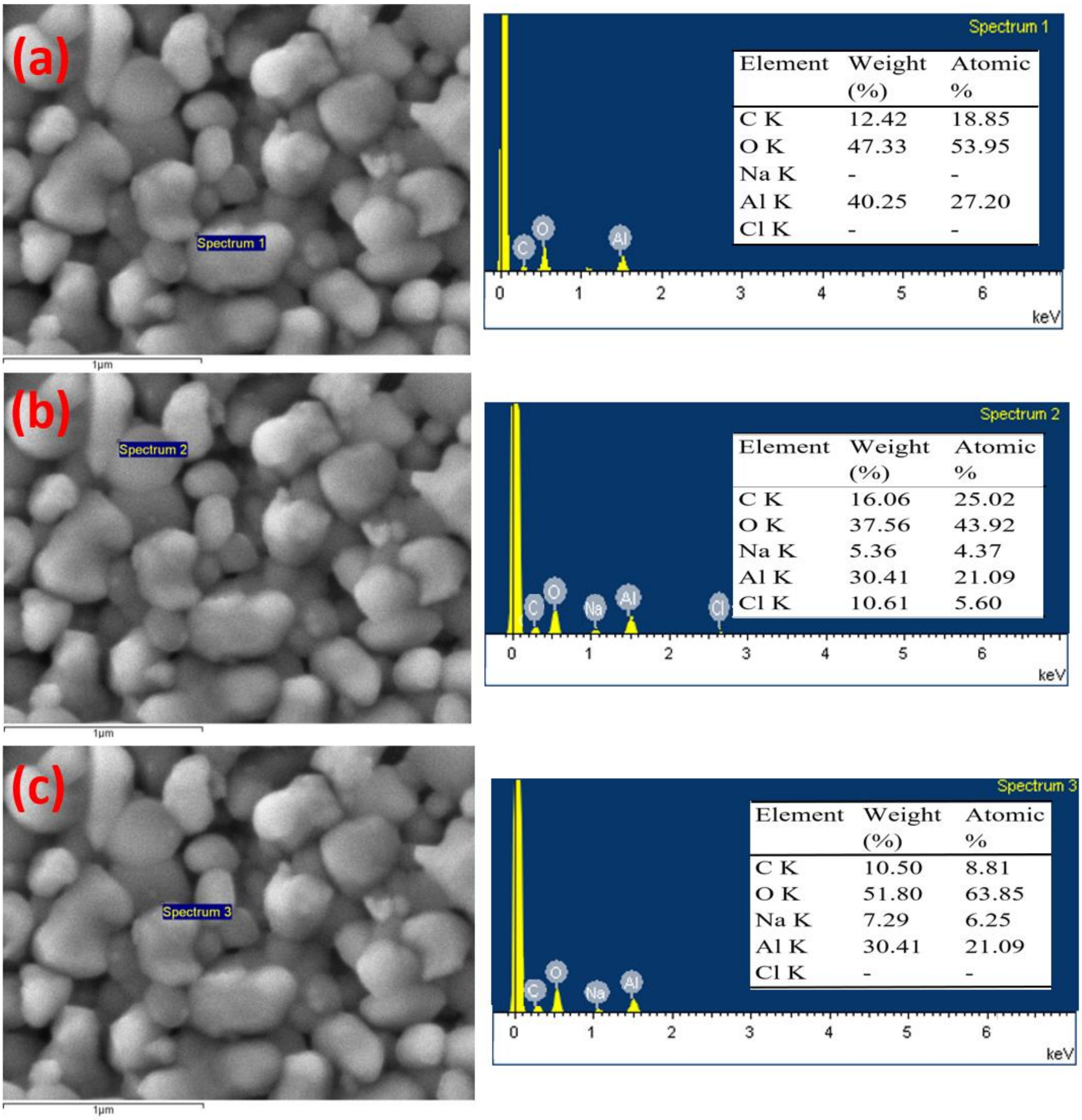

Element	Weight (%)	Atomic %
C K	12.42	18.85
O K	47.33	53.95
Na K	-	-
Al K	40.25	27.20
Cl K	-	-

Element	Weight (%)	Atomic %
C K	16.06	25.02
O K	37.56	43.92
Na K	5.36	4.37
Al K	30.41	21.09
Cl K	10.61	5.60

Element	Weight (%)	Atomic %
C K	10.50	8.81
O K	51.80	63.85
Na K	7.29	6.25
Al K	30.41	21.09
Cl K	-	-

Figure 6-6 Representative SEM micrographs of CSP-post annealed composite at 850°C with corresponding EDS spectrums and elemental compositions of species (a) Al and O (b) Al, O, N and Cl (c) Al, O and Na at alumina particles grain boundaries

Figure 6-7 shows the schematic representation of microstructure evolution of CSP-post annealed Alumina-NaCl at 850°C, its TEM images and SEM microstructure at 1200 °C annealing temperature. Figure 6-7a shows that at cold sintering stage, as-pressed Alumina-NaCl has large pores presence. The addition of small amount of liquid reduces only the atomic diffusion distance and promotes particles rearrangement aided by applied uniaxial pressure.

Subsequently, dissolution-precipitation process takes place by the application of heat under pressure. Thus, a dense composite structure was formed with small residual pores within the alumina particles of less than 2% as shown in Figure 6-2a and b. At CSP-post annealing temperature of 850°C, NaCl melts, circulates, and volatilizes creating more pores in the entire structure. Figure 6-7b shows the alumina particles grain boundary TEM images of CSP-post annealed composite at 850°C at varying magnifications. It shows sintered bonds between alumina particles are formed with nano pores created by structural rearrangement and volatilization of NaCl.

Furthermore, the insolubility of alumina in molten salts has been widely reported [415, 416]. Thus, rules out the possibility of alumina particles liquid phase sintering at low temperatures. The beginning of alumina sintering at 850°C and formation of well sintered porous alumina structure at 1200°C clearly demonstrate the role of CSP. The correlation between cold sintered composite relative density, phase structure, microstructure, and its non-dissolution in water after thermal treatment is interesting and remarkable from which the following rationales are drawn: 1) NaCl dissolve and diffuse in between alumina particles during the cold sintering step (with water) but alumina does not cold sinter with itself, 2) NaCl diffuse in between the alumina particles during the cold sintering step with water, melts during thermal cycle at 850 °C but molten NaCl does not help in alumina liquid phase sintering as the latter is insoluble in the former [415, 416]. Thus, liquid phase of pure alumina precursor species in molten NaCl cannot be formed at this low temperature, 3) Alumina interact with NaCl during CSP, creates alumina defects and undergoes both atomic rearrangement, structural stabilization, and subsequent sintering beginning from 850°C annealing temperature. Based on the rationales, we speculated and proposed a mechanism from the perspectives of defects chemistry that at cold sintering stage causes alumina defects formation, and in a medium of molten salt during annealing undergoes atomic rearrangement to sinter at ≥ 850°C but lower than conventional alumina sintering temperature.

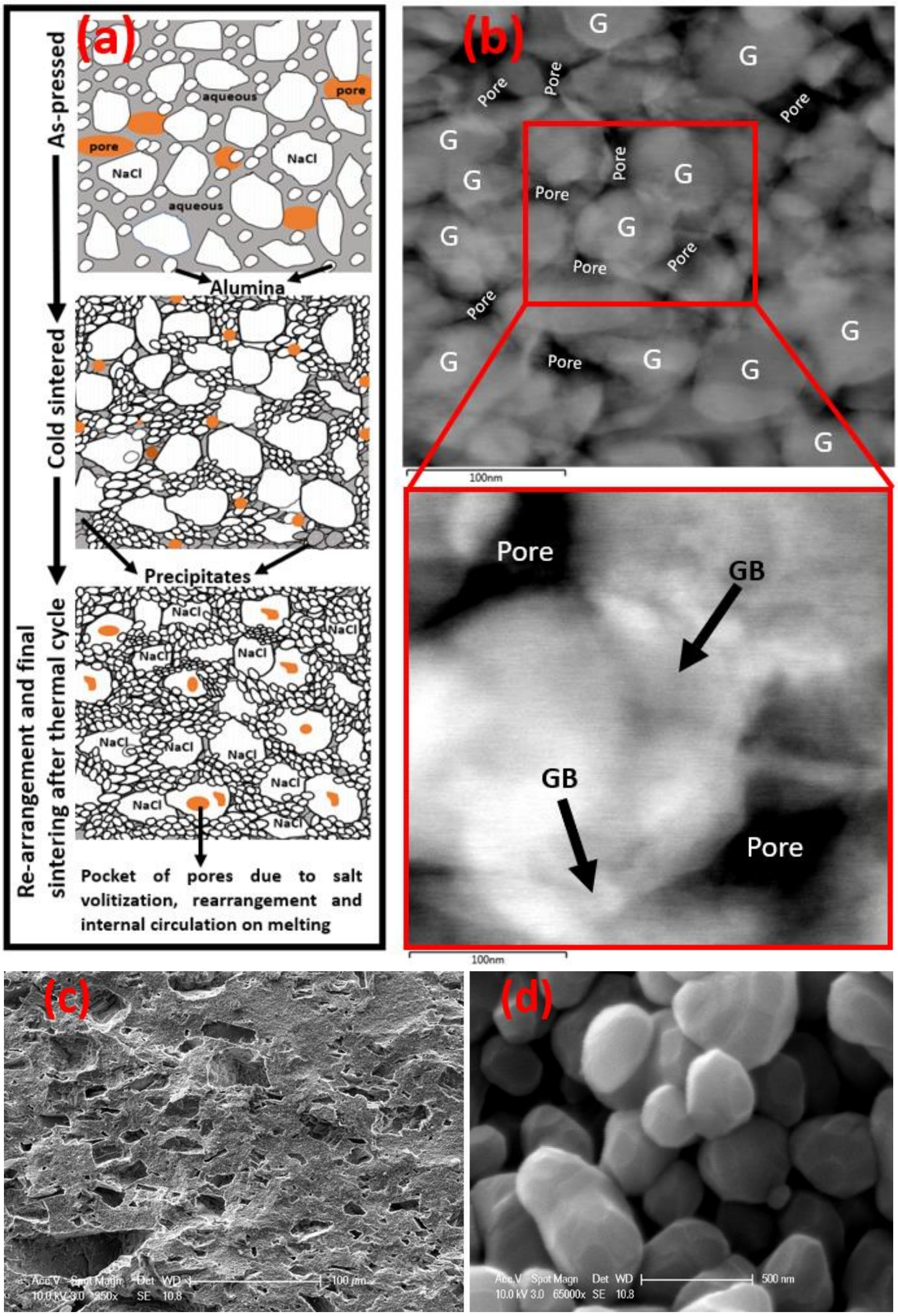

Figure 6-7 (a) Schematic representation of microstructure evolution of Alumina-NaCl composite during CSP and CSP-post annealing (b) Representative TEM micrograph of the CSP-post annealed composite at 850°C with high resolution image of the area outlined to show the well-sintered alumina-alumina grain boundary (c-d) Representative fractured surface SEM micrograph of the CSP-post annealed composite at 1200℃

6.2.2 Chemistry defects mechanism at CSP stage

Alumina-NaCl composite cold sintering drives complex mechanisms such as the conventional dissolution-precipitation, plastic deformation, and the observed chemical reaction. The first two effects are at CSP stage and are responsible for the pore removal governed by the NaCl matrix. Also, CSP of a pure alumina system could not drive the desired sintering of alumina particles as it is completely insoluble in water. However, in the presence of water and NaCl, chemical gradient is created in the composite responsible for interparticle formation NaCl /Al_2O_3 [396]. Thus, causes alumina defect formation and subsequent sintering during CSP-post annealing [24]. The chemical structure of alumina and its characteristic sigma and pi bonds are shown in Equation 6-1 with electronic configuration of aluminium having 3 electrons in its outermost shell s and p orbitals as $3s^2$ and $3p^1$ respectively. The later p orbitals are characterized by dumbbell shape while the s-orbitals are spherical. The present of only 3 electrons in Aluminium outermost shell means 5 empty orbitals present as an inherent imperfection. The 3 electrons result into oxidation state of 3 and is the most common. However, because of the close energy level, one of the 3s electron can move to 3p orbital and are shared as Px^1, Py^1 and Pz^0 π-bonds. Thus, this yields Al^{+3} oxidation state. When bonded to an electronegative atom (as in alumina), and under thermodynamic conditions (excess heat or pressure), an electron can be lost to the electronegative atom [417, 418, 419].

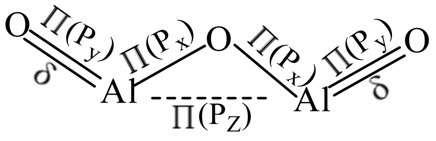

(6-1)

The addition of water to the sodium chloride causes it to dissociate into $Na^+$and Cl^-.Under the influence of applied pressure of mixing and hot pressing, solvated $Na^+$and Cl^-freely flows and becomes readily available. The lone pairs of oxygen in alumina in Figure 6-8 are shared with Na^+ creating partial positive charge on oxygen at its maximum valency. Thus, it cannot take electrons from chlorine (Although more electronegative), but it draws more of the electrons it shares with aluminium [417, 418, 419]. Thus, in the subsequent stage, Cl^- helps to create electron deficient aluminium as it attaches itself to create intermediate A and defect as shown in Figure 6-8.

The presence of excess electron around aluminium and readily available Na^+ in the system causes it to give-up the excess e^- to oxygen (P_x), which in turn pick up Na^+ to form Na_2O and $Al = O$ defect as new species added to the system. The unstable Intermediate A in excess $Na^+$and Cl^-, further yield more alumina defects as shown in Figure 6-8. The defect $Al\ = O$ has only 2 electrons available for bonding, and thus Al^{3+} shifted to Al^{2+}All the electrons occupy P_z orbitals with vacancy at P_x orbital [417, 418, 419]. The electron in-balance creates instability. The influence of electron delocalization associated with resonance effect allows some measure of stability to exist as shown in Figure 6-8.

The combined action of the pressure and water at CSP stage initiates chemical interaction between NaCl and alumina [24]. The interaction is triggered by heat under continuous pressing to create defects in the material chemistry. [420, 421, 422]. This results into the formation of new species (AlO_h• and ONa_2) and chlorine gas being liberated as shown in Equation 6-2. The stability of these species has been shown to be stable by Zhang et al. [420] and Lin et al. [421].

$$Al_2O_3 + 2NaCl \xrightarrow[\text{Pressure (400MPa)}]{H_2O \text{ (moisture)}} 2AlO + Na_2O + Cl_2 \qquad (6\text{-}2)$$

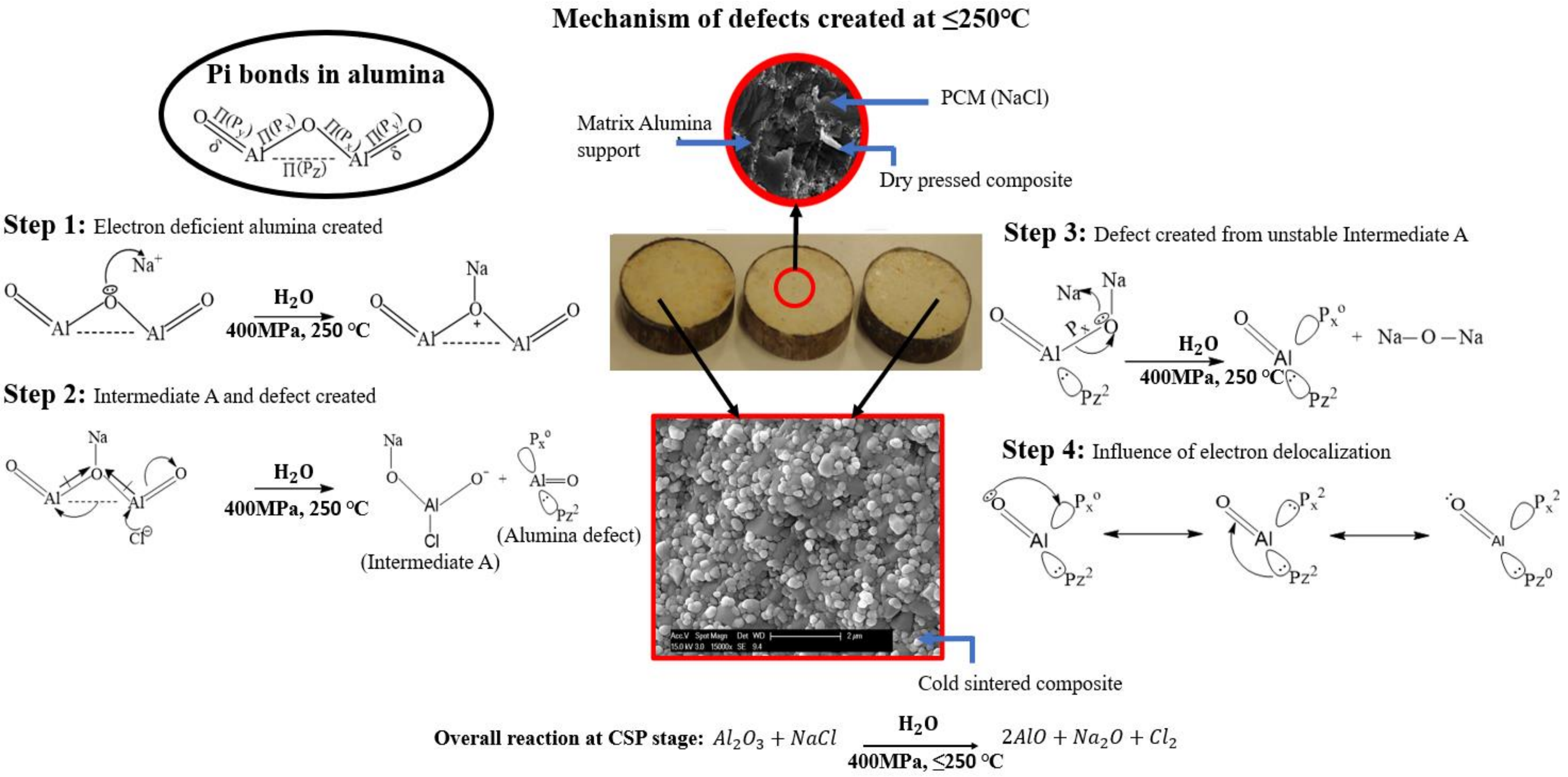

Figure 6-8 Schematic representation of the reaction and microstructure of cold sintered composite at ≤250°C [417, 418, 419].

6.2.3 Mechanism at CSP-post annealing stage

6.2.3.1 Formation mechanism of Al-Al and Al-ONa

The role of cold sintering process stage enables formation of ONa_2 and $AlO_h\bullet$ from Al_2O_3 and NaCl. With or without Al_2O_3 left over after CSP, sintering is activated between the available species at CSP-post annealing stage. According to the EDS analysis in Figure 10, $Al-Al\ and$ $Al-ONa$ bonds are formed at the grain boundary of Alumina particles with both scenarios competing. The final sintering process during CSP-post annealing occurs in two ways according to step 1 and 2 reactions in Figure 6-10. The first is the oxygen lone pair in the ONa_2 is shared to the empty P_x orbital of the defect $AlO_h\bullet$. This creates a positive charge on oxygen while maintaining two (2) electrons in the Pz orbital of aluminium. The Pz electrons are shared to the aluminium in the alumina and causes one of the $Al-O$ double bond to break. After atomic rearrangement, Al-Al and $Al-O$ (with partial positive oxygen) bonds are formed responsible for the observed partial negative charge on the oxygen in the alumina [422].

The second is ONa_2 react with $AlO_h\bullet$ and the oxygen lone pair electrons in ONa_2 are shared with the defect $AlO_h\bullet$ via its empty Px orbital. A partial positive on oxygen in the ONa_2 is created with two lone electrons in the Pz orbital of $AlO_h\bullet$ defect. These electrons are shared with empty Px orbital of another defect and $Al-O$ double bond in the defect is broken while $Al-Al$ and $Al-ONa$ bonds are formed with partial positive on ONa_2 and partial negative on oxygen as shown in the step 1 second reaction in Figure 6-9. Subsequently, electrons are drawn towards the oxygen in ONa_2 and Na^+ is released and attached to the partial negative oxygen. This creates double bond between ONa and aluminium via the two free electrons in Pz orbital of aluminium. These are readily available to interact with more defects as sintering progresses during post-CSP annealing [422].

6.2.3.2 Formation mechanism of $Al - O - Al$ and $Al - Na$

The ONa_2 and $AlO_h\cdot$ species formed during CSP can also interact with themselves in different ways during CSP-post annealing. The lone pair oxygen electrons in the ONa_2 are deposited into the empty Px orbital of the defect aluminium as shown in the step 2 reaction in Figure 6-9. This creates partial positive charge on oxygen of ONa_2 and causes cleavage of the defect $Al - O$ double bond. Subsequently, oxygen draws all electrons it shares with Al to form a partial negative charge of excess electrons. These are deposited into another defect responsible for the formation of $Al - O - Al$ and $Al - Na$ bonds with partial negative oxygen on the reacted defect. Thus, two interaction points for further extensive branching and propagation are created namely the partial negative oxygen and aluminium ${P_z}^2$ orbital. These two points contains unshared electrons readily available for bond formation by electron deposition into the ${P_x}^0$ orbital of defect aluminium. Subsequent reactions further create more of these points to propagate into multi layered structure of sintered composite in a molten NaCl media [422].

In a limited amount of water, Alumina >> $AlO_h\cdot$ and final sintering at CSP-post annealing stage results into a more streamline product and slower rate as shown in Equation 6-3. The intermediate specie B forms a monomer type molecule and dimerizes with itself (and resulting multiples) in a polymeric reaction scenario. However, product-wise like polymeric type reaction (uncommon in this study) is observed when excess amount of water is used, less defects are created when Na^+ are not free to cause defect as it is fully solvated. Equation 6-4 shows that when oxygen pulled the shared electron more towards itself, it results into partial positive charge on Aluminium. Subsequently, unzipped reaction occurred and pellet dissolve when place in water after CSP-post annealing at 850℃ [423, 424].

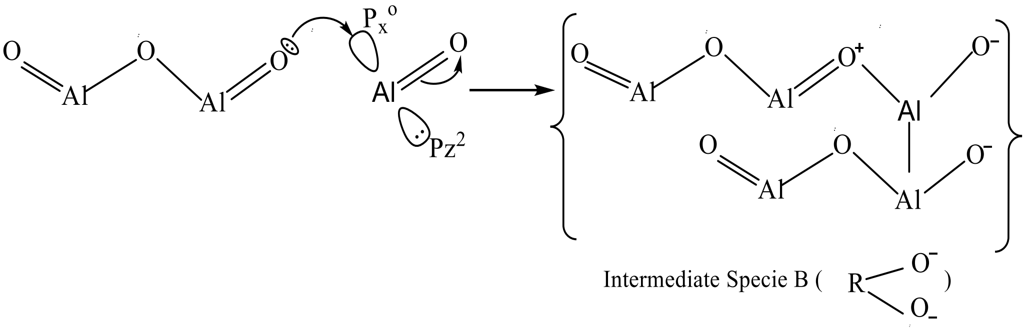

(6-3)

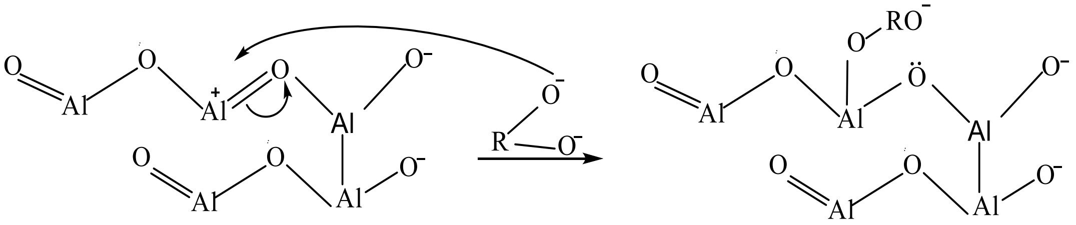

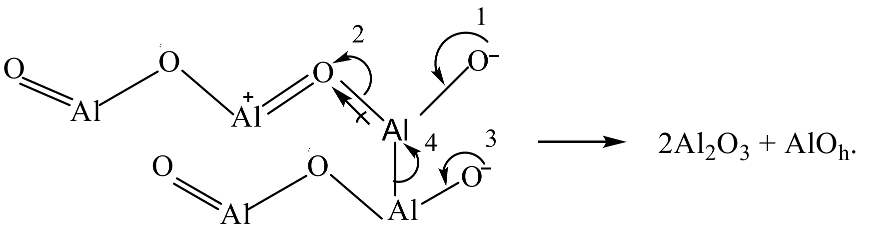

(6-4)

Conclusively, Al_2O_3 -NaCl composite was cold sintered to a relative density of ~98% at 250°C. Dissolution-precipitation process dominates the composite CSP with NaCl precipitating in between alumina particles. Under the influence of heat and applied uniaxial pressure, precipitated NaCl interact with alumina to create alumina vacancy defect. Cold sintered and dry pressed composites dissolve immediately when placed in water and therefore, confirmed absence of alumina sintered bonds at CSP stage. In the present of 30 wt % water/ 0.6g NaCl, sufficient defects are created and undergoes atomic rearrangement to sinter during CSP-post annealing at ≥850 °C. The dry pressed composite Al_2O_3-NaCl sintered through the salt only with defined boundary between the composite species limiting alumina defects formation. In a limited amount of water insufficient defects are created responsible for unzipped reaction requiring high conventional alumina sintering temperature like dry pressed composite. The insolubility of alumina in molten salt rules out the possibility of liquid phase sintering [415, 416, 423]. Therefore, signifies the role of CSP responsible for the observed beginning of alumina sintering at 850 °C. The mechanism of the composite alumina defect formation at CSP stage and subsequent sintering at CSP-post annealing stage are based on the observed phase structure, microstructure, and EDS analysis at the alumina grain boundary. In this study, novel CSP mechanism different from traditional dissolution−precipitation in cold sintering process is proposed and unveiled, i.e., a grain boundary vacancy defect created by Aluma interaction with NaCl that drives sintering of Alumina during CSP-post annealing at moderately low elevated temperature. In addition to the defects, the strong reduction potential of sodium over aluminium also promotes the sintering process as demonstrated in the production of Na from lime ash in 1807 by Humphrey Davy as further supported by the work of Vuthaluru et al. [423]. Humphrey used electricity to split the substances and isolated sodium via electrolysis of dried soda ash. It was observed that sodium was only deposited when the ash was moist but not in solution, while Vuthaluru et al., showed that deposition of sodium in fly ash was improved in the presence of aluminium.

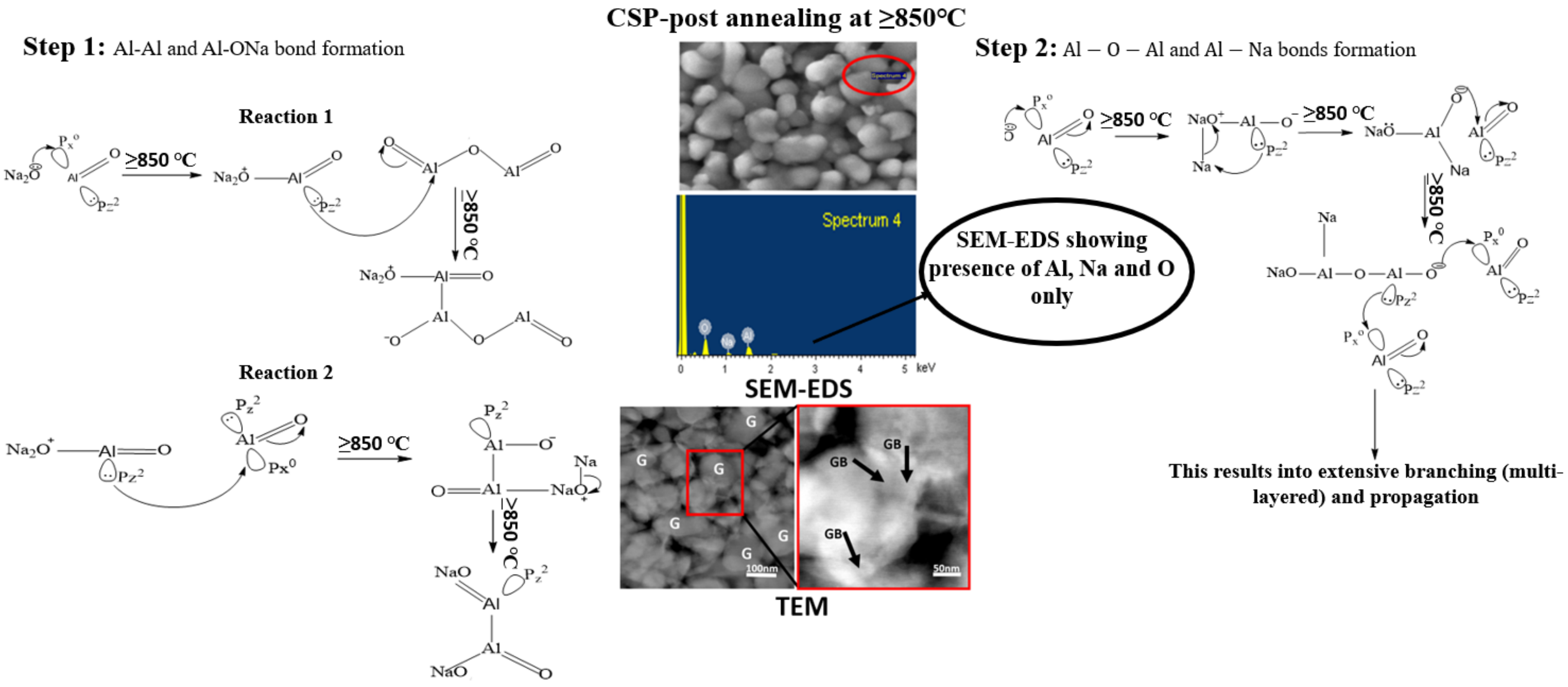

Figure 6-9 Schematic representation of the reaction and microstructure of CSP-post annealed composite at ≥850°C [422]

6.3 Summary

This chapter present the mechanism of cold sintering process of Alumina-NaCl composite, with focus on the role of applied pressure and water on the composite densification. Different from traditional CSP dissolution−precipitation mechanism, it is proposed that the alumina vacancy defect interaction with wetted NaCl drives alumina sintering during CSP-post annealing. Presence of water in NaCl causes Na^{+} and Cl^{-} to create high vacancy defect on alumina under uniaxial pressing and at high temperature, atomic rearrangement takes place and alumina particles sintering manifest from 850°C. The proposed mechanism is supported by the experimental observations and as-cold sintered (CSPed) and CSP-post annealed samples XRD-FTIR characterization, micro-structural analysis, TEM, and EDS analysis. The composite is fully sintered during annealing temperature between 850 to 1200 °C, which is much lower than conventional alumina sintering temperature.

CHAPTER SEVEN

CONCLUSION AND RECOMMENDATIONS

7.1 Introduction

The world demand for energy is rapidly increasing and the growing demands and shift to renewable energy is being faced with numerous challenges. Integrating renewable energy sources into the current energy generation and distribution network requires efficient energy storage system since its supply is intermittent. To phase out the existing method of using batteries, environmentally friendly and cheaper composite phase change materials are being used to store enormous amount of thermal energy in its latent form and use it when needed. The process of charging and discharging process via repeated melting and solidification processes is required and therefore, materials with required structural, thermal, and mechanical properties are required. The current conventional sintering method of composite phase change materials fabrication is limited by high energy consumption and differences in melting temperature making it impossible to achieve desired strong structural scaffolding and thermal properties particularly for high temperature application using ceramic materials as matrix support. Thus, the need to develop a new low temperature fabrication method to design CPCM that suit high temperature application requirement, lower fabrication cost, and provide means for material integration to target specific properties.

7.2 Conclusion

The present research work described experimental work carried out to develop efficient CPMs using an innovative low temperature cold sintering process to lower energy consumption, reduce sintering time, facilitate materials integration, and unveil the process fundamental mechanism. The main CSP variables namely the amount of water used, pressure, temperature and dwelling time were experimentally determined and their influence on the key sintering measures investigated.

The present research work described experimental work carried out to develop efficient CPMs using an innovative low temperature cold sintering process to lower energy consumption, reduce sintering time, facilitate materials integration, and unveil the process fundamental mechanism. The main CSP variables namely the amount of water used, pressure, temperature and dwelling time were experimentally determined and their influence on the key sintering measures were investigated. The experimental study includes cold sintering of Al_2O_3-NaCl composite for thermal energy storage, fabrication of porous Al_2O_3 structure using CSP approach and unveiling the process fundamental mechanism from defect chemistry perspectives. The major outcome of this work is summarised as follows:

- The cold sintering process of Al2O3-NaCl at temperature up to 250 ℃ is purely densification rather than sintering. The alumina particles during the cold sintering step with water does not cold sinter with itself. Initially, NaCl dissolves at CSP stage, diffuses and precipitates between Al2O3 particles under pressure and temperature to remove every pore space, governed by NaCl matrix. A more stable structure without precipitation is observed in a dry pressed composite but alumina can only be sintered when heated to its conventional sintering temperature. CSP lowers the sintering temperature to as low as 1200 ℃ from 1700 ℃ in conventional sintering.
- At CSP stage, relative density ≥99% was obtained with 30 wt% NaCl as water in 1:1 Al2O3-NaCl composite ratio, at temperature of 250 ℃ under 400MPa pressure, for 90 minutes. The amount of water present (30 wt% of NaCl) and applied uniaxial pressure of 400 MPa are the most significant that influence the CSP the most. Time and temperature increase influences only to a limited extent. Plastic deformation mechanism apart from the main dissolution-precipitation process contributes to the composite densification during cold sintering and dry pressing.

However, the cold sintered composite density increases and is not limited by high pressure pressing as observed in pure NaCl cold sintered. Relative density and physical robustness of CSPed composite rapidly increased with increase in water content, pressure and temperature but fractured during thermal cycle when the amount of water exceeded 30 wt% of the NaCl under 400MPa and 250°C.

- Though, decrease in peak intensity was observed in cold sintered sample but no appearance of new phase (s) from both XRD and FTIR analysis. However, interaction of Al2O3 with NaCl in the presence of water at CSP stage influences the beginning of alumina sintering during annealing at 850°C. No leakage of NaCl was observed during thermal cycle annealing at 850°C but it volatilizes, leaving a mechanically weak porous structure. The precipitated NaCl between alumina particles melts during thermal cycle at 850 °C but does not help in alumina liquid phase sintering as the latter is insoluble in the former.

- Increase in the CSP-post annealing temperature to 1200°C, causes complete volatilization of NaCl to form a porous structure of sintered alumina. The porosity decreases and mechanical strength increases with further increase in the annealing temperature. The approach provides a new method of porous alumina fabrication. It was concluded that alumina interact with NaCl during CSP, creates alumina defects and undergoes both atomic rearrangement, structural stabilization, and subsequent sintering beginning from 850°C annealing temperature

- The SEM-EDS analysis at the grain boundary of CSP-post annealed samples revealed presence of only Al, Na and O in many grain boundaries. This coupled with absence of new species during CSP and decreased peak intensity from XRD and FTIR, we concluded that the mechanism of Al2O3-NaCl cold sintering densification and subsequent sintering at annealing stage can be proposed from the perspective of defect chemistry.

- The mechanism proposed that at CSP stage, besides dissolution-precipitation and plastic deformation mechanisms, alumina defects are created under heat and pressure. At subsequent annealing stage, Al-Al, Al-ONa, Al-O-Al and Al-Na bonds were formed responsible for a full alumina to alumina particles sintering. The research showed that CSP has the potential and may be compatible to different chemistries and their composites to fabricate a wide range of composite thermal storage materials for medium and high temperature application. The present study revealed that chloride salts of Na and K can generally be used to serve as sintering and pore forming agent of porous ceramic materials to target TES application requirements.

7.3 Recommendation

Based on the experimental analysis carried out in this work to cold sinter Al_2O_3-NaCl composite TES materials and further unveil CSP mechanism understanding, the following recommendations are made to advance the CPCMs fabrication by this method and better understand the process mechanism:

- A more detail study on the chemical interaction of Al_2O_3 and NaCl is required to fully unveil the mechanism at CSP stage and provide more detail understanding on the role of CSP.
- Cold sintering process of alumina-based composites with high melting non-chloride PCMs should be studied using appropriate solvents and determine if ceramics can be fully sintered at CSP stage or at low annealing temperatures without volatilization.
- The cold sintering process mechanism should be studied for different chemistries and their composite to fully unveil its fundamental mechanism.
- CSP is an extremely low-temperature sintering process, and it needs deep research to achieve optimization

- Porous alumina fabricated by CSP should be studied as potential support material for medium and high temperature PCMs, and the influence of particle size on cold sintered composite and the porous alumina should be fully investigated.

References

[1] Ge, Z.; Li, Y.; Li, D.; Sun, Z.; Jin, Y.; Liu, C.; Li, C.; Leng, G.; Ding, Y., Thermal energy storage: Challenges and the role of particle technology. *Particuology* 2014, 15, 2-8.

[2] Liu, C., Li, F., Ma, L.-P. & Cheng, H.-M. 2010. Advanced Materials for Energy Storage. *Advanced Materials,* 22**,** E28-E62.

[3] Zhang, H., Baeyens, J., Cáceres, G., Degrève, J. & Lv, Y. 2016. Thermal energy storage: Recent developments and practical aspects. *Progress in Energy and Combustion Science,* 53**,** 1-40.

[4] Fernandes, D., Pitié, F., Cáceres, G. & Baeyens, J. 2012. Thermal energy storage: “How previous findings determine current research priorities”. *Energy,* 39**,** 246-257.

[5] Diouf, B. & Pode, R. 2015. Potential of lithium-ion batteries in renewable energy. *Renewable Energy,* 76**,** 375-380.

[6] Dinker, A., Agarwal, M. & Agarwal, G. D. 2017. Heat storage materials, geometry and applications: A review. *Journal of the Energy Institute,* 90**,** 1-11.

[7] Xu, T., Li, Y., Chen, J. & Liu, J. 2017. Preparation and thermal energy storage properties of LiNO3-KCl-NaNO3/expanded graphite composite phase change material. *Solar Energy Materials and Solar Cells,* 169**,** 215-221.

[8] Zhu, J. Q., Li, R. G., Zhou, W. B., Zhang, H. G. & Cheng, X. M. 2016. Fabrication of Al2O3-NaCl Composite Heat Storage Materials by One-step Synthesis Method. *Journal of Wuhan University of Technology-Materials Science Edition,* 31**,** 950-954.

[9] Kuravi, S., Trahan, J., Goswami, D. Y., Rahman, M. M. & Stefanakos, E. K. 2013. Thermal energy storage technologies and systems for concentrating solar power plants. *Progress in Energy and Combustion Science,* 39**,** 285-319.

[10] Ge, Z., Ye, F. & Ding, Y. 2014. Composite Materials for Thermal Energy Storage: Enhancing Performance through Microstructures. *ChemSusChem,* 7**,** 1318-1325.

[11] Agyenim, F., Hewitt, N., Eames, P. & Smyth, M. 2010. A review of materials, heat transfer and phase change problem formulation for latent heat thermal energy storage systems (LHTESS). *Renewable and Sustainable Energy Reviews,* 14**,** 615-628.

[12] Li, C., Li, Q., Cao, H., Leng, G., Li, Y., Wang, L., Zheng, L. & Ding, Y. 2018. Wettability of eutectic NaLiCO3 salt on magnesium oxide substrates at 778 K. *Applied Surface Science,* 442**,** 148-155.

[13] Mehrali, M., Latibari, S. T., Mehrali, M., Indra Mahlia, T. M., Cornelis Metselaar, H. S., Naghavi, M. S., Sadeghinezhad, E. & Akhiani, A. R. 2013. Preparation and characterization of palmitic acid/graphene nanoplatelets composite with remarkable thermal conductivity as a novel shape-stabilized phase change material. *Applied Thermal Engineering,* 61**,** 633-640.

[14] Chen, K., Yu, X., Tian, C. & Wang, J. 2014. Preparation and characterization of form-stable paraffin/polyurethane composites as phase change materials for thermal energy storage. *Energy Conversion and Management,* 77**,** 13-21.

[15] Wei, G. S., Wang, G., Xu, C., Ju, X., Xing, L. J., Du, X. Z. & Yang, Y. P. 2018. Selection principles and thermophysical properties of high temperature phase change materials for thermal energy storage: A review. *Renewable & Sustainable Energy Reviews*, 81**,** 1771-1786.

[16] Liu, W., Zhang, L., Ma, Y., Cai, Q., Zhu, W., Wang, R. & Wen, Z. 2020. Low temperature co–sintering of tungsten alloy/steel composite structure. *International Journal of Refractory Metals and Hard Materials,* 90**,** 105224.

[17] Liu, M., Fernández, A. I. & Segarra, M. 2018. Chapter 8 - Materials for Phase Change Material at High Temperature. *In:* CABEZA, L. F. & TAY, N. H. S. (eds.) *High Temperature Thermal Storage Systems Using Phase Change Materials.* Academic Press.

[18] Guo, Q. & Wang, T. 2014. Preparation and Characterization of Sodium Sulfate/Silica Composite as a Shape-stabilized Phase Change Material by Sol-gel Method. *Chinese Journal of Chemical Engineering,* 22**,** 360-364.

[19] liu, S. Y. & Yang, H. M. 2016. Porous ceramic stabilized phase change materials for thermal energy storage. Rsc Advances, 6, 48033-48042.

[20] Notter, W., Lechner, T., Groß, U. & Hahne, E. 1993. Thermophysical properties of the composite ceramic-salt system (SiO2 /Na2SO4). *Thermochimica Acta,* 218**,** 455-463.

[21] Guo, H., Guo, J., Baker, A. & Randall, C. A. 2016. Hydrothermal-Assisted Cold Sintering Process: A New Guidance for Low-Temperature Ceramic Sintering. *ACS Applied Materials & Interfaces,* 8**,** 20909-20915

[22] German, R.M., *Sintering: From Empirical Observations to Scientific Principles*. Sintering: From Empirical Observations to Scientific Principles. 2014, Oxford: Butterworth-Heinemann. 1-536.

[23] Vandiver, P. B.; Soffer, O.; Klima, B.; Svoboda, J., The Origins Of Ceramic Technology At Dolni-Vestonice, Czechoslovakia. Science 1989, 246 (4933), 1002-1008.

[24] Rahaman, M. N., Sintering of ceramics / Mohamed N. Rahaman. Boca Raton, Fla. : CRC London : Taylor & Francis distributor: Boca Raton, Fla. : London, 2008.

[25] German, R. M., Sintering theory and practice / Randall M. German. New YorkChichester: Wiley: New York Chichester, 1996.

[26] Guo, J.; Guo, H. Z.; Baker, A. L.; Lanagan, M. T.; Kupp, E. R.; Messing, G. L.; Randall, C. A., Cold Sintering: A Paradigm Shift for Processing and Integration of Ceramics. *Angewandte Chemie-International Edition* 2016, 55 (38), 11457-11461.

[27] Bordia, R. K.; Kang, S.-J. L.; Olevsky, E. A., Current understanding and future research directions at the onset of the next century of sintering science and technology. Journal of the American Ceramic Society 2017, 100 (6), 2314-2352.

[28] Rahaman, M. N., 2 - Kinetics and mechanisms of densification. In Sintering of Advanced Materials, Fang, Z. Z., Ed. Woodhead Publishing: 2010; pp 33-64.

[29] Courtney, T. H., Densification and structural development in liquid phase sintering. Metallurgical and Materials Transactions A 1984, 15 (6), 1065-1074.

[30] Medri, V.; Servadei, F.; Bendoni, R.; Natali Murri, A.; Vaccari, A.; Landi, E., Nano-to-macroporous TiO2 (anatase) by cold sintering process. Journal of the European Ceramic Society 2019, 39 (7), 2453-2462.

[31] Gu, J. and Z. Fu, *Pressure-enhanced densification of TaC ceramics during flash spark plasma sintering.* Journal of the American Ceramic Society, 2019. **102**(1): p. 98-103.

[32] Ibrahim, M. K.; Hamzah, E.; Saud, S. N.; Nazim, E. M., Powder Metallurgy Fabrication of Porous 51(at.%)Ni–Ti Shape Memory Alloys for Biomedical Applications. Shape Memory and Superelasticity 2018, 4 (2), 327-336.

[33] Biesuz, M.; Sglavo, V. M., Flash sintering of ceramics. Journal of the European Ceramic Society 2019, 39 (2), 115-143.

[34] Radajewski, M.; Decker, S.; Krüger, L., Direct temperature measurement via thermocouples within an SPS/FAST graphite tool. Measurement 2019, 147, 106863.

[35] German, R. M.; Suri, P.; Park, S. J., Review: liquid phase sintering. Journal of Materials Science 2009, 44 (1), 1-39.

[36] Maria, J.-P.; Kang, X.; Floyd, R. D.; Dickey, E. C.; Guo, H.; Guo, J.; Baker, A.; Funihashi, S.; Randall, C. A., Cold sintering: Current status and prospects. Journal of Materials Research 2017, 32 (17), 3205-3218.

[37] Guo, H. Z.; Baker, A.; Guo, J.; Randall, C. A., Protocol for Ultralow-Temperature Ceramic Sintering: An Integration of Nanotechnology and the Cold Sintering Process. Acs Nano 2016, 10 (11), 10606-10614.

[38] Guo, H.; Baker, A.; Guo, J.; Randall, C. A., Cold Sintering Process: A Novel Technique for Low-Temperature Ceramic Processing of Ferroelectrics. *Journal of the American Ceramic Society* 2016, 99 (11), 3489-3507.

[39] Gonzalez-Julian, J.; Neuhaus, K.; Bernemann, M.; Pereira da Silva, J.; Laptev, A.; Bram, M.; Guillon, O., Unveiling the mechanisms of cold sintering of ZnO at 250 °C by varying applied stress and characterizing grain boundaries by Kelvin Probe Force Microscopy. *Acta Materialia* 2018, 144, 116-128.

[40] Funahashi, S.; Guo, H.; Guo, J.; Baker, A. L.; Wang, K.; Shiratsuyu, K.; Randall, C. A., Cold sintering and co-firing of a multilayer device with thermoelectric materials. Journal of the American Ceramic Society 2017, 100 (8), 3488-3496.

[41] Hong, W. B.; Li, L.; Cao, M.; Chen, X. M., Plastic deformation and effects of water in room-temperature cold sintering of NaCl microwave dielectric ceramics. Journal of the American Ceramic Society 2018, 101 (9), 4038-4043.

[42] Bouville, F.; Studart, A. R., Geologically inspired strong bulk ceramics made with water at room temperature. Nature Communications 2017, 8, 8.

[43] Nakaya, H.; Iwasaki, M.; de Beauvoir, T. H.; Randall, C. A., Applying cold sintering process to a proton electrolyte material: CsH2PO4. Journal of the European Ceramic Society 2019, 39 (2), 396-401.

[44] Hong, W. B.; Li, L.; Yan, H.; Chen, X. M., Cold sintering and microwave dielectric properties of dense HBO2-II ceramics. J. Am. Ceram. Soc. 2019, 102 (10), 5934-5940.

[45] Guo, H. Z.; Bayer, T. J. M.; Guo, J.; Baker, A.; Randall, C. A., Current progress and perspectives of applying cold sintering process to ZrO2-based ceramics. Scripta Materialia 2017, 136, 141-148.

[46] Gyan, D. S.; Dwivedi, A., Structural and electrical characterization of NaNbO3-PVDF nanocomposites fabricated using cold sintering synthesis route. Journal of Applied Physics 2019, 125 (2), 024103.

[47] Suleiman, B.; Yu, Q.; Ding, Y.; Li, Y., Fabrication of form stable NaCl-Al2O3 composite for thermal energy storage by cold sintering process. Frontiers of Chemical Science and Engineering 2019, 13 (4), 727-735.

[48] Liu, M.; Jin, Q.; Shen, P., Cold sintering of NaNO3/MgO heat-storage composite. Ceramics International 2020, 46 (18, Part A), 28955-28960.

[49] Yu, Q.; Jiang, Z.; Cong, L.; Lu, T.; Suleiman, B.; Leng, G.; Wu, Z.; Ding, Y.; Li, Y., A novel low-temperature fabrication approach of composite phase change materials for high temperature thermal energy storage. Applied Energy 2019, 237, 367-377.

[50] Vakifahmetoglu, C.; Karacasulu, L., Cold sintering of ceramics and glasses: A review. Current Opinion in *Solid State and Materials Science* 2020, 24 (1), 100807.

[51] Gonzalez-Julian, J.; Neuhaus, K.; Bernemann, M.; da Silva, J. P.; Laptev, A.; Bram, M.; Guillon, O., Unveiling the mechanisms of cold sintering of ZnO at 250 degrees C by varying applied stress and characterizing grain boundaries by Kelvin Probe Force Microscopy. Acta Materialia 2018, 144, 116-128.

[52] Grasso, S.; Biesuz, M.; Zoli, L.; Taveri, G.; Duff, A. I.; Ke, D.; Jiang, A.; Reece, M. J., A review of cold sintering processes. Advances in Applied Ceramics 2020, 119 (3), 115-143.

[53] Guo, J.; Floyd, R.; Lowum, S.; Maria, J.-P.; Herisson de Beauvoir, T.; Seo, J.-H.; Randall, C. A., Cold Sintering: Progress, Challenges, and Future Opportunities. Annual Review of Materials Research 2019, 49 (1), 275-295.

[54] Funahashi, S.; Guo, J.; Guo, H.; Wang, K.; Baker, A. L.; Shiratsuyu, K.; Randall, C. A., Demonstration of the cold sintering process study for the densification and grain growth of ZnO ceramics. Journal of the American Ceramic Society 2017, 100 (2), 546-553.

[55] Zhang, X.; Spiers, C. J.; Peach, C. J., Compaction creep of wet granular calcite by pressure solution at 28°C to 150°C. Journal of Geophysical Research: Solid Earth 2010, 115 (B9).

[56] Kang, S.J.L., *5 - Liquid phase sintering*, in *Sintering of Advanced Materials*, Z.Z. Fang, Editor. 2010, Woodhead Publishing. p. 110-129.

[57] German, R.; Suri, P.; Park, S., Review: liquid phase sintering. Journal of Materials Science 2009, 44 (1), 1-39.

[58] Hosoi, K.; Kawai, S.; Yanagisawa, K.; Yamasaki, N., Densification process for spherical glass powders with the same particle size by hydrothermal hot pressing. Journal of Materials Science 1991, 26 (23), 6448-6452.

[59] Urai, J.; Schléder, Z.; Spiers, C.; Kukla, P., Flow and Transport Properties of Salt Rocks. 2008; pp 277-290.

[60] Kingery, W. D.; Woulbroun, J. M.; Charvat, F. R., Effects of Applied Pressure on Densification During Sintering in the Presence of a Liquid Phase. Journal of the American Ceramic Society 1963, 46 (8), 391-395.

[61] Carter, N. L.; Horseman, S. T.; Russell, J. E.; Handin, J., Rheology of rocksalt. Journal of Structural Geology 1993, 15 (9), 1257-1271.

[62] Chen, M.; Wu, S.; Xu, S.; Yu, B.; Shilbayeh, M.; Liu, Y.; Zhu, X.; Wang, J.; Gong, J., Caking of crystals: Characterization, mechanisms and prevention. Powder Technology 2018, 337, 51-67.

[63] Langer, J.; Hoffmann, M. J.; Guillon, O., Electric Field-Assisted Sintering and Hot Pressing of Semiconductive Zinc Oxide: A Comparative Study. Journal of the American Ceramic Society 2011, 94 (8), 2344-2353.

[64] Guo, J.; Floyd, R.; Lowum, S.; Maria, J. P.; de Beauvoir, T. H.; Seo, J. H.; Randall, C. A., Cold Sintering: Progress, Challenges, and Future Opportunities. In Annual Review of Materials Research, Vol 49, Clarke, D. R., Ed. Annual Reviews: Palo Alto, 2019; Vol. 49, pp 275-295.

[65] Cong, L.; Huajing, W.; Jianzhang, M.; Baoyu, D.; Xiao, W.; Tengfei, L.; Xinghua, Z.; Xing, Y., Effect of dwell time on cold sintering assisted sintering based highly transparent 0.9K0.5Na0.5NbO3-0.1LiBiO3 ceramics. Journal of Alloys and Compounds 2020, 826, 154249.

[66] Haug, M.; Bouville, F.; Ruiz-Agudo, C.; Avaro, J.; Gebauer, D.; Studart, A. R., Cold densification and sintering of nanovaterite by pressing with water. Journal of the European Ceramic Society 2020, 40 (3), 893-900.

[67] Li, L.; Hong, W. B.; Yang, S.; Yan, H.; Chen, X. M., Effects of water content during cold sintering process of NaCl ceramics. Journal of Alloys and Compounds 2019, 787, 352-357.

[68] Kang, X.; Floyd, R.; Lowum, S.; Cabral, M.; Dickey, E.; Maria, J.-P., Mechanism studies of hydrothermal cold sintering of zinc oxide at near room temperature. *Journal of the American Ceramic Society* 2019, 102 (8), 4459-4469.

[69] Taveri, G., Grasso, S., Gucci, F., Toušek, J., & Dlouhy, I. (2018). Bio-Inspired Hydro-Pressure Consolidation of Silica. *Advanced Functional Materials, 28*(48), 1805794. doi:10.1002/adfm.201805794

[70] Shen, H.-Z.; Guo, N.; Zhao, L.; Shen, P., Role of ion substitution and lattice water in the densification of cold-sintered hydroxyapatite. Scripta Materialia 2020, 177, 141-145.

[71] Feng, D.; Feng, Y.; Qiu, L.; Li, P.; Zang, Y.; Zou, H.; Yu, Z.; Zhang, X., Review on nanoporous composite phase change materials: Fabrication, characterization, enhancement and molecular simulation. Renewable and Sustainable Energy Reviews 2019, 109, 578-605.

[72] Lau, A. P. S., Porous materials: processing and applications / by P.S. Liu, G.F. Chen. Burlington: Elsevier Science: Burlington, 2014.

[73] Yadav, A. K.; Bhattacharyya, S., A new approach for the fabrication of porous alumina beads using acid leachate of kaolin. Microporous and Mesoporous Materials 2020, 293, 109795.

[74] Yuan, B.; Wu, H.; Sun, X.; Wang, G.; Li, H., Fabrication of porous alumina green bodies from suspension emulsions by gelcasting. Materials Letters 2012, 81, 151-154.

[75] Oh, S.-T.; Tajima, K.-i.; Ando, M.; Ohji, T., Fabrication of porous Al2O3 by microwave sintering and its properties. Materials Letters 2001, 48 (3), 215-218.

[76] Takahashi, R.; Onishi, A.; Sato, F.; Kuramoto, M., Preparation of bimodal porous alumina using propylene glycol oligomers. Journal of the Ceramic Society of Japan 2017, 125 (10), 742-746.

[77] Wan, Z.; Zhang, X.; Guan, L.; Cai, C.; Feng, Y.; Ding, H.; Gui, H., Sintering Kinetics of Porous Ceramics from High-Alumina Fly Ash. Transactions of the Indian Ceramic Society 2017, 76 (3), 171-175.

[78] Liu, R. P.; Li, Y. T.; Wang, C. A.; Tie, S. N., Fabrication of porous alumina-zirconia ceramics by gel-casting and infiltration methods. Materials & Design 2014, 63, 1-5.

[79] Shingubara, S., Fabrication of nanomaterials using porous alumina templates. Journal of Nanoparticle Research 2003, 5 (1-2), 17-30.

[80] Zhou, K.; Zhang, Y.; Zhang, D.; Zhang, X.; Li, Z.; Liu, G.; Button, T., Porous hydroxyapatite ceramics fabricated by an ice-templating method. 2011.

[81] Liu, R.; Wang, C.-a., Effects of mono-dispersed PMMA micro-balls as pore-forming agent on the properties of porous YSZ ceramics. Journal of the European Ceramic Society 2013, 33 (10), 1859-1865.

[82] Liu, G. Fabrication of porous ceramics and composites by a novel freeze casting process / by Gang Liu. Thesis (PhD)--University of Birmingham, School of Metallurgy and Materials, College of Engineering and Physical Sciences. Birmingham : University of Birmingham, Birmingham, 2011.

[83] Lazarowich, R. J.; Taborek, P.; Yoo, B. Y.; Myung, N. V., Fabrication of porous alumina on quartz crystal microbalances. Journal of Applied Physics 2007, 101 (10), 104909.

[84] Fukasawa, T.; Ando, M.; Ohji, T.; Kanzaki, S., Synthesis of Porous Ceramics with Complex Pore Structure by Freeze-Dry Processing. Journal of the American Ceramic Society 2001, 84 (1), 230-232.

[85] Ibrahim, N. I.; Al-Sulaiman, F. A.; Rahman, S.; Yilbas, B. S.; Sahin, A. Z., Heat transfer enhancement of phase change materials for thermal energy storage applications: A critical review. Renewable and Sustainable Energy Reviews 2017, 74, 26-50.

[86] Wu, W.; Yang, X.; Zhang, G.; Chen, K.; Wang, S., Experimental investigation on the thermal performance of heat pipe-assisted phase change material based battery thermal management system. Energy Conversion and Management 2017, 138, 486-492.

[87] Xiao, X.; Zhang, P.; Li, M., Experimental and numerical study of heat transfer performance of nitrate/expanded graphite composite PCM for solar energy storage. Energy Conversion and Management 2015, 105, 272-284.

[88] Zhou, L.; Tang, L.-S.; Tao, X.-F.; Yang, J.; Yang, M.-B.; Yang, W., Facile fabrication of shape-stabilized polyethylene glycol/cellulose nanocrystal phase change materials based on thiol-ene click chemistry and solvent exchange. Chemical Engineering Journal 2020, 396, 125206.

[89] Karaipekli, A.; Sarı, A., Development and thermal performance of pumice/organic PCM/gypsum composite plasters for thermal energy storage in buildings. Solar Energy Materials and Solar Cells 2016, 149, 19-28.

[90] Tang, L.-S., Yang, J., Bao, R.-Y., Liu, Z.-Y., Xie, B.-H., Yang, M.-B., & Yang, W. (2017). Polyethylene glycol/graphene oxide aerogel shape-stabilized phase change materials for photo-to-thermal energy conversion and storage via tuning the oxidation degree of graphene oxide. *Energy Conversion and Management, 146*, 253-264.

[91] Xu, B.; Li, P.; Chan, C., Application of phase change materials for thermal energy storage in concentrated solar thermal power plants: A review to recent developments. Applied Energy 2015, 160, 286-307.

[92] Fang, G.; Tang, F.; Cao, L., Preparation, thermal properties and applications of shape-stabilized thermal energy storage materials. Renewable and Sustainable Energy Reviews 2014, 40, 237-259.

[93] Liu, H.; Wang, X.; Wu, D., Innovative design of microencapsulated phase change materials for thermal energy storage and versatile applications: a review. Sustainable energy & fuels 2019, 3 (5), 191-1149.

[94] Drissi, S.; Ling, T.-C.; Mo, K. H.; Eddhahak, A., A review of microencapsulated and composite phase change materials: Alteration of strength and thermal properties of cement-based materials. Renewable and Sustainable Energy Reviews 2019, 110, 467-484.

[95] Zhou, Y.; Wu, S.; Ma, Y.; Zhang, H.; Zeng, X.; Wu, F.; Liu, F.; Ryu, J. E.; ; Guo, Z., Recent Advances in Organic/Composite Phase Change Materials for Energy Storage. ES Energy & Environment 2020, 9, 28-40.

[96] Alva, G.; Liu, L.; Huang, X.; Fang, G., Thermal energy storage materials and systems for solar energy applications. Renewable and Sustainable Energy Reviews 2017, 68, 693-706.

[97] Xie, Y.; Yang, Y.; Liu, Y.; Wang, S.; Guo, X.; Wang, H.; Cao, D., Paraffin/polyethylene/graphite composite phase change materials with enhanced thermal conductivity and leakage-proof. Advanced Composites and Hybrid Materials 2021.

[98] Zhang, H.; Balram, A.; Tiznobaik, H.; Shin, D.; Santhanagopalan, S., Microencapsulation of molten salt in stable silica shell via a water-limited sol-gel process for high temperature thermal energy storage. Applied Thermal Engineering 2018, 136, 268-274.

[99] Huang, Y.; Cheng, X.; Li, Y.; Shi, D.; Li, G.; Xu, K., Effect of sol-gel combustion synthesis of nanoparticles on thermal properties of KNO3-NaNO3. Solar Energy Materials and Solar Cells 2018, 188, 190-201.

[100] Zhang, G.; Deng, Z.; Lu, Y.; Hao, J.; Ren, Z.; Yang, C.; Xu, G.; Wang, T., Thermal energy storage using composite phase change materials with molten salt particles encapsulated/ceramic composite by sol-gel method. Energy Sources, Part A: Recovery, Utilization, and Environmental Effects 2019, 1-11.

[101] Wu, J.; Li, J.; Xu, X.; Yang, L.; Wu, J.; Zhao, F.; Li, C., Molten salts/ceramic-foam matrix composites by melt infiltration method as energy storage material. Journal of Wuhan University of Technology-Mater. Sci. Ed. 2009, 24 (4), 651-653.

[102] Qian, T.; Li, J.; Min, X.; Deng, Y.; Guan, W.; Ning, L., Diatomite: A promising natural candidate as carrier material for low, middle and high temperature phase change material. Energy Conversion and Management 2015, 98, 34-45.

[103] Ge, Z.; Ye, F.; Cao, H.; Leng, G.; Qin, Y.; Ding, Y., Carbonate-salt-based composite materials for medium- and high-temperature thermal energy storage. Particuology 2014, 15, 77-81.

[104] Li, C.; Li, Q.; Cong, L.; jiang, F.; Zhao, Y.; Liu, C.; Xiong, Y.; Chang, C.; Ding, Y., MgO based composite phase change materials for thermal energy storage: The effects of MgO particle density and size on microstructural characteristics as well as thermophysical and mechanical properties. Applied Energy 2019, 250, 81-91.

[105] Ran, X.; Wang, H.; Zhong, Y.; Zhang, F.; Lin, J.; Zou, H.; Dai, Z.; An, B., Thermal properties of eutectic salts/ceramics/expanded graphite composite phase change materials for high-temperature thermal energy storage. Solar Energy Materials and Solar Cells 2021, 225, 111047.

[106] Al Shannaq, R.; Farid, M. M., 10 - Microencapsulation of phase change materials (PCMs) for thermal energy storage systems. In Advances in Thermal Energy Storage Systems, Cabeza, L. F., Ed. Woodhead Publishing: 2015; pp 247-284.

[107] Zhao, Y.; Zhang, X.; Hua, W., Review of preparation technologies of organic composite phase change materials in energy storage. Journal of Molecular Liquids 2021, 336, 115923.

[108] Memon, S. A., Phase change materials integrated in building walls: A state of the art review. Renewable and Sustainable Energy Reviews 2014, 31, 870-906.

[109] Yu, F.; Chen, Z.-H.; Zeng, X.-R., Preparation, characterization, and thermal properties of microPCMs containing n-dodecanol by using different types of styrene-maleic anhydride as emulsifier. Colloid and Polymer Science 2009, 287 (5), 549-560.

[110] Su, J.-F.; Wang, S.-B.; Zhang, Y.-Y.; Huang, Z., Physicochemical properties and mechanical characters of methanol-modified melamine-formaldehyde (MMF) shell microPCMs containing paraffin. Colloid and Polymer Science 2011, 289 (2), 111-119.

[111] Pan, L.; Tao, Q.; Zhang, S.; Wang, S.; Zhang, J.; Wang, S.; Wang, Z.; Zhang, Z., Preparation, characterization and thermal properties of micro-encapsulated phase change materials. Solar Energy Materials and Solar Cells 2012, 98, 66-70.

[112] Zhang, X.-x.; Fan, Y.-f.; Tao, X.-m.; Yick, K.-l., Crystallization and prevention of supercooling of microencapsulated n-alkanes. Journal of Colloid and Interface Science 2005, 281 (2), 299-306.

[113] Boh, B.; Knez, E.; Staresinic, M., Microencapsulation of higher hydrocarbon phase change materials by in situ polymerization. J Microencapsul 2005, 22 (7), 715-35.

[114] Lan, X.-Z.; Tan, Z.-C.; Zou, G.-L.; Sun, L.-X.; Zhang, T., Microencapsulation of n-Eicosane as Energy Storage Material. Chinese Journal of Chemistry 2004, 22 (5), 411-414.

[115] Huang, X.; Chen, X.; Li, A.; Atinafu, D.; Gao, H.; Dong, W.; Wang, G., Shape-stabilized phase change materials based on porous supports for thermal energy storage applications. Chemical Engineering Journal 2019, 356, 641-661.

[116] Zhang, L.; Liao, W.; Wei, Y.; Tong, Z.; Wang, Y.; Gao, Y., Fabrication, characterization and in vitro digestion of food-grade β-carotene high loaded microcapsules: A wet-milling and spray drying coupling approach. LWT 2021, 151, 112176.

[117] Fei, B.; Lu, H.; Qi, K.; Shi, H.; Liu, T.; Li, X.; Xin, J. H., Multi-functional microcapsules produced by aerosol reaction. Journal of Aerosol Science 2008, 39 (12), 1089-1098.

[118] Hawlader, M. N. A.; Uddin, M. S.; Khin, M. M., Microencapsulated PCM thermal-energy storage system. 2003.

[119] Jiang, F.; Zhang, L.; She, X.; Li, C.; Cang, D.; Liu, X.; Xuan, Y.; Ding, Y., Skeleton materials for shape-stabilization of high temperature salts based phase change materials: A critical review. Renewable and Sustainable Energy Reviews 2020, 119, 109539.

[120] Yu, K.; Liu, Y.; Yang, Y., Review on form-stable inorganic hydrated salt phase change materials: Preparation, characterization and effect on the thermophysical properties. Applied Energy 2021, 292, 116845.

[121] Goitandia, A. M.; Beobide, G.; Aranzabe, E.; Aranzabe, A., Development of content-stable phase change composites by infiltration into inorganic porous supports. Solar Energy Materials and Solar Cells 2015, 134, 318-328.

[122] Zhang, D.; Tian, S.; Xiao, D., Experimental study on the phase change behavior of phase change material confined in pores. Solar Energy 2007, 81 (5), 653-660.

[123] do Couto Aktay, K. S.; Tamme, R.; Müller-Steinhagen, H., Thermal Conductivity of High-Temperature Multicomponent Materials with Phase Change. International Journal of Thermophysics 2008, 29 (2), 678-692.

[124] Bauer, T.; Tamme, R.; Christ, M.; Öttinger, O., PCM-Graphite Composites for High Temperature Thermal Energy Storage. 2006.

[125] Aktay, K. S.; Tamme, R.; Müller-Steinhagen, H., PCM-Graphite Storage Materials for the Temperature Range 100-300°C. 2005.

[126] Rathore, P. K. S.; Shukla, S. k., Improvement in thermal properties of PCM/Expanded vermiculite/expanded graphite shape stabilized composite PCM for building energy applications. Renewable Energy 2021, 176, 295-304.

[127] Lan, H., Dutta, S., Vahedi, N., Neti, S., Romero, C. E., Oztekin, A., . . . Ruales, R. (2020). Graphite foam infiltration with mixed chloride salts as PCM for high-temperature latent heat storage applications. *Solar Energy, 209*, 505-514.

[128] Zhang, Z.; Fang, X., Study on paraffin/expanded graphite composite phase change thermal energy storage material. Energy Conversion and Management 2006, 47 (3), 303-310.

[129] Li, M.; Wu, Z.; Kao, H.; Tan, J., Experimental investigation of preparation and thermal performances of paraffin/bentonite composite phase change material. Energy Conversion and Management 2011, 52 (11), 3275-3281.

[130] Wang, W.; Yang, X.; Fang, Y.; Ding, J., Preparation and performance of form-stable polyethylene glycol/silicon dioxide composites as solid–liquid phase change materials. Applied Energy 2009, 86 (2), 170-174.

[131] Feng, L.; Zhao, W.; Zheng, J.; Frisco, S.; Song, P.; Li, X., The shape-stabilized phase change materials composed of polyethylene glycol and various mesoporous matrices (AC, SBA-15 and MCM-41). Solar Energy Materials and Solar Cells 2011, 95 (12), 3550-3556.

[132] Zhu, S.; Chen, J.; Li, H.; Cao, Y.; Yang, Y.; Feng, Z., Preparation and properties of montmorillonite/poly(ethylene glycol) grafted polypropylene/polypropylene nanocomposites. Applied Clay Science 2014, 87, 303-310.

[133] Tian, B.; Yang, W.; Luo, L.; Wang, J.; Zhang, K.; Fan, J.; Wu, J.; Xing, T., Synergistic enhancement of thermal conductivity for expanded graphite and carbon fiber in paraffin/EVA form-stable phase change materials. Solar Energy 2016, 127, 48-55.

[134] Li, Y.; Guo, B.; Huang, G.; Kubo, S.; Shu, P., Characterization and thermal performance of nitrate mixture/SiC ceramic honeycomb composite phase change materials for thermal energy storage. Applied Thermal Engineering 2015, 81, 193-197.

[135] Mochane, M. J.; Luyt, A. S., The effect of expanded graphite on the flammability and thermal conductivity properties of phase change material based on PP/wax blends. Polymer Bulletin 2015, 72 (9), 2263-2283.

[136] Ling, Z.; Chen, J.; Xu, T.; Fang, X.; Gao, X.; Zhang, Z., Thermal conductivity of an organic phase change material/expanded graphite composite across the phase change temperature range and a novel thermal conductivity model. Energy Conversion and Management 2015, 102, 202-208.

[137] Seki, Y.; İnce, Ş.; Ezan, M. A.; Turgut, A.; Erek, A., Graphite nanoplates loading into eutectic mixture of Adipic acid and Sebacic acid as phase change material. Solar Energy Materials and Solar Cells 2015, 140, 457-463.

[138] Tang, F.; Su, D.; Tang, Y.; Fang, G., Synthesis and thermal properties of fatty acid eutectics and diatomite composites as shape-stabilized phase change materials with enhanced thermal conductivity. Solar Energy Materials and Solar Cells 2015, 141, 218-224.

[139] Wu, Y.; Wang, T., Hydrated salts/expanded graphite composite with high thermal conductivity as a shape-stabilized phase change material for thermal energy storage. Energy Conversion and Management 2015, 101, 164-171.

[140] Zhong, L.; Zhang, X.; Luan, Y.; Wang, G.; Feng, Y.; Feng, D., Preparation and thermal properties of porous heterogeneous composite phase change materials based on molten salts/expanded graphite. Solar Energy 2014, 107, 63-73.

[141] Chieruzzi, M.; Miliozzi, A.; Crescenzi, T.; Torre, L.; Kenny, J. M., A New Phase Change Material Based on Potassium Nitrate with Silica and Alumina Nanoparticles for Thermal Energy Storage. Nanoscale Research Letters 2015, 10 (1), 273.

[142] Miliozzi, A.; Chieruzzi, M.; Torre, L., Experimental investigation of a cementitious heat storage medium incorporating a solar salt/diatomite composite phase change material. Applied Energy 2019, 250, 1023-1035.

[143] Li, R.; Zhu, J.; Zhou, W.; Cheng, X.; Li, Y., Thermal compatibility of Sodium Nitrate/Expanded Perlite composite phase change materials. Applied Thermal Engineering 2016, 103, 452-458.

[144] Li, R.; Zhu, J.; Zhou, W.; Cheng, X.; Li, Y., Thermal properties of sodium nitrate-expanded vermiculite form-stable composite phase change materials. Materials & Design 2016, 104, 190-196.

[145] Tian, H.; Wang, W.; Ding, J.; Wei, X.; Huang, C., Preparation of binary eutectic chloride/expanded graphite as high-temperature thermal energy storage materials. Solar Energy Materials and Solar Cells 2016, 149, 187-194.

[146] Chen, Y.; Wu, X.; Situ, Y.; Liu, J.; Huang, H., Ethylene-Propylene Terpolymer-Modified Polyethylene-Based Phase Change Material with Enhanced Mechanical and Thermal Properties for Building Application. Industrial & Engineering Chemistry Research 2019, 58 (1), 179-186.

[147] AlMaadeed, M. A.; Labidi, S.; Krupa, I.; Karkri, M., Effect of expanded graphite on the phase change materials of high density polyethylene/wax blends. Thermochimica Acta 2015, 600, 35-44.

[148] Chen, F.; Wolcott, M., Polyethylene/paraffin binary composites for phase change material energy storage in building: A morphology, thermal properties, and paraffin leakage study. Solar Energy Materials and Solar Cells 2015, 137, 79-85.

[149] Li, L.; Wang, G.; Guo, C., Influence of intumescent flame retardant on thermal and flame retardancy of eutectic mixed paraffin/polypropylene form-stable phase change materials. Applied Energy 2016, 162, 428-434.

[150] Su, J.-F.; Wang, L.-X.; Ren, L.; Huang, Z.; Meng, X.-W., Preparation and characterization of polyurethane microcapsules containing n-octadecane with styrene-maleic anhydride as a surfactant by interfacial polycondensation. Journal of Applied Polymer Science 2006, 102 (5), 4996-5006.

[151] Chashchilov, D. V.; Samoylenko, V. V.; Atyasova, E. V.; Khabazin, I. S.; Blaznov, A. N.; Firsov, V. V.; Sakoshev, Z. G.; Bychin, N. V., Development of a Polymer Composite Material with an Epoxy Binder for Producing a High-Pressure Cylinder. Chemical and Petroleum Engineering 2021, 57 (3), 339-345.

[152] Ren, J.; Ma, B.; Si, W.; Zhou, X.; Li, C., Preparation and analysis of composite phase change material used in asphalt mixture by sol–gel method. Construction and Building Materials 2014, 71, 53-62.

[153] Xu, L.; Zhang, J.; Liu, C.; Li, N.; Chen, L.; Zhang, S.; Wang, Z., Fast Thermal Response of Shape-Stabilized Thermal Storage Materials: The Case of Interconnected Netlike Graphene/Hexadecane/HDPE Composites. ACS omega 2020, 5 (21), 12415-12420.

[154] Nomura, T.; Okinaka, N.; Akiyama, T., Technology of Latent Heat Storage for High Temperature Application: A Review. Isij International 2010, 50, 1229-1239.

[155] Chen, C., L. Wang, and Y. Huang, *Electrospinning of thermo-regulating ultrafine fibers based on polyethylene glycol/cellulose acetate composite.* Polymer, 2007. **48**(18): p. 5202-5207.

[156] Cai, Y., Sun, G., Liu, M., Zhang, J., Wang, Q., & Wei, Q. (2015). Fabrication and characterization of capric–lauric–palmitic acid/electrospun SiO2 nanofibers composite as form-stable phase change material for thermal energy storage/retrieval. *Solar Energy, 118,* 87-95

[157] Kuo, J.-C.; Lee, S.-C.; Hsu, K.-C.; Liu, S.-J.; Chou, B.-Y.; Fu, Y.-S., Fabrication of LiNi0.5+δMn0.5−δO2 nanofibers by electrospinning. Materials Letters 2008, 62 (30), 4594-4596.

[158] Long, Y.-Z., Yan, X., Wang, X.-X., Zhang, J., & Yu, M. (2019). Chapter 2 - Electrospinning: The Setup and Procedure. In B. Ding, X. Wang, & J. Yu (Eds.), *Electrospinning: Nanofabrication and Applications* (pp. 21-52): William Andrew Publishing.

[159] Amin, M.; Putra, N.; Kosasih, E. A.; Prawiro, E.; Luanto, R. A.; Mahlia, T. M. I., Thermal properties of beeswax/graphene phase change material as energy storage for building applications. Applied Thermal Engineering 2017, 112, 273-280.

[160] Xiao, J.; Huang, J.; Zhu, P.; Wang, C.; Li, X., Preparation, characterization and thermal properties of binary nitrate salts/expanded graphite as composite phase change material. Thermochimica Acta 2014, 587, 52-58.

[161] Safira, L., Putra, N., Trisnadewi, T., Kusrini, E., & Mahlia, T. M. I. (2020). Thermal properties of sonicated graphene in coconut oil as a phase change material for energy storage in building applications1. *International Journal of Low-Carbon Technologies, 15*(4), 629-636.

[162] Deng, Y.; Li, J.; Qian, T.; Guan, W.; Wang, X., Preparation and Characterization of KNO3/Diatomite Shape-Stabilized Composite Phase Change Material for High Temperature Thermal Energy Storage. *Journal of Materials Science & Technology* 2017, 33 (2), 198-203.

[163] Ge, Z. W.; Li, Y. L.; Li, D. C.; Sun, Z.; Jin, Y.; Liu, C. P.; Li, C.; Leng, G. H.; Ding, Y. L., Thermal energy storage: Challenges and the role of particle technology. Particuology 2014, 15, 2-8.

[164] Qian, T. T.; Li, J. H.; Mm, X.; Deng, Y.; Guan, W. M.; Ning, L., Radial-like mesoporous silica sphere: A promising new candidate of supporting material for storage of low-, middle-, and high-temperature heat. Energy 2016, 112, 1074-1083.

[165] Liu, S. Y.; Yang, H. M., Porous ceramic stabilized phase change materials for thermal energy storage. Rsc Advances 2016, 6 (53), 48033-48042.

[166] Li, Q.; Cong, L.; Zhang, X.; Dong, B.; Zou, B.; Du, Z.; Xiong, Y.; Li, C., Fabrication and thermal properties investigation of aluminium based composite phase change material for medium and high temperature thermal energy storage. Solar Energy Materials and Solar Cells 2020, 211, 110511.

[167] Jiang, Y.; Sun, Y.; Li, S., Performance of novel Na2SO4-NaCl-ceramic composites as high temperature phase change materials for solar power plants (Part II). Solar Energy Materials and Solar Cells 2019, 194, 285-294.

[168] Qin, Y.; Leng, G.; Yu, X.; Cao, H.; Qiao, G.; Dai, Y.; Zhang, Y.; Ding, Y., Sodium sulfate–diatomite composite materials for high temperature thermal energy storage. Powder Technology 2015, 282, 37-42.

[169] Xu, G.; Leng, G.; Yang, C.; Qin, Y.; Wu, Y.; Chen, H.; Cong, L.; Ding, Y., Sodium nitrate – Diatomite composite materials for thermal energy storage. Solar Energy 2017, 146, 494-502.

[170] Sang, L.; Li, F.; Xu, Y., Form-stable ternary carbonates/MgO composite material for high temperature thermal energy storage. Solar Energy 2019, 180, 1-7.

[171] NAVARRO Maria Elena1, P. A., HUGHES Tomos1, CONNOLLY Chloe1, UPPAL Harkiran1, CONG Lin1, LEI Xianzhang2, QIAO Geng1,2, LENG Guanghui1, DING Yulong1, Ceramic-salt based composites for thermal energy storage. Energy Storage Science and Technology 2017, 6 (4), 688-695.

[172] Gokon, N.; Nakano, D.; Inuta, S.; Kodama, T., High-temperature carbonate/MgO composite materials as thermal storage media for double-walled solar reformer tubes. Solar Energy 2008, 82 (12), 1145-1153.

[173] German, R. M., 1 - Thermodynamics of sintering. In Sintering of Advanced Materials, Fang, Z. Z., Ed. Woodhead Publishing: 2010; pp 3-32.

[174] German, R. M., Chapter One - Introduction. In Sintering: from Empirical Observations to Scientific Principles, German, R. M., Ed. Butterworth-Heinemann: Boston, 2014; pp 1-12.

[175] German, R. M., Chapter Two - History of Sintering. In Sintering: from Empirical Observations to Scientific Principles, German, R. M., Ed. Butterworth-Heinemann: Boston, 2014; pp 13-40.

[176] Aizenberg, J.; Muller, D. A.; Grazul, J. L.; Hamann, D. R., Direct Fabrication of Large Micropatterned Single Crystals. Science 2003, 299 (5610), 1205-1208.

[177] Petrovich, R., Rates of chemical weathering of rocks and minerals: edited by S. M. Colman and D. P. Dethier. Academic Press, 1986, xviii + 603 p., $95.00. Geochimica et Cosmochimica Acta 1987, 51 (3), 765.

[178] Kittrick, J. A., Rates of chemical weathering of rocks and minerals: edited by Steven M. Colman and David P. Dethier. Academic Press, 1986, 603p., $99.00 (ISBN 0-12-181490-4). Geochimica et Cosmochimica Acta 1989, 53 (8), 2133.

[179] Jon-Paul, M.; Kang, X.; Floyd, R. D.; Dickey, E. C.; Guo, H.; Guo, J.; Baker, A.; Funihashi, S.; Randall, C. A., Cold sintering: Current status and prospects. Journal of Materials Research 2017, 32 (17), 3205-3218.

[180] Zamora, V.; Ortiz, A. L.; Guiberteau, F.; Nygren, M., Crystal-size dependence of the spark-plasma-sintering kinetics of ZrB 2 ultra-high-temperature ceramics. Journal of the European Ceramic Society 2012, 32 (2), 271-276.

[181] Thompson, M.; Fahrenholtz, W. G.; Hilmas, G., Effect of Starting Particle Size and Oxygen Content on Densification of ZrB2. Journal of the American Ceramic Society 2011, 94 (2), 429-435.

[182] Cologna, M.; Rashkova, B.; Raj, R., Flash Sintering of Nanograin Zirconia in <5 s at 850°C. Journal of the American Ceramic Society 2010, 93 (11), 3556-3559.

[183] Guillon, O.; Gonzalez-Julian, J.; Dargatz, B.; Kessel, T.; Schierning, G.; Rathel, J.; Herrmann, M., Field-Assisted Sintering Technology/Spark Plasma Sintering: Mechanisms, Materials, and Technology Developments. Advanced Engineering Materials 2014, 16 (7), 830-849.

[184] Anselmi-Tamburini, U., Spark Plasma Sintering. In Encyclopedia of Materials: Technical Ceramics and Glasses, Pomeroy, M., Ed. Elsevier: Oxford, 2021; pp 294-310.

[185] Takeuchi, T.; Suyama, Y.; Sinclair, D. C.; Kageyama, H., Spark-plasma-sintering of fine BaTiO3 powder prepared by a sol-crystal method. Journal of Materials Science 2001, 36 (9), 2329-2334.

[186] Baraki, R.; Schwarz, S.; Guillon, O., Effect of Electrical Field/Current on Sintering of Fully Stabilized Zirconia. Journal of the American Ceramic Society 2012, 95 (1), 75-78.

[187] Omori, M. (2000). Sintering, consolidation, reaction and crystal growth by the spark plasma system (SPS). *Materials Science and Engineering: A*, *287*(2), 183-188.

[188] Olevsky, E. A.; Rolfing, S. M.; Maximenko, A. L., Flash (Ultra-Rapid) Spark-Plasma Sintering of Silicon Carbide. Scientific Reports 2016, 6 (1), 33408.

[189] Pournajaf, R.; Hassanzadeh-Tabrizi, S. A.; Ebrahimi-Kahrizsangi, R.; Alhaji, A.; Nourbakhsh, A. A., Polycrystalline infrared-transparent MgO fabricated by spark plasma sintering. CERAMICS INTERNATIONAL 2019, 45 (15), 18943-18950.

[190] Li, Z.; Qi, W.; Cao, J.; Li, Y.; Viola, G.; Yan, H., Spark plasma sintering of grain-oriented Sr2Bi4Ti5O18 aurivillius phase ceramics. Journal of Alloys and Compounds 2019, 782, 6-9.

[191] Huang, Y. H.; Wu, Y. J.; Qiu, W. J.; Li, J.; Chen, X. M., Enhanced energy storage density of Ba0.4Sr0.6TiO3–MgO composite prepared by spark plasma sintering. Journal of the European Ceramic Society 2015, 35 (5), 1469-1476.

[192] Tao, P.; Liu, W.; Wang, Y., Fabrication of SiCf/Ti3SiC2 composites with high thermal conductivity by spark plasma sintering. Ceramics International 2020, 46 (2), 2571-2575.

[193] Mistarihi, Q. M.; Raj, V.; Kim, J. H.; Ryu, H. J., Thermal conductivity of Mo-reinforced ZrO2 composites fabricated by spark plasma sintering for inert matrix fuels. Materials & Design 2017, 134, 476-485.

[194] Oliver, U. C.; Sunday, A. V.; Christain, E. I.-E. I.; Elizabeth, M. M., Spark plasma sintering of aluminium composites—a review. The International Journal of Advanced Manufacturing Technology 2021, 112 (7), 1819-1839.

[195] Hu, C.; Li, F.; Qu, D.; Wang, Q.; Xie, R.; Zhang, H.; Peng, S.; Bao, Y.; Zhou, Y., 8 - Developments in hot pressing (HP) and hot isostatic pressing (HIP) of ceramic matrix composites. In *Advances in Ceramic Matrix Composites*, Low, I. M., Ed. Woodhead Publishing: 2014; pp 164-189.

[196] Itoh, H.; Naka, S.; Matsudaira, T.; Hamamoto, H., Preparation of TiB2 sintered compacts by hot pressing. Journal of Materials Science 1990, 25 (1), 533-536.

[197] Nguyen, V.-H.; Ali Delbari, S.; Ahmadi, Z.; Shahedi Asl, M.; Ghassemi Kakroudi, M.; Le, Q. V.; Sabahi Namini, A.; Shokouhimehr, M.; Mohammadi, M.; Peng, W., TEM characterization of hot-pressed ZrB2-SiC-AlN composites. Results in Physics 2020, 19, 103348.

[198] Sonber, J. K.; Murthy, T. S.; Majumdar, S.; Kain, V., Processing of ZrB2- and HfB2-Based Ultra-High Temperature Ceramic Materials: A Review. Materials Performance and Characterization 2021, 10 (2), 89-121.

[199] Lee, E. J.; Lee, D. H.; Kim, J. C.; Kim, D. J., Densification behavior of high purity SiC by hot pressing. Ceramics International 2014, 40 (10, Part B), 16389-16392.

[200] Li, J.; Ren, X.; Zhang, Y.; Hou, H., Silicon carbide hot pressing sintered by magnesium additive: microstructure and sintering mechanism. Journal of Materials Research and Technology 2020, 9 (1), 520-529.

[201] Zhang, X.; Zhang, Z.; Nie, B.; Chen, H.; Wang, Y.; Zheng, L.; Bai, Y.; Wang, W., Microstructure and mechanical properties of fine-grained boron carbide ceramics fabricated by high-pressure hot pressing combined with high-energy ball milling. Ceramics International 2018, 44 (9), 10766-10772

[202] Ma, B.; Zhang, X.; Han, J.; Han, W., Fabrication of hot-pressed ZrC-based composites. Proceedings of the Institution of Mechanical Engineers, Part G: Journal of Aerospace Engineering 2009, 223 (8), 1153-1157.

[203] Oghbaei, M.; Mirzaee, O., Microwave versus conventional sintering: A review of fundamentals, advantages and applications. Journal of Alloys and Compounds 2010, 494 (1), 175-189.

[204] Breval, E.; Cheng, J. P.; Agrawal, D. K.; Gigl, P.; Dennis, M.; Roy, R.; Papworth, A. J., Comparison between microwave and conventional sintering of WC/Co composites. Materials Science and Engineering: A 2005, 391 (1), 285-295.

[205] Agrawal, D., 12 - Microwave sintering of metal powders. In *Advances in Powder Metallurgy*, Chang, I.; Zhao, Y., Eds. Woodhead Publishing: 2013; pp 361-379.

[206] Fan, B. B.; Li, W.; Zhang, F.; Li, H. X.; Zhang, R.; Liu, G. Q.; Qian, F.; Chen, Y. Q., Fabrication and properties of Si2N2O ceramics for microwave sintering furnace. PROCESSING AND APPLICATION OF CERAMICS 2020, 14 (1), 32-39.

[207] Marina, M.; Zamzuri, M. Z. M.; Derman, M. N.; Selamat, M. A.; Nooraizedfiza, Z., Comparison Study in Consolidation of Yttria Reinforced Iron-Chromium Composites using Conventional and Microwave Sintering Technique. In ADVANCED MATERIALS ENGINEERING AND TECHNOLOGY II, 2014; Vol. 594-595, pp 832-+.

[208] Cheng, Y.; Sun, S. S.; Hu, H. P., Preparation of Al2O3/TiC micro-composite ceramic tool materials by microwave sintering and their microstructure and properties. CERAMICS INTERNATIONAL 2014, 40 (10), 16761-16766.

[209] Agrawal, D., Microwave Sintering of Ceramics, Composites and Metallic Materials, and Melting of Glasses. Transactions of the Indian Ceramic Society 2006, 65 (3), 129-144.

[210] Agrawal, D., 9 - Microwave sintering of ceramics, composites and metal powders. In Sintering of Advanced Materials, Fang, Z. Z., Ed. Woodhead Publishing: 2010; pp 222-248.

[211] Fliflet, A. W.; Bruce, R. W.; Fischer, R. P.; Lewis, D.; Kurihara, L. K.; Bender, B. A.; Chow, G. M.; Rayne, R. J., A study of millimeter-wave sintering of fine-grained alumina compacts. IEEE TRANSACTIONS ON PLASMA SCIENCE 2000, 28 (3), 924-935.

[212] Brosnan, K. H.; Messing, G. L.; Agrawal, D. K., Microwave Sintering of Alumina at 2.45 GHz. Journal of the American Ceramic Society 2003, 86 (8), 1307-1312.

[213] Heuguet, R.; Marinel, S.; Thuault, A.; Badev, A., Effects of the Susceptor Dielectric Properties on the Microwave Sintering of Alumina. Journal of the American Ceramic Society 2013, 96 (12), 3728-3736.

[214] Seyednezhad, M.; Rajabi, A.; Muchtar, A.; Somalu, M. R., Nanostructured and Nonsymmetrical NiO-SDC/SDC Composite Anode Performance via a Microwave-Assisted Route for Intermediate-Temperature Solid Oxide Fuel Cells. MATERIALS AND MANUFACTURING PROCESSES 2016, 31 (10), 1301-1305.

[215] Kumari, S.; Kumar, R.; Agrawal, P. R.; Prakash, S.; Mondal, D. P.; Dhakate, S. R., Fabrication of lightweight and porous silicon carbide foams as excellent microwave susceptor for heat generation. MATERIALS CHEMISTRY AND PHYSICS 2020, 253.

[216] Garcia, D. E.; Klein, A. N.; Hotza, D., Advanced Ceramics with dense and fine-grained microstructures through fast firing. *Reviews on Advanced Materials Science* 2012, 30 (3), 273-281.

[217] Klein, A.; Hotza, D., Advanced ceramics with dense and fine-grained microstructures through fast firing. Reviews on Advanced Materials Science 2012, 30.

[218] Yanagisawa, K.; Nishioka, M.; Ioku, K.; Yamasaki, N., Densification of silica gels by hydrothermal hot-pressing. Journal of Materials Science Letters 1993, 12 (14), 1073-1075.

[219] Yanagisawa, K.; Ioku, K.; Yamasaki, N., Post-sintering of anatase compact prepared by hydrothermal hot-pressing. Journal of Materials Science Letters 1995, 14 (3), 161-163.

[220] Ndayishimiye, A., Largeteau, A., Mornet, S., Duttine, M., Dourges, M.-A., Denux, D., . . . Goglio, G. (2018). Hydrothermal Sintering for Densification of Silica. Evidence for the Role of Water. *Journal of the European Ceramic Society, 38*(4), 1860-1870.

[221] Yamasaki, N.; Weiping, T., Hydrothermal hot-pressing of calcium carbonate with sea water. Journal of Materials Science Letters 1993, 12 (7), 516-519.

[222] Yamasaki, N.; Tang, W.; Ke, J., Low-temperature sintering of calcium carbonate by a hydrothermal hot-pressing technique. Journal of Materials Science Letters 1992, 11 (13), 934-936.

[223] Yamasaki, N.; Weiping, T.; Lei, H.; Hosoi, K., Solidification of aragonite-type CaCO3 powder containing chitosan with acetic acid by hydrothermal hot pressing. Journal of Materials Science Letters 1995, 14 (24), 1751-1753.

[224] Hosoi, K.; Hashida, T.; Takahashi, H.; Yamasaki, N.; Korenaga, T., Low temperature solidification of calcium carbonate through vaterite-calcite wet transformation. Journal of Materials Science Letters 1996, 15 (9), 812-814.

[225] Hosoi, K.; Hashida, T.; Takahashi, H.; Yamasaki, N.; Korenaga, T., Solidification behaviour of calcium carbonate via aragonite-calcite wet transformation with hydrothermal hot pressing. Journal of Materials Science Letters 1997, 16 (5), 382-385.

[226] Yamasaki, N.; Fei, L.; Shimomto, S.; Chen, Q., Fabrication of colored CaCO3 compacts by hydrothermal hot-pressing method. Materials Research Innovations 1998, 2 (1), 45-48.

[227] Yanagisawa, K.; Feng, Q.; Yamasaki, N., Preparation of ceramics by hydrothermal hot-pressing. High Pressure Research 2001, 20 (1-6), 343-349.

[228] Ndayishimiye, A.; Largeteau, A.; Prakasam, M.; Pechev, S.; Dourges, M.-A.; Goglio, G., Low temperature hydrothermal sintering process for the quasi-complete densification of nanometric α-quartz. Scripta Materialia 2018, 145, 118-121.

[229] Suzuki, N.; Huang, Y.-T.; Nemoto, Y.; Nakahira, A.; Yamauchi, Y., Highly Densified Mesoporous Bulk Silica Prepared with Colloidal Mesoporous Silica Nanoparticles toward a New Low-k Material. Chemistry Letters 2012, 41 (11), 1518-1519.

[230] Nakahira, A.; Hamada, T.; Yamauchi, Y., Synthesis and properties of dense bulks for mesoporous silica SBA-15 by a modified hydrothermal method. Materials Letters 2010, 64 (19), 2053-2055.

[231] Nakahira, A.; Nagata, H.; Onoki, T.; Yamasaki, Y., Evaluation of microstructures and properties of bulk mesoporous silica. Research on Chemical Intermediates 2008, 34 (4), 347-352.

[232] Takimura, M.; Nagata, H.; Yamasaki, Y.; Nakahira, A., Synthesis of dense mesoporous silica with high surface area by hydrothermal hot-pressing (HHP) method. In Solid State Phenomena, 2007; Vol. 124-126, pp 1833-1836.

[233] Takimura, M.; Nagata, H.; Yamasaki, Y.; Suzuki, T.; Ikuhara, Y.; Nakahira, A., Synthesis and Characterization of Bulky FSM with Interconnected Mesopore-Networks Using an HHP Method. Journal of the Ceramic Society of Japan 2006, 114 (1330), 554-557.

[234] Nagata, H.; Takimura, M.; Yamasaki, Y.; Nakahira, A., Syntheses and Characterization of Bulky Mesoporous Silica MCM-41 by Hydrothermal Hot-Pressing Method. MATERIALS TRANSACTIONS 2006, 47 (8), 2103-2105.

[235] Yanagisawa, K.; Ioku, K.; Yamasaki, N., Pore Size Control of Porous Silica Ceramics by Hydrothermal Hot-Pressing. Journal of the Ceramic Society of Japan 1994, 102 (1190), 966-971.

[236] Yamasaki, N.; Kai, T.; Nishioka, M.; Yanagisawa, K.; Ioku, K., Porous hydroxyapatite ceramics prepared by hydrothermal hot-pressing. Journal of Materials Science Letters 1990, 9 (10), 1150-1151.

[237] Ioku, K.; Yamamoto, K.; Yanagisawa, K.; Yamasaki, N., LOW TEMPERATURE SINTERING OF HYDROXYAPATITE BY HYDROTHERMAL HOT-PRESSING. Phosphorus Research Bulletin 1994, 4, 65-70.

[238] Hosoi, K.; Korenaga, T.; Hashida, T.; Takahashi, H.; Yamasaki, N., New Synthesis Technique for Making Hydroxyapatite Ceramics Using Hydrothermal Hot-Pressing. THE REVIEW OF HIGH PRESSURE SCIENCE AND TECHNOLOGY 1998, 7, 1405-1407.

[239] Nakahira, A.; Murakami, T.; Onoki, T.; Hashida, T.; Hosoi, K., Fabrication of Porous Hydroxyapatite Using Hydrothermal Hot Pressing and Post-Sintering. Journal of the American Ceramic Society 2005, 88 (5), 1334-1336.

[240] Yanagisawa, K.; Zhu, K.; Fujino, T.; Onda, A.; Kajiyoshi, K.; Ioku, K., Preparation of hydroxyapatite ceramics by hydrothermal hot-pressing technique. In Key Engineering Materials, 2006; Vol. 309-311 I, pp 57-60.

[241] Kim, J.-H.; Yanagisawa, K.; Onda, A.; Sasabe, E.; Yamamoto, T., Densification behavior of hydroxyapatite green pellets prepared by different methods. Journal of the Ceramic Society of Japan 2015, 123 (1444), 1097-1101.

[242] Mejía-Martínez, E. E.; Matamoros-Veloza, Z.; Yanagisawa, K.; Rendón-Ángeles, J. C.; Moreno-Pérez, B., Influencia de la temperatura en la compactación hidrotérmica en caliente de polvos de magnesio hidroxiapatita. Boletín de la Sociedad Española de Cerámica y Vidrio 2018, 57 (2), 45-54.

[243] Yanagisawa, K.; Ioku, K.; Yamasaki, N., Crystallization of Amorphous Hydrous Titania under Hydrothermal Hot-Pressing Conditions. Journal of the Ceramic Society of Japan 1994, 102 (1191), 1091-1093.

[244] Nakahira, A.; Kubo, T.; Yamasaki, Y., Microstructural Control of Mesoporous Bulk Composed of TiO2-Derived Titanate Nanotubes. ACS Applied Materials & Interfaces 2010, 2 (4), 1136-1140.

[245] Yamasaki, N.; Yanagisawa, K.; Nishioka, M.; Kanahara, S., A hydrothermal hot-pressing method: Apparatus and application. Journal of Materials Science Letters 1986, 5 (3), 355-356.

[246] Li, J.; Hashida, T., Preparation of hydroxyapatite ceramics by hydrothermal hot-pressing method at 300 °C. Journal of Materials Science 2007, 42 (13), 5013-5019.

[247] Takezoe, S.; Hosoi, K.; Tajika, M.; Yamasaki, Y.; Nakahira, A., Syntheses of Bulky Y-Zeolite by Hydrothermal Hot-Pressing (HHP) Technique. Key Engineering Materials 2006, 317-318, 97-100.

[248] De Silva, P.; Bucea, L.; Sirivivatnanon, V.; Moorehead, D. R., Carbonate binders by “cold sintering” of calcium carbonate. Journal of Materials Science 2007, 42 (16), 6792-6797.

[249] Schwarz, S.; Thron, A. M.; Rufner, J.; van Benthem, K.; Guillon, O., Low Temperature Sintering of Nanocrystalline Zinc Oxide: Effect of Heating Rate Achieved by Field Assisted Sintering/Spark Plasma Sintering. Journal of the American Ceramic Society 2012, 95 (8), 2451-2457.

[250] Dargatz, B.; Gonzalez-Julian, J.; Bram, M.; Jakes, P.; Besmehn, A.; Schade, L.; Röder, R.; Ronning, C.; Guillon, O., FAST/SPS sintering of nanocrystalline zinc oxide—Part I: Enhanced densification and formation of hydrogen-related defects in presence of adsorbed water. Journal of the European Ceramic Society 2016, 36 (5), 1207-1220.

[251] Dargatz, B.; Gonzalez-Julian, J.; Bram, M.; Shinoda, Y.; Wakai, F.; Guillon, O., FAST/SPS sintering of nanocrystalline zinc oxide—Part II: Abnormal grain growth, texture and grain anisotropy. Journal of the European Ceramic Society 2016, 36 (5), 1221-1232.

[252] Gallas, M. R.; Rosa, A. R.; Costa, T. H.; Jornada, J. A. H. d., High pressure compaction of nanosize ceramic powders. Journal of Materials Research 1997, 12 (3), 764-768.

[253] Brito, J. B.; Costa, T. M. H.; Rodembusch, F. S.; Balzaretti, N. M., Photoluminescence of silica monoliths prepared from cold sintering of nanometric aerosil precursors under high pressure. Journal of Luminescence 2017, 187, 154-159.

[254] Kähäri, H.; Teirikangas, M.; Juuti, J.; Jantunen, H., Dielectric Properties of Lithium Molybdate Ceramic Fabricated at Room Temperature. Journal of the American Ceramic Society 2014, 97 (11), 3378-3379.

[255] Väätäjä, M.; Kähäri, H.; Juuti, J.; Jantunen, H., Li2MoO4-based composite ceramics fabricated from temperature- and atmosphere-sensitive MnZn ferrite at room temperature. Journal of the American Ceramic Society 2017, 100 (8), 3626-3635.

[256] Kähäri, H.; Teirikangas, M.; Juuti, J.; Jantunen, H., Room-temperature fabrication of microwave dielectric Li2MoO4–TiO2 composite ceramics. Ceramics International 2016, 42 (9), 11442-11446.

[257] Kähäri, H.; Ramachandran, P.; Juuti, J.; Jantunen, H., Room-temperature-densified Li2MoO4 ceramic patch antenna and the effect of humidity. International Journal of Applied Ceramic Technology 2017, 14 (1), 50-55.

[258] Ramachandran, P.; Kähäri, H.; Juuti, J.; Jantunen, H., Room temperature densified ceramics for weight optimized circular polarized GPS antenna design. Microwave and Optical Technology Letters 2018, 60 (4), 1061-1066.

[259] Bouville, F.; Studart, A. R., Geologically-inspired strong bulk ceramics made with water at room temperature. Nature Communications 2017, 8 (1), 14655.

[260] Waurzyniak, P., Cold Sintering Process Saves Energy, Material. Manufacturing Engineering 2017, 159 (4), 35.

[261] Cold Sintering Creates New Avenues for Advanced Composites Manufacture. Chemical Engineering Progress 2017, 113 (9), 14.

[262] Kähäri, H.; Teirikangas, M.; Juuti, J.; Jantunen, H., Improvements and Modifications to Room-Temperature Fabrication Method for Dielectric Li2MoO4 Ceramics. Journal of the American Ceramic Society 2015, 98 (3), 687-689.

[263] ul Hassan, M.; Iqbal, S.; Yun, J.-I.; Ryu, H. J., Immobilization of radioactive corrosion products by cold sintering of pure hydroxyapatite. *Journal of Hazardous Materials* 2019, 374, 228-237.

[264] Gutmanas, E. Y.; Rabinkin, A.; Roitberg, M., Cold sintering under high pressure. Scripta Metallurgica 1979, 13 (1), 11-15.

[265] Guo, H. Z.; Baker, A.; Guo, J.; Randall, C. A., Cold Sintering Process: A Novel Technique for Low-Temperature Ceramic Processing of Ferroelectrics. *J. Am. Ceram. Soc.* 2016, 99 (11), 3489-3507.

[266] Dai, J.; Lee, W.; Gomez, E. D.; Yamamoto, N., Demonstrating low-temperature sintering of boron carbide powders. International Journal of Ceramic Engineering & Science 2019, 1 (4), 178-184.

[267] dos Santos, A. M.; Thomazini, D.; Gelfuso, M. V., Cold sintering and thermoelectric properties of Ca3Co4O9 ceramics. Ceramics International 2020, 46 (9), 14064-14070.

[268] Kang, X.; Floyd, R.; Lowum, S.; Long, D.; Dickey, E.; Maria, J.-P., Cold sintering with dimethyl sulfoxide solutions for metal oxides. Journal of Materials Science 2019, 54 (10), 7438-7446.

[269] Jing, Y.; Luo, N.; Wu, S.; Han, K.; Wang, X.; Miao, L.; Wei, Y., Remarkably improved electrical conductivity of ZnO ceramics by cold sintering and post-heat-treatment. Ceramics International 2018, 44 (16), 20570-20574.

[270] Lowum, S.; Floyd, R.; Bermejo, R.; Maria, J.-P., Mechanical strength of cold-sintered zinc oxide under biaxial bending. Journal of Materials Science 2019, 54 (6), 4518-4522.

[271] Nur, K.; Mishra, T. P.; Silva, J. G. P. d.; Gonzalez-Julian, J.; Bram, M.; Guillon, O., Influence of powder characteristics on cold sintering of nano-sized ZnO with density above 99 %. *Journal of the European Ceramic Society* 2021, 41 (4), 2648-2662.

[272] Ndayishimiye, A.; Grady, Z. A.; Tsuji, K.; Wang, K.; Bang, S. H.; Randall, C. A., Thermosetting polymers in cold sintering: The fabrication of ZnO-polydimethylsiloxane composites. Journal of the American Ceramic Society 2020, 103 (5), 3039-3050.

[273] Floyd, R. D.; Lowum, S.; Maria, J.-P., Cold sintering zinc oxide with a crystalline zinc acetate dihydrate mass transport phase. Journal of Materials Science 2020, 55 (31), 15117-15129.

[274] Serrano, A.; Caballero-Calero, O.; García, M. Á.; Lazić, S.; Carmona, N.; Castro, G. R.; Martín-González, M.; Fernández, J. F., Cold sintering process of ZnO ceramics: Effect of the nanoparticle/microparticle ratio. Journal of the European Ceramic Society 2020, 40 (15), 5535-5542.

[275] Kermani, M.; Biesuz, M.; Dong, J.; Deng, H.; Bortolotti, M.; Chiappini, A.; Reece, M. J.; Sglavo, V. M.; Hu, C.; Grasso, S., Flash cold sintering: Combining water and electricity. Journal of the European Ceramic Society 2020, 40 (15), 6266-6271.

[276] Guo, J.; Legum, B.; Anasori, B.; Wang, K.; Lelyukh, P.; Gogotsi, Y.; Randall, C. A., Cold Sintered Ceramic Nanocomposites of 2D MXene and Zinc Oxide. Advanced Materials 2018, 30 (32), 1801846.

[277] Liu, J.-A., Li, C.-H., Shan, J.-J., Wu, J.-M., Gui, R.-F., & Shi, Y.-S. (2018). Preparation of high-density InGaZnO4 target by the assistance of cold sintering. *Materials Science in Semiconductor Processing, 84,* 17-23.

[278] Zhao, X.; Guo, J.; Wang, K.; Herisson De Beauvoir, T.; Li, B.; Randall, C. A., Introducing a ZnO–PTFE (Polymer) Nanocomposite Varistor via the Cold Sintering Process. *Advanced Engineering Materials* 2018, 20 (7), 1700902.

[279] Hérisson de Beauvoir, T.; Tsuji, K.; Zhao, X.; Guo, J.; Randall, C., Cold sintering of ZnO-PTFE: Utilizing polymer phase to promote ceramic anisotropic grain growth. Acta Materialia 2020, 186, 511-516.

[280] Coutinho, L.; Aredes, R. G.; Antonelli, E., Cold sintering and electric characterization of ZnO-BaTiO3 composites. Cerâmica 2021, 67 (381), 105-110.

[281] Chi, M.; Ma, W.; Guo, J.; Wu, J.; Li, T.; Wang, S.; Zhang, P., Effect of NaCl on the microstructure and electrical properties of K0.5Na0.5NbO3 ceramics prepared by cold sintering process. Journal of Materials Science: Materials in Electronics 2019, 30 (24), 21435-21443.

[282] Heidary, D. S. B.; Guo, J.; Seo, J.-H.; Guo, H.; Rajagopalan, R.; Randall, C. A., Microstructures and electrical properties of V2O5and carbon-nanofiber composites fabricated by cold sintering process. Japanese Journal of Applied Physics 2018, 57 (2), 025702.

[283] Guo, J.; Guo, H.; Heidary, D. S. B.; Funahashi, S.; Randall, C. A., Semiconducting properties of cold sintered V2O5 ceramics and Co-sintered V2O5-PEDOT:PSS composites. *Journal of the European Ceramic Society* 2017, 37 (4), 1529-1534.

[284] Zhao, Y.; Berbano, S. S.; Gao, L.; Wang, K.; Guo, J.; Tsuji, K.; Wang, J.; Randall, C. A., Cold-sintered V2O5-PEDOT:PSS nanocomposites for negative temperature coefficient materials. Journal of the European Ceramic Society 2019, 39 (4), 1257-1262.

[285] Guo, J.; Guo, H. Z.; Baker, A. L.; Lanagan, M. T.; Kupp, E. R.; Messing, G. L.; Randall, C. A., Cold Sintering: A Paradigm Shift for Processing and Integration of Ceramics. *Angewandte Chemie-International Edition* 2016, 55 (38), 11457-11461.

[286] Falk, G. S.; Yesid Gómez González, S.; Hotza, D., Low-energy microwave synthesis and cold sintering of nanograined TiO2-Nb2O5. Materials Letters 2020, 278, 128418.

[287] Induja, I. J.; Sebastian, M. T., Microwave dielectric properties of cold sintered Al2O3-NaCl composite. Materials Letters 2018, 211, 55-57.

[288] Santha, N., Rakhi, M., & Subodh, G. (2020). Fabrication of high quality factor cold sintered MgTiO3–NaCl microwave ceramic composites. *Materials Chemistry and Physics, 255*, 123636.

[289] Induja, I. J., & Sebastian, M. T. (2017). Microwave dielectric properties of mineral sillimanite obtained by conventional and cold sintering process. *Journal of the European Ceramic Society, 37*(5), 2143-2147.

[290] Hao, J.; Guo, J.; Zhao, E.; Si, M.; Yuan, X.; Yao, F.-Z.; Wang, H., Grain size effect on microwave dielectric properties of Na2WO4 ceramics prepared by cold sintering process. Ceramics International 2020, 46 (17), 27193-27198.

[291] Wang, D.; Zhang, S.; Zhou, D.; Song, K.; Feteira, A.; Vardaxoglou, Y.; Whittow, W.; Cadman, D.; Reaney, I. M., Temperature Stable Cold Sintered (Bi0.95Li0.05)(V0.9Mo0.1)O4-Na2Mo2O7 Microwave Dielectric Composites. Materials 2019, 12 (9).

[292] Guo, J.; Guo, H.; Baker, A. L.; Lanagan, M. T.; Kupp, E. R.; Messing, G. L.; Randall, C. A., Cold Sintering: A Paradigm Shift for Processing and Integration of Ceramics. Angewandte Chemie - International Edition 2016, 55 (38), 11457-11461.

[293] Guo, J.; Baker, A. L.; Guo, H.; Lanagan, M.; Randall, C. A., Cold sintering process: A new era for ceramic packaging and microwave device development. Journal of the American Ceramic Society 2017, 100 (2), 669-677.

[294] Liu, Y.; Liu, P.; Hu, C., Low-temperature preparation and microwave dielectric properties of cold sintered Li2Mg3TiO6 nanocrystalline ceramics. Ceramics International 2018, 44 (17), 21047-21052.

[295] Faouri, S. S.; Mostaed, A.; Dean, J. S.; Wang, D.; Sinclair, D. C.; Zhang, S.; Whittow, W. G.; Vardaxoglou, Y.; Reaney, I. M., High quality factor cold sintered Li2MoO4BaFe12O19 composites for microwave applications. Acta Materialia 2019, 166, 202-207.

[296] Zhou, D.; Pang, L.-X.; Wang, D.-W.; Reaney, I. M., Novel water-assisting low firing MoO3 microwave dielectric ceramics. Journal of the European Ceramic Society 2019, 39 (7), 2374-2378.

[297] Wang, D.; Zhou, D.; Zhang, S.; Vardaxoglou, Y.; Whittow, W. G.; Cadman, D.; Reaney, I. M., Cold-Sintered Temperature Stable Na0.5Bi0.5MoO4–Li2MoO4 Microwave Composite Ceramics. ACS Sustainable Chemistry & Engineering 2018, 6 (2), 2438-2444.

[298] Baker, A.; Guo, H. Z.; Guo, J.; Randall, C., Utilizing the Cold Sintering Process for Flexible-Printable Electroceramic Device Fabrication. Journal of the American Ceramic Society 2016, 99 (10), 3202-3204.

[299] Akmal, M.; Hassan, M. u.; Afzal, M.; Ryu, H. J., Novel approach to sintering hydroxyapatite-alumina nanocomposites at 300 °C. Materials Chemistry and Physics 2021, 260, 124187.

[300] Venkatesan, S.; Hassan, M. u.; Ryu, H. J., Adsorption and immobilization of radioactive ionic-corrosion-products using magnetic hydroxyapatite and cold-sintering for nuclear waste management applications. Journal of Nuclear Materials 2019, 514, 40-49.

[301] Hassan, M. u.; Ryu, H. J., Cold sintering and durability of iodate-substituted calcium hydroxyapatite (IO-HAp) for the immobilization of radioiodine. Journal of Nuclear Materials 2019, 514, 84-89.

[302] Galotta, A.; Giust, E.; Bortolotti, M.; Sorarù, G. D.; Sglavo, V. M.; Biesuz, M., Cold sintering of diatomaceous earth. Journal of the American Ceramic Society 2021, 104 (9), 4329-4340.

[303] Guo, N.; Liu, M.; Shen, J.-Y.; Shen, H.-Z.; Shen, P., Surface hydrate-assisted low- and medium-temperature sintering of MgO. Scripta Materialia 2022, 206, 114258.

[304] Hamao, N.; Yamaguchi, Y.; Hamamoto, K., Densification of a NASICON-Type LATP Electrolyte Sheet by a Cold-Sintering Process. Materials 2021, 14 (16).

[305] Nakaya, H.; Iwasaki, M.; Randall, C. A., Thermal-assisted cold sintering study of a lithium electrolyte: Li13.9Sr0.1Zn(GeO4)4. Journal of Electroceramics 2020, 44 (1), 16-22.

[306] Grady, Z.; Ndayishimiye, A.; Randall, C., A dramatic reduction in the sintering temperature of the refractory sodium beta "-alumina solid electrolyte via cold sintering. JOURNAL OF MATERIALS CHEMISTRY A 2021, 9 (38), 22002-22014.

[307] Grady, Z.; Fan, Z.; Ndayishimiye, A.; Randall, C. A., Design and Sintering of All-Solid-State Composite Cathodes with Tunable Mixed Conduction Properties via the Cold Sintering Process. ACS Applied Materials & Interfaces 2021, 13 (40), 48071-48087.

[308] Seo, J.-H.; Nakaya, H.; Takeuchi, Y.; Fan, Z.; Hikosaka, H.; Rajagopalan, R.; Gomez, E. D.; Iwasaki, M.; Randall, C. A., Broad temperature dependence, high conductivity, and structure-property relations of cold sintering of LLZO-based composite electrolytes. Journal of the European Ceramic Society 2020, 40 (15), 6241-6248.

[309] Cong, L.; Hanying, L.; Yuming, H.; Shiyong, Z.; Xiao, W.; Tengfei, L.; Xinghua, Z.; Xing, Y., Phase evolution and enhanced sinterability of cold sintered Fe2O3-doped 8YSZ. Ceramics International 2020, 46 (9), 14217-14223.

[310] Grady, Z. M.; Tsuji, K.; Ndayishimiye, A.; Hwan-Seo, J.; Randall, C. A., Densification of a Solid-State NASICON Sodium-Ion Electrolyte Below 400 degrees C by Cold Sintering With a Fused Hydroxide Solvent. ACS APPLIED ENERGY MATERIALS 2020, 3 (5), 4356-4366.

[311] Guo, J.; Berbano, S. S.; Guo, H.; Baker, A. L.; Lanagan, M. T.; Randall, C. A., Cold Sintering Process of Composites: Bridging the Processing Temperature Gap of Ceramic and Polymer Materials. *Advanced Functional Materials* 2016, 26 (39), 7115-7121.

[312] Guo, J.; Zhao, X. T.; De Beauvoir, T. H.; Seo, J. H.; Berbano, S. S.; Baker, A. L.; Azina, C.; Randall, C. A., Recent Progress in Applications of the Cold Sintering Process for Ceramic-Polymer Composites. *Advanced Functional Materials* 2018, 28 (39).

[313] van Krevelen, D. W.; te Nijenhuis, K.; Te Nijenhuis, K.; W, V. K., Properties of Polymers: Their Correlation with Chemical Structure Their Numerical Estimation and Prediction from Additive Group Contributions. Oxford: Elsevier Science & Technology: Oxford, 2009.

[314] Li, Y.; Guo, B.; Huang, G.; Shu, P.; Kiriki, H.; Kubo, S.; Ohno, K.; Kawai, T., Eutectic compound (KNO3/NaNO3 : PCM) quasi-encapsulated into SiC-honeycomb for suppressing natural convection of melted PCM. International Journal of Energy Research 2015, 39 (6), 789-804.

[315] Yu, Q.; Jiang, Z.; Cong, L.; Lu, T.; Suleiman, B.; Leng, G.; Wu, Z.; Ding, Y.; Li, Y., A novel low-temperature fabrication approach of composite phase change materials for high temperature thermal energy storage. Applied Energy 2019, 237, 367-377.

[316] Guo, H.; Baker, A.; Guo, J.; Randall, C. A., Protocol for Ultralow-Temperature Ceramic Sintering: An Integration of Nanotechnology and the Cold Sintering Process. ACS Nano 2016, 10 (11), 10606-10614.

[317] Ma, J.-P.; Chen, X.-M.; Ouyang, W.-Q.; Wang, J.; Li, H.; Fang, J.-L., Microstructure, dielectric, and energy storage properties of BaTiO3 ceramics prepared via cold sintering. Ceramics International 2018, 44 (4), 4436-4441.

[318] Wang, D.; Guo, H.; Morandi, C. S.; Randall, C. A.; Trolier-McKinstry, S., Cold sintering and electrical characterization of lead zirconate titanate piezoelectric ceramics. APL Materials 2018, 6 (1), 016101.

[319] Boston, R.; Guo, J.; Funahashi, S.; Baker, A. L.; Reaney, I.; Randall, C., Reactive intermediate phase cold sintering in strontium titanate. RSC Advances 2018, 8, 20372-20378.

[320] Shi, C.; Lai, Q.; He, A.; Chen, X.; Liang, T.; Wei, Y.; Luo, N., Structure and electrical properties of cold sintered 8mol% scandia stabilized zirconia ceramics. Ceramics International 2021, 47 (15), 21582-21587.

[321] Ndayishimiye, A.; Sengul, M. Y.; Bang, S. H.; Tsuji, K.; Takashima, K.; Hérisson de Beauvoir, T.; Denux, D.; Thibaud, J.-M.; van Duin, A. C. T.; Elissalde, C.; Goglio, G.; Randall, C. A., Comparing hydrothermal sintering and cold sintering process: Mechanisms, microstructure, kinetics and chemistry. Journal of the European Ceramic Society 2020, 40 (4), 1312-1324.

[322] Jayasayee, K.; Clark, S.; King, C.; Dahl, P. I.; Richard Tolchard, J.; Juel, M., Cold Sintering as a Cost-Effective Process to Manufacture Porous Zinc Electrodes for Rechargeable Zinc-Air Batteries. Processes 2020, 8 (5).

[323] Seo, J.-H.; Verlinde, K.; Guo, J.; Heidary, D. S. B.; Rajagopalan, R.; Mallouk, T. E.; Randall, C. A., Cold sintering approach to fabrication of high rate performance binderless LiFePO4 cathode with high volumetric capacity. Scripta Materialia 2018, 146, 267-271.

[324] Lee, W.; Lyon, C. K.; Seo, J.-H.; Lopez-Hallman, R.; Leng, Y.; Wang, C.-Y.; Hickner, M. A.; Randall, C. A.; Gomez, E. D., Ceramic–Salt Composite Electrolytes from Cold Sintering. Advanced Functional Materials 2019, 29 (20), 1807872.

[325] Berbano, S. S.; Guo, J.; Guo, H.; Lanagan, M. T.; Randall, C. A., Cold sintering process of Li1.5Al0.5Ge1.5(PO4)3 solid electrolyte. Journal of the American Ceramic Society 2017, 100 (5), 2123-2135.

[326] Seo, J.-H.; Guo, J.; Guo, H.; Verlinde, K.; Heidary, D. S. B.; Rajagopalan, R.; Randall, C. A., Cold sintering of a Li-ion cathode: LiFePO4-composite with high volumetric capacity. *Ceramics International* 2017, 43 (17), 15370-15374.

[327] Nayir, S.; Waryoba, D. R.; Rajagopalan, R.; Arslan, C.; Randall, C. A., Cold Sintering of a Covalently Bonded MoS2/Graphite Composite as a High Capacity Li–Ion Electrode. ChemNanoMat 2018, 4 (10), 1088-1094.

[328] Leng, H. Y.; Huang, J. J.; Nie, J. Y.; Luo, J., Cold sintering and ionic conductivities of Na3.256Mg0.128Zr1.872Si2PO12 solid electrolytes. Journal of Power Sources 2018, 391, 170-179.

[329] Seo, J.-H., Verlinde, K., Rajagopalan, R., Gomez, E. D., Mallouk, T. E., & Randall, C. A. (2019). Cold sintering process for fabrication of a high volumetric capacity Li4Ti5O12 anode. *Materials Science and Engineering: B, 250*, 114435.

[330] Zhang, Y.; Liu, A.; Shi, Z.; Ge, S.; Zhang, J., Microstructure and ion conductivity of Al-LLZO solid electrolyte prepared by molten salt and cold sintering process. International Journal of Applied Ceramic Technology 2021, n/a (n/a).

[331] Zhao, F.; Alahakoon, S. H.; Adair, K.; Zhang, S.; Xia, W.; Li, W.; Yu, C.; Feng, R.; Hu, Y.; Liang, J.; Lin, X.; Zhao, Y.; Yang, X.; Sham, T.-K.; Huang, H.; Zhang, L.; Zhao, S.; Lu, S.; Huang, Y.; Sun, X., An Air-Stable and Li-Metal-Compatible Glass-Ceramic Electrolyte enabling High-Performance All-Solid-State Li Metal Batteries. Advanced Materials 2021, 33 (8), 2006577.

[332] Thabet, K.; Quarez, E.; Joubert, O.; Le Gal La Salle, A., Application of the cold sintering process to the electrolyte material BaCe0.8Zr0.1Y0.1O3-δ. Journal of the European Ceramic Society 2020, 40 (9), 3445-3452.

[333] N, S.; Rajan, A.; G, S., Garnet mineral based composites through cold sintering process: Microstructure and dielectric properties. Journal of the European Ceramic Society 2020, 40 (2), 371-375.

[334] Ma, J.; Li, H.; Wang, H.; Lin, C.; Wu, X.; Lin, T.; Zheng, X.; Yu, X., Composition, microstructure and electrical properties of K0.5Na0.5NbO3 ceramics fabricated by cold

sintering assisted sintering. Journal of the European Ceramic Society 2019, 39 (4), 986-993.

[335] Guo, H.; Guo, J.; Baker, A.; Randall, C. A., Cold sintering process for ZrO2-based ceramics: significantly enhanced densification evolution in yttria-doped ZrO2. Journal of the American Ceramic Society 2017, 100 (2), 491-495.

[336] Guo, H. Z.; Bayer, T. J. M.; Guo, J.; Baker, A.; Randall, C. A., Cold sintering process for 8 mol%Y2O3-stabilized ZrO2 ceramics. Journal of the European Ceramic Society 2017, 37 (5), 2303-2308.

[337] Charoonsuk, T.; Sukkha, U.; Kolodiazhnyi, T.; Vittayakorn, N., Enhancing the densification of ceria ceramic at low temperature via the cold sintering assisted two-step sintering process. Ceramics International 2018, 44, S54-S57.

[338] Zaengle, T. H.; Ndayishimiye, A.; Tsuji, K.; Fan, Z.; Bang, S. H.; Perini, J.; Misture, S. T.; Randall, C. A., Single-step densification of nanocrystalline CeO2 by the cold sintering process. Journal of the American Ceramic Society 2020, 103 (5), 2979-2985.

[339] Li, L.; Yan, H.; Hong, W. B.; Wu, S. Y.; Chen, X. M., Dense gypsum ceramics prepared by room-temperature cold sintering with greatly improved mechanical properties. Journal of the European Ceramic Society 2020, 40 (13), 4689-4693.

[340] Wang, D.; Tsuji, K.; Randall, C. A.; Trolier-McKinstry, S., Model for the cold sintering of lead zirconate titanate ceramic composites. Journal of the American Ceramic Society 2020, 103 (9), 4894-4902.

[341] Liu, Y.; Sun, Q.; Wang, D.; Adair, K.; Liang, J.; Sun, X., Development of the cold sintering process and its application in solid-state lithium batteries. Journal of Power Sources 2018, 393, 193-203.

[342] Randall, C. A., Guo, J., BAKER, A., Lanagan, M., & Guo, H. (2017). Cold sintering ceramics and composites. In: Google Patents.

[343] Nie, J.; Zhang, Y.; Chan, J. M.; Huang, R.; Luo, J., Water-assisted flash sintering: Flashing ZnO at room temperature to achieve ~ 98% density in seconds. Scripta Materialia 2018, 142, 79-82.

[344] Sengul, M. Y.; Guo, J.; Randall, C. A.; van Duin, A. C. T., Water-Mediated Surface Diffusion Mechanism Enables the Cold Sintering Process: A Combined Computational and Experimental Study. Angewandte Chemie International Edition 2019, 58 (36), 12420-12424.

[345] Kang, X.; Floyd, R.; Lowum, S.; Cabral, M.; Dickey, E.; Maria, J.-P., Mechanism studies of hydrothermal cold sintering of zinc oxide at near room temperature. *Journal of the American Ceramic Society* 2019, 102 (8), 4459-4469.

[346] Du, J.; Rimsza, J. M., Atomistic computer simulations of water interactions and dissolution of inorganic glasses. npj Materials Degradation 2017, 1 (1), 16.

[347] Manzano, H.; Zhang, W.; Raju, M.; Dolado, J. S.; López-Arbeloa, I.; van Duin, A. C. T., Benchmark of ReaxFF force field for subcritical and supercritical water. The Journal of Chemical Physics 2018, 148 (23), 234503.

[348] Jiang, X.; Zhu, G.; Xu, H.; Dong, L.; Song, J.; Zhang, X.; Zhao, Y.; Yan, D.; Yu, A., Preparation of high density ZnO ceramics by the Cold Sintering Process. Ceramics International 2019, 45 (14), 17382-17386.

[349] Zhang, Y.; Nie, J.; Chan, J. M.; Luo, J., Probing the densification mechanisms during flash sintering of ZnO. Acta Materialia 2017, 125, 465-475.

[350] Galotta, A.; Sglavo, V. M., The cold sintering process: A review on processing features, densification mechanisms and perspectives. *Journal of the European Ceramic Society* 2021, 41 (16), 1-17.

[351] Rahaman, M. N. C. P., Ceramic Processing and Sintering 2003.

[352] Guo, H.; Bayer, T. J. M.; Guo, J.; Baker, A.; Randall, C. A., Cold sintering process for 8 mol%Y2O3-stabilized ZrO2 ceramics. Journal of the European Ceramic Society 2017, 37 (5), 2303-2308.

[353] Gratier, J.-P.; Dysthe, D. K.; Renard, F., Chapter 2 - The Role of Pressure Solution Creep in the Ductility of the Earth's Upper Crust. In Advances in Geophysics, Dmowska, R., Ed. Elsevier: 2013; Vol. 54, pp 47-179.

[354] Rahaman, M. N., Ceramic processing / by Mohamed N. Rahaman. Second edition. ed.; Boca Raton, Florida London New York : CRC Press, 2017.: 2017.

[355] Yu, T.; Cheng, J.; Li, L.; Sun, B.; Bao, X.; Zhang, H., Current understanding and applications of the cold sintering process. Frontiers of Chemical Science and Engineering 2019, 13 (4), 654-664.

[356] Guo, H. Z.; Guo, J.; Baker, A.; Randall, C. A., Hydrothermal-Assisted Cold Sintering Process: A New Guidance for Low Temperature Ceramic Sintering (vol 8, pg 20909, 2016). Acs Applied Materials & Interfaces 2016, 8 (49), 34170-34170.

[357] Lewin, S. (1960). The solubility product principle: an introduction to its uses and limitations / by S. Lewin. In. London: London: I. Pitman & Sons.

[358] Samiee, M.; Radhakrishnan, B.; Rice, Z.; Deng, Z.; Meng, Y. S.; Ong, S. P.; Luo, J., Divalent-doped Na3Zr2Si2PO12 natrium superionic conductor: Improving the ionic conductivity via simultaneously optimizing the phase and chemistry of the primary and secondary phases. Journal of Power Sources 2017, 347, 229-237.

[359] Leng, H.; Nie, J.; Luo, J., Combining cold sintering and Bi2O3-Activated liquid-phase sintering to fabricate high-conductivity Mg-doped NASICON at reduced temperatures. Journal of Materiomics 2019, 5 (2), 237-246.

[360] Grady, Z. M.; Tsuji, K.; Ndayishimiye, A.; Hwan-Seo, J.; Randall, C. A., Densification of a Solid-State NASICON Sodium-Ion Electrolyte Below 400 °C by Cold Sintering With a Fused Hydroxide Solvent. ACS Applied Energy Materials 2020, 3 (5), 4356-4366.

[361] Wang, D. X.; Guo, H. Z.; Morandi, C. S.; Randall, C. A.; Trolier-McKinstry, S., Cold sintering and electrical characterization of lead zirconate titanate piezoelectric ceramics. Apl Materials 2018, 6 (1).

[362] Yang, C.; Li, J.; Yang, D.; Li, S.; Qin, Y.; Meng, S.; Du, S., ZrW2O8 with Negative Thermal Expansion Fabricated at Ultralow Temperature: An Energy-Efficient Strategy for Metastable Material Fabrication. ACS Sustainable Chemistry & Engineering 2019, 7 (17), 14747-14755.

[363] Huang, H.; Tang, J.; Liu, J., Preparation of Na0.5Bi0.5TiO3 ceramics by hydrothermal-assisted cold sintering. Ceramics International 2019, 45 (6), 6753-6758.

[364] Ozmen, O.; Ozsoy-Keskinbora, C.; Suvaci, E., Chemical stability of KNbO3, NaNbO3, and K0.5Na0.5NbO3 in aqueous medium. Journal of the American Ceramic Society 2018, 101 (3), 1074-1086.

[365] Sato, T.; Shimada, M., Transformation of Yttria-Doped Tetragonal ZrO2 Polycrystals by Annealing in Water. Journal of the American Ceramic Society 1985, 68 (6), 356-356.

[366] Dargatz, B.; Gonzalez-Julian, J.; Bram, M.; Jakes, P.; Besmehn, A.; Schade, L.; Röder, R.; Ronning, C.; Guillon, O., FAST/SPS sintering of nanocrystalline zinc oxide-Part I: Enhanced densification and formation of hydrogen-related defects in presence of adsorbed water. *Journal of the European Ceramic Society* 2016, 36 (5), 1207-1220.

[367] Bang, S. H.; Tsuji, K.; Ndayishimiye, A.; Dursun, S.; Seo, J.-H.; Otieno, S.; Randall, C. A., Toward a size scale-up cold sintering process at reduced uniaxial pressure. Journal of the American Ceramic Society 2020, 103 (4), 2322-2327.

[368] Berbano, S. S.; Guo, J.; Guo, H. Z.; Lanagan, M. T.; Randall, C. A., Cold sintering process of Li1.5Al0.5Ge1.5(PO4)(3) solid electrolyte. *Journal of the American Ceramic Society* 2017, 100 (5), 2123-2135.

[369] Yang, C.; Li, J.; Shi, H.; Yang, D.; Meng, S.; Du, S., Effects of the liquid phase content on the microstructure and properties of the ZrW2O8 ceramics with negative thermal expansion fabricated by the cold sintering process. Journal of the European Ceramic Society 2020, 40 (15), 6079-6086.

[370] German, R.M., *Chapter Four - Measurement Tools and Experimental Observations*, in *Sintering: from Empirical Observations to Scientific Principles*, R.M. German, Editor. 2014, Butterworth-Heinemann: Boston. p. 71-130.

[371] Guo, H.; Bayer, T. J. M.; Guo, J.; Baker, A.; Randall, C. A., Current progress and perspectives of applying cold sintering process to ZrO2-based ceramics. Scripta Materialia 2017, 136, 141-148.

[372] Mazaheri, M.; Valefi, M.; Hesabi, Z. R.; Sadrnezhaad, S. K., Two-step sintering of nanocrystalline 8Y2O3 stabilized ZrO2 synthesized by glycine nitrate process. Ceramics International 2009, 35 (1), 13-20.

[373] Song, X.; Lu, J.; Zhang, T.; Ma, J., Two-Stage Master Sintering Curve Approach to Sintering Kinetics of Undoped and Al2O3-Doped 8 Mol% Yttria-Stabilized Cubic Zirconia. Journal of the American Ceramic Society 2011, 94 (4), 1053-1059.

[374] Anselmi-Tamburini, U.; Garay, J. E.; Munir, Z. A.; Tacca, A.; Maglia, F.; Spinolo, G., Spark plasma sintering and characterization of bulk nanostructured fully stabilized zirconia: Part I. Densification studies. Journal of Materials Research 2004, 19 (11), 3255-3262.

[375] Mazaheri, M., A.M. Zahedi, and M.M. Hejazi, *Processing of nanocrystalline 8mol% yttria-stabilized zirconia by conventional, microwave-assisted and two-step sintering.* Materials Science and Engineering: A, 2008. **492**(1): p. 261-267.

[376] Ghosh, A.; Suri, A. K.; Rao, B. T.; Ramamohan, T. R., Low-Temperature Sintering and Mechanical Property Evaluation of Nanocrystalline 8 mol% Yttria Fully Stabilized Zirconia. Journal of the American Ceramic Society 2007, 90 (7), 2015-2023.

[377] Janney, M. A.; Calhoun, C. L.; Kimrey, H. D., Microwave Sintering of Solid Oxide Fuel Cell Materials: I, Zirconia-8 mol% Yttria. Journal of the American Ceramic Society 1992, 75 (2), 341-346.

[378] Murase, Y.; Kato, E., Role of Water Vapor in Crystallite Growth and Tetragonal-Monoclinic Phase Transformation of ZrO2. Journal of the American Ceramic Society 1983, 66 (3), 196-200.

[379] Song, J.; Cao, L.; Jiang, L.; Liang, G.; Gao, J.; Li, D.; Wang, S.; Lv, M., Effect of HfN, HfC and HfB2 additives on phase transformation, microstructure and mechanical properties of ZrO2-based ceramics. Ceramics International 2018, 44 (5), 5371-5377.

[380] Arlt, G., The Influence Of Microstructure On The Properties Of Ferroelectric Ceramics. Ferroelectrics 1990, 104 (1), 217-227.

[381] Guo, H.Z., et al., *Structure evolution and dielectric behavior of polystyrene-capped barium titanate nanoparticles.* Journal of Materials Chemistry, 2012. **22**(45): p. 23944-23951.

[382] Verkerk, M.J., B.J. Middelhuis, and A.J. Burggraaf,. Solid State Ionics, 1982. **6**(2): p. 159-170.

[383] Aoki, M.; Chiang, Y. M.; Kosacki, I.; Lee, L. J. R.; Tuller, H.; Liu, Y., Solute segregation and grain-boundary impedance in high-purity stabilized zirconia. Journal of the American Ceramic Society 1996, 79 (5), 1169-1180.

[384] Guo, H., et al., *Cold sintering process for ZrO2-based ceramics: significantly enhanced densification evolution in yttria-doped ZrO2.* Journal of the American Ceramic Society, 2017. **100**(2): p. 491-495.

[385] Leng, H., et al., *Cold sintering and ionic conductivities of Na3.256Mg0.128Zr1.872Si2PO12 solid electrolytes.* Journal of Power Sources, 2018. **391**: p. 170-179.

[386] Jolley, A. G.; Cohn, G.; Hitz, G. T.; Wachsman, E. D., Improving the ionic conductivity of NASICON through aliovalent cation substitution of Na3Zr2Si2PO12. Ionics 2015, 21 (11), 3031-3038.

[387] Zhu, J.; Li, R.; Zhou, W.; Zhang, H.; Cheng, X., Fabrication of Al2O3-NaCl composite heat storage materials by one-step synthesis method. Journal of Wuhan University of Technology-Mater. Sci. Ed. 2016, 31 (5), 950-954.

[388] Kahari, H.; Teirikangas, M.; Juuti, J.; Jantunen, H., Improvements and Modifications to Room-Temperature Fabrication Method for Dielectric Li2MoO4 Ceramics. Journal of the American Ceramic Society 2015, 98 (3), 687-689.

[389] German, R.M., *Chapter Eleven - Mixed Powders and Composites*, in *Sintering: from Empirical Observations to Scientific Principles*, R.M. German, Editor. 2014, Butterworth-Heinemann: Boston. p. 355-385.

[390] Haynes, W. M., CRC Handbook of Chemistry and Physics. CRC Press: 2016.

[391] German, R.M., *Chapter Ten - Sintering With External Pressure*, in *Sintering: from Empirical Observations to Scientific Principles*, R.M. German, Editor. 2014, Butterworth-Heinemann: Boston. p. 305-354.

[392] Coble, R., Mechanisms of Densification During Hot Pressing in Sintering and Related Phenomena, edited by GC Kuczynski, NA Hooten, and CF Gibson. New York: Gordon and Breach: 1967.

[393] Agbadua, S.A., et al., *Thermal Cycling Effects on the Fatigue Behaviour of Low Carbon Steel.* Journal of Minerals and Materials Characterization and Engineering, 2011: p. 1345-1357.

[394] Maria, J. P.; Kang, X. Y.; Floyd, R. D.; Dickey, E. C.; Guo, H. Z.; Guo, J.; Baker, A.; Funihashi, S.; Randall, C. A., Cold sintering: Current status and prospects. Journal of Materials Research 2017, 32 (17), 3205-3218.

[395] Grady, Z.; Ndayishimiye, A.; Randall, C., A dramatic reduction in the sintering temperature of the refractory sodium β″-alumina solid electrolyte via cold sintering. Journal of Materials Chemistry A 2021, 9 (38), 22002-22014.

[396] Biesuz, M.; Taveri, G.; Duff, A. I.; Olevsky, E.; Zhu, D.; Hu, C.; Grasso, S., A theoretical analysis of cold sintering. Advances in Applied Ceramics 2020, 119 (2), 75-89.

[397] Alzukaimi, J.; Jabrah, R., The preparation and characterization of porous alumina ceramics using an eco-friendly pore-forming agent. International Journal of Applied Ceramic Technology 2019, 16 (2), 820-831.

[398] Ye, L.; Tang, C.; Chen, Y.; Yang, S.; Tang, M., The thermal physical properties and stability of the eutectic composition in a Na2CO3–NaCl binary system. Thermochimica Acta 2014, 596, 14-20.

[399] Kubaschewski, O., Metallurgical thermochemistry / by O.Kubaschewski, E.Ll.Evans and C.B.Alcock. 4th ed. revised & enlarged. ed.; Alcock, C. B.; Evans, E. L., Eds. Oxford: Pergamon: Oxford, 1967.

[400] Yadav, A.K. and S. Bhattacharyya, *A new approach for the fabrication of porous alumina beads using acid leachate of kaolin.* Microporous and Mesoporous Materials, 2019: p. 109795.

[401] Sotomayor, F.J., K. Cychosz, and M. Thommes. *Characterization of Micro / Mesoporous Materials by Physisorption : Concepts and Case Studies*. 2018.

[402] Sobhani, M., et al., *Preparation of macro-mesoporous γ-alumina via biology gelatin assisted aqueous sol-gel process.* Ceramics International, 2019. 45(1): p. 1385-1391.

[403] Ceron-Nicolat, B.; Fey, T.; Greil, P., Processing of Ceramic Foams with Hierarchical Cell Structure. Advanced Engineering Materials 2010, 12 (9), 884-892.
[404] Montanaro, L.; Jorand, Y.; Fantozzi, G.; Negro, A., Ceramic foams by powder processing. Journal of the European Ceramic Society 1998, 18 (9), 1339-1350.
[405] Colombo, P.; Hellmann, J. R.; Shelleman, D. L., Mechanical Properties of Silicon Oxycarbide Ceramic Foams. Journal of the American Ceramic Society 2001, 84 (10), 2245-2251.
[406] Dhara, S.; Bhargava, P., Influence of Slurry Characteristics on Porosity and Mechanical Properties of Alumina Foams. International Journal of Applied Ceramic Technology 2006, 3 (5), 382-392.
[407] Studart, A. R.; Gonzenbach, U. T.; Tervoort, E.; Gauckler, L. J., Processing Routes to Macroporous Ceramics: A Review. Journal of the American Ceramic Society 2006, 89 (6), 1771-1789.
[408] Tallon, C.; Chuanuwatanakul, C.; Dunstan, D. E.; Franks, G. V., Mechanical strength and damage tolerance of highly porous alumina ceramics produced from sintered particle stabilized foams. Ceramics International 2016, 42 (7), 8478-8487.
[409] Jamaludin, A. R.; Kasim, S. R.; Ismail, A. K.; Abdullah, M. Z.; Ahmad, Z. A., The effect of sago as binder in the fabrication of alumina foam through the polymeric sponge replication technique. Journal of the European Ceramic Society 2015, 35 (6), 1905-1914.
[410] Brezny, R.; Green, D. J., Uniaxial Strength Behavior of Brittle Cellular Materials. Journal of the American Ceramic Society 1993, 76 (9), 2185-2192.
[411] Rice, R. W., Limitations of pore-stress concentrations on the mechanical properties of porous materials. Journal of Materials Science 1997, 32 (17), 4731-4736.
[412] Chen, Z.; Brandon, N., Inkjet printing and nanoindentation of porous alumina multilayers. Ceramics International 2016, 42 (7), 8316-8324.
[413] Rice, R. W., Evaluation and extension of physical property-porosity models based on minimum solid area. Journal of Materials Science 1996, 31 (1), 102-118.
[414] Rahaman, M.N., *Sintering of ceramics*. 2007: CRC press.
[415] Chang, Y.; Wu, J.; Zhang, M.; Kupp, E.; Messing, G. L., Molten salt synthesis of morphology controlled α-alumina platelets. Ceramics International 2017, 43 (15), 12684-12688.
[416] International Conference on Molten Slags, F., et al. *Molten 2009 : proceedings of the VIII International Conference on Molten Slags, Fluxes & Salts, 18-21 January 2009, Santiago, Chile*. Concepción, Chile: Universidad de Concepción, Department of Metallurgical Engineering
[417] Korotin, M.A., Kurmaev, E.Z. Electronic Structure of Aluminum Oxide with Oxygen Vacancies. *Phys. Metals Metallogr* 2018, 119, 707–712
[418] Kaveh E., Ikuro F., Shuhei T., Yuki N., Kazuki K., Hadi R., Makoto A., Motonori W., Xavier S., Taner A., Tatsumi I., Masayoshi F., Zenji H. Photocatalytic activity of aluminum oxide by oxygen vacancy generation using high-pressure torsion straining. Scripta Materialia, 173, 120-124.
[419] Mao-Sheng Miao and Roald Hoffmann. Accounts of Chemical Research 2014, *47* (4), 1311-1317.
[420] Zhang, W., Oganov, A. R., Goncharov, A. F., Zhu, Q., Boulfelfel, S. E., Lyakhov, A. O., , Konôpková, Z. (2013). Unexpected stable stoichiometries of sodium chlorides. *Science, 342*(6165), 1502-1505.
[421] Lin, J., Du, X., Yang, G. (2019). Pressure-induced new chemistry. Chinese Physics B 2019, 28(10), 106106.

[422] Jeurgens, L. P. H., Sloof, W. G., Tichelaar, F. D., Mittemeijer, E. J. (2002). Growth kinetics and mechanisms of aluminum-oxide films formed by thermal oxidation of aluminum. Journal of applied physics, 92(3), 1649-1656

[423] Kimura T. "Molten salt synthesis of ceramic powders." Advances in ceramics-synthesis and characterization, processing and specific applications 2011, 75-100.

[424] Katz, E. (2021). Electrochemical contributions: Sir Humphry Davy (1778–1829). Electrochemical Science Advances, 1(2), e2160004.